UNIVERSIDAD NACIONAL AUTÓNOMA DE MÉXICO
PROGRAMA DE POSGRADO EN CIENCIAS DE LA TIERRA
INSTITUTO DE GEOFÍSICA

"Caracterización morfométrica de las edades y evolución post-eruptiva de conos volcánicos monogenéticos a partir de modelos digitales de elevación".

TESIS
QUE PARA OPTAR POR EL GRADO DE:
DOCTORA EN CIENCIAS DE LA TIERRA

PRESENTA:
MARIA CRISTINA ZARAZÚA CARBAJAL

DR. SERVANDO DE LA CRUZ REYNA
INSTITUTO DE GEOFÍSICA

DRA. MARIE-NOËLLE GUILBAUD
INSTITUTO DE GEOFÍSICA
DR. JUAN MANUEL ESPÍNDOLA
INSTITUTO DE GEOFÍSICA

CIUDAD UNIVERSITARIA, CD. MX., DICIEMBRE 2021

De adentro viene el golpe,
la cabalgata sombría,
la estampida de lo invisible,
explosión de lo que suponemos
inmóvil
y bulle siempre.

J. Emilio Pacheco

AGRADECIMIENTOS

La realización de este trabajo no habría sido posible sin el apoyo de muchas personas.

Agradezco a mi asesor, el Dr. Servando De La Cruz Reyna, por brindarme la oportunidad de trabajar con él, por su paciencia, motivación, interés, tiempo dedicado, discusiones sobre el tema y la vulcanología en general y sobre todo por la excelente orientación y acompañamiento que me ayudaron a mantener claro el objetivo de este trabajo. Fue un verdadero gusto.

A mi comité académico, la Dra. Marie-Noelle Guilbaud y el Dr. Juan Manuel Espíndola, por sus comentarios, cuestionamientos durante todo el desarrollo del trabajo.

A los miembros del Jurado: Dra. Marie-Noelle Guilbaud, Dr. Denis Legrand, Dr. Lorenzo Vázquez Selem y Dr. Javier Carrera Hernández, por sus comentarios y el tiempo dedicado a revisar esta Tesis.

A Araceli Chamán por su excelente disposición y el apoyo en cada trámite.

A la Universidad Nacional Autonoma de México, en especial al Posgrado en Ciencias de la Tierra.

A Mariana, Patricia y Manuel Z. por siempre estar ahí, apoyando hasta en los trámites.

A Lula por siempre estar dispuesta a corregir mi escritura en inglés.

A Rosy y César por ayudarme a tener todas esas horas extra para trabajar.

A Manuel por todo el apoyo y a Valentina, por mantenerme con los pies en la tierra y la mente en el presente.

ÍNDICE

CAPÍTULO 1: **5**

INTRODUCCIÓN

CAPÍTULO 2: **10**
ARTÍCULO: Morfocronología de los conos de escoria monogenéticos a partir de sus curvas de nivel. Aplicaciones al campo monogenético de Chichinautzin, Centro de México.

Morpho-chronology of monogenetic cones from their level contour curves and vertical cross sections. Applications to the Chichinautzin monogenetic field, Central Mexico.
Zarazúa-Carbajal,M.C. and De la Cruz-Reyna, S. (2020) .
Journal of Volcanology and Geothermal Research. Vol 407C, 107093.
https://doi.org/10.1016/j.jvolgeores.2020.107093

CAPÍTULO 3..... **29**

ARTÍCULO: Efectos de la resolución del modelo de elevación digital: sobre el análisis morfológico orientado a la cronometría de conos de escoria en un extenso campo volcánico, la Sierra Chichinautzin, centro de México.

Digital Elevation Model resolution: Effects on the chronometry-oriented morphological analysis of scoria cones in an extensive volcanic field, the Sierra Chichinautzin, central Mexico.
Zarazúa-Carbajal,M.C. and De la Cruz-Reyna, S. (2021) .
Geomorphology, Vol 389, 107842.
https://doi.org/10.1016/j.geomorph.2021.107842

CAPÍTULO 4..... **48**

ARTÍCULO: Una aplicación de Matlab para calcular el grado de erosión relacionado con la edad de conos de escoria monogenéticos a partir de Modelos Digitales de Elevación.

A MATLAB App for calculating the age-related degree of erosion of monogenetic scoria cones from DEM data.
Zarazúa-Carbajal,M.C. and De la Cruz-Reyna, S. (2021) .
MethodsX, Vol 8c, 101454
10.1016/j.mex.2021.101454

CAPÍTULO 5: **84**

CONCLUSIONES

CAPÍTULO 6: **90**

TRABAJO A FUTURO

APÉNDICE: **92**

PARÁMETROS MORFOMÉTRICOS DE LOS CONOS ANALIZADOS

REFERENCIAS..... **106**

CAPÍTULO 1

INTRODUCCIÓN

La evaluación del peligro asociado a volcanes centrales (poligenéticos) ha mostrado avances considerables en los últimos 50 años. Sin embargo, el problema que representa la determinación del peligro asociado a una actividad eruptiva espacialmente dispersa, como es el caso del vulcanismo monogenético, no ha mostrado el mismo grado de avance, aun cuando los campos volcánicos monogenéticos (CVM) representan la manifestación más abundante de vulcanismo sub-aéreo en la Tierra y están presentes en todos los ambientes tectónicos (Kereszturi y Németh, 2012). Grandes ciudades, como la Ciudad de México o Auckland, por citar algunos ejemplos, están construidas sobre CVM activos o muy cercanas a ellos. Los suelos fértiles de estas regiones en todo el mundo están por lo general densamente poblados, por lo que es de gran importancia desarrollar metodologías específicas de evaluación del peligro y el riesgo asociados a este tipo de vulcanismo. Esta situación requiere determinar la evolución espacio-temporal de los campos volcánicos, lo que implica obtener el mayor número posible de fechamientos de conos individuales. Para ello, considerando la gran abundancia de conos monogenéticos, es necesario desarrollar métodos de fechamiento complementarios a los radiométricos que estén basados en características más fácilmente cuantificables, como es la morfología de los conos.

El fechamiento basado en características morfométricas de conos volcánicos, como la razón entre la altura del cono y el diámentro de su base (H/Wco), o el valor de las pendientes de sus flancos, ha sido usado ampliamente para estimar las edades aproximadas de conos de escoria en distintos campos volcánicos en el mundo, como por ejemplo, el campo volcánico de San Francisco (Wood, 1980b), la Sierra Chichinautzin (Bloomfield, 1975; Martin del Pozo, 1982, Nieto y Martin del Pozo, 2019), el CVM de Michoacán-Guanajuato (Hasenaka y Carmichael, 1985), de Colima (Hooper and Sheridan, 1994), y de Bakony–Balaton en Hungría (Kereszturi et al, 2012). Dicho método

parte del supuesto de que los conos adquieren un valor fijo del parámetro H/Wco cercano a 0.18 al momento de su formación, determinado por el ángulo de reposo de tefra en el rango de tamaños de partícula entre 1 y 10 cm en una pendiente libre (Porter, 1972), y qué tanto esa razón de aspecto, como la pendiente de los flancos varían en forma casi lineal con la edad (Porter, 1972, Hasenaka y Carmichael, 1985). La suposicion sobre la igualdad en el estado inicial de la morfología para todos los conos resulta en una incertidumbre en ese tipo de fechamiento morfométrico, ya que debido a la complejidad de los procesos de formación de volcanes es difícil sostener que todos ellos tengan como resultado conos con la misma morfología inicial (Keresztury et al., 2012, Bemis y Ferencz, 2017). Por ello, la principal crítica a la consistencia de los fechamientos de conos de escoria monogenéticos basados en características morfométricas, principalmente la razón de aspecto (*H/Wco*) se enfoca en el desconocimiento de las morfologías iniciales, resultantes de los procesos de formación particulares para cada cono de escoria. Algunas propuestas alternativas al uso de la razón de aspecto para caracterizar el grado de erosión de un cono consisten en inferir el volumen de material removido, tomando como referencia morfologías ideales (Dohrenwend et al. 1986, Parrot, 2007). Estos aspectos se discuten en detalle en el Capítulo 3, en la primera parte del artículo (Zarazúa-Carbajal y De la Cruz-Reyna , 2021a) .

Por lo anterior, para desarrollar nuevos métodos morfométricos de fechamiento de conos monogenéticos, es necesario buscar alternativas independientes, o menos sensibles al estado inicial de la morfología del cono.

Esta investigación doctoral parte de la hipótesis de que existe una relación entre el estado de degradación erosiva de un cono de escoria y su edad, el cual puede ser medido a partir de cambios cuantificables en sus características morfológicas. Los cambios se miden respecto a un estado morfologico inicial, que no necesariamente es el mismo en todos los casos, y que puede ser descrito por medio del análisis morfométrico del relieve actual de la geoforma. Dicha hipótesis consideda además que el estado de degradación erosiva de un cono monogenético se puede separar en dos componentes geométricas:

1) Una componente de degradación vertical, consecuencia del transporte del material hacia abajo por las laderas del cono volcánico y 2) una componente de degradación horizontal, que se manifiesta con la formación de canales y cárcavas sobre la superficie de la estructura volcánica. Las modificaciones en ambos componentes pueden ser unívocamente cuantificadas en parámetros independientes y existe una relación funcional entre dichos parámetros y la edad del cono.

Como resultado del trabajo doctoral se desarrolló una metodología para cuantificar con un solo parámetro un índice de erosión promedio (*AEI*) que describe la presencia, cantidad, anchura y profundidad de cárcavas en un cono de escoria a distintas elevaciones. Asimismo se establecen las capacidades de dicho factor como un nuevo parámetro morfocronométrico que permite la estimación remota de las edades de conos de escoria en un campo monogenético a partir de modelos digitales de elevación del terreno con resoluciones suficientes. El estudio incluye los resultados obtenidos al analizar y correlacionar los conos de escoria de la Sierra del Chichinautzin que han sido fechados radiométricamente.

Esta metodología esta basada en el análisis de las curvas de contorno de cada edificio volcánico obtenidas de modelos digitales de elevación (MDE) en un rango de resoluciones de hasta 12 m. Dicho análisis se realiza utilizando Descriptores Elípticos de Fourier (DEF), un método para el estudio morfométrico de curvas cerradas, es decir, que separan el espacio en dos áreas, una de las cuales es necesariamente limitada, pero no necesariamente holomórfica, esto es, que líneas radiales emitidas desde un centroide de la forma pueden interceptarla en dos o más puntos. Los DEF consisten de una expansión del contorno cerrado como una suma de elipses que corresponden a los coeficientes del desarrollo en series de Fourier de las posiciones de los puntos que conforman el contorno (Kuhl and Giardina, 1982; Schmittbuhl et al., 2003). La metodología de análisis de los contornos de elevación utilizados en este trabajo se describe en detalle en la primera parte del Capítulo 2, en el artículo de Zarazúa-Carbajal y De la Cruz-Reyna (2020) que lo conforma, y su implemetación en códigos de Matlab se describe en el Capítulo 4, en el artículo de MethodsX (Zarazúa-Carbajal y De la Cruz-Reyna , 2021b).

El fechamiento de conos monogeneticos de escoria es fundamental para analizar el peligro y evaluar el riesgo asociado a los campos volcánicos monogenéticos. Mexico tiene varios campos monogenéticos, entre los cuales destacan tres considerados activos, el campo volcánico Michoacán-Guanajuato, que contiene la mayor concentración de bocas monogenéticas del mundo asociadas con vulcanismo continental derivado de subducción (Hasenaka y Carmichael, 1985; Connor, 1987; Ban et al., 1992 ;Hasenaka, 1994; Guilbaud et al., 2011; Ownby et al., 2011; Guilbaud et al., 2012; Siebe et al., 2014; Gómez-Vasconcelos et al., 2015; Chevrel et al., 2016; Kshirsagar et al., 2016; Mahgoub et al. , 2017; Reyes-Guzman et al., 2017; Reyes-Guzman et al., 2018; Osorio-Ocomapo et al., 2018; Larrea et. al., 2019; Avellán et al., 2020; Gómez-Vasconcelos et al., 2020; Gómez-Vasconcelos et al., 2021; Guilbaud et al. 2021), el campo volcánico de la Sierra del Chichinautzin (Bloomfield, 1975; Martin Del Pozzo, 1982; Kirianov et al., 1990; Siebe, 2000; Siebe et al., 2004; Siebe et al., 2005; Agustín-Flores et al., 2011; Guilbaud et al., 2015; Arce et al., 2013; Arce et al., 2015; Jaimes-Viera et al., 2018), ambos con actividad histórica y el campo volcánico de los Tuxtlas, cuyo origen y evolución representan un reto y en el que la actividad histórica se asocia al San Martín Tuxtla, un volcán poligenético ubicado en la parte central del campo monogenético (e.g. Espíndola et al., 2016; Sieron et al., 2021).

La existencia de modelos digitales de elevacion (MDE, o DEM en inglés) de alta resolución brindan la opción de estudiar áreas extensas de terreno de una manera sistemática y rápida. En el caso particular de los campos volcánicos monogenéticos, los MDE son una herramienta muy útil para obtener en forma extensiva carácteristicas morfométricas de conos volcánicos, que reflejen su estado actual de degradación, al menos en términos relativos. Asimismo, en complemento con los estudios de campo y fechamientos radiométricos disponibles, pueden usarse para desarrollar y probar métodos morfométricos de fechamiento de conos de escoria, y con ellos obtener posibles escenarios de evolución espacio temporal de los campos volcánicos monogenéticos, en forma eficiente.

Recapitulando, en esta tesis se integran los resultados de tres ramas de un proyecto de investigación, cuyos resultados convergen en tres artículos publicados alrededor de un objetivo común: La caracterización morfocronométrica de conos de escoria en campos monogenéticos. El primero se enfoca en describir el método propuesto y desarrollado para la caracterización de la erosión en la componente horizontal, el segundo introduce algunas modificaciones a los métodos tradicionalmente utilizados para la caracterización morfométrica de la erosión en la componente vertical, así como la influencia de la resolución de los modelos digitales de elevación en las caracterizaciones morfométricas de ambas componentes erosivas (horizontal y vertical) y se establecen los rangos mínimos de resolución para este tipo de análisis. El tercer artículo presenta el desarrollo de las metodologías y los códigos para aplicar las metodologías propuestas a cualquier cono de escoria que mantenga algunas características mínimas de volumen y simetría, y que cuente con algún tipo de modelo digital de elevación en un rango de resoluciones que incluye bases de datos aéreas y satelitales.

CAPITULO 2

MORFOCRONOLOGÍA DE LOS CONOS DE ESCORIA MONOGENÉTICOS A PARTIR DE SUS CURVAS DE NIVEL. APLICACIONES AL CAMPO MONOGENÉTICO DE CHICHINAUTZIN, CENTRO DE MÉXICO

En este artículo (https://doi.org/10.1016/j.jvolgeores.2020.107093), publicado en el "*Journal of Volcanology and Geothermal research*" se introducen las bases teóricas del método propuesto para la cuantificación del estado relativo de erosión en la componente horizontal de un cono de escoria, a partir del análisis de sus curvas de nivel. Además, se presentan los resultados de aplicar el método a 19 conos, fechados por métodos radiométricos, de la Sierra del Chichinautzin.

A continuación se resume el contenido del artículo:

La génesis, distribución y peligros asociados con los campos volcánicos monogenéticos plantean dificultades particulares derivadas de su carácter disperso. Para comprender mejor la naturaleza de la génesis y evolución de los campos volcánicos monogenéticos, así como para establecer criterios más precisos de evaluación del peligro asociado a ellos, es necesario establecer una relación entre las distribuciones espacial y de edad de los conos volcánicos que los conforman. En este trabajo se presenta un nuevo método, desarrollado específicamente para cuantificar el grado de erosión dependiente de la edad de conos de escoria individuales, y cuyo objetivo es estimar las edades relativas de conos no fechados pertenecientes a un mismo campo volcánico monogenético. Esto se logra a partir de un análisis morfométrico de las curvas de contorno de los conos, obtenidas a partir de Modelos digitales de elevación (MDE). Este método se basa en la hipótesis de que la edad y el grado y tipo de erosión que provocan cambios morfológicos significativos en los conos de escoria están unívocamente correlacionados. Se supone que, en el momento de su formación, los volcanes monogenéticos tienen formas diversas pero caracterizadas por superficies suaves o lisas, que se van modificando gradualmente debido a procesos mecánicos de

desgaste erosivo en función del tiempo. Esta evolución en la morfología se evidencia tanto como cambios en las laderas del volcán, como con la formación de ondulaciones de la superficie. Estas ondulaciones, que son principalmente cárcavas o canales generadas por la ablación hidrometeorológica, se manifiestan en las curvas de nivel obtenidas de los MDE, que, de no haber erosión, se asume serían lisas y uniformes. En este trabajo, se determina la dependencia del tiempo en la forma y el tamaño de las ondulaciones de las curvas de nivel de los conos volcánicos, mediante un análisis basado en los Descriptores Elípticos de Fourier de cada curva de contorno. Para probar los efectos del tipo y resolución de los datos MDE en este fechamiento morfocronológico, se analizan las correlaciones de edades radiométricas de conos publicadas con el análisis de las curvas de contorno obtenidas de dos bases de datos independientes del campo volcánico monogenético de la Sierra Chichinautzin en el centro de México (SCVF): uno obtenido mediante LIDAR aerotransportados (INEGI, México) y el otro, de una misión de radar satelital (TanDEM-X DLR, Alemania).

Journal of Volcanology and Geothermal Research 407 (2020) 107093

Contents lists available at ScienceDirect

Journal of Volcanology and Geothermal Research

journal homepage: www.elsevier.com/locate/jvolgeores

Morpho-chronology of monogenetic scoria cones from their level contour curves. Applications to the Chichinautzin monogenetic field, Central Mexico

María Cristina Zarazúa-Carbajal [a,*], Servando De la Cruz-Reyna [b]

[a] Posgrado en Ciencias de la Tierra, Instituto de Geofísica, Universidad Nacional Autónoma de México (UNAM), CDMX 04510, Mexico
[b] Instituto de Geofísica, Universidad Nacional Autónoma de México (UNAM), CDMX 04510, Mexico

ARTICLE INFO

Article history:
Received 24 March 2020
Received in revised form 2 October 2020
Accepted 14 October 2020
Available online 17 October 2020

Keywords:
Monogenetic volcanism
Sierra Chichinautzin Volcanic Field
Volcano relative dating
Volcano morphology
Morpho-chronology
Scoria cones
Elliptic Fourier descriptors

ABSTRACT

The genesis, distribution and hazards associated with monogenetic volcanic fields pose particular difficulties derived from their dispersed character. Establishing a relationship between the spatial and the age distributions of volcanic cones is necessary both to understand the nature of monogenetic field formation and evolution and to set supported hazard-assessment criteria. We present here a new method –specifically developed to quantify the degree of age-dependent erosion of individual scoria cones– aimed to estimate the relative ages of undated scoria cones in a monogenetic volcanic field from a contour level morphometric analysis of the field digital elevation model (DEM). This method is based on the hypothesis that age and the degree and type of erosion causing significant morphological changes on scoria cones are markedly correlated. It is assumed that, at the time of their formation, monogenetic volcanoes have diverse, yet smooth shapes, which mechanical processes of wearing gradually change in different spatial scales. This evolution is largely evidenced both as changes of the volcano slopes and as height-dependent undulations of the cone surface generated by the hydrometeorological ablation in the otherwise uniform elevation contour lines. Here, we characterize the time-dependence of the shape and size of the altitude isoline undulations by means of the Elliptical Fourier Descriptor spectra of the contour curves of volcanic cones. To test the effects of the DEM data type and resolution on this morpho-chronological dating, we analyze the correlations of published radiometric ages of cones with two datasets of contour curves from the Sierra Chichinautzin monogenetic volcanic field in Central Mexico (SCVF): one obtained from airborne LIDAR surveys (INEGI, Mexico) and the other from a satellite radar mission (DLR, Germany).

1. Introduction

Monogenetic volcanic fields (MVF) constitute the most widespread manifestation of sub-aerial volcanism on Earth (Smith and Németh, 2017). Since many cities and infrastructure works are settled upon or near potentially active MVF, the assessment of the hazard this type of volcanism poses is a priority. This requires a broad understanding of the age-constraints of the field (Connor and Hill, 1995; Condit and Connor, 1996; Conway et al., 1998; Bebbington and Cronin, 2011; Marrero et al., 2019; Nieto-Torres and Martin Del Pozzo, 2019). Without such information, a time-sensitive hazard assessment of extensive monogenetic volcanic fields becomes a challenging task. In addition, given that radiometric dating is difficult and expensive for MVF comprised of hundreds or thousands of cones, developing alternative techniques to efficiently estimate the age of volcanic cones is a need that we intend to address here.

Morpho-chronologic dating based on shape parameters, such as the aspect height-to-base diameter ratio (*Ar*), has been widely used to estimate the age of scoria cones. This method has been applied worldwide to different volcanic areas, for example, the San Francisco Volcanic Field (Wood, 1980), the Sierra Chichinautzin volcanic field (Bloomfield, 1975; Martin del Pozzo, 1982; Nieto-Torres and Martin Del Pozzo, 2019), Colima (Hooper, 1995), and the Bakony–Balaton Highland Volcanic Field in Hungary (Kereszturi and Németh, 2012a). The method assumes that scoria cones acquire a predetermined value of *Ar* at the time of their formation (Porter, 1972) and the variation of *Ar* results from time-dependent erosional processes. Such processes were modeled in detail using a diffusive-transport model by Hooper and Sheridan (1998). However, it has been argued that dating based on the aspect ratios or flank slopes may be highly uncertain. This is because the notion of all scoria cones having the same, or very similar, initial aspect ratios and slopes is difficult to support due to the complexity of the

* Corresponding author.
E-mail address: mariac.zarazua@gmail.com (M.C. Zarazúa-Carbajal).

https://doi.org/10.1016/j.jvolgeores.2020.107093
0377-0273/

volcano formation processes (Kervyn et al., 2012; Kereszturi and Németh, 2012a, 2012b; Bemis and Ferencz, 2017).

The use of a parameter reflecting erosional features in the horizontal direction, less dependent on the initial shape, should contribute to improve the accuracy of morphometric dating. Among the earliest efforts in that direction are the works by Dohrenwend et al., (1986). Based on eleven radiometrically dated cinder cones from the Cima Volcanic Field in the Mojave Desert, California, USA; they observed that under arid and semi-arid climate conditions, the progressive development of the drainage networks –related to the vertical cross-section erosional processes– was also an age-dependent parameter by itself. In addition, they quantified this dependence as an increasing "drainage-way volume loss" characterized by a morphological evolution of the cone surface from scattered, irregular, small-volume rills and gullies, to more regular, deeper, wider, and longer gullies with larger cumulative volumes. Similarly, Hasenaka and Carmichael (1985) reported that the density of gullies on a cone surface resulted in an age-related erosional feature, where the number of gullies per 90 degrees of arc decreased as a function of age; this, visually determined from aerial photography of seven scoria cones (<40 ka) in the Michoacán-Guanajuato Volcanic Field in Central Mexico. Using a similar approach, Bemis (1995) compared the number of gullies to the cone dimensions of 106 cinder cones in the Ipala Graben in South-East Guatemala. However, she failed to find a significant correlation between age and that parameter concluding that the volcanic cones were poorly eroded in that region.

In a different environment, Dóniz et al. (2011) also studied gully density and mean length dependence on age in seventeen scoria cones of Tenerife, Canary Islands. Using 1:10,000 topographic maps, 1:25,000 geological maps and 1:18,000 aerial photographs, they found that most Pleistocene cones had characteristically well-developed gullies. However, they also noticed some ambiguity in the age dependence of gully formation on Holocene cones emplaced on areas with broad topographical gradients, likely caused by the existence of previously developed hydrological networks.

Here, we propose a new morpho-chronologic method based on a nonlinear advective-diffusive description of erosion, where material is transported downwards and sideward causing the formation of age-dependent gullies with diverse geometries. The lack of significant runoff, caused by the high infiltration capacity in young scoria cones, inhibits the formation of deep gullies (Hooper and Sheridan, 1998). Over the course of time, unevenly spaced rills, usually forming on the lower cone slopes, result in incipient gully formation. In older cones, the rills and gullies increase in length, width and depth evolving into large, widely spaced ravines. In the following sections we develop a methodology to quantify such process combining different erosion-related variables into a single contour-shape parameter, which provides a potential measure of the age of scoria cones. This parameter $<D>$, obtained from the analysis of the level contour curves is compared with available radiometric ages of monogenetic volcanoes purporting to establish a new morpho-chronologic criterion to readily estimate the ages of other non-dated cones in the same volcanic field, or in volcanic fields with similar geographic and climatic conditions. Hence, by correlating that contour shape parameter, calculated from two different digital elevation models (DEM), with published radiometric ages of selected scoria cones of the Sierra Chichinautzin, (and a few from the Michoacán-Guanajuato) monogenetic fields in Mexico, we introduce an alternate morpho-chronometric functional relationship.

2. The Sierra Chichinautzin monogenetic volcano field

The Sierra Chichinautzin volcanic field (SCVF) is located in the central trans-Mexican volcanic belt (TMVB), extending from the east of Toluca Valley to the west of Popocatepetl volcano in the most densely populated region of central Mexico (Fig. 1). It comprises more than 220 monogenetic volcanoes, mostly scoria cones, as well as shield volcanoes and maars (Márquez et al., 1999). The most recent eruption was Xitle (Delgado et al., 1998; Siebe, 2000), which was born about 1600 yr BP (Siebe, 2000) in a currently suburban region of southern Mexico City.

Most of the SCVF activity probably began in the late Pleistocene (Bloomfield, 1975; Martin del Pozzo, 1982). However, Arce et al. (2013) located a group of scoria cones with ages over 1 Ma further to the west and south-west. Recently, Jaimes-Viera et al. (2018) divided the SCVF in four fields, based on chemical analyses, $^{40}Ar/^{39}Ar$ dates, morphometric analysis, and the spatial distribution of 227 volcanoes: The Young Chichinautzin Volcanic Field, with cones younger than 35 ka; the Older Chichinautzin Volcanic Field, with cone ages ranging from 238 to 85 ka; the Peñón Monogenetic Volcanic Group, comprising cones in the range 1274–765 ka; and the Sierra Santa Catarina, with ages ranging from 132 to 2 ka.

In our study we consider scoria cones from the previously mentioned monogenetic volcanic sub-fields, and include also scoria cones from the Tenango monogenetic volcanic field, which Bloomfield (1975) considers part of the Chichinautzin Volcanic Field. Additionally, we choose the SCVF due to its high concentration of monogenetic cones in the heavily populated central part of the Mexican Volcanic Belt, a region with similar highland climatic conditions throughout its extension. Furthermore, two separate digital elevation datasets, with different spatial resolutions, were available for this area, as well as a relatively high number of published radiometric datings of scoria cones (about 41 to the date of this submission: Bloomfield, 1975; Kirianov et al., 1990; Siebe, 2000; Velasco-Tapia and Verma, 2001; Siebe et al., 2004; Siebe et al., 2005; Agustín-Flores et al., 2011; Arce et al., 2013; Guilbaud et al., 2015; Kshirsagar et al., 2015; Jaimes-Viera et al., 2018; Alcalá-Reygosa et al., 2018).

2.1. Digital elevation models of the Chichinautzin Volcanic Field

The two digital elevation model databases (DEM) used in this work cover the majority of the SCVF. The first, which covers the whole monogenetic field, is a satellite synthetic-aperture radar DEM, kindly provided by Tandem-X Satellite from the German Space Center (DLR), and will hereafter be referred as DLR. It has a 12 m horizontal resolution and 2–4 m (depending on slope) vertical resolution. The second, which covers approximately 60% of the SCVF, is a light detection and ranging (LIDAR) DEM, generously provided by the Mexican National Institute of Statistics and Geography INEGI, and will hereafter be referred as LIDAR. It has 5 m horizontal resolution, and 1 m vertical resolution.

3. A new morpho-chronological formulation

Morpho-chronological determination of the scoria cones' age distribution in a monogenetic volcanic field involves the assumption that all cones in the study area have been exposed to similar erosive conditions (e.g. climate, grain size and composition, tectonic activity), and that the cumulative effects of erosion over a cone's surface is a function of time. Therefore, quantifying the degree of erosion of cones can lead to a measure of the cones' age, or at least of their relative ages (Fig. 2). The most commonly used measure of the age-dependent erosion is the height-to-base diameter ratio of a cone, *Ar*, which involves the additional assumption that all cones have the same *Ar* at the time of their formation (Porter, 1972). Attempting to avoid the need of that assumption, we present here a method to estimate a measure of the time-dependent erosion in terms of the level of development of gullies and rills on the surface of the cones (hereafter concisely referred as "horizontal erosion", in contrast with the *Ar* measure of "vertical erosion"). Instead, we start from the premise that the surface of the cones have smooth contours at the time of the cone's formation. Younger cones are expected to have smoother surfaces, perhaps with some narrow rills (left cone of Fig. 2), while older

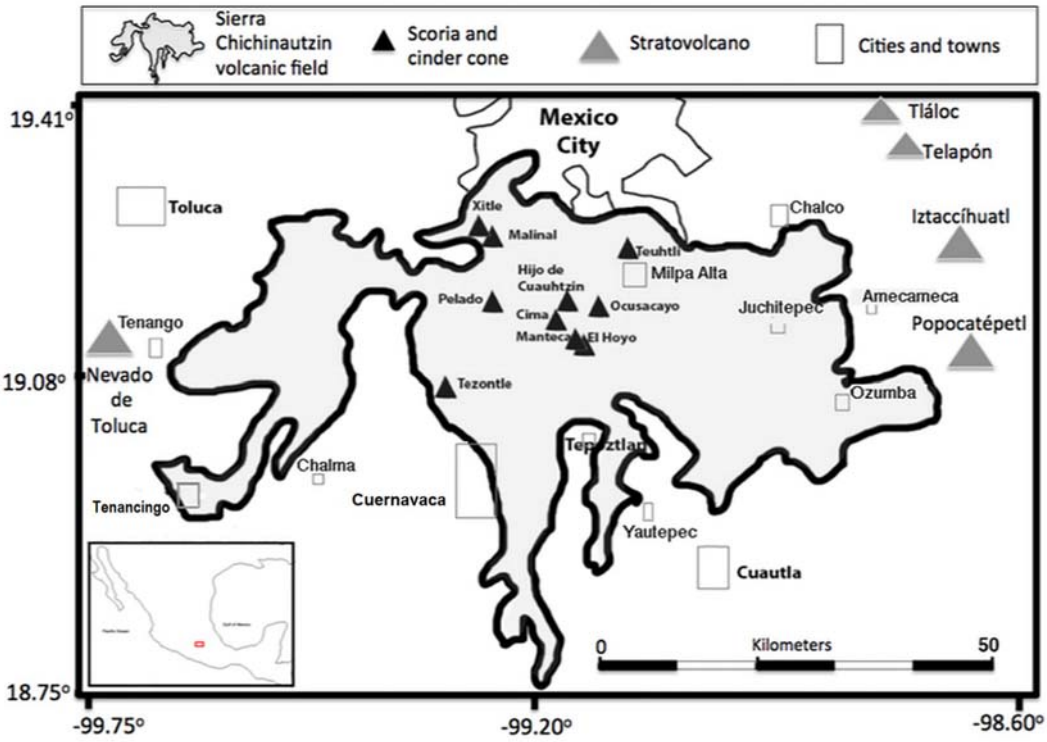

Fig. 1. The Sierra Chichinautzin Volcanic Field. Gray triangles are major polygenetic volcanoes. Black triangles represent some of the C^{14} -dated monogenetic cones. Rectangles are major towns. The thin black line marks the southern limits of Mexico City's political division, which is smaller than the actual metropolitan area.

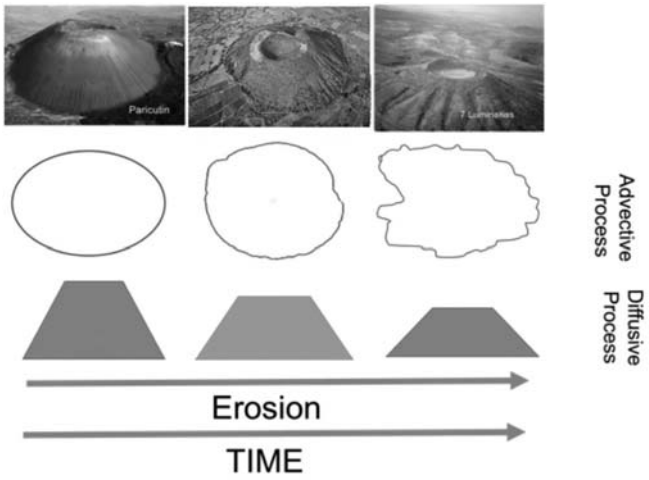

Fig. 2. Some basic features of the age-dependent morphological evolution of an increasingly eroded scoria cone, schematically represented in the horizontal and vertical planes.

cones should present deeper and larger rills and gullies irregularly distributed across their surface (right cone of Fig. 2).

3.1. Quantifying "horizontal erosion"

In this section, we introduce a conceptual framework and methodology aimed to quantify in a single parameter the "horizontal" erosional state of a scoria cone, capable of describing the effects of the time-dependent erosion on the surface of the cone. This is accomplished by measuring the degree of erosion in terms of the development of hydrologic features on the surface of monogenetic cones, through an innovative analysis of the level contour curves obtained from the available DEMs of an MVF.

This contour shape analysis requires a mathematical tool capable of uniquely characterizing complex closed lines, including non-holomorphic shapes (irregular shapes where the polar coordinate vector may intersect the contour curve in more than one point). A tool that has proven useful in describing and characterizing such complex contours is the Elliptical Fourier Descriptor, EFD, (Kuhl and Giardina, 1982). It has been successfully used to describe shapes in many biological, paleontological and anthropological studies (e.g. Tort, 2003; Guy et al., 2008; Soares et al., 2011), and to characterize complex geodetic features of different structures (e.g. Schmittbuhl et al., 2003; Tort and Finizola, 2005).

The main idea behind our approach is to characterize the relative erosional state of different scoria cones in a volcanic field with similar climatic conditions, by means of an EFD analysis of the level contour curves. The EFD method measures a key age-dependent erosion signature: the degree in which gullies and rills have developed and distributed on the surface of a cinder cone. In the following sections, we describe the properties of EFD, and its applications to the morphometric characterization of such monogenetic volcanoes.

3.1.1. Elliptical Fourier Descriptors

EFD can be applied to any closed contour with perimeter Q. Sampling of this curve generates an array $N(x,y)$, composed by n points with Cartesian coordinates (x,y). To describe any shape of a contour, the coordinates of each point should be parametrized as a function of a third quantity q, that is $(x(q),y(q))$, where q marks the sequential position of each point sampled along the contour (Fig. 3).

Then, $x(q)$ and $y(q)$ become bijective (holomorphic) functions of q, hence an expansion in Fourier Series can be performed. Such expansion is expressed in matrix notation (Kuhl and Giardina, 1982; Schmittbuhl et al., 2003) by:

$$\mathbf{N}(q) = \mathbf{A_0}(q) + \sum_{j=1}^{m} \mathbf{A}_j(q)\cdot\mathbf{M}_j(q) \tag{1}$$

where j denotes the order of each single harmonic, and m is the number of harmonics required to fully reconstruct the contour $N(x,y)$. The maximum value of m is limited by the Nyquist frequency (k_{Nyquist}), corresponding to half the total number of points constituting the curve $N(x, y)$ (Kuhl and Giardina, 1982). For our analysis, we introduce an additional index k ($1 \le k \le m$) representing the number at which the summation in Eq. (1) may be truncated to analyze the shape of a contour partially reconstructed with k harmonics, and to assess the contribution of each additional single harmonic j to that shape. Henceforth k will be referred as the harmonic contents, and j as the particular harmonic which increases k by 1.

Eq. (1) represents a point-wise reconstruction of the curve $\boldsymbol{N}(q)$ in the Fourier basis $\mathbf{M}_j(q)$ where:

$$\mathbf{N}(q) = \begin{bmatrix} x(q) \\ y(q) \end{bmatrix} \tag{2}$$

$$\mathbf{A_0}(q) = \begin{bmatrix} a_0 \\ c_0 \end{bmatrix} \tag{3}$$

$$\mathbf{A_j}(q) = \begin{bmatrix} a_j & b_j \\ c_j & d_j \end{bmatrix} \tag{4}$$

$$\mathbf{M_j}(q) = \begin{bmatrix} cos\left(\frac{2j\pi q}{Q}\right) \\ sin\left(\frac{2j\pi q}{Q}\right) \end{bmatrix} \tag{5}$$

The coefficients a_j, b_j, c_j, d_j from $\mathbf{A}_j(q)$ are calculated by:

$$a_j = \frac{1}{2j^2\pi^2}\sum_{i=1}^{n}\frac{\Delta x_i}{\Delta t_i}\left[cos\left(\frac{2j\pi q_i}{Q}\right) - cos\left(\frac{2j\pi q_{i-1}}{Q}\right)\right] \tag{6}$$

$$b_j = \frac{1}{2j^2\pi^2}\sum_{i=1}^{n}\frac{\Delta x_i}{\Delta t_i}\left[sin\left(\frac{2j\pi q_i}{Q}\right) - sin\left(\frac{2j\pi q_{i-1}}{Q}\right)\right] \tag{7}$$

$$c_j = \frac{1}{2j^2\pi^2}\sum_{i=1}^{n}\frac{\Delta y_i}{\Delta t_i}\left[cos\left(\frac{2j\pi q_i}{Q}\right) - cos\left(\frac{2j\pi q_{i-1}}{Q}\right)\right] \tag{8}$$

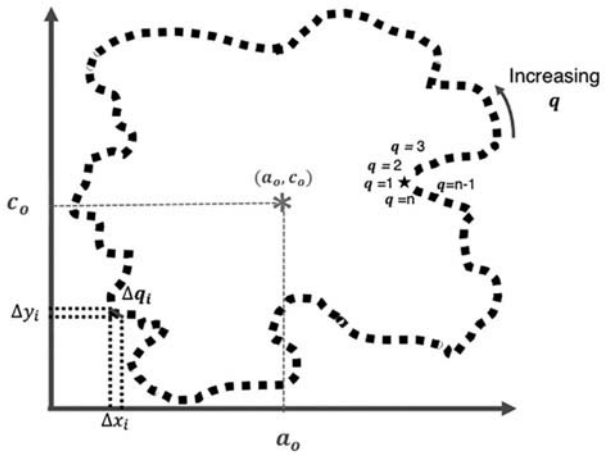

Fig. 3. Graphical representation of the q-parametrization of a contour curve with Cartesian coordinates (x(q),y(q)). Numbers 1,2,3, …n represent the values of the sequential parameter q, and n is the total number of points conforming the contour. The star symbol represents the initial point x(q = 1),y(q = 1).

$$d_j = \frac{1}{2j^2\pi^2}\sum_{i=1}^{n}\frac{\Delta y_i}{\Delta t_i}\left[sin\left(\frac{2j\pi q_i}{Q}\right) - sin\left(\frac{2j\pi q_{i-1}}{Q}\right)\right] \tag{9}$$

where i is the index associated to each sequential point, and n is the total number of points conforming the closed contour. Additionally, the coefficients a_0, c_0 represent the center of the curve, and are computed as follows (illustrated in Fig. 3):

$$a_0 = \frac{1}{Q}\sum_{i=1}^{n}\frac{1}{2}\frac{\Delta x_i}{\Delta q_i}\left[q_i^2 - q_{i-1}^2\right] - \frac{\Delta x_i}{\Delta q_i}q_i \tag{10}$$

$$c_0 = \frac{1}{Q}\sum_{i=1}^{n}\frac{1}{2}\frac{\Delta y_i}{\Delta q_i}\left[q_i^2 - q_{i-1}^2\right] - \frac{\Delta y_i}{\Delta q}q_i \tag{11}$$

The EFD are invariant under rotations, translations and dilatations, as well as independent of the initial point ($q = 1$) selection. They can be visualized as a series of ellipses –decreasing in size as j increases– whose semi- major (EM_j) and semi-minor (Em_j) axis are the eigenvalues of the matrix $\mathbf{L}_j$ given by,

$$\mathbf{L}_j = \left(\mathrm{A_j}^{-1}\right)^T \mathrm{A_j}^{-1} \tag{12}$$

T and -1 denote the transpose and the inverse of the matrix respectively, and $\mathbf{A}_j$ is the matrix of the elliptical Fourier descriptors defined in Eq. (4). For a detailed explanation see Schmittbuhl et al., (2003).

To illustrate how the EFD approximates to any contour, a graphical representation of the steps to reconstruct two points of a section from an arbitrary contour is shown in Fig. 4. The first EFD harmonic (Fig. 4a) represents an ellipse with its major axis aligned with the major axis of the original sampled contour, while the subsequent harmonics ($j > 1$) correspond to displacements of the positions of each reconstructed point $(x(q),y(q))$. Each point in the curve may have a different displacement for a given harmonic, but it is constrained by the semi-minor (Em_j) and semi-major (EM_j) axes of the ellipse representing that harmonic (Fig. 4b and c). The ellipses standing for each harmonic j are henceforth referred as 'EFD-Ellipses'. See Schmittbuhl et al., (2003) for a detailed explanation.

Fig. 5 illustrates how the shape of the reconstruction of a closed contour evolves as the harmonic contents k increase, converging to the original contour. The last contour (lower right) is the original sampled contour. The first contour (upper, left, harmonic content $k = 1$) is a smooth ellipse reflecting the main features of the contour such as elongation and orientation. The intermediate contours illustrate how that initial ellipse gradually approximates to the original sampled contour, fully converging by the harmonic contents 376.

Based on the previous discussion, we postulate that the contributions of higher harmonics (j) in the reconstruction of the contour curves from a DEM database will be more important in the presence of narrow rills and gullies, while the contributions of lower harmonics will be larger in presence of wide and deep gullies (Fig. 5). In this way, we conclude that the information concerning the type and degree of erosion on a cinder cone is contained within the distribution of the EFD harmonics describing the shape of its level contours.

3.1.2. The Erosion Index. An age dependent morphometric parameter

To interpret and quantify the type and degree of erosion, we next examine the relative contribution of each j harmonic to the full reconstruction of the original DEM contour. To that end, we first evaluate the contribution of partial EFD harmonic contents to the contour, measuring the distance $S1_k(q)$, Eq. (13), between the sampled contour curve ('original contour'), and a succession of curves built with increasing harmonic contents k ('partially reconstructed contours').

$$S1_k(q) = \sqrt{\left(x_k(q) - x_{or}(q)\right)^2 + \left(y_k(q) - y_{or}(q)\right)^2} \tag{13}$$

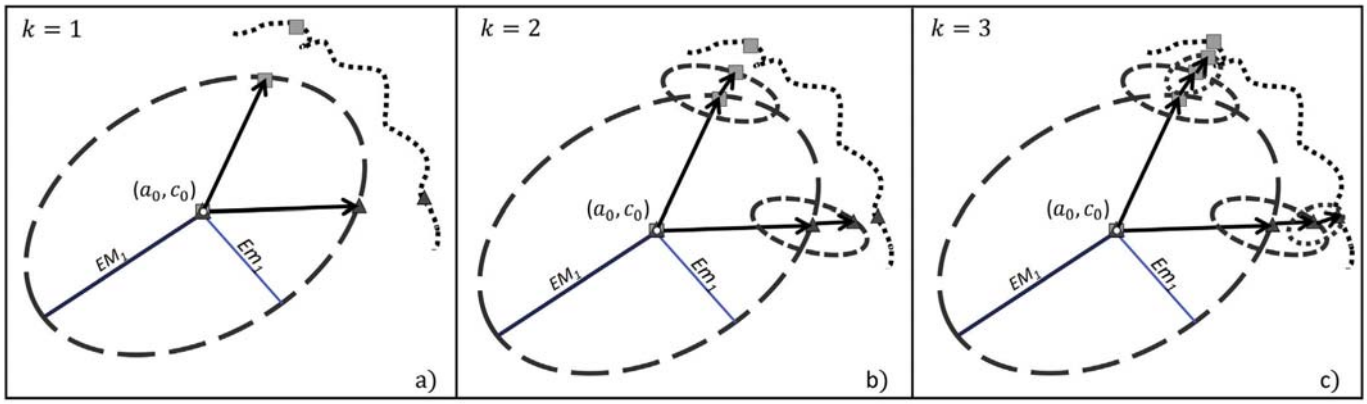

Fig. 4. Graphical representation of the steps to reconstruct two points (represented as displacing squares and triangles for the respective points) of an arbitrary contour section (dotted line) using EFD. k represent the harmonic contents and j represent the order of each EFD harmonic. a) illustrates the first EDF harmonic (k = 1, j = 1). The central point (a_0,c_0) is the circular point, overlapped with the initial square and triangle points. Each EFD point (triangle, square) follows a path (represented by arrows) determined by the characteristics of the first 'EFD-Ellipse'(long-dash line) with semi-major and semi-minor axes EM_1 and Em_1 respectively. In this step, both points are on the same main ellipse. b) shows the next convergence step (k = 2, j = 1,2). For j = 2, each point (square and triangle) have their equivalent individual EFD (small-dash ellipses). c) illustrates a further step of the EFP convergence (k = 3, j = 1,2,3). Again, for j = 3 each point has its individual EFD-Ellipse (shorter dashed line). At this step the point represented by the triangle has converged to its correspondent original contour point, while the square point would require further steps.

The parameter $S1_k(q)$ in Eq. (13), measures the Euclidean distance between each q-parametrized point in the original sampled contour $(x_{or}(q),y_{or}(q))$ and its corresponding position in the partially reconstructed contour with a kth EFD harmonic content $(x_k(q),y_k(q))$. An example is illustrated in Fig. 6. The function $S1_k(q)$ can be conceived as a set of k vectors, with q elements each.

In order to reduce the dimensionality of $S1_k(q)$, we intruduce the averaging function $\langle S1_k\rangle$ (Eq. (14)) as a measure of the mean distance from all n points forming the original sampled contour to each partially reconstructed contour:

$$\langle S1_k\rangle = \frac{1}{n}\sum_{i=1}^{n} S1_k(q_i) \tag{14}$$

$\langle S1_k\rangle$ represents a measure of the overall similarity between the original and the kth-reconstructed EFD contours. Its value converges to zero as the contents of harmonics approaches the Nyquist frequency ½ n, thus measuring to what extent each partially reconstructed contour approximates to the original sampled one. We will thus refer to this function as the "Similarity function".

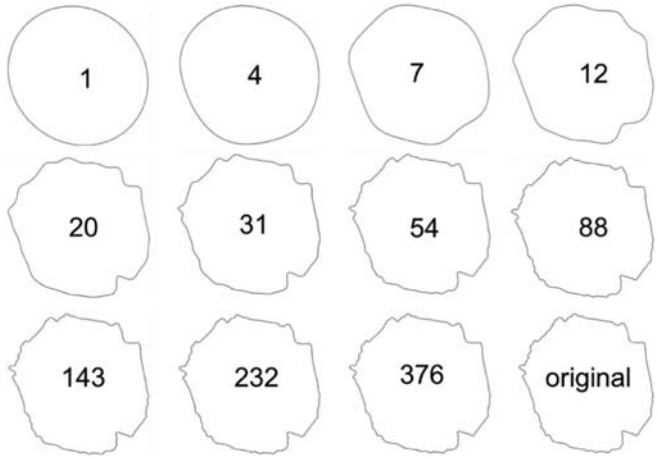

Fig. 5. Example of the reconstruction of a sampled contour curve by increasing the amount of EFD harmonics. The numbers represent the kth EFD harmonic contents. The first harmonic encompasses the overall contour of the original —sampled— contour curve. The original curve is reproduced with a harmonic contents of 376 EFD harmonics.

Since we are interested in quantifying the net contribution of each j-harmonic added to a contour partially reconstucted to the $(k\text{-}1)th$ EDF harmonic contents, we compute the difference between consecutive elements of the Similarity function:

$$\Delta S_{(\,j=k)} = (\langle S1_k\rangle - \langle S1_{k-1}\rangle) \tag{15}$$

where j is the single harmonic that increases the harmonic contents from $k\text{-}1$ to k.

To evaluate the importance of the contribution of each harmonic $j = k$ as a measure of the type and degree of erosion, we also introduce F_j, (Eq. (16)), a function that compares ΔS_j with the maximum possible contribution of each jth harmonic, which is the semi-major axis EM_j of the EFD ellipse for that particular harmonic.

$$F_j = \frac{\Delta S_j}{EM_j} \tag{16}$$

Next, we define a measure of the erosion constructed as the difference ΔS_j weighted by the function F_j/ max (F_j), where max(F_j) is the maximum value reached by the ratio $\Delta S_j/EM_j$, and it is used to limit the weighting function range between 0 and 1. Its algebraic expression is:

$$D_j = \Delta S_j \left(\frac{F_j}{\max(F_j)}\right) \tag{17}$$

The function D_j provides a reliable measure of the average separation between each kth reconstructed contour and the original sampled contour, as the weighting function enhances the contribution of harmonics with higher F_j values. D_j may be considered an analogue to a Fourier spectrum, since it reveals the relative contribution of each harmonic j to the EFD representation of the original sampled contour, as illustrated in Fig. 7. We thus call the function D_j the "Erosion Spectrum".

To condense the information contained in the function D_j into a single value, we define the "Erosion Index" D as the summation of D_j values from a reference harmonic $(j = p1)$ up to the Nyquist frequency $k_{Nyquist}$ (Eq. (18)). This departing harmonic defines a "reference contour", which is a partially reconstructed contour with harmonic contents from $j = 1$ to $k = p1$.

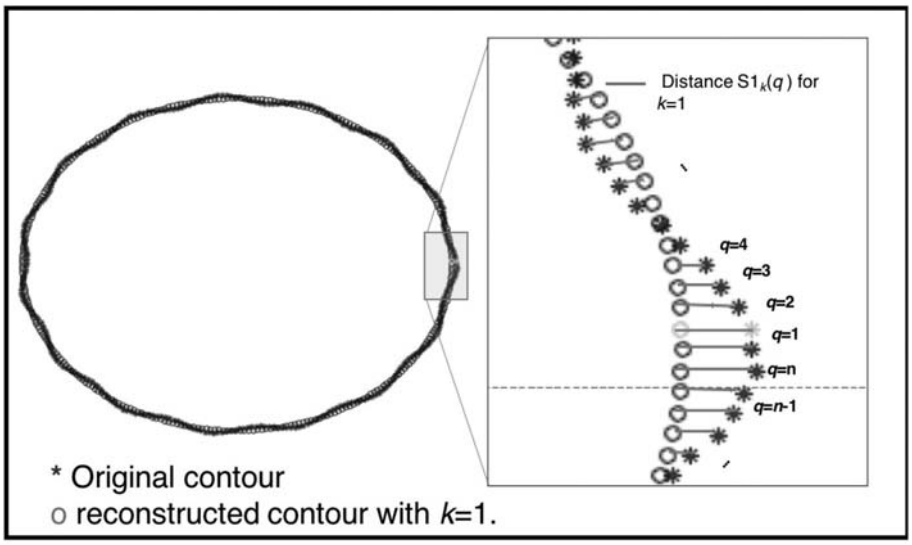

Fig. 6. Example of distance between points $S1_k(q)$ (Eq. (13) of an EDM contour and the partially reconstructed one using the Elliptical Fourier Descriptors of the harmonic k = 1.

$$D = \sum_{j=p1}^{k_{Nyquist}} D_j \tag{18}$$

We hypothesize that this reference contour depicts a smooth contour of a recently formed volcano, and represents the cross-sectional shape of the young un-eroded scoria cone. The selection criteria for this reference harmonic content $p1$ and its interpretation is discussed in the following sections.

The Erosion index D is thus a quantity measuring an average separation between a reference "un-eroded" contour and a sampled "eroded" contour. The summation represents a measure of the area enclosed between the smooth reference contour with harmonic contents $p1$ and the closest reconstructed contour to the original sampled contour, with harmonic contents $k_{Nyquist}$. The wavelength and amplitude of undulations in the sampled contour –and in its full harmonic contents representation– may thus be related to the shape, size and density of rills and gullies, and thus to the volume of volcanic material displaced from the cone surface as time goes on, and the degree of erosion increases. Larger values of D represent greater deviations from the smooth reference contour, and thus a higher degree of erosion.

3.1.3. The "Flattening function". A morphometric description of a young scoria cone

Given that the first harmonic of the EFD expansion of a contour curve is an EFD-ellipse with its major axis EM_1, aligned with the major axis of the contour, why is the first harmonic ($j = 1$) not chosen as $p1$? Choosing the first harmonic as $p1$ would imply the assumption that all cinder cones are formed with a perfect elliptical horizontal cross-section, an unsupported assumption that we preclude in this methodology, as most newly formed scoria cones are far from such symmetry. Instead, we assume that the first few EFD harmonics ($1 \le j \le p1$) represent wide morphological features that we interpret as 'birth marks', i.e., deviations from a perfect cone caused by the complexity of the monogenetic eruption process. However, from a certain value on ($j > p1$), the EFD harmonics begin to represent shorter wavelength separations from a smooth closed shape. We interpret such undulations as the age-dependent erosional features, such as gullies and rills.

To determine the value of $p1$, we first define a separate set of ellipses, henceforth referred as 'LS-Ellipses', employing a least squares algorithm to fit an ellipse to the points conforming each of the EFD contours reconstructed with increasing harmonics contents k (Fig. 7a). We then examine the ratio between the minor '$mA(k)$' and major '$MA(k)$' axes of such

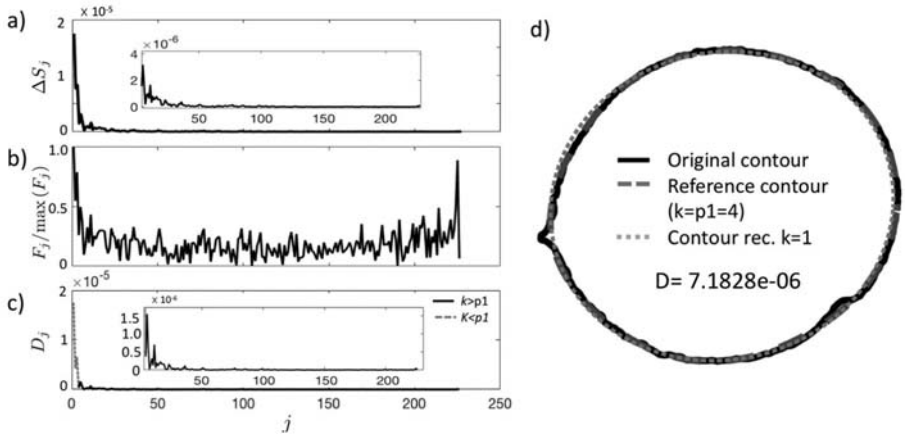

Fig. 7. Example of the functions used to calculate the "Erosion spectrum" D_j of a contour curve belonging to the intermediate height region of XITLE scoria cone (extracted from the DEM LIDAR). a) Similarity difference, showing net contribution per harmonic, b) The normalized F_j function. c) The Erosion Spectrum D_j. Insets show the same functions considering only harmonics higher than p1. d) Contour with its corresponding Erosion Index (D) value. Contour rec. k = 1, refers to the partially reconstructed contour, with a single harmonic contents 1.

LS-ellipses (not to be confused with the shrinking EFD-ellipses) by means of a "flattening" function, defined in Eq. (19).

$$flattening(k) = 1 - \frac{mA(k)}{MA(k)} \tag{19}$$

For low k values, the flattening function of the LS-ellipses show significant variations (Fig. 8a). However, as k increases, it reaches a clear change point, then maintaining an approximate constant value for the remaining range of k, up to its Nyquist value. We select as $p1$ the next harmonic to this change point ($j = p1 = change\ point + 1$) and define the reference contour as the EFD reconstructed contour (with harmonic contents $k = p1$) that depicts the above-mentioned birth marks of the volcano, i.e., the long-wavelength features of the young cone's contour curves. The point $p1$ is determined locating the largest change point of the *flattening*(k) function, using the MATLAB's "*findchangepts*" function, with the option "linear" for the type of Statistic. For most cases, this change point is a positive "peak" followed by an unvarying flattening function. Unchanging *flattening* values mean that the ellipse that best adjusts the whole reconstructed contour no longer changes (Fig. 8b); therefore, further deviations of the curve are measured regarding a "fixed" or 'taped' ellipse, which is just what we assume happens with the rills and gullies distorting the original contour. Fig. 8c illustrates the behavior of the Similarity function $\langle S1_k \rangle$, where it decays rapidly at low harmonics, and then becomes decreasingly sensitive to higher values of k.

Summarizing, we attribute the above described behavior of the Similarity function $\langle S1_k \rangle$ to the fact that the present shape of a volcanic cone is controlled by two independent factors: a) the volcano formation process, which involves depositions of large amounts of mass in the relatively short duration of volcanic cone building eruption, generating wide (in length along the contour) departures from a perfect circle or ellipse described by the harmonic content lower than $p1$, typically $k = 1$ to about $k = 5$; and b) the time-dependent erosion processes beginning after the end of the cone formation, producing shorter wavelengths along the reference contour (harmonic contents k higher than $p1$).

3.1.4. Additional sources of age-independent shape irregularities

To prevent errors in the contour characterization derived from phenomena occurring in very different time scales, namely open crater regions caused by sector collapses, lava flows or by the presence of other topographical features of different origins, such regions were excluded from the analysis, as shown in Fig. 9a. Nevertheless, the information of the remaining contour sectors was not discarded. Since the EFD analysis requires closed contours, the limiting initial (*ip*), and end (*ep*) points of the broken contours were connected using equally spaced points from the sector of an ellipse. This ellipse is constructed such that its center coincides as much as possibly with the center of the contour, while passing through points *ip* and *ep*, in such a way that the contour is continuous and smooth at the jointing points, as illustrated in Fig. 9b and c. This was done by finding the equation of an ellipse, centered at an initial point (xc, yc), with a fixed major axis inclination Φ respect to the E-W direction, and crossing points *ip*, *ep* following a hierarchical criteria: First, we use the center and major axis inclination of the corresponding LS-ellipse to the contour points as (xc, yc) and Φ respectively, and try to find the ellipse centered there that crosses through points *ip*, *ep*. Secondly, if it is not possible to find an elliptical transect smoothly connecting the limiting points, we then proceed to relocate (xc, yc) at the center of the LS-ellipse corresponding to the base of the cone with its major axis inclination as Φ. Thirdly, if still no sector of such ellipse can smoothly connect to *ip* and *ep*, we finally use as center the mean latitude (y-coordinate) and mean longitude (x-coordinate) of the points conforming the contours, keeping Φ unchanged. It is important to emphasize that points from this filled-in or completed elliptical sectors are only used to meet the EFD condition of having a closed contour, but are excluded in the calculation of the Erosion Spectrum (Eq. (17)), since their proximity to an ideal ellipse would underestimate the Erosion Index (Eq. (18)).

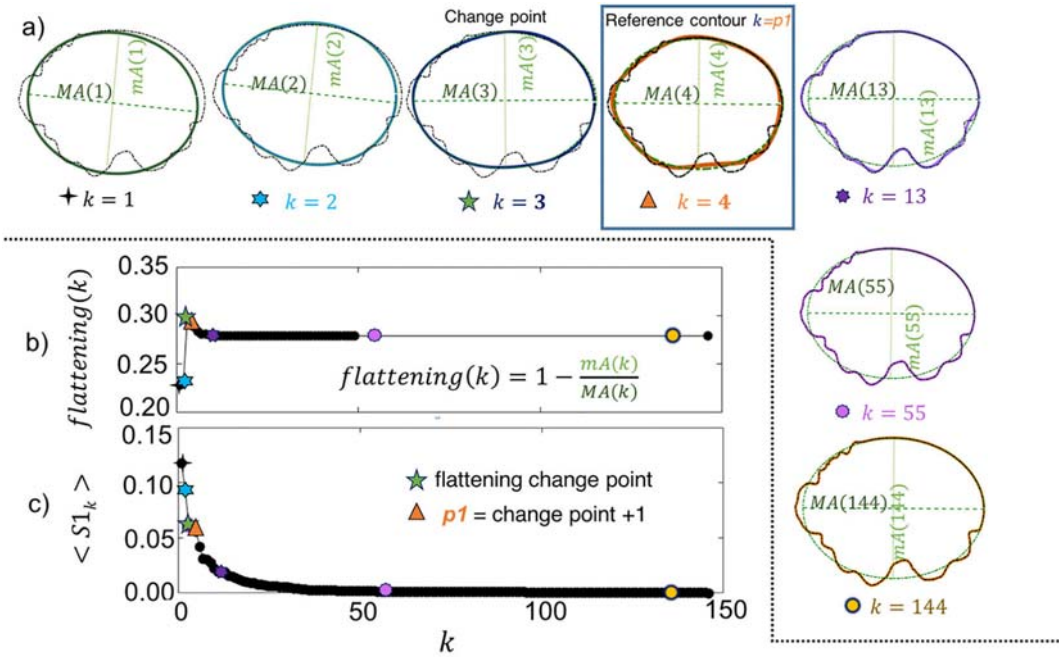

Fig. 8. a) Example of 'LS-Ellipses' which are least-squares best-fitted ellipses to the EFD reconstructed contours using up to k-harmonic contents, and the flattening function. The dotted black curve (..) is the original contour. mA(k) and MA(k) are the minor (..) and major (—-) axes of the 'LS-Ellipses'. Thicker contours represent the reconstructed contours using harmonic contents k = 1,2,3,4,13,55, and 144 harmonics. The 'LS-Ellipses' are delimited with dotted (—.) lines and filled with light gray color. It can be observed that only the reconstructed contour with k = 1 is a perfect ellipse. b) Example of the selection of harmonic p1, based on the convergence of the flattening of the best-fitted ellipse to the reconstructed contours. c) Corresponding Similarity function.

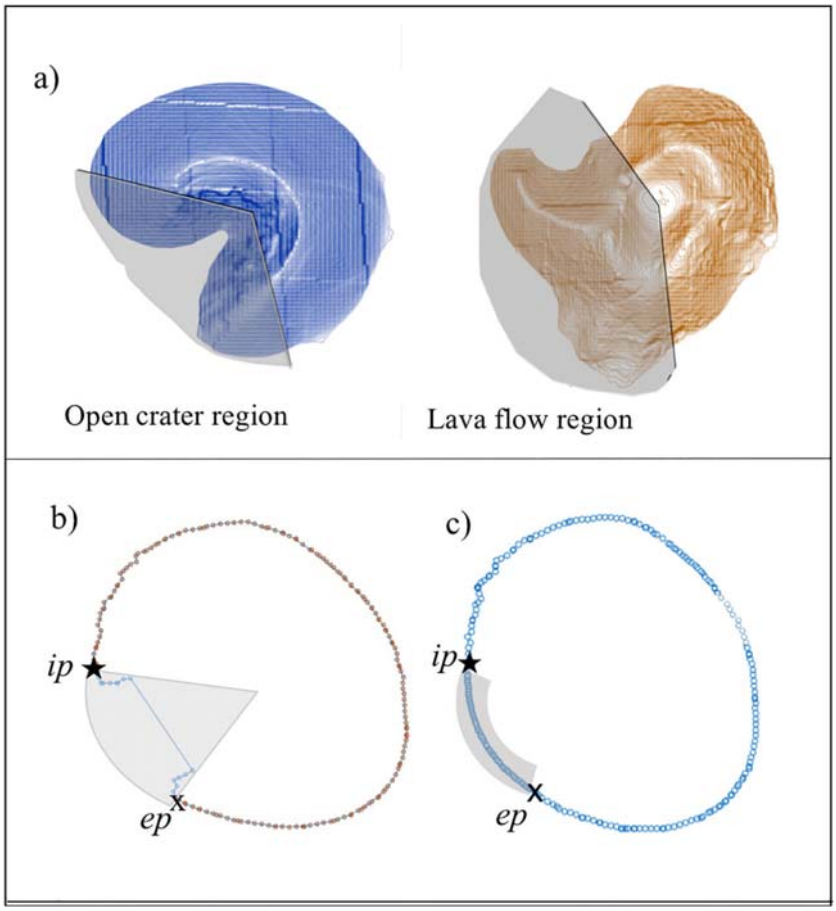

Fig. 9. a) Example of open cones with excluded regions, namely sectors with features that are not the result of long-term erosive processes. b) Identification of excluded sectors. The shadowed sector is disregarded from the analysis. c) Completed contour. Shadowed area marks the filled-in points.

3.2. Characterization of the "horizontal erosion" in a scoria cone

Contours were considered part of a scoria cone if they fall between a best-fitted ellipse to points delimiting the base of the cone and a best-fitted ellipse to the points delimiting the crater rim (Fig. 10a, b). In particular, to characterize the age-dependent horizontal erosion, we analyzed the contours in the intermediate section of that region. This selection was made attempting to avoid both, the region near the crater rim, where contours are frequently incomplete, and the region near the base of the cone, where contours are often deformed by age-independent effects, such as lava flows, or by the inclination of the underlying terrain. Aiming to retrieve as much information as possible excluding those contours, we define an intermediate section of the cone as the contours in the elevation range $[E_b + \Delta E, E_{cr} - \Delta E]$, where E_b is the elevation of the cone's base, E_{cr}, is the maximum elevation of the crater rim and $\Delta E = \frac{1}{4}(E_{cr} - E_b)$ as illustrated in Fig. 10c. The base of the cone E_b is selected

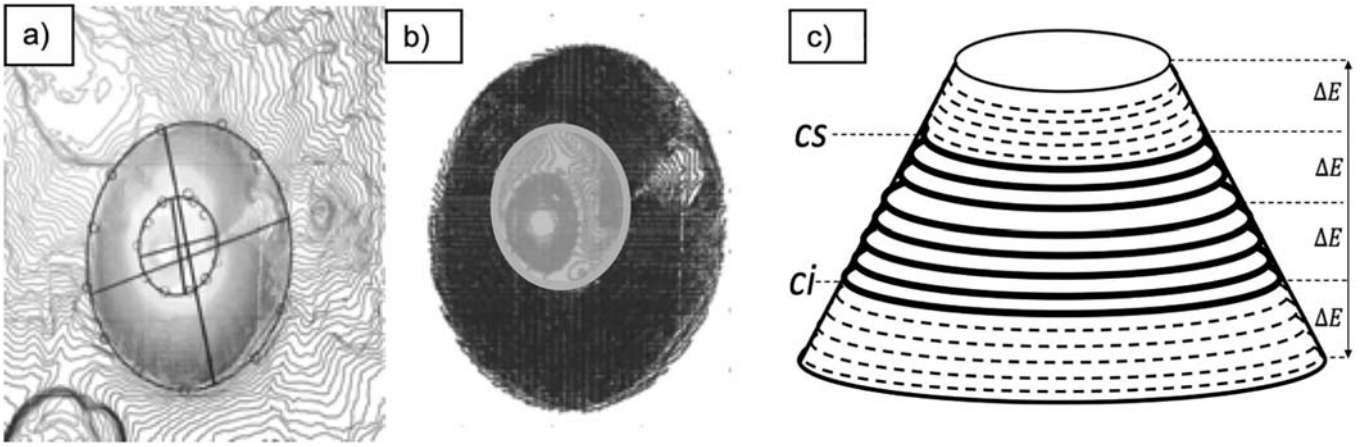

Fig. 10. (a): Example of the contour curves selection criteria. (b) Only contour curves inside the outermost ellipse (corresponding to the volcanic cone base) are selected. Crater contours (within the highlighted area) are excluded from the analysis. (c) Vertical regions of contours. Solid black contours represent the intermediate height region.

as the lowermost closed contour of the cone. Although this sample layering is arbitrary, we expect such intermediate region to be the most representative age-modified region of the volcanic cone.

To obtain an overall value that quantifies the general degree of erosion of a scoria cone, we computed the average of the Erosion Index values D calculated from Eq. (18) of all contours belonging to the intermediate vertical section of the volcanic cone, which is delimited by the lower and upper contours (*ci* and *cs* respectively). In open cones this average was calculated weighting the Erosion Index of each "completed" contour with the proportion of actual to filled points, as described below.

We will then refer to the average value of the Erosion indexes of contours in the intermediate region as the Average Erosion Index (AEI) $\langle D \rangle$, defined by

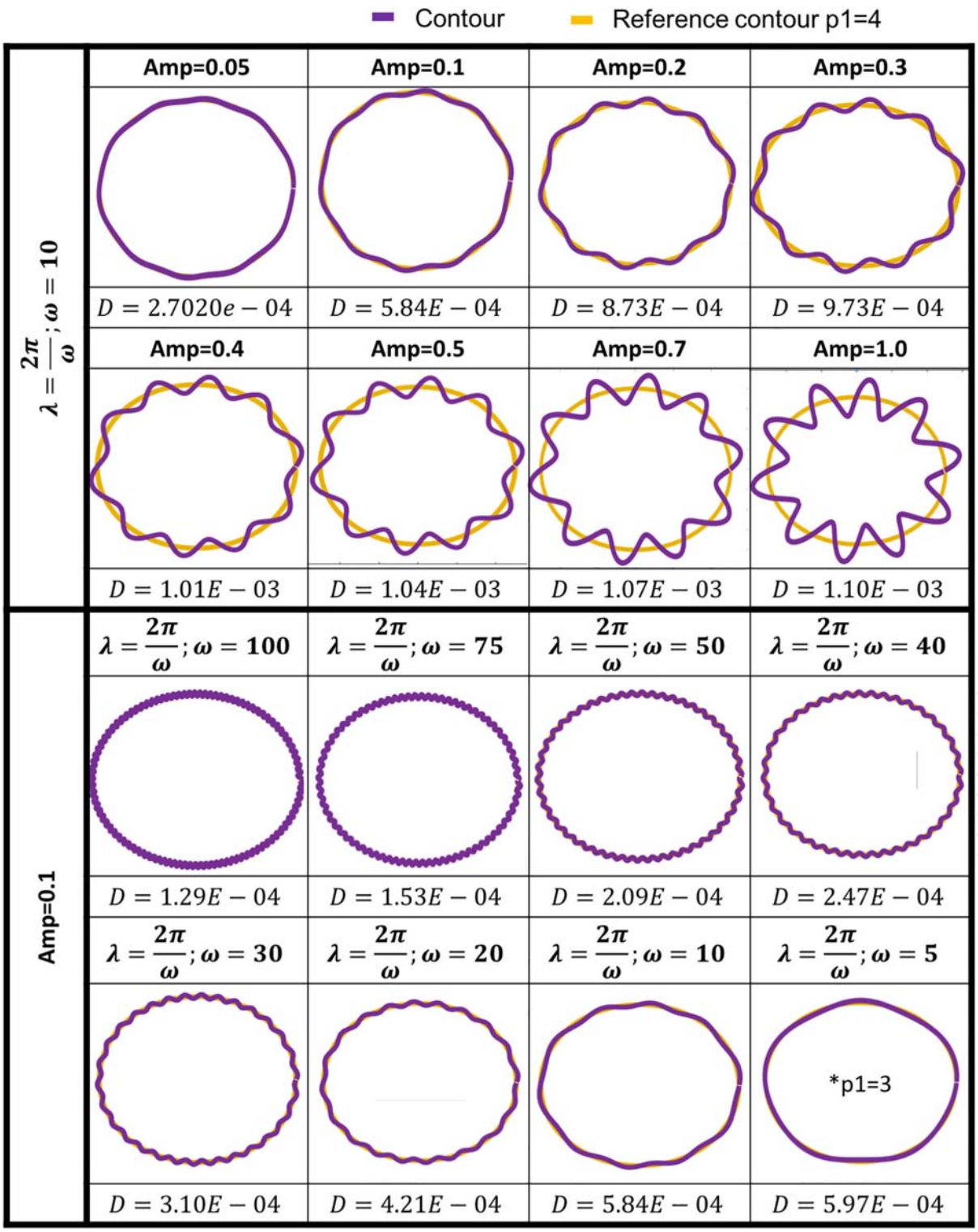

Fig. 11. Example of increasing Erosion Index D as the width and the amplitude of undulations increase. For this example a = 5 and b = 4.

Table 1
Location and calibrated radiometric dates of selected scoria cones. Calibrated ages were obtained for cones dated with 14-C using OxCal 4.2 2 (https://c14.arch.ox.ac.uk/embed.php?File=oxcal.html). References: (1) Kirianov et al., 1990; (2) Agustín-Flores et al., 2011; (3) Siebe, 2000; (4) Siebe et al., 2004; 5) Siebe et al., 2005; (6) Guilbaud et al., 2015; (7) Arce et al., 2015; (8) Jaimes-Viera et al., 2018; (9) Bloomfield, 1975; (10) Arce et al., 2013, (11) Alcalá-Reygosa et al., 2018. *Only available in DLR DEM. The cone marked in boldface belongs to the Michoacán-Guanajuato Volcanic Field.

Volcano name	Lat(N)	Lon (E)	Elevation of cone base (m.a.s.l)	Radiometric age ka ($\pm\delta Age$)	Calibrated age ka ($\pm\delta Age$)	Reference
Malinal	19.2228	−99.2179	3000	18.9 ± 0.6 (^{14}C)	22.896 ± 0.714	1
Xitle	19.2467	−99.2223	2900	1.67 ± 0.035 (^{14}C)	1.580 ± 0.049	3
Pelado	19.1511	−99.2175	3350	10 ± 0.5 (^{14}C)	11.599 ± 0.683	4
Ninfa (S dos Cerros)	19.1530	−98.9322	2850	14 ± 0.5 (^{14}C)	16.978 ± 0.667	2
Raices	19.1041	99.2566	3000	15.57 ± 0.30 (^{14}C)	18.87±0.345	1
El Hoyo	19.0893	−99.1688	3060	>2.835 ± 0.070 (^{14}C) <4.690 ± 0.090 (^{14}C)	>2.961 ± 0.094 <5.415 ± 0.120	4
Manteca	19.0894	−99.1780	3100	>2.835 ± 0.070 (^{14}C) <4.690 ± 0.090 (^{14}C)	>2.961 ± 0.094 <5.415 ± 0.120	4
Teuhtli	19.2242	−99.0294	2540	>14 ± 0.5 (^{14}C) <31.790 + 0.755/−0.690 (^{14}C)	>16.978 ± 0.667 < 35.908 ± 0.908	5 6
Hijo de Cuauhtzin	19.1558	−99.0927	3200	>20.895 ± 0.245 (^{14}C)	>25.150 ± 0.322	5
Jumento	19.21	−99.31	3620		ca. 2	7,11
Pelagatos	19.09	−98.96	2960	>2.520 ± 0.105 (^{14}C) <14 (^{14}C)	>2.566 ± 0.122 <16.978 ± 0.667	2
Cuatzontle	19.2392	−99.2117	2930	222 ± 52 (^{40}Ar/^{39}Ar)		8
Cuautepel	19.0911	−98.8603	2550	34 ± 5 (^{40}Ar/^{39}Ar)		8
Malacatepec	19.1625	−99.2592	3200	95 ± 12 (^{40}Ar/^{39}Ar)		8
Aholo	19.0911	−98.8544	2550	23 ± 15 (^{40}Ar/^{39}Ar)		8
Mezontepec	19.1883	−99.2292	3450	11 ± 3 (^{40}Ar/^{39}Ar)		8
*Tlayacapan	18.9729	−98.9358	1850	133 ± 32 (^{40}Ar/^{39}Ar)		8
*Yuhualixqui	19.3178	−99.0317	2250	62 ± 98 (^{40}Ar/^{39}Ar)		8
*Zitlaltepetl	18.9820	−98.8936	1930	35 ± 4 (^{40}Ar/^{39}Ar)		8
*Chimalhuacan	19.2392	−99.2117	2250	1124 ± 23 (^{40}Ar/^{39}Ar)		8
*La Estrella	19.3989	−98.9562	2250	765 ± 30 (^{40}Ar/^{39}Ar)		8
*Jumiltepec	18.9086	−98.7822	1100	846 ± 8 (^{40}Ar/^{39}Ar)		8
*Tezontle	19.0311	−99.4616	2600	21.860 ± 0.380 (^{14}C)	26.21 ± 0.405	9
*15 Santa Fe	19.1647	−99.4461	2660	30.500 ± 1.160 (^{14}C)	34.87 ± 1.365	9
*Cuauatl	19.1647	−99.4208	2800	<19.630 ± 0.160 (^{14}C)	<23.52 ± 0.222	9
*Tres Cruces	19.0925	−99.4841	2900	<8.490 ± 0.070 (^{14}C)	<9.44 ± 0.700	9
*Atlacholoaya	18.7252	−99.21150	1050	1020 ± 160 (^{40}Ar/^{39}Ar)		10
*Tespomayo (N dos Cerros)	19.1530	−98.9400	2920	14 ± 0.5 (^{14}C)	16.978 ± 0.667	2
***Paricutin**	**19.4925**	**−102.2511**	**2550**	**0.075**		**Historic**

$$\langle D\rangle = \left[\sum_{c=ci}^{cs}(D_c{\cdot}W_c)\right] / \left[\sum_{c=ci}^{cs} W_c\right] \tag{20}$$

where D_c is the Erosion Index value of each contour belonging to the intermediate section, and W_c is a weight assigned to contours in open cones, quantifying the proportion of filled-in points completing each broken contour. W_c = *countour points before completion/total number of points after completion*. This weight is one in contours not requiring any completion. In such completed contours the value of D_c was computed using all of the originally sampled points (i.e. points outside the shadowed region in Fig. 9).

Additionally, we characterize the dispersion of D among the considered contours as the weighted standard deviation of D_c as:

$$\Delta D = \left(\left[\sum_{ci}^{cs}\left(W_c{\cdot}(D_c-\langle D\rangle)^2\right)\right] / \left[\sum_{ci}^{cs} W_c\right]\right)^{1/2} \tag{21}$$

using the same weighting criterion as in Eq. (20).

4. Results

4.1. How the Erosion Index D measures the degree of age-dependent erosion

To illustrate how the erosion index D conveys information about the degree of erosion in a scoria cone, we tested the behavior of D on a series of synthetic closed contours with undulations of different amplitudes and wavelengths, simulating rills and gullies with different width and depth combinations. Synthetic contours were generated superposing an ellipse with adjustable semi-axes (a,b), centered in the origin of a polar coordinates plane (r,θ) with sinusoidal undulations of adjustable amplitude *Amp* and wavelength λ. For the trials, we first kept the wavelength constant while varying the amplitude (simulating increasingly deeper features), and then changed the wavelength keeping a constant amplitude (simulating an evolution from narrow rills to wider gullies).

The results of these tests are summarized in Fig. 11. It is clear there that the Erosion Index D increases with either manifestation of age-dependent erosion (deeper or wider rills and gullies) or with any combination of them and can be used to resolve different levels of erosion in scoria cones.

It is however important to emphasize that in this simplified example D may not be a monotonic function of the level of erosion in terms of amplitudes and wavelengths of a contour undulations only, since contours with different combinations of *Amp* and λ can yield similar values of D. Nonetheless, we uphold that the Erosion Index D indeed represents the age-dependent erosion on the surface of a scoria cone, since it is a measure of the area enclosed between the "young cone" reference contour and the sampled contour; and two cones may be considered to have similar degrees of erosion if the average cross sectional areas of their rills and gullies are equivalent regardless of their shape, size or location. This argument is congruent with the "drainage-way volume loss" measure of age-dependent erosion by Dohrenwend et al. (1986).

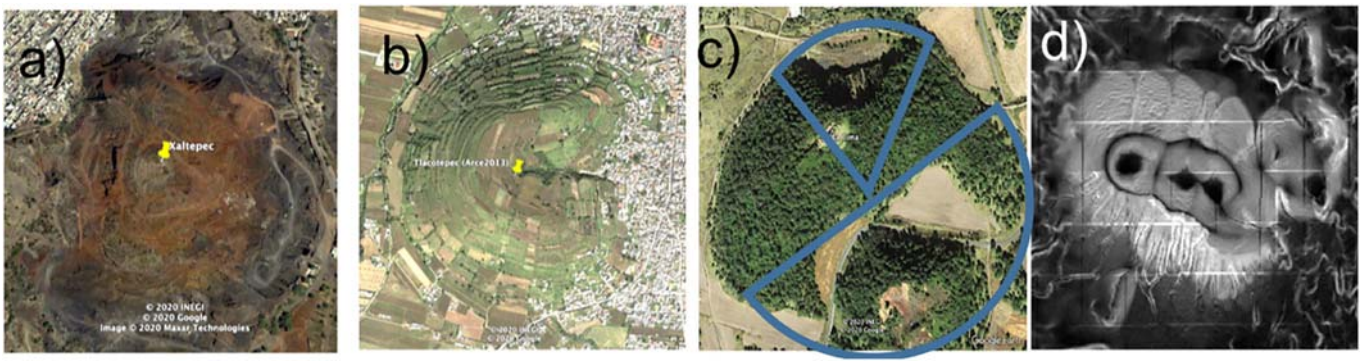

Fig. 12. Examples of cones that cannot be analyzed with the Erosion Index methodology. a) Xaltepec (19°19′17.83″N, 99°1′19.14″W), heavily mined. b) Tlacotepec scoria cone (19°13′28.00″N, 99°40′42.00″W), completely covered by active farmlands C) La Cima (19° 6′42.83″N, 99°11′41.99″W) more than 70% of the surface breached and mined. D) Tlaloc (19° 6′34.81″N, 99° 2′2.76″W), a row of 3 cones lacking well-defined limits.

4.2. Testing the Average Erosion Index on scoria cones in the Chichinautzin Volcanic Field

In the previous section we tested the behavior of the Erosion Index *D* using single synthetic contours. To test the Erosion Index methodology on actual scoria cones, we applied the previously described analysis to 16 radiometrically dated scoria cones of the Sierra Chichinautzin Volcanic Field (Table 1) with clearly defined contours that could be retrieved from both DEM databases, and to 13 others, only available in the DLR DEM database (marked with an asterisk). One of the latter, Paricutin,

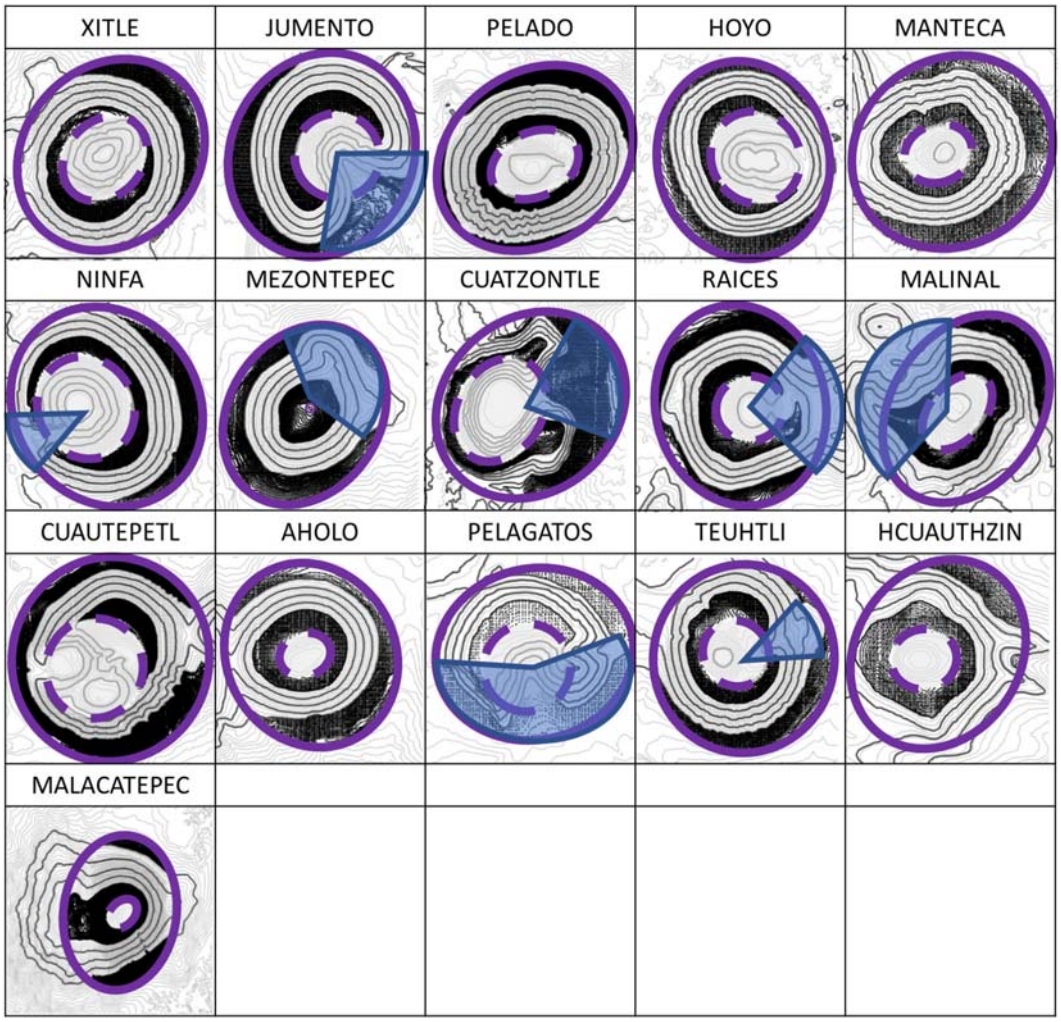

Fig. 13. The gray closed lines are examples of contours in the intermediate regions of cones from the LIDAR DEM. Only contour points contained between the superposed ellipses (dashed and solid thick lines) were analyzed. Black regions represent the excluded upper and lower regions of the cones. Shadowed areas mark regions excluded from the analysis (e.g. open regions). HCUAUTHZIN stands for "Hijo de Cuahutzin".

in the Michoacán-Guanajuato Monogenetic Field, is only 75 years old and erosional features have not yet developed in any significant way for this method.

For the purpose of the test we discarded other scoria cones with published radiometric ages for which this methodology cannot be applied: cones with a clear evidence of anthropogenic alteration such as mining or active farming (Las Tetillas, Peñon de Baños, Tetecón, Tezoyuca1, Tezoyuca2, Xaltepec, Tenancingo, Tlacotepec, Palpan, and Villa Guerrero); cones with more than 70% of their surface breached, collapsed or buried (La Cima, San Miguel); volcanoes lacking well-defined boundaries, preventing the identification of individual scoria cones (Tlaloc, Ocusacayo, Chichinautzin, Cerro del Agua, Xistune,

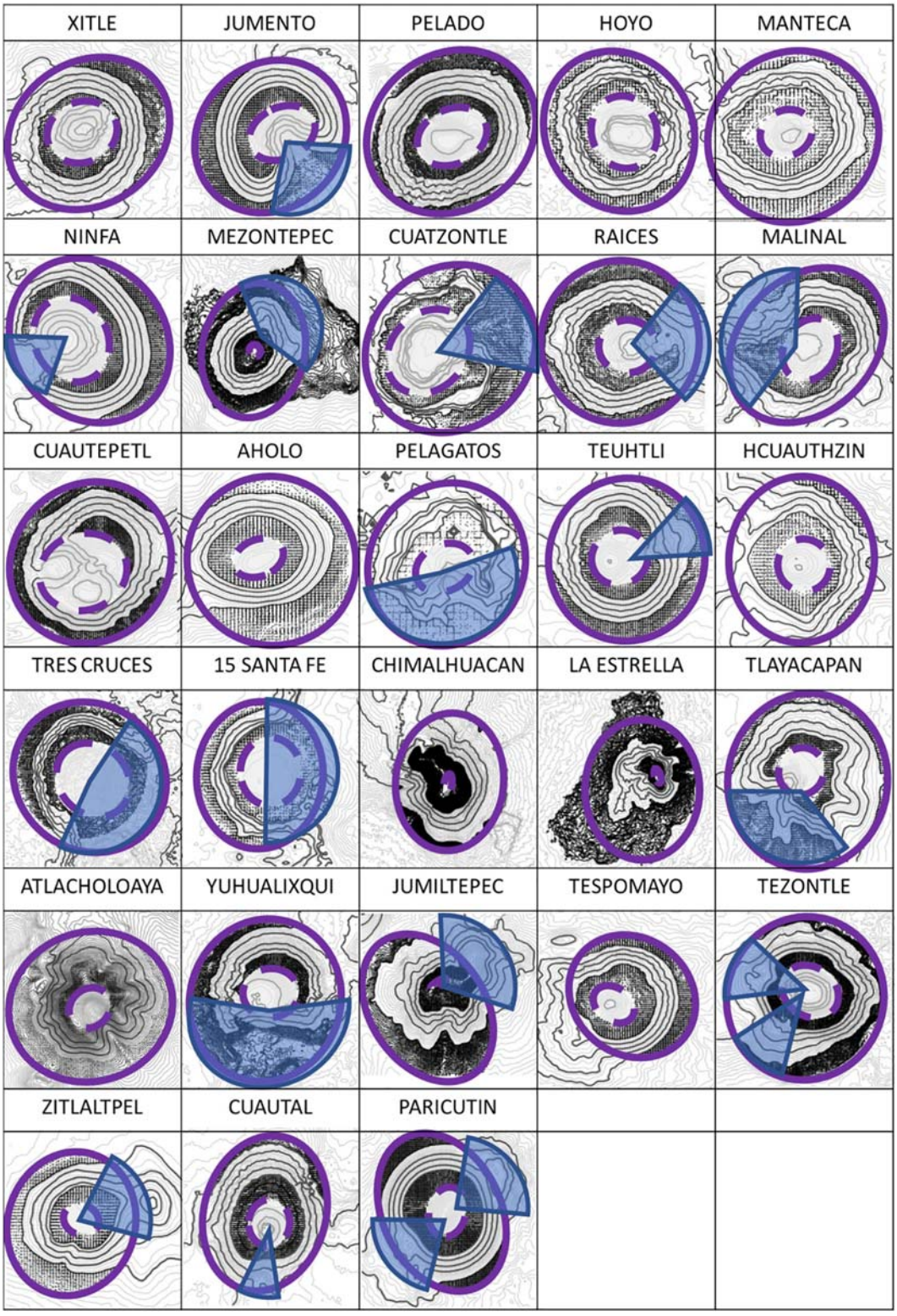

Fig. 14. Examples of contours from the intermediate regions of cones from the DLR DEM. The features in the figure are as described in Fig. 13.

Oyameyo, El Palomito, and El Caballito); and dated cones without any explicit of specific published location coordinates, or with a published location not coinciding with a conical shape in the DEMs (Molcajete and Couxusco). Examples of the first three cases are shown in Fig. 12.

The selected cones were located feeding their coordinates in both DEMs: "DLR" and "LIDAR", and the contour curves were generated using the MATLAB contour function with *2* m vertical separation. Figs. 13 and 14 illustrate the contours picked out from the intermediate regions of each analyzed scoria cone, and its respective source DEM. The spatial sampling rate of the contours depends on the DEM resolution, so a contour obtained from the LIDAR DEM has more sampled points than a contour from the DLR DEM.

We apply the methodology to the intermediate sections of selected cones, illustrated in Figs. 13 and 14, and we show the resulting Erosion Index $\langle D\rangle$ (from Eq. (20)) with its respective standard deviations ΔD (from Eq. 21) in Table 2. The AEI $\langle D\rangle$ values, rendered in degrees (of order 10^{-4}) by the databases, were converted to meters, multiplying by the conversion factor C_f in Eq. (22) for course-independent short distances on the Earth's surface using $R_T = 6378$ km as an average Earth radius.

$$C_f = \frac{2\pi\cdot 1^\circ\cdot R_T\cdot \cos(\phi)}{360^\circ} \tag{22}$$

Inspection of Table 2 shows that in some cones the calculated values of $\langle D\rangle$ had significantly higher standard deviations. We identified two main causes for such increased dispersion of $\langle D\rangle$. The first relates to the contour closing algorithm used in open cones with a high proportion of completed contours. The completion algorithm may lead to some unwanted contributions at the junction points between completed and sampled regions, generating less accurate D_c values for those particular contours. This causes higher standard deviations, and/or the possibility of a different selection of $p1$, even when the completed region is being excluded from the analysis. Examples are the open crater contours of Jumento and the steep terrain at the base of Hijo de Cuahutzin. Our completion algorithm generates sufficiently smooth contours to avoid these problems in approximately 90% of cases, and we are working to improve it.

The second cause is related to the erosive process itself, and we thus interpret these standard deviations as a "dispersion" rather than an "error or uncertainty". Erosion causes deeper and wider undulations towards the base of the cones (e.g. Dohrenwend et al., 1986), an effect reflected as an increasing value of D_c towards the base of the cone that raises the standard deviation, quite notorious in much eroded cones (e.g. Chimalhuacan, Jumiltepec, Atlacholoaya, La Estrella). Despite the higher values of the standard deviations in such cases, the AEI $\langle D\rangle$ is still able to convey the age-related erosion information. We are working on a more adaptative criterion for the definition of the "intermediate zone" or an alternative approach to incorporate the information of the ΔD in the analysis, since it may also contain additional information on the degree of erosion.

Table 2
Conversion factors C_f, AEI $\langle D\rangle$ and its respective standard deviation obtained for each individual scoria cone in each DEM, in meters. The correlation with radiometric ages was set using the scoria cones in boldface. Only cones Cuauatl, Tres Cruces and Hijo de Cuahutzin were not used as their reported radiometric data are single age bounds, obtained from samples under- or over-lying eruption products, and may induce heavily biased trends. (See Table 1). NA = not available.

Volcano name		DLR		LIDAR	
	C_f (km)	$\langle D\rangle$ [m]	ΔD [m]	$\langle D\rangle$ [m]	ΔD [m]
Xitle	105.10	0.96	0.28	0.69	0.19
Jumento	105.12	0.64	0.19	0.63	0.30
Pelado	105.16	1.39	0.30	1.37	0.30
Raices	105.19	2.21	0.62	2.41	0.43
Ninfa	105.16	1.29	0.86	1.05	0.43
Malinal	105.11	1.93	0.51	2.29	0.67
Cuautepetl	105.19	2.04	0.47	2.36	0.39
Hoyo	105.20	1.38	0.22	1.12	0.20
Manteca	105.20	0.89	0.17	1.37	0.38
Pelagatos	105.19	NA	NA	0.59	0.36
Hijo de Cuahutzin	105.16	2.25	1.11	2.18	1.20
Teuhtli	105.11	1.68	0.64	1.45	0.52
Malacatepec	105.15	NA	NA	2.88	1.39
Mezontepec	105.14	1.60	0.36	1.25	0.34
Aholo	105.19	0.93	0.25	0.65	0.15
Cuatzontle	105.10	4.84	2.03	4.26	1.46
Jumiltepec	105.42	7.26	4.17	NA	NA
Tlayacapan	105.27	5.22	1.95	NA	NA
Yuhualixqui	105.05	2.24	0.61	NA	NA
Zitlaltpel	105.26	1.63	0.16	NA	NA
Chimalhuacan	105.03	8.92	3.34	NA	NA
La Estrella	105.00	10.09	1.86	NA	NA
Tezontle	105.23	4.34	1.13	NA	NA
15 Santa Fe	105.15	1.74	0.28	NA	NA
Cuauatl	105.15	2.30	1.17	NA	NA
Trescruces	105.19	1.83	0.45	NA	NA
Atlacholoaya	105.42	10.15	1.63	NA	NA
Tespomayo	105.16	1.56	0.66	NA	NA
Paricutin	104.94	0.35	0.09	NA	NA

4.3. Is the AEI $<D>$ a useful morphometric parameter to estimate the age of monogenetic cinder cones?

We believe that there is enough evidence to give an affirmative answer to this question. To support this answer, we searched for a robust functional relationship between the radiometric ages of the cones and the AEI $\langle D\rangle$. To that end, we used available radiometric data of eruption products, and only excluded single age-bound data, obtained from samples under- or over-lying direct eruption products that could cause undue trends of the results. We also excluded other cones that could not be properly resolved by the DEM, like Pelagatos and Mezontepec, unresolvable in the DLR DEM. We therefore used 15 cones from the DEM LIDAR and 24 from the DEM DLR (Fig. 15). We found that for both DEMs the age of the cones fitted well a power function of the AEI expressed by Eq. (23).

$$Age = \beta_1(\langle D\rangle)^{\beta_2} \tag{23}$$

To linearize this function, we apply a logarithmic transformation:

$$log_{10}(Age) = a * log_{10}(\langle D\rangle) + b \tag{24}$$

where $a = \beta_2$ and $b = log_{10}(\beta_1)$.

To estimate β_1 and β_2 we used the York linear fit approximation (York, 1966) which accounts for the errors and dispersion of both variables, *age* and $< D >$. Denoting these dispersions as (δAge) and (ΔD) respectively, the logarithmic transformation of the uncertainties are (Baird, 1994):

$$\delta(log_{10}(Age)) = (\delta Age/Age)(1/\ln(10)) \tag{25}$$

$$\delta(log_{10}(\langle D\rangle)) = (\Delta D/\langle D\rangle)(1/\ln(10))$$

Fits to Eq. (24) were obtained separately for the selected cones from DEM LIDAR, and from DEM DLR.

Fig. 15 shows the plot of $log_{10}(Age)$ vs $log_{10}(\langle D\rangle)$ for scoria cones with available central radiometric ages of direct eruptive products (marked in boldface in Table 2) with their correspondent transformed uncertainties, $\delta(log_{10}(Age))$ and $\delta(log_{10}(\langle D\rangle))$, as error bars. The dashed lines represent the best linear fits with the hatched regions marking the 95% confidence intervals of the fitting. For cones with both upper and lower radiometric age bounds, obtained from samples under- and over-lying direct eruption products, we used the average value of the age limits as a central age value, with a standard deviation corresponding to the age uncertainty.

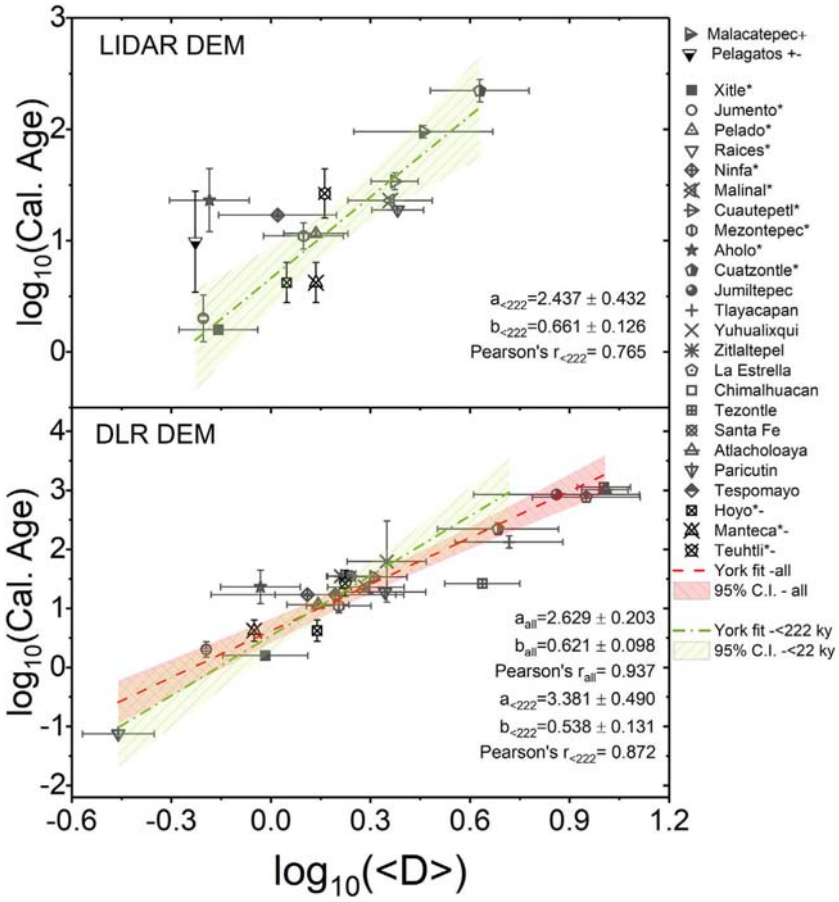

Fig. 15. Plots of the volcanoes' age dependence upon the AEI ⟨D⟩. The linear trend in a log-log graph illustrates the power relationship (Eq. (22)). a) log(age) as a function of log(⟨D⟩) obtained from volcanoes younger than 222 ka (which is the oldest cone in the LIDAR database. Fit has a Pearson correlation coefficient r = 0.765. b) log(age) as a function of log(⟨D⟩) obtained for cones in the DLR database. A good fit (Perason correlation coefficient r = 0.87) is obtained using only DEM data from volcanoes younger than 222 ka (dash-dot line). The inclusion of older cones (dashed line –) increase the Pearson's correlation coefficient to r = 0.937. Error bars in both x and y directions represent $\delta(\log_{10}(\langle D\rangle))$ and $\delta(\log_{10}(\text{Age}))$ respectively. All correlation coefficients in the figure resulted from the process of calculating the volcano age dependence on < D > with the set of cones listed on the right side of the figure. Cones marked + are only available in LIDAR DEM. Cones marked * are available in both in DLR and LIDAR DEMS. The - mark indicates that the radiometric age assigned to the cone is the average of the upper and lower stratigraphic radiometric age limits.

The LIDAR DEM sample included fifteen cones, all younger than 222 ka. The linear fit approximation for those cones rendered the values $\beta_1 = 4.581 \pm 1.334$ and $\beta_2 = 2.437 \pm 0.432$. The radiometric age range of the cones in the DLR DEM is wider, extending to 1200 ka. Thus, for comparison purposes we made separate fits for the cones in DLR younger than 222 ka and for the full age range in that DEM. For this DEM and considering only twenty cones younger than 222 ka: $\beta_1 = 3.457 \pm 1.043$ and $\beta_2 = 3.381 \pm 0.490$. Inclusion of the additional four cones in the DLR DEM with radiometric ages up to 1200 ka rendered: $\beta_1 = 4.177 \pm 0.951$ and $\beta_2 = 2.629 \pm 0.203$.

We tested the effect of including the age-bounded cones on the linear fit approximation. We found that including or excluding them does not alter significantly the values of regression coefficients β_1 and β_2. Only in the LIDAR DEM, the inclusion of Pelagatos cone, with a standard deviation exceeding its average age, causes the Pearson's correlation coefficient to drop from 0.80 to 0.76.

In conclusion, the consistency of the power age dependence of $\langle D \rangle$ and the stability of its parameters are supported by the similar correlations among the different data sets and age groups, as illustrated in Fig. 15. The applicability of these relations to additional volcanoes is discussed in the next section.

5. Appraisal of the proposed morpho-chronologic method

Table 3 shows the morpho-chronologic results for all the volcanoes listed in Table 1, calculated with Eq. (23) for each DEM. For cones from the DEM DLR we used the coefficients β_1 and β_2 obtained for the whole range from 0.75 to 1200 ka. These results were compared with their radiometric ages. The correlations found between radiometric and morpho-chronologic ages for the extended list of volcanoes, which includes 3 cones with only upper or lower age-bounds (Cuauatl, Tres Cruces and Hijo de Cuahutzin), were good. Pearson correlations render values >0.95, and Spearman rank correlation coefficients are 0.74 and 0.85 for LIDAR DEM and DLR DEM respectively, suggesting reliability in the determination of relative ages for the cinder cones of the SCVF. The graphical comparison between the morpho-chronologic ages and the calibrated radiometric ages is illustrated in Fig. 16.

Additionally, in an attempt to detect and scale other possible causes leading to substantial differences between the morphometric and radiometric ages, we searched for correlations between the relative errors listed in Table 3 and each of five possible sources. 1) The average proportion of level contour completion of the processed contours per scoria cone, required by the methodology, and measured as the average value of the weights *Wc* described in Section 3.2. 2) The altitude. 3) The latitude of the cone base (both climate-related). 4) The inclination of the terrain underlying the cone, and 5) The radiometric age of the cone. None of those factors seemed to be the sources of the differences, as Pearson correlation coefficients between the age relative errors and each of the above parameters were negligible, with values −0.03, −0.01, −0.03, −0.14 and − 0.15 respectively.

Table 3
Morphometric age estimations from the AEI ⟨D⟩ for both DEM databases. Names in bold show the cones used for the regression analysis between ⟨D⟩ and radiometric ages. The errors assigned to the morphometric ages were obtained using error propagation of Eq. (23), considering the errors of coefficients β_1 ($\delta\beta_1$) and β_2 ($\delta\beta_2$) as the representative errors ($[\delta Age]^2 = [(\langle D\rangle)^{\beta_2}(\delta\beta_1)]^2 + [\beta_1 \ln(\langle D\rangle)(\langle D\rangle)^{\beta_2}(\delta\beta_2)]^2$). Reported Spearman and Pearson coefficients were computed between radiometric age-values and estimated morphometric ages using ⟨D⟩ obtained from both DEMs DLR and LIDAR for all cones in Table 1. For cones lacking central radiometric values we used the mean of upper and lower bounds when available. Cones with only a lower or an upper age bound, that were not used in the calibration of this model, are included here only for comparison purposes. Small P-values (less than 0.05), indicate that the corresponding Pearson and Spearman coefficients are significantly different from zero. SCVF denotes cones belonging to the Sierra Chichinautzin volcanic field. Relative errors between morphometric ages and radiometric ages are estimated as the difference between the obtained morphometric ages and the radiometric ages, divided by the radiometric ages. In the last row of the table **SCVF** in bold, means that only cones in bold were used for calculating the Pearson and Spearman correlation coefficients, whereas SCVF (all) indicates that all cones in table were used for the computation of Spearman and Pearson's correlation coefficients.

		DLR			LIDAR		
Name	**Cal. Radimetric Age (ka)**	**Age = f(D) (ka)**	**Error (ka)**	**Relative Error**	**Age = f(D) (ka)**	**Error (ka)**	**Relative Error**
Xitle	1.58 +/− 0.049	3.77	0.86	1.39	1.89	0.55	0.19
Jumento	2 +/− 0.1	1.29	0.32	−0.36	1.47	0.51	−0.27
Hoyo	>2.96 +/− 0.009, < 5.42 +/− 0.120	9.72	2.30	1.32	6.00	1.94	0.43
Manteca	>2.96 +/− 0.009, < 5.42 +/− 0.120	3.09	s1	−0.26	9.82	2.90	1.34
Trescruces	<9.44 +/− 0.70	20.51	5.31	1.17	NA	NA	NA
Pelagatos	>2.57 +/− 0.12, < 16.98 ±0.66	NA	NA	NA	1.28	0.59	−0.87
Mezontepec	11 +/− 3	14.44	3.57	0.31	4.58	1.63	−0.58
Pelado	11.58 +/− 0.49	9.87	2.34	−0.15	9.81	3.17	−0.15
Ninfa	16.98 +/− 0.66	8.15	1.90	−0.52	5.14	1.60	−0.70
Tespomayo	16.98 +/− 0.66	13.55	3.32	−0.20	NA	NA	NA
Raices	18.87 +/− 0.34	33.54	9.36	0.78	39.10	17.56	1.07
Malinal	22.9 +/− 0.71	23.63	6.24	0.03	34.46	14.03	0.50
Aholo	23 +/− 15	3.45	0.79	−0.85	1.63	0.48	−0.93
Cuauatl	<23.52 +/− 0.22	37.35	10.60	0.59	NA	NA	NA
Hijo de Cuahutzin	>25.96 +/− 0.21	35.22	9.90	0.36	30.70	13.98	0.18
Tezontle	26.21 +/− 0.40	198.02	74.30	6.55	NA	NA	NA
Teuhtli	>16.98 ±0.66, <35.96 +/− 0.91	16.25	4.08	−0.39	11.40	4.18	−0.57
Cuautepetl	34 +/− 6	27.29	7.37	−0.20	37.15	15.75	0.09
15stafe	34.87 +/− 1.36	17.98	4.57	−0.48	NA	NA	NA
Zitlaltpel	35 ±4	15.05	3.74	−0.57	NA	NA	NA
Yuhualixqui	62 +/− 98	34.69	9.73	−0.44	NA	NA	NA
Malacatepec	95 +/− 12	NA	NA	NA	60.46	17.61	−0.36
Tlayacapan*	133 +/− 32	322.33	130.79	1.42	NA	NA	NA
Cuatzontle	222 +/− 52	263.74	103.66	0.19	156.57	115.90	−0.29
Laestrella*	765 +/− 30	1319.20	659.11	0.72	NA	NA	NA
Jumiltepec*	846 +/− 8	766.23	354.50	−0.09	NA	NA	NA
Atlacholoaya*	1020 +/− 160	1853.16	969.46	0.82	NA	NA	NA
Chimalhuacan*	1124 +/− 23	1824.21	952.31	0.62	NA	NA	NA
Paricutin	0.075	0.26	0.08	2.45	NA	NA	NA
			DLR			LIDAR	
		Pearson	0.97	0.97		0.96	0.96
		p-value	7.22E-15	7.71E-17		5.95E-09	2.34E-09
		Spearman	0.90	0.85		0.71	0.74
		p-value	2.37E-09	1.14E-08		1.10E-03	1.10E-03
			SCVF+ Paricutin	SCVF (all) + Paricutin		**SCVF**	SCVF(all)

5.1. Limitations of the proposed morpho-chronometric analysis

The method based on the EFD analysis of the DEM contours proposed here has not been tested in different volcanic fields. Other cinder cone clusters may require recalculating the model parameters in Eq. (23) to account for their particular erosional conditions. In addition, a morpho-chronological study of a scoria cone may render incorrect or misleading results if performed over volcanoes with the following characteristics:

- Cones lacking well-defined contours (e.g. Malacatepec in the DLR DEM).
- Heavily breached or open cones with insufficient (less than 30%) sectors of the original volcano contours (e.g. Cima scoria cone).
- Very small cones in a DEM with a resolution lower than 1/30 th of the basal diameter, e.g. Pelagatos in the DEM DLR (smaller than about 320 m in the basal mayor-axis).
- Multiple-vents compound volcanoes in which the limits between adjacent vents or cones are not clear, precluding the selection of single cone contours (e.g. Tlaloc).
- Cones with evident anthropogenic intervention, such as agriculture or mining.

6. Discussion and conclusions

Monogenetic volcanoes are abundant on Earth, and their origins and evolution are diverse and complex (De la Cruz-Reyna and Yokoyama, 2011; Yokoyama, 2019). The extensive fertile lands and relatively low birth-eruption rates of such volcanic fields have encouraged a rapid growth of population in and around them. A spatio-temporal hazard and a time sensitive risk assessment of that type of volcanism requires a fast and inexpensive method to figure the age distribution over the extension of volcanic fields that may include hundreds of cones.

We present here what we believe is a promising method to find such distribution from the analysis of the contour curves of a digital elevation model with sufficient resolution. Our results indicate that available satellite DEMs may have enough resolution to render morpho-chronologic results for scoria cones comparable to those from a higher resolution airborne LIDAR DEM.

The age-dependent morphometric characterization of scoria cones is calculated using the properties of the Elliptical Fourier Descriptors to quantify, in a single parameter D (Eq. (18)), the shape of closed level contours identified in a DEM. In particular, we show that D increases as the undulations along a closed contour gains presence. The number, wavelength and amplitude of the undulations –interpreted as the erosion-

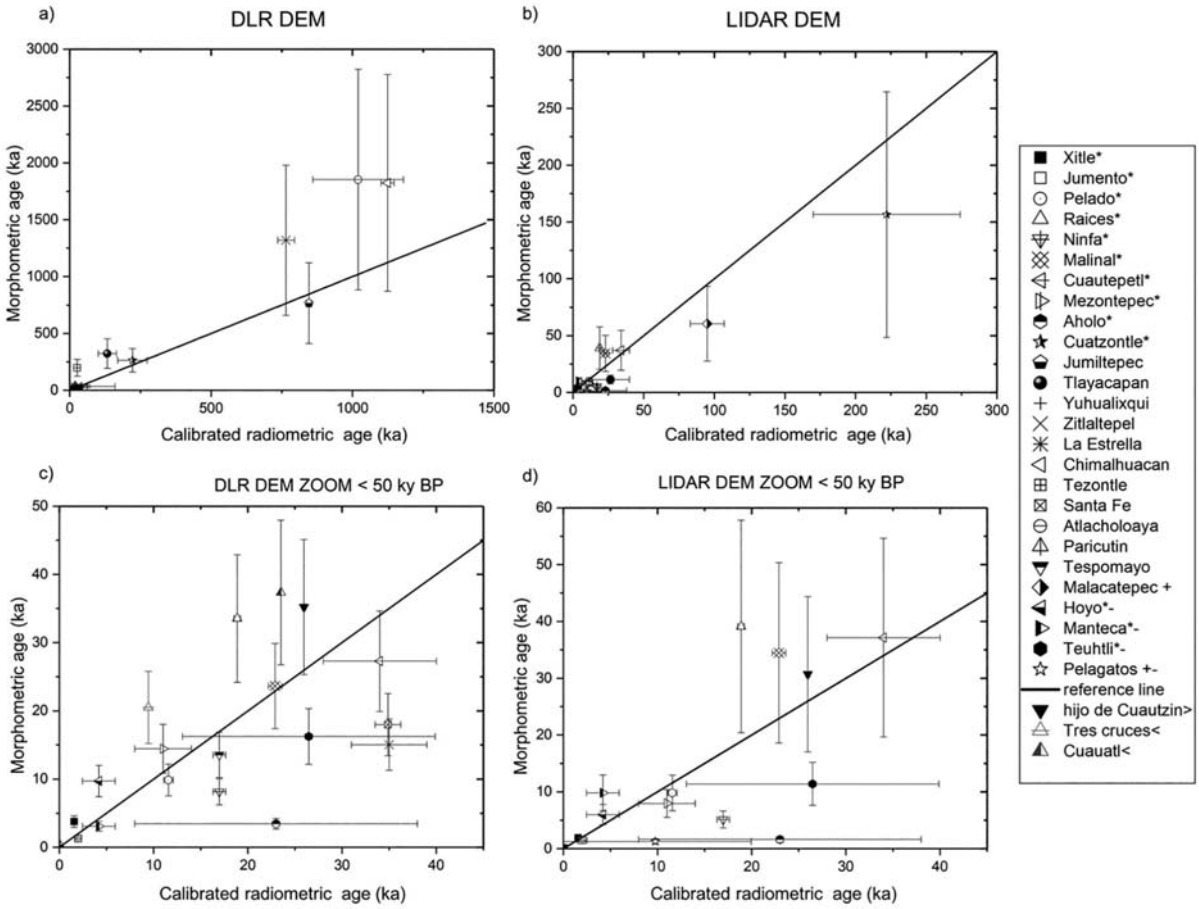

Fig. 16. Comparison between morphometric-ages (obtained from Eq. (23)) and calibrated radiometric ages. a) DLR DEM in the age range 0–1200 ky; b) LIDAR DEM in the range 0–250 ky; c) DLR DEM Zoom to the region 0–50 ky; d) LIDAR DEM Zoom to the region 0–50 ky. A dash - indicates that the radiometric age assigned to the cone is the average of the upper and lower stratigraphic radiometric age limits. The plus + marks cones only available in LIDAR DEM. The asterik * marks cones available both in DLR and LIDAR DEMS, The symbol > stands for cones whose radiometric age is a lower age bound, and < stands for scones whose radiometric age is an upper age bound. The single-bound cones (< or >) are included in this plots only to illustrate their compatibility with the morpho-chronological model (Eq. (23)) obtained with radiometric ages of volcanic products. The solid lines with slope equal to one serve as a reference.

related density, width and depth of rills and gullies on the cone's surface– are thus incorporated into that single parameter for each level contour. Since these features may vary along the height of a volcanic cone, we condense the contribution of several contours into a single averaged value $\langle D \rangle$, which measures the mean degree of modification of the cone surface from its assumed original smooth shape, thus providing information about the overall erosional condition of the scoria cone. This parameter makes the assumption of all monogenetic cones having the same conical shape at the time of formation unnecessary and replaces it with the more likely presumption that pristine cones are born with smooth surfaces, or have at most shallow and ephemeral rills.

We then tested the relation between $\langle D \rangle$ and age comparing selected radiometrically dated scoria cones from the Sierra Chichinautzin Volcanic Field with their morphometric parameter AEI calculated from DEMs of different resolutions. The correlation results support the assumption that $\langle D \rangle$ effectively measures the cumulative time-dependent effects of erosive processes and can thus provide a fair estimation of the relative ages of scoria cones in that monogenetic volcanic field.

For the Sierra Chichinautzin Volcanic Field, the age and the AEI $\langle D \rangle$ are related through a power function that, according to the available data, may be valid over the age range 0.1 to 1200 ka. Although its parameters were calculated for that volcanic field, we speculate that the power relationship may be applicable to other monogenetic volcanic fields –if some radiometric age determinations are available–, provided its coefficients are recalculated to account for different climatic and erosive conditions.

As a final remark, we wish to emphasize that two independent DEMs with different resolutions –one of them with world-wide coverage– render satisfactory and comparable results. We hope that further testing of the model on volcanic fields with different age ranges and environmental conditions would define with more precision the limits of its applicability.

CRediT authorship contribution statement

M.C. Zarazua-Carbajal: Conceptualization, Methodology, Software, Investigation, Data Curation, Visualization, Formal Analysis, Writing - Original Draft.

S. De la Cruz-Reyna: Conceptualization, Supervision, Investigation, Formal Analysis, Verification, Writing-Reviewing and Editing, Funding Acquisition.

Declaration of Competing Interest

The authors declare that they have no known competing financial interests or personal relationships that could have appeared to influence the work reported in this paper.

Acknowledgements

The authors are grateful to the Mexican Science Council (CONACYT) and the National Researchers Systems (SNI) for the research assistant

support grant (EXP. AYTE. 15617), to the DGAPA-PAPIIT-UNAM programme (grant IN-109616) for partially financing this research and very especially to the Tandem-X satellite (DEM_GEOL1097) from the German Aerospace Center (DLR) and the Mexican National Institute of Geography and Statistics (INEGI) for respectively providing the satellite and LIDAR DEMs. Special thanks to both anonymous reviewers whose comments and suggestions greatly helped to improve this paper, and to the Editor for his efficient management of the manuscript.

References

Agustín-Flores, J., Siebe, C., Guilbaud, M.-N., 2011. Geology and geochemistry of Pelagatos, Cerro del Agua, and Dos Cerros monogenetic volcanoes in the Sierra Chichinautzin volcanic field, south of México City. J. Volcanol. Geotherm. Res. 201, 143–162.

Alcalá-Reygosa, J., Arce, J.L., Schimmelpfennig, I., Muñoz Salinas, E., Castillo Rodriguez, M., Léanni, L., ASTER Team, Aumaître, G., Bourlès, D., Keddadouche, K., 2018. Revisiting the age of the Jumento volcano, Chichinautzin Volcanic Field (Central Mexico), using in situ-produced cosmogenic 10Be. J. Volcanol. Geotherm. Res. 366, 112–119.

Arce, J.L., Layer, P.W., Lassiter, J.C., Benowitz, J.A., Macías, J.L., Ramírez-Espinosa, J., 2013. 40Ar/39Ar dating, geochemistry, and isotopic analyses of the quaternary Chichinautzin volcanic field, south of Mexico City: implications for timing, eruption rate, and distribution of volcanism. Bull. Volcanol. 75, 774. https://doi.org/10.1007/s00445-013-0774-6.

Arce, J.L., Muñoz-Salinas, E., Castillo, M., Salinas, I., 2015. The ~2000 yr BP Jumento volcano, one of the youngest edifices of the Chichinautzin Volcanic Field, Central Mexico. J. Volcanol. Geotherm. Res. 308, 30–38.

Baird, D.C., 1994. Experimentation: An Introduction to Measurement Theory and Experiment Design. 3rd ed. Benjamin Cummings (ISBN 978-0133032987).

Bebbington, M.S., Cronin, S., 2011. Spatio-temporal hazard estimation in the Auckland Volcanic Field, New Zealand, with a new event-order model. Bull. Volcanol. 73, 55–72. https://doi.org/10.1007/s00445-010-0403-6.

Bemis, K.G., 1995. A Morphometric Study of Volcanoes in Guatemala, Iceland, the Snake River Plain, and the South Pacific. PhD thesis. The State University of New Jersey, Rutgers.

Bemis, K., Ferencz, M., 2017. Morphometric analysis of scoria cones: the potential for inferring process from shape. Geol. Soc. Lond., Spec. Publ. 446, 61–100. https://doi.org/10.1144/SP446.9.

Bloomfield, K., 1975. A late quaternary monogenetic volcano field in Central Mexico. Geol. Rundsch. 6, 476–497.

Condit, C.D., Connor, C.B., 1996. Recurrence rates of volcanism in basaltic volcanic fields: an example from the Springerville volcanic field, Arizona. Geol. Soc. Am. Bull. 108, 1225–1241.

Connor, C.B., Hill, B.E., 1995. Three nonhomogeneous Poisson models for the probability of basaltic volcanism: application to the Yucca Mountain region. Nevada. J. Geophys. Res. 100, 10107–10125.

Conway, F.M., Connor, C.B., Hill, B.E., Condit, C.D., Mullaney, K., Hall, C.M., 1998. Recurrence rates of basaltic volcanism in SP cluster, San Francisco volcanic field, Arizona. Geology 26, 655–658.

De la Cruz-Reyna, S., Yokoyama, I., 2011. A geophysical characterization of monogenetic volcanism. Geofis. Int. 50 (4), 465–484.

Delgado, H., Molinero, R., Cervantes, P., Nieto-Obregón, J., Lozano-Santa Cruz, R., Macías-González, H.L., Mendoza-Rosales, C., Silva-Romo, G., 1998. Geology of Xitle volcano in southern Mexico- city. A 2000 year-old monogenetic volcano in an urban area. Revista Mexicana de Ciencias Geológicas 15 (2), 115–131.

Dohrenwend, J.C., Wells, S.G., Turrin, B.D., 1986. Degradation of Quaternary cinder cones in the Cima volcanic field, Mojave Desert, California. Geol. Soc. Am. Bull. 97, 421–427.

Dóniz, J., Romero, C., Carmona, J., García, A., 2011. Erosion of Cinder Cones in Tenerife by Gully Formation, Canary Islands, Spain. Phys. Geogr. 32 (2), 139–160. https://doi.org/10.2747/0272-3646.32.2.139.

Guilbaud, M.-N., Arana-Salinas, L., Siebe, C., Barba-Pingarrón, L.A., Ortiz, A., 2015. Volcanic stratigraphy of a high-altitude Mammuthus columbi (Tlacotenco, Sierra Chichinautzin), Central México. Bull. Volcanol. 77, 17.

Guy, F., Mackaye, H.-T., Likius, A., Vignaud, P., Schmittbuhl, M., Brunet, M., 2008. Symphyseal shape variation in extant and fossil hominoids, and the symphysis of Australopithecus bahrelghazali. J. Hum. Evol. 55, 37–47.

Hasenaka, T., Carmichael, I.S.E., 1985. A compilation of location, size and geomorphological parameters of volcanoes of the Michoacán-Guanajuato volcanic field, Central Mexico. Geofis. Int. 24 (4), 577–607.

Hooper, Donald, 1995. Computer-simulation Models of Scoria Cone Degradation in the Colima and Michoacán-Guanajuato Volcanic Fields. 34. Geofísica Internacional, Mexico, pp. 321–340.

Hooper, D.M., Sheridan, M.F., 1998. Computer-simulation models of scoria cone degradation. J. Volcanol. Geotherm. Res. 83, 241–267.

Jaimes-Viera, M.C., Martin Del Pozzo, A., Layer, P.W., Benowitz, J.A., Nieto-Torres, A., 2018. Timing the evolution of a monogenetic volcanic field: Sierra Chichinautzin, Central Mexico. J. Volcanol. Geotherm. Res. 356, 241–267. https://doi.org/10.1016/j.jvolgeores.2018.03.013.

Kereszturi, G., Németh, K., 2012a. Structural and morphometric irregularities of eroded Pliocene scoria cones at the Bakony–Balaton Highland Volcanic Field, Hungary. Geomorphology 136, 45–58.

Kereszturi, G., Németh, K., 2012b. Monogenetic basaltic volcanoes: Genetic classification, growth, geomorphology and degradation. In: Nemeth, K. (Ed.), Updates in Volcanology - New Advances in Understanding Volcanic Systems. InTech https://doi.org/10.5772/51387.

Kervyn, M., Ernst, G.G.J., Carracedo, J.-C., Jacobs, P., 2012. Geomorphometric variability of "monogenetic" volcanic cones: evidence from Mauna kea, Lanzarote and experimental cones. Geomorphology 136, 59–75.

Kirianov, V.Y., Koloskov, A.B., De la Cruz, S., Martin del Pozzo, A.L., 1990. The Major Stages of Manifestation of Recent Volcanism in the Chichinautzin Zone. Geological Series. 311. USSR Academy of Sciences, pp. 432–434.

Kshirsagar, P., Siebe, C., Guilbaud, M.-N., Salinas, S., Layer, P.W., 2015. Late Pleistocene Alberca de Guadalupe maar volcano (Zacapu basin, Michoacán): Stratigraphy, tectonic setting, and paleo-hydrogeological environment. J. Volcanol. Geotherm. Res. 304, 214–236.

Kuhl, F., Giardina, C.R., 1982. Elliptic Fourier features of a closed contour: Comput. Graph. Image Process. 18, 236–258.

Márquez, A., Surendra, P. Verma, Anguita, F., Oyarzun, R., Brandle, J.L., 1999. Tectonics and volcanism of Sierra Chichinautzin: extension at the front of the central trans-Mexican volcanic belt. J. Volcanol. Geotherm. Res. 93, 125–150.

Marrero, J.M., García, A., Berrocoso, M., Llinares, A., Rodriguez-Lozada, A., Ortiz, R., 2019. Strategies for the development of volcanic hazard maps in monogenetic volcanic fields: the example of La Palma (Canary Islands). J. Appl. Volcanol. 8, 6.

Martin del Pozzo, A.L., 1982. Monogenetic vulcanism in Sierra Chichinautzin, México. Bull. Volcanol. 45, 9–24.

Nieto-Torres, A., Martin Del Pozzo, A.L., 2019. Spatio-temporal hazard assessment of a monogenetic volcanic field, near México City. J. Volcanol. Geotherm. Res. 371, 46–58. https://doi.org/10.1016/j.jvolgeores.2019.01.006.

Porter, S.C., 1972. Distribution, morphology, and size-frequency of cinder Cones on Mauna Kea Volcano, Hawaii. Geol. Soc. Am. Bull. 83, 3607–3612. https://doi.org/10.1130/0016-7606(1972)83[3607:DMASFO]2.0.CO;2.

Schmittbuhl, M., Allenbach, B., Le Minor, J.M., Schaaf, A., 2003. Elliptical descriptors: some simplified morphometric parameters for the quantification of complex outlines. Math. Geol. 35 (7), 853–871.

Siebe, C., 2000. Age and archaeological implications of Xitle volcano, southwestern basin of Mexico-City. J. Volcanol. Geotherm. Res. 104, 45–64.

Siebe, C., Rodriguez-Lara, V., Schaaf, P., 2004. Radiocarbon ages of holocene Pelado, Guespalapa, and Chichinautzin scoria cones, south of Mexico city: implications for archaeology and future hazards. Bull. Volcanol. 66, 203–225.

Siebe, C., Arana-Salinas, L., Abrams, M., 2005. Geology and radiocarbon ages of Tlaloc, Tlacotenco, Cuauhtzin, Hijo del Cuauhtzin, Teuhtli, and Ocusacayo monogenetic volcanoes in the central part of the Sierra Chichinautzin, Mexico. J. Volcanol. Geotherm. Res. 141, 225–243.

Smith, I.E.M., Németh, K., 2017. Source to surface model of monogenetic volcanism: a critical revies. Geol. Soc. Lond., Spec. Publ. 446, 1–28. https://doi.org/10.1144/SP446.14.

Soares, M.L.C., Mayo, S.J., Gribel, R., Kirkup, D., 2011. Elliptic Fourier Analysis of leaf outlines in five species of Heteropsis (Araceae) from the Reserva Florestal Adolpho Ducke, Manaus, Amazonas, Brazil. Kew Bull. 66, 1–8.

Tort, A., 2003. Elliptical Fourier functions as a morphological descriptor of the genus Stenosarina (Brachiopoda, Terebratulida, New Caledonia). Math. Geol. 35, 873–885. https://doi.org/10.1023/B:MATG.0000007784.18452.73.

Tort, A., Finizola, A., 2005. The buried caldera of Misti volcano, Peru, revealed by combining a self-potential survey with elliptic Fourier function analysis of topography. J. Volcanol. Geotherm. Res. 141, 283–297. https://doi.org/10.1016/j.jvolgeores.2004.11.005.

Velasco-Tapia, F., Verma, S., 2001. Estado actual de la investigación geoquímica en el campo monogenético de la Sierra de Chichinautzin: análisis de información y perspectivas. Revista Mexicana de Ciencias Geológicas 18 (1), 1–36.

Wood, C.A., 1980. Morphometric analysis of cinder cone degradation. J. Volcanol. Geotherm. Res. 8, 137–160.

Yokoyama, I., 2019. Clusters of small monogenetic cones: a particular type of confined volcanism. Ann. Geophys. 62 (6), VO678. https://doi.org/10.4401/ag-8176.

York, D., 1966. Least-squares fitting of a straight line. Can. J. Phys. 44, 1079–1086.

CAPITULO 3

EFECTOS DE LA RESOLUCIÓN DEL MODELO DE ELEVACIÓN DIGITAL: SOBRE EL ANÁLISIS MORFOLÓGICO ORIENTADO A LA CRONOMETRÍA DE CONOS DE ESCORIA EN UN EXTENSO CAMPO VOLCÁNICO, LA SIERRA CHICHINAUTZIN, CENTRO DE MÉXICO.

En este artículo (https://doi.org/10.1016/j.geomorph.2021.107842), publicado en la revista "*Geomorphology",* se compara la caracterización morfométrica de conos de escoria, mediante el análisis de perfiles de elevación y curvas de contorno obtenidos de dos MDE de distintas resoluciones, se discuten los alcances y limitaciones del uso cronométrico de distintos parámetros morfométricos y la influencia de la resolución del MDE en la interpretación y uso de modelos morfocronométricos.

Resumen:

La caracterización morfológica de los conos monogenéticos proporciona información esencial sobre diferentes características genéticas y evolutivas, relacionadas con el peligro del vulcanismo dispersivo. Específicamente, se puede usar para medir el grado de alteración por erosión de la forma de los conos de escoria y, a partir de ahí, para estimar la edad relativa de volcanes individuales en campos volcánicos extensos y las implicaciones de peligro en función de la distribución espacial de edades de los conos. En este trabajo se compara el efecto de la resolución de los Modelos digitales de elevación (MDE) en la caracterización morfométrica de conos de escoria, mediante la comparación de 13 parámetros morfométricos resultantes del análisis de los perfiles verticales de elevación más la nueva métrica basada en un parámetro introducido en el artículo del capítulo 2, que describe y cuantifica la forma de las curvas de nivel de los conos. El análisis se realizó con 19 conos monogenéticos de escoria fechados radiométricamente y localizados en el Campo Volcánico de la Sierra Chichinautzin. Los parámetros se calcularon a partir de dos modelos digitales de elevación independientes,

con diferentes resoluciones: la base de datos SAR TanDEM-X (12 m resolución horizontal) y un MDE LIDAR aéreo de mayor resolución (5 m resolución horizontal). A partir del análisis de la información disponible sobre los conos volcánicos en el rango de edad de 1.6 a 222 ka, se concluye que los parámetros morfométricos relevantes para la edad calculados a partir del MDE del satélite TanDEM-X representan valores similares y funcionan igual de bien que la base de datos aérea LIDAR para la caracterización morfocronológica de los conos de escoria, ampliando el papel de los datos digitales de elevación satelitales al estudio de las características detalladas del vulcanismo distribuido a nivel global.

Geomorphology 389 (2021) 107842

Contents lists available at ScienceDirect

Geomorphology

journal homepage: www.elsevier.com/locate/geomorph

Digital Elevation Model resolution: Effects on the chronometry-oriented morphological analysis of monogenetic scoria cones in the Sierra Chichinautzin, central Mexico

María Cristina Zarazúa-Carbajal [a,*], Servando De la Cruz-Reyna [b]

[a] Posgrado en Ciencias de la Tierra, Instituto de Geofísica, Universidad Nacional Autónoma de México (UNAM), CDMX 04510, Mexico
[b] Instituto de Geofísica, Universidad Nacional Autónoma de México (UNAM), CDMX 04510, Mexico

ARTICLE INFO

Article history:
Received 18 November 2020
Received in revised form 15 June 2021
Accepted 26 June 2021
Available online 30 June 2021

Keywords:
Scoria cone morphology
Digital Elevation Model
Resolution
Dispersive volcanism
Monogenetic volcanic fields

ABSTRACT

Morphological characterization of monogenetic cones provides essential information on different genetic, evolutionary, and hazard-related features of dispersive volcanism. Specifically, it may be used to measure the degree of erosional shape alteration of scoria cones, and from there, to estimate the age of individual volcanoes in extensive volcanic fields and the hazard implications of the cones' age distribution. Here we compare diverse morphometric parameters, some resulting from the elevation profiles analyses, and a novel one obtained from a shape characterization of elevation contours using Elliptical Fourier Descriptors, of 19 radiometrically-dated monogenetic scoria cones in the Sierra Chichinautzin Volcanic Field in Central Mexico. The parameters were calculated from two independent Digital Elevation Models with different resolutions: the 12 m resolution TanDEM-X SAR database, and a 5 m resolution airborne LIDAR DEM. From the analysis of the available information on the volcanic cones in the age range 1.6 to 222 ka, we conclude that the age-relevant morphometric parameters calculated from the TanDEM-X satellite DEM render alike values and perform equally well as the LIDAR airborne DEM for the morpho-chronological characterization of scoria cones, expanding the role of digital satellite elevation data to the study of detailed features of distributed volcanism at a global level.

1. Introduction

Monogenetic volcanic fields (MVF), formed by a large number of individual volcanoes clustered over extensive areas, are a distributed manifestation of magmatism and the most abundant expression of subaerial magma vents on Earth. Such clusters appear in different continental tectonic settings (Németh, 2010). The individual volcanoes forming those clusters are relatively small structures (compared with central, polygenetic volcanoes), which commonly erupt only once in effusive or moderately explosive episodes with low magma-production rates that can last for several years, and may blanket hundreds of square kilometers with lava flows, rendering arable lands useless (De la Cruz-Reyna and Yokoyama, 2011). Because of its abundance, large spatial dispersion, and long recurrence time between monogenetic volcano births, and fertility of the volcanic soils, an increasing population all over the world has settled in monogenetic volcanic fields. The nature of this volcanism makes its hazard and risk appraisals a complex problem (e.g. Bebbington and Cronin, 2011; Nieto-Torres and Martin Del Pozzo, 2019), since, unlike central volcanoes where a time-sensitive hazard assessment requires a knowledge of the time distribution of past eruptions produced in a fixed point in space, a MVF requires a knowledge of the spatio-temporal distribution of monogenetic volcano births. In the case of central volcanoes, this is achieved radiometrically or stratigraphically dating samples of past eruptions products, which is a laborious and expensive procedure (e.g. Bronk Ramsey, 2008). This has been done in a relatively small proportion of the monogenetic volcanoes (e.g. Lindsay and Leonard, 2009; Avellán et al., 2020), but exhaustive radiometric dating may be impractical in wide fields like the Sierra Chichinautzin monogenetic volcanic field (SCMVF), comprising over 220 monogenetic volcanoes distributed in an area near 3000 km^2 (Márquez et al., 1999). Furthermore, thorough radiometric coverage of a large field such as the Michoacán-Guanajuato volcanic field (MGVF), including more than 1200 volcanic vents covering an area of 40,000 km^2 (Hasenaka and Carmichael, 1985), would be unviable. Both volcanic fields are located in densely populated areas of Mexico (Fig. 1).

A way to address this problem is to look for alternative age estimation methods, such as measuring the age-dependent shape evolution of individual monogenetic volcanoes. Considering the diversity of monogenetic volcano types, these methods have been usually applied to scoria cones that may have a clearer or simpler shape evolution. However, the use of some of these methods for morpho-chronological dating has been somewhat controversial. For instance, age estimations

* Corresponding author.
E-mail address: mczarazua@comunidad.unam.mx (M.C. Zarazúa-Carbajal).

https://doi.org/10.1016/j.geomorph.2021.107842
0169-555X/

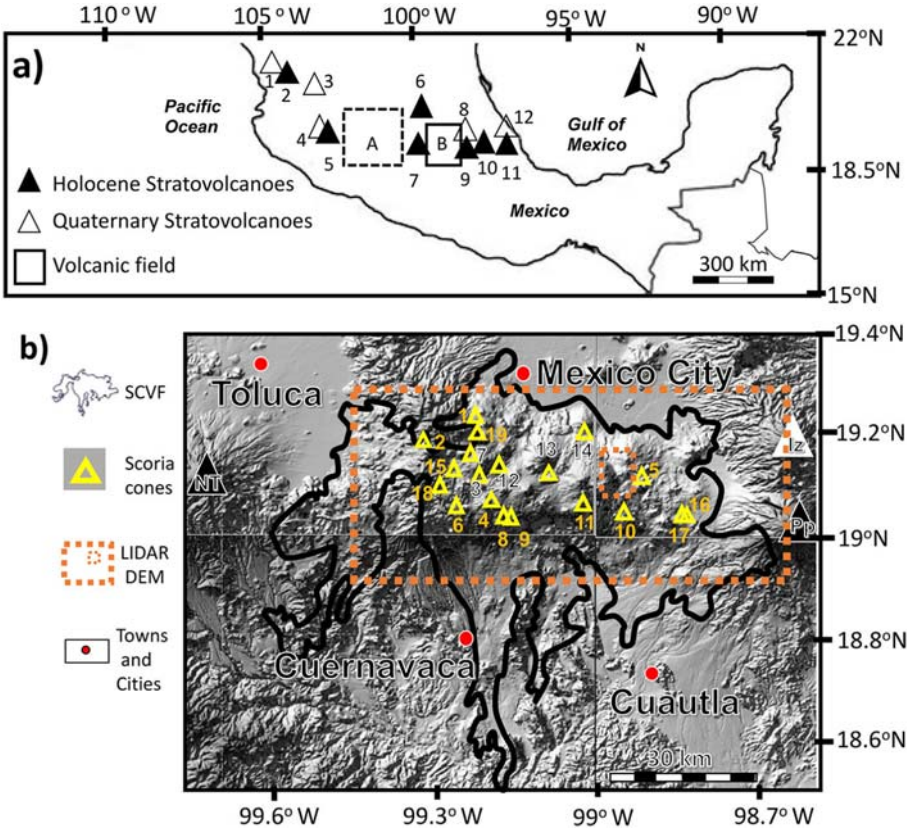

Fig. 1. a) Principal volcanic features along the Trans Mexican-Volcanic Belt: Central volcanoes: 1. Sangangüey, 2. Ceboruco, 3. Tequila, 4. Nevado de Colima, 5. Fuego de Colima, 6. Jocotitlán, 7. Nevado de Toluca, 8. Iztaccihuatl, 9. Popocatepetl, 10. La Malinche, 11. Pico de Orizaba, 12. Cofre de Perote, A: Michoacán-Guanajuato volcanic field; B: Sierra Chichinautzin volcanic field. b) Central region of the Trans Mexican-Volcanic Belt, including major metropolitan areas (red dots). The thick irregular line marks the limits of the Sierra Chichinautzin volcanic field. The orange dotted lines enclose the area covered by two DEMs: a 5 m horizontal resolution (LIDAR DEM) and the 12 m horizontal resolution TanDEM-X (DLR DEM). The smaller orange rectangle within the larger rectangle lacks Lidar data. Radiometrically dated scoria cones included in both DEMs are marked as yellow triangles numbered according to Table 1 and Fig. 4. NT: Nevado de Toluca, Iz: Iztaccihuatl, Pp: Popocatepetl.

based on the vertical cross-sectional shape of cinder cones implicitly assumes that all cones acquired the same general shape at the time of their formation, determined by the hillslope repose angle of accumulating tephra and that they degrade at similar rates in response to regional erosive factors (Porter, 1972; Wood, 1980a,b), which are unsupported assumptions according to Kereszturi and Németh (2012), Kervyn et al. (2012), Kereszturi et al. (2013), and Bemis and Ferencz (2017).

Nevertheless, some volcanic fields show acceptable correlations between some shape parameters and their radiometric ages, making morpho-chronological dating a promising alternative to expensive radioisotope methods (Bloomfield, 1975; Wood, 1980b; Hooper and Sheridan, 1998; Gilichinsky et al., 2010; Inbar et al., 2011; Nieto-Torres and Martin Del Pozzo, 2019).

The main objective of the present work is to determine the sensitivity of several age-related morphological parameters of radiometrically dated scoria cones, to the resolution of different Digital Elevation Models (DEM). Such morphological parameters include those characterizing the cone's vertical cross-section, as well as a novel –recently introduced– parameter resulting from a Fourier analysis of the elevation contours providing additional morpho-chronological clues (Zarazúa-Carbajal and De la Cruz-Reyna, 2020). The examined DEMs are a 5 m resolution airborne LIDAR (Light Imaging Detection and Ranging) database covering a limited area of the SCMVF (Fig. 1B), and the TanDEM-X 12 m resolution satellite database with worldwide coverage.

Since different relations between the morphometric parameters and the volcanoes' age may result from different DEMs, it is necessary to assure that the data resolution does not significantly affect the outcomes of morphometric analysis. Indeed, previous studies (e.g. Thompson et al., 2001) on the importance of DEM's vertical and horizontal resolutions on the characterization of landscapes, reported significantly different terrain attributes obtained with DEMs with 10 m or 30 m horizontal resolutions, and 0.1 m or 10 m vertical accuracy. Similarly, Kervyn et al. (2008) concluded from simulated DEMs with resolutions of 1, 10, 30, and 90 m that there is an increasing underestimation of heights, and an overestimation of horizontal measures as the resolution of the DEM decreases and that the importance of these effects strongly depends on the size, slope, and sharpness of breaks in the terrain slope. They observed that the identification of small-scale topographic features (like hills ~100 m in size) is hindered when the DEM spatial resolution is coarser than ~1/3 of the characteristic dimension of the feature. In a separate study on cinder cones in central Kamchatka, Gilichinsky et al. (2010) compared morphometric parameters obtained with five different DEMs: a 10 m map-based DEM, the 14 m ALOS DEM, an ASTER 30 m-generated DEM, and the 90 m (3 arc-second) spatial resolution SRTM3 DEM. They found that the morphometric parameters of each cinder cone were directly affected by a decrease in DEM resolution: lower-resolution DEMs were inherently less able to represent smaller elevation variations, yielding lower calculated slopes and height/width ratio values. They concluded that the straightforward numerical comparison of morphometric values measured from different resolution DEMs might be erroneous unless adequate correlations among them are preserved. Fornaciai et al. (2012) compared morphometric characterizations based on volume, slope, cone height, and basal and crater widths (but not crater depths) of 26 scoria cones (with volumes up to 35×10^6 m^3) located in the flanks of Etna, obtained from a 2 m LIDAR DEM, the 10 m TINITALY/01 DEM, and the 30 m ASTER GDEM, and of 120 scoria cones (with volumes up to 270×10^6 m^3) located in the San Francisco, Springville, Mauna Kea and Newberry volcanic fields,

using a 10 m NED DEM and the 30 m ASTER GDEM. They concluded that the 10 m DEMs were suitable for studying scoria cone morphometry, while ASTER GDEM was reliable only for cones with volumes exceeding 30×10^6 m^3. Similarly, Grosse et al. (2012) compared morphometric characterizations (including crater depths) of 13 composite volcanoes in Nicaragua (volumes between 0.08 and 15 km^3) using the 30 m ASTER GDEM, the 90 m STRM DEM, and an 80 m DEM derived from digitizing topographic maps (TOPO). They concluded that those DEMs may provide useful morphological information for large composite volcanoes, but they did not have enough resolution to study smaller constructs such as scoria cones. In addition, another recent study by Grosse et al. (2020), suggests that a 12 m resolution like that of the TanDEM-X DEM is probably the lower limit to resolve morphological features of scoria cones and their craters.

In the present work, we intend to determine to what extent differences in age-dependent erosional terrain attributes may be significant in well-delimited landscape features (such as scoria cones), sampled from independent DEMs with 5 m or 12 m horizontal resolutions and 1 m or 2 m vertical accuracy. As a main result, we conclude that essential morphometric parameters required for the characterization of the erosional state of scoria cones, and thus for their age estimation, may be calculated with similar precision with either type of DEM, within the resolution range characterizing those airborne and satellite databases.

2. Geological setting and topographic datasets

2.1. The Sierra Chichinautzin Monogenetic Volcanic Field

As mentioned above, the SCMVF clusters over 220 monogenetic volcanoes, including scoria cones (Márquez et al., 1999). It is located in the middle trans-Mexican volcanic belt (TMVB), in a densely populated region limited by some of the largest stratovolcanoes in Mexico: Nevado de Toluca to the west and Popocatépetl and Iztaccíhuatl to the east (Fig. 1B).

The volcanic rocks of the SCMVF are mostly andesites with subordinate basalts and dacites that define a calc-alkaline series (Gunn and Mooser, 1971; Swinamer, 1989; Wallace and Carmichael, 1999; Siebe et al., 2005). Their origins are related to the subduction of the Cocos Plate under the North American Plate. Paleomagnetic evidence place the earliest rocks in the Brunhes chron, namely younger than about 790 ky (Urrutia-Fucugauchi and Martin Del Pozzo, 1993). Afterward, the products of numerous eruptions constructed the massive Sierra Chichinautzin, blocking the Mexico City basin drainage to the south (Fries, 1960). The SCMVF may still be considered an active volcanic field given the young age of the latest eruption that formed Xitle volcano, whose products covered Cuicuilco and other human settlements (Siebe, 2000).

The scoria cones analyzed in this study are listed in Table 1, and their particular features can be found in the references within the table.

2.2. Digital Elevation Models

In the present case, we elaborate a morphological characterization of selected scoria monogenetic cones in the SCMVF using the abovementioned DEMs: An interferometric synthetic aperture radar (InSAR) DEM, kindly provided by the TanDEM-X mission from the German Aerospace Center (DLR), with ~12 m horizontal resolution, and 2–4 m slope-dependent relative vertical accuracy (henceforth referred as DLR DEM), generated by combinations of ascending and descending acquisitions, allowing proper resolution even in areas affected by shadow or layover in steep slopes (Rizzoli et al., 2017). The other is an airborne LIDAR DEM, kindly provided by the Mexican National Institute of Geography and Statistics (INEGI, https://www.inegi.org.mx/), with 5 m horizontal resolution and 1 m vertical accuracy (henceforth referred to as LIDAR DEM). The LIDAR DEM covers about 60% of the monogenetic volcano field, while the DLR DEM covers the whole area (Fig. 1B).

3. Methodology

The morphological parameters resolution-testing methodology involves two procedures: one is the analysis and characterization of elevation profiles, mostly based on the morphometric methods of Favalli et al. (2009) and Bemis and Ferencz (2017) employing 12 morphologic parameters to describe the vertical cross-section of a scoria cone. The second is the analysis of elevation contours, which results in a single parameter measuring the degree of contour shape modification assumedly caused by erosion on the cone surface, the Average Erosion Index *AEI* (Zarazúa-Carbajal and De la Cruz-Reyna, 2020). From there,

Table 1
Location and calibrated radiometric dates of selected scoria cones. Calibrated ages were obtained using OxCal 4.2 2 (https://c14.arch.ox.ac.uk/embed.php?File=oxcal.html). References: (1) Kirianov et al. (1990); (2) Siebe (2000); (3) Siebe et al. (2004); (4) Siebe et al. (2005); (5) Agustín-Flores et al. (2011); (6) Guilbaud et al. (2015); (7) Arce et al. (2015); (8) Jaimes-Viera et al. (2018). Cone number (CN) according to Fig. 4.

CN	Volcano name	Lat (N)	Lon (E)	Radiometric age ka	Calibrated age ka	Reference
1	Xitle	19.2467	−99.2223	1.67 ± 0.035 (^{14}C)	1.580 ± 0.049	2
2	Jumento	19.21	−99.31		ca. 2	7
3	Pelado	19.1511	−99.2175	10 ± 0.5 (^{14}C)	11.599 ± 0.683	3
4	La Cima	19.1116	−99.1951	10.16 ± 0.07 (^{14}C)	11.810 ± 0.161	1
5	La Ninfa	19.1530	−98.9322	14 ± 0.5 (^{14}C)	16.978 ± 0.667	5
6	Raices	19.1041	99.2566	15.57 ± 0.30 (^{14}C)	18.87 ± 0.345	1
7	Malinal	19.2228	−99.2179	18.9 ± 0.6 (^{14}C)	22.896 ± 0.714	1
8	El Hoyo	19.0893	−99.1688	>2.835 ± 0.070 (^{14}C)	>2.961 ± 0.094	3
				<4.690 ± 0.090 (^{14}C)	<5.415 ± 0.120	
9	Manteca	19.0894	−99.1780	>2.835 ± 0.070 (^{14}C)	>2.961 ± 0.094	3
				<4.690 ± 0.090 (^{14}C)	<5.415 ± 0.120	
10	Pelagatos	19.09	−98.96	>2.520 ± 0.105 (^{14}C)	>2.566 ± 0.122	5
				<14 ± 0.5 (^{14}C)	<16.978 ± 0.667	
11	Tlaloc	19.1091	−99.0333	<6.200 ± 0.085 (^{14}C)	<7.095 ± 0.107	4
12	Oyameyo	19.1755	−99.1805	>8.315 ± 0.155 (^{14}C)	>9.629 ± 0.181	3
				<14 ± 0.5 (^{14}C)	<16.978 ± 0.667	
13	Teuhtli	19.2242	−99.0294	>14 ± 0.5 (^{14}C)	>16.978 ± 0.667	4
				<31.790 + 0.755/−0.690 (^{14}C)	<35.908 ± 0.908	6
14	Hijo de Cuauhtzin	19.1558	−99.0927	>20.895 ± 0.245 (^{14}C)	>25.150 ± 0.322	4
15	Aholo	19.0911	98.8544	23 ± 15 (^{40}Ar/^{39}Ar)		8
16	Mezontepec	19.1883	99.2292	11 ± 3 (^{40}Ar/^{39}Ar)		8
17	Cuautepel	19.0911	98.8603	34 ± 5 (^{40}Ar/^{39}Ar)		8
18	Malacatepec	19.1625	99.2592	95 ± 12 (^{40}Ar/^{39}Ar)		8
19	Cuatzontle	19.2392	99.2117	222 ± 52 (^{40}Ar/^{39}Ar)		8

we identify the morphometric parameters that may be more sensitive to age-dependent erosional processes, and less sensitive to the DEM resolution.

3.1. Analysis of elevation profiles

From the analysis of elevation profiles, we obtain the average dimensions of each scoria cone, as well as the dimensionless parameters characterizing its shape. The values of some morphometric shape parameters, especially the ratio between the cone's height and the cone's basal diameter, are highly dependent on the criteria used to measure the volcano standard morphometric parameters such as the cone height, and the cone and crater widths (Favalli et al., 2009) and on how the volcano edifice boundary limits are selected (Grosse et al., 2012). Examples of such different criteria may be found in Scott and Trask (1971), Porter (1972), Bloomfield (1975), Settle (1979), Wood (1980a,b), Hasenaka and Carmichael (1985), Hooper and Sheridan (1998), Favalli et al. (2009), Gilichinsky et al. (2010), Bemis et al. (2011), Inbar et al. (2011), Grosse et al. (2012), Kervyn et al. (2012), Kereszturi et al. (2013), Bemis and Ferencz (2017), and Nieto-Torres and Martin Del Pozzo (2019).

In this work, for each scoria cone, and following a methodology similar to that devised by Bemis and Ferencz (2017), we analyze six elevation profiles, four crossing the cone's center and two crossing the crater's center, as illustrated in Fig. 2. The centers of the cone and the crater are defined as the centroids of the best-fitted ellipses to the points delimiting the volcanic edifice and the crater rim (**X** marks in Fig. 2a and b); such points are visually identified as the well-defined changes in the vertical gradients and crosschecking with the contour map for the regions with the highest density of closed contours. Elevation profiles crossing the center of each cone were generated with an azimuthal separation of 45° with respect to the orientation of the major axis of the best-fitted ellipse to the horizontal cross-section of the cone. Elevation profiles crossing the center of each crater were generated in a similar way, one along the major axis of the best-fitted ellipse to the crater and the second at 45° relative to that orientation. From each elevation profile, we calculate two cone heights (*Hco*), a basal diameter (*Wco*), the crater diameter (*Wcr*), two hillslope angles (θ_1, θ_2), the terrain or substratum inclination (θ_{sus}) and the crater depth (*Dcr*), all illustrated in Fig. 3. The selection of points P1, P2, P3, and P4 (in Fig. 3) is determined by visually identifying slope breaks along each of the elevation profiles. P5 is selected as the point with the lowest elevation within the crater limits.

To analyze the vertical profiles we use two approaches, similar to those proposed by Favalli et al. (2009), a cone morphometric characterization disregarding the inclination of the terrain, and another weighing such inclination denoted by the subscript '*incl*' in the parameters. We thus estimate the representative cone height *Hco* as the average of the vertical distances Hco_1 and Hco_2 (dashed vertical arrows in Fig. 3) between the crater rim and the horizontal or inclined limits of the base of the cone (marked with **X** in Fig. 3) for the eight elevation profiles.

In a regionally tilted terrain, the height considering the inclination of the substratum Hco_{incl} is measured as the average of the minimum perpendicular distances between the point of maximum elevation on each side of the eight profiles and the line that defines the inclination of the substrate. We consider this approach, instead of the vertical distance between the crater rim and the inclined plane as Favalli et al. (2009) do, to make the estimation of the volume easier by simpler geometrical

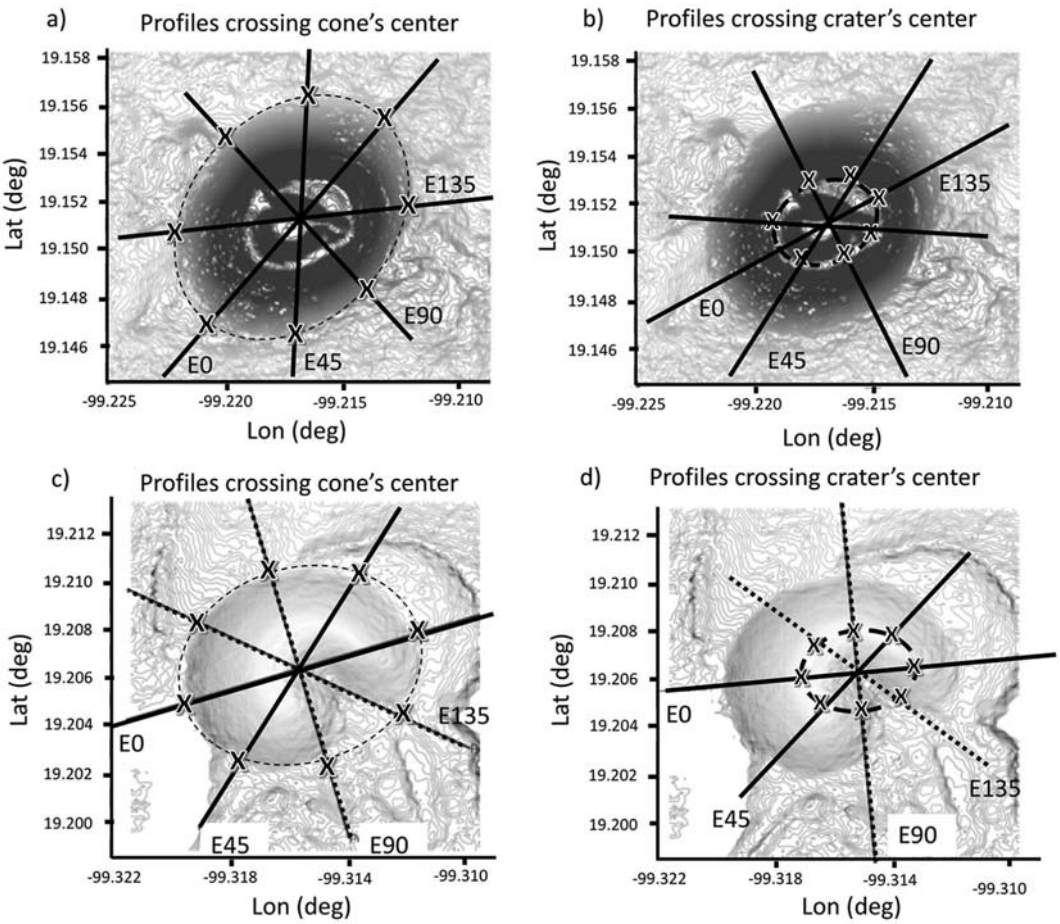

Fig. 2. Plan view of elevation profiles. a) and b) show the elevation contours of the nearly ideally shaped Pelado scoria cone in LIDAR DEM. c) and d) show the elevation contours of the horseshoe-shaped scoria cone Jumento in LIDAR DEM. The **X** marks represent points delimiting the base of the cone in (a) and (c), and the crater in (b) and (d). Dotted lines in c) and d) represent profiles crossing breached sectors and therefore omitted in the analysis.

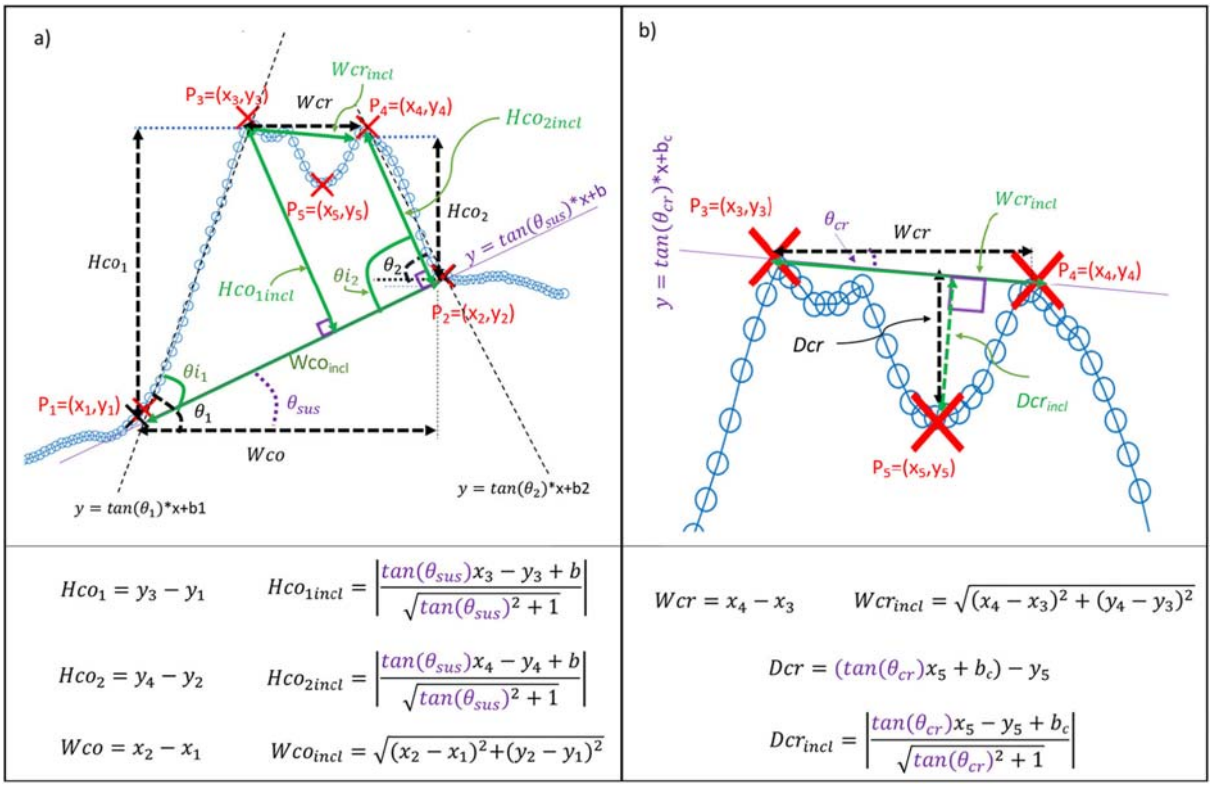

Fig. 3. Schematic elevation profile and related morphometric parameters. a) Parameters characterizing the morphometry of the cone across an elevation profile. b) Parameters characterizing the morphometry of the crater across an elevation profile. Squares denote right angles.

relations. Furthermore, the height values calculated with the Favalli et al. (2009) approach can be readily obtained from our approach by just dividing our value by the cosine of the substratum angle, yielding the same values for a horizontal substratum.To estimate the basal diameter of the cone *Wco*, we average the horizontal distance between each pair of points delimiting the base of the cone obtained from the eight elevation profiles. Similarly, to compute the inclined diameter Wco_{incl}, we average the Euclidean distance between each of the eight pairs of points delimiting the tilted base of the cone. We also obtain the *long axis length* of the cone's base as the maximum *Wco* value of the eight profiles, and the *short axis length* as the *Wco* value of the profile perpendicular to the *long axis*. The same selection criteria are used to estimate the *inclined long* and *short-axis lengths*. The diameters of the crater *Wcr* and Wcr_{incl} are estimated in the same way, but using only the four profiles crossing the center of the crater. The depths of the crater *Dcr* and Dcr_{incl} are respectively defined as the maximum values of the vertical and perpendicular distances between the deepest points within the crater and the lines crossing the two points delimiting the crater for each of the four elevation profiles crossing its center.

We calculate the inclination of the elevation profile base (θ_{sus}) from the equation of a straight line joining 2 points at the base of the profile (*P1* and *P2* in Fig. 3).

$$y = tan(\theta_{sus})x + b \tag{1}$$

Then,

$$\theta_{sus} = atan\left(\frac{y_2 - y_1}{x_2 - x_1}\right) \tag{2}$$

and

$$b = y_2 - x_2\left(\frac{y_2 - y_1}{x_2 - x_1}\right) \tag{3}$$

The actual hillslope of a cone is a variable that strongly depends on the volcano surface materials and contains information of many genetic and further erosional processes (Riedel et al., 2003; Kervyn et al., 2012). To consistently determine a characteristic value of a hillslope angle 'θ' from different DEMs, and to include possible differences among different sides of the cones, we estimate the value of the tangent of the hillslope angles '*Z*' by fitting straight lines ($y = Z\,x + b$) to all points conforming each of the hillslopes of the profiles. Therefore, for each elevation profile, we obtain two values of the hillslope tangent Z (Eq. (4)), one for each side of the elevation profile whose corresponding angles are represented as θ_1 and θ_2 in Fig. 3.

$$Z = tan(\theta) \tag{4}$$

To correct the hillslope angle θ for the terrain inclination, the slope θ_{sus} is added or subtracted (Fig. 3). The inclined hillslope tangent Z_{incl} is then given by Eq. (5).

$$Z_{incl} = \begin{cases} tan(|\theta| + |\theta_{sus}|) & if\ tan(\theta)\cdot tan(\theta_{sus}) < 0 \\ tan(|\theta| - |\theta_{sus}|) & if\ tan(\theta)\cdot tan(\theta_{sus}) > 0 \end{cases} \tag{5}$$

Using the cone dimensions obtained from the elevation profiles described in Fig. 3, we calculate six additional morphometric parameters using the nomenclature of Bemis and Ferencz (2017): Aspect ratio '*Ar*' (Eq. (6)), flat-topped-ness '*f*' (Eq. (7)), relative crater-depth '*DcrH*' (Eq. (8)), elongation '*el*' (Eq. (9)), orientation '*or*' (Eq. (10)), and volume '*V*' (Eq. (11)). The brackets ⟨ ⟩ denote averages over all of the considered elevation profiles, *max* represents the maximum measured value from all considered profiles, *sa*, *la*, and $\propto_{la}$ respectively stand for *short axis length*, *long axis length*, and *azimuth of long axis*, respectively.

$$Ar = \langle Hco/Wco \rangle \tag{6}$$

$$f = \langle Wcr/Wco \rangle \tag{7}$$

$$DcrH = Dcr / max\,(Hco) \tag{8}$$

$$el = sa/la \tag{9}$$

$$or = \propto_{la} \tag{10}$$

We approximate the material volume of the cone as the difference between the volume of a truncated cone of elliptical cross-section and the volume of a conical-shaped crater with elliptical cross-section:

$$V = \frac{\pi H_{co}}{3}\left(\frac{A^2B - a^2b}{A - a}\right) - \frac{\pi D_{cr}ab}{3} \tag{11}$$

where A and B and a and b are the *long and short axes lengths* of the base and the crater respectively.

We also estimate the ratio between the maximum depth of the crater and the average diameter of the crater *CI* (Eq. (12)), a parameter related to crater in-fill (Grosse et al., 2020) in cones with well-defined craters.

$$CI = Dcr/\langle Wcr\rangle \tag{12}$$

Similarly, to prevent the above-mentioned error in the calculation of the shape parameters caused by the regional terrain inclination (Favalli et al., 2009; Kervyn et al., 2012), we calculate terrain-inclination corrected versions of the shape parameters: inclined Aspect ratio 'Ar_{incl}' (Eq. (13)), inclined flat-topped-ness 'f_{incl}' (Eq. (14)), inclined relative crater-depth '$DcrH_{incl}$' (Eq. (15)), inclined elongation el_{incl} (Eq. (16)), ratio between the inclined maximum depth of the crater and the inclined average diameter of the crater CI_{incl} (Eq. (17)), and inclined volume V_{incl} (Eq. (18)).

$$Ar_{incl} = \langle Hco_{incl}/Wco_{incl}\rangle \tag{13}$$

$$f_{incl} = \langle Wcr_{incl}/Wco_{incl}\rangle \tag{14}$$

$$DcrH_{incl} = Dcr_{incl}/\max\,(Hco_{incl}) \tag{15}$$

$$el_{incl} = sa_{incl}/la_{incl} \tag{16}$$

$$CI_{incl} = Dcr_{incl}/\langle Wcr_{incl}\rangle \tag{17}$$

$$V_{incl} = \frac{\pi Hco_{incl}}{3}\left(\frac{A_{incl}{}^2B_{incl} - a_{incl}{}^2b_{incl}}{A_{incl} - a_{incl}}\right) - \frac{\pi Dcr_{incl}a_{incl}b_{incl}}{3} \tag{18}$$

where A_{incl} and B_{incl}, and a_{incl} and b_{incl} are the *long* and *short axes lengths* of the inclined base and the crater respectively.

Parameters Z, *Ar*, *f* (Eqs. (4), (6) and (7)), and their inclined versions (Eqs. (5), (13) and (14)) are obtained from the average of the 8 elevation profiles, with their standard deviations accounting for the deviations from a perfect conical shape, which are considerably larger than the uncertainties caused by the DEM resolution alone.

Elevation profiles crossing breached sectors of open scoria cones are omitted, as illustrated in the examples of Fig. 2c and d. Uncertainties in volumes, elongation, *DcrH*, and *CI*, both inclined and non-inclined, are estimated using an error propagation formula that estimates the error of a given function $U(k_j)$ from the errors associated with its *n*-independent variables k_j as: $(\Delta U)^2 = \sum_{j=1}^{n}\left(\partial U/\partial k_j\right)^2(\Delta k_j)^2$ (Baird, 1994), considering the horizontal resolution of the DEM as the error in the long and short axes values, the vertical resolution of the DEM as the errors in *Dcr* and 'max(*Hco*)', and the standard deviations as the errors of the averaged quantities.

3.2. Analysis of elevation contours

Monogenetic volcanoes result from a single eruption lasting years or decades, which in most cases build scoria cones with cup-shaped craters. Many such cones are nearly circular or elongated in ground plan and have rather smooth surfaces at the time of their formation, manifested as closed, simple contour curves. As time passes, erosional processes forming rills and gullies on the cone surface appear as growing undulations of those level isolines. To measure the widths and amplitudes of such undulations along DEM contours, we have devised a single parameter, the Average Erosion Index (*AEI*), calculated utilizing Elliptical Fourier Descriptors (EFD) (Kuhl and Giardina, 1982; Schmittbuhl et al., 2003) with the methodology described in Zarazúa-Carbajal and De la Cruz-Reyna (2020). The shape of each contour is described by parametrizing the coordinates of each point in terms of a sequential quantity that marks the ordered position of each point along the contour. A Fourier analysis of the resulting sequence generates a set of transformed functions, the EFD, which permits decomposing the shape of the contour in terms of the predominant wavelengths and amplitudes describing the contour shape. The lowest harmonics represent a smoother contour, likely resembling the original planform shape of the un-eroded cone. The average distance *D* between the points of the undulations in the DEM contour and the "pristine" original contour measures the degree of erosion at the level of the contour. We then select an intermediate region of the cone, half its height, and equidistant from its base and crater. The mean of the *D* values in that region is the Average Erosion Index *AEI*. Increasing values of the *AEI* indicate increased degrees of age-dependent erosion, making the parameter *AEI* a promising morpho-chronometric tool.

Breached cones may be analyzed by completing the open sector with a best-fitted ellipse with a methodology also described in Zarazúa-Carbajal and De la Cruz-Reyna (2020), and extracting the Fourier analysis information from the subsisting sector, but if the open sector is more than 70% of the cone, the information that may be subtracted is insufficient for a morpho-chronometric analysis. Similarly, very small cones in a DEM with a horizontal resolution lower than about 1/30 of their basal diameter may not provide reliable information from this analysis.

4. Results

As an assessment of the age-related morphometric characterizations for different-scale DEMs, we analyzed the 19 radiometrically dated scoria cones from the SCMVF available in the satellite and airborne DEMs using the above-described methodology. Those volcanoes have different shape types illustrated in Fig. 4: ideal, gully, horseshoe, amorphous, and crater row, according to the classification of Bemis and Ferencz (2017). Fig. 5 illustrates an example of how the cones look in the different DEMs. The only cone from DLR DEM that could not be analyzed was 'Pelagatos', which is a very small horseshoe cone, with a volume smaller than 0.01 km^3, 51 m average height, and 298 m average basal diameter, located in a markedly inclined terrain close to a much higher landform, an added difficulty to properly resolve the landform in the DLR DEM, as illustrated in Fig. 5c.

4.1. Analysis of the Digital Elevation Model resolution on the vertical profile morphometric parameters

We analyzed the elevation profiles of the 19 scoria cones from each DEM. Figs. 6 to 9 show that almost all parameters from both DEMs, dimensional, and dimensionless, are statistically equivalent, regardless of the shape type.

This equivalence is appraised by fitting a straight line to the values obtained with DLR DEM plotted as a function of the values obtained from LIDAR DEM, with the ordinates intercept set to 0. All slopes are close to one, with coefficients of determination (R^2) greater than 0.95. To assess the difference in precision on both DEMs caused by the

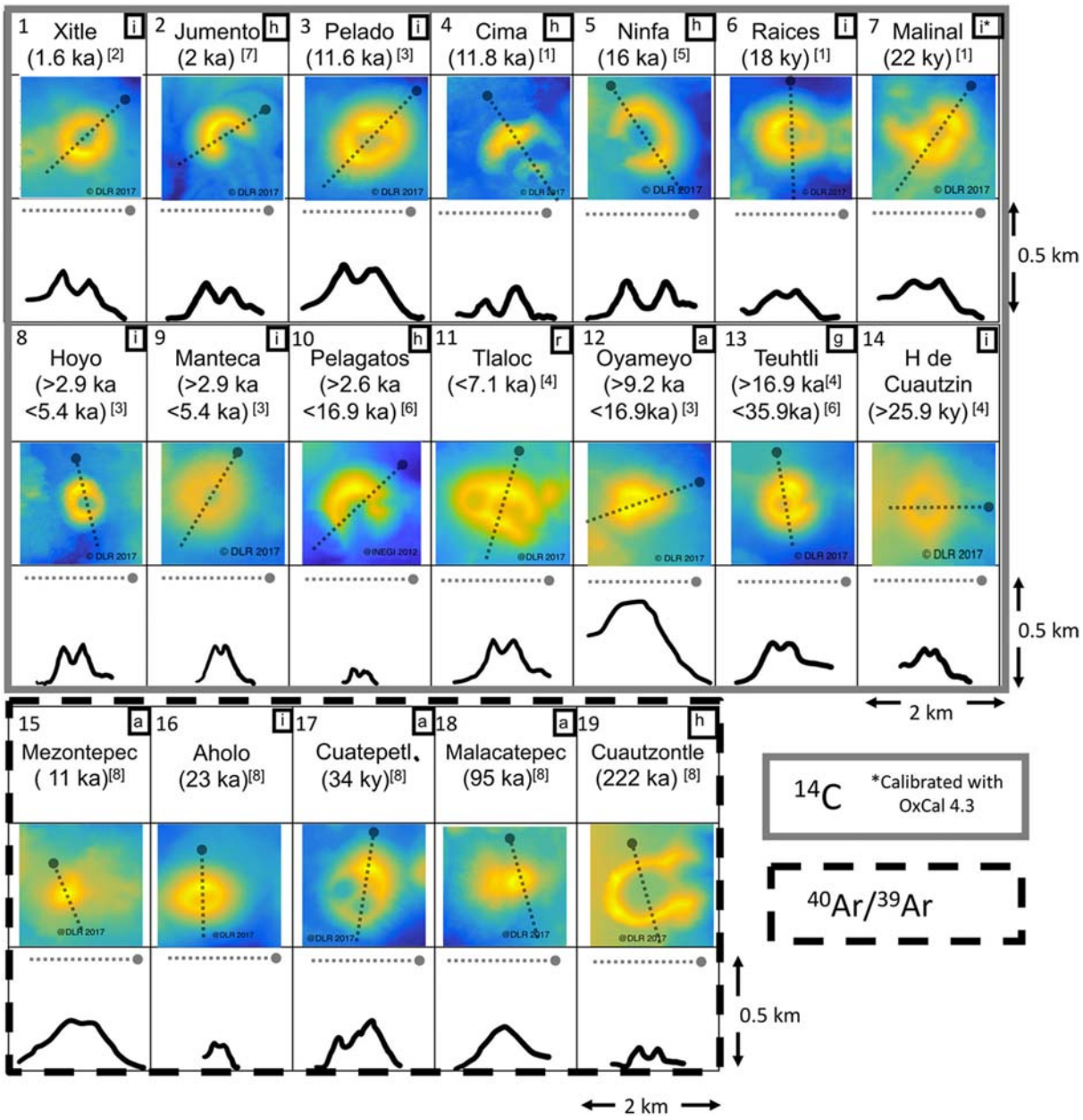

Fig. 4. Shape types, ages, and relative dimensions of the 19 analyzed scoria cones in the SCMVF. All images are from DLR DEM, except Pelagatos which is from LIDAR DEM. Dotted lines indicate the direction of the vertical cross-sections. Letters inside the squares denote the shape type: i: ideal, i* almost ideal, g: gully, a: amorphous, h: horseshoe, and r: crater row. Age references: [1] Kirianov et al. (1990); [2] Siebe (2000); [3] Siebe et al. (2004); [4] Siebe et al. (2005); [5] Agustín-Flores et al. (2011); [6] Guilbaud et al. (2015); [7] Arce et al. (2015); [8] Jaimes-Viera et al. (2018).

difference in resolution, we compared their coefficients of variation (*CV*, the ratio between the standard deviation and the mean value). The comparison is illustrated by boxplots representing the difference in the coefficient of variation of the LIDAR DEM and the DLR DEM ($CV_{LID} - CV_{DLR}$) as shown in plots 'd)' of Figs. 6 to 9. All parameters show that the precision of both DEMs is similar (and marginally better for the higher resolution LIDAR DEM). In addition, we perform a one-sample, two-tailed *t*-test for each morphometric parameter, to test the null hypothesis that there is no significant difference between the population morphometric parameters means. Table 2 shows that the null hypothesis for the parameters calculated from both DEMs having the same means may be accepted to the 5% level of significance, except for *Z* and *Zincl* which satisfy the null hypothesis of having a difference between their means equal to 0.005, which is anyways smaller than the average uncertainty of the measurement of both variables (0.07).

Analogously, we search for possible differences between the inclined and non-inclined morphometric parameters. The most sensitive parameters to the terrain inclination are the cone's height '*Hco*' and those directly depending on it ('*Ar*', '*DcrH*' and '*V*'). The rest of the parameters are not sensitive, as shown in plots 'c)' of Figs. 6 to 9. Comparison of the coefficients of variation for inclined and non-inclined calculations ($CV - CV_{incl}$) indicates that inclination-corrected parameters are more precise for values depending on '*Hco*', as shown in plots 'd)' of Figs. 6 to 9.

4.2. Average Erosion Index Parameter AEI

To test the influence of the database resolution on the *AEI*, we estimated this parameter calculated from both DEMs for each of the volcanic cones fulfilling the conditions discussed in Section 3.2 and listed in

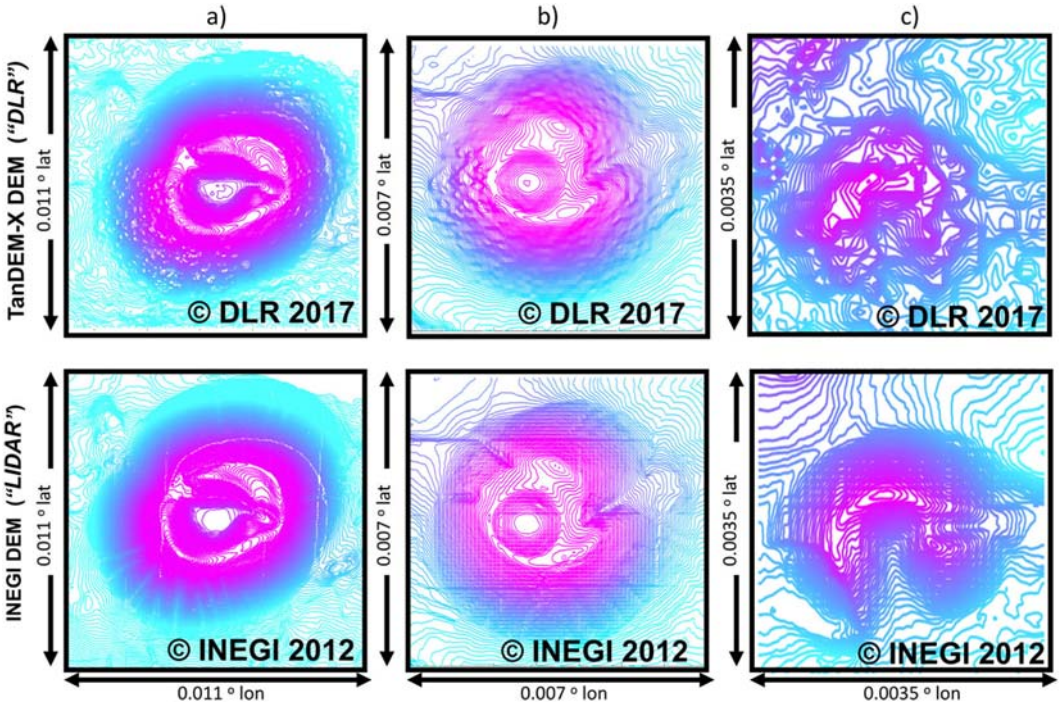

Fig. 5. Contours of cones with different sizes obtained from DLR and LIDAR DEMs. a) Pelado ($V \sim 0.3$ km^3). b) Teuhtli ($V \sim 0.1$ km^3). c) Pelagatos ($V \sim 0.01$ km^3).

Table 2. The method renders the *AEI* values in degrees, as supplied by the databases. The *AEI* values were converted to meters (Table 3), multiplying by the conversion factor C_f in Eq. (19), which is the distance in kilometers equivalent to one degree at latitude ϕ, considering the mean radius of the Earth at the Equator $R_T = 6378$ km, and that the perimeter of the Earth parallel at latitude ϕ (in degrees) is that of a circle with radius $R_\phi = R_T \cdot \cos(\phi)$. This scale factor is used as *AEI* is an average distance independent of the course in which the distance is measured. It was selected to avoid working with angular values smaller than ~10^{-4}.

$$C_f = 2\pi \cdot 1^\circ R_T \cdot \cos(\phi)/360^\circ \quad (19)$$

Fig. 10 shows that no significant difference exists between *AEI* values obtained from either DEM, regardless of the use of degrees or meters in the measurements. A paired, two-tailed *t*-test accepts, with a significance level of 0.05, the null hypothesis that *AEI* values obtained from both DEMs have the same mean, both when *AEI* is measured in degrees (*t*-value = 1.78, p-value = 0.09) and meters (*t*-value = 1.91, *p*-value = 0.07).

We conclude that both DEMs provide the necessary information about the erosional processes using the *AEI* metrics, even if they were sampled at significantly different spatial rates (a 12 m resolution satellite DEM and a 5 m resolution airborne DEM) since it is sensitive to both, the amplitude and the width of the erosion-related undulations of the contour curves (Zarazúa-Carbajal and De la Cruz-Reyna, 2020).

4.3. Constraints of the resolution on the morphological parameters

To establish additional criteria on the threshold of the DEM resolution needed for reproducible morphometric analysis of scoria cones according to their size and to the parameter type, we selected three "ideal" cones with different sizes: Aholo (0.05 km^3), Xitle (0.1 km^3), and Pelado (0.3 km^3). We then compared the morphometric characterizations obtained from the 5 m resolution LIDAR DEM undersampled at 10 m, 15 m, and so forth to a horizontal resolution of 50 m, and from the 30 m horizontal resolution –and 16.7 m vertical accuracy– (Gesch et al., 2016; NASA/METI/AIST/Japan Spacesystems and U.S./Japan ASTER Science Team, 2019) ASTER GDEM V3, with the 12 m DLR DEM. Results from the analysis of elevation profiles confirm the results of Grosse et al. (2020) that broad parameters such as W_{co}, H_{co},

Table 2
One-sample, two-tailed hypothesis *t*-test for the null hypothesis that there is no significant difference at a 5% significance level between the mean values of parameters obtained from both DEMs datasets ($NH: \mu_{LID} - \mu_{DLR} = 0$). All tests have the same number of degrees of freedom df = 17. SE = Standard Error. NH=Null Hypothesis. For *Z*, the accepted NH is $NH: \mu_{LID} - \mu_{DLR} = 0.005$, meaning that the difference between the means equals 0.005.

Parameter	Mean	S.E.	*t*-Value	p-Value	*NH*	Parameter	mean	S.E.	*t*-Value	p-Value	*NH*
Hco	−1.60	2.15	−0.74	0.46	Accept	Hco_{incl}	−1.82	2.24	−0.81	0.42	Accept
Wco	−9.54	14.48	−0.66	0.52	Accept	Wco_{incl}	−8.72	14.46	−0.60	0.55	Accept
Wcr	0.51	2.99	0.17	0.87	Accept	Wcr_{incl}	−0.11	2.96	−0.04	0.97	Accept
Dcr	0.64	1.07	0.60	0.56	Accept	Dcr_{incl}	0.66	1.07	0.62	0.55	Accept
Ar	−1.4E-03	1.2E-03	−1.15	0.27	Accept	Ar_{incl}	−1.6E-03	1.3E-03	−1.26	0.23	Accept
f	−1.0E-03	3.5E-03	−0.29	0.77	Accept	f_{incl}	−4.9E-04	3.7E-03	−0.13	0.89	Accept
Z	−1.1E-02	4.0E-03	−1.62	0.01	Accept	Z_{incl}	−1.2E-02	3.7E-03	−1.86	0.01	Accept
DcrH	3.8E-02	1.9E-02	2.04	0.06	Accept	$DcrH_{incl}$	4.2E-02	2.1E-02	2.02	0.06	Accept
elongation	9.4E-03	9.1E-03	1.04	0.32	Accept	$elongation_{incl}$	6.5E-02	5.7E-02	1.15	0.29	Accept
V	−4.8E-03	3.8E-03	−1.27	0.22	Accept	V_{incl}	−5.3E-03	4.1E-03	−1.29	0.21	Accept
Orientation	14	9.9	1.4	0.50	Accept						
CI	2.3E-03	3.7E-03	0.62	0.55	Accept	CI_{incl}	2.9E-03	3.5E-03	0.81	0.43	Accept

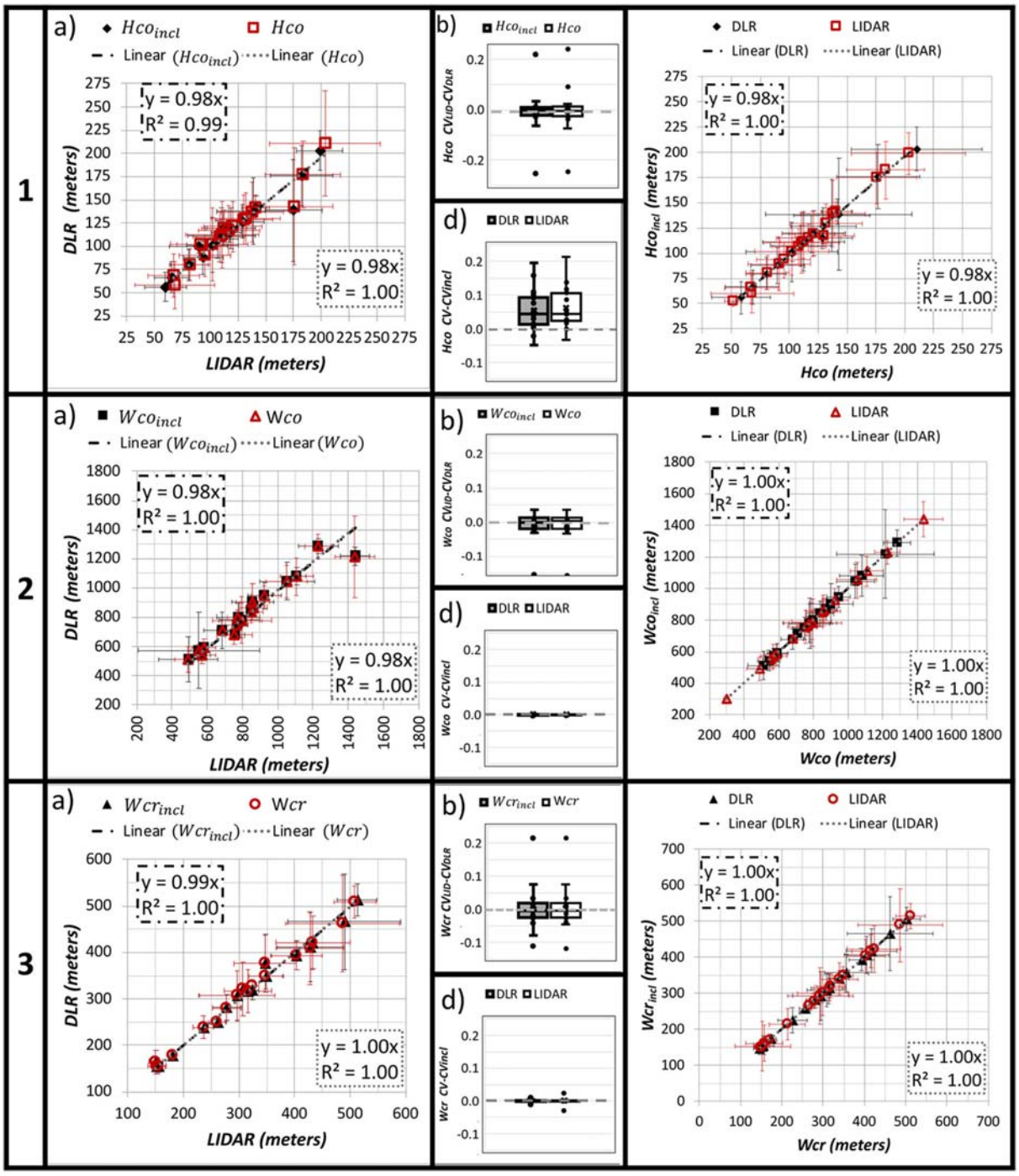

Fig. 6. Comparison of the dimensions of cones. Rows 1, 2, and 3 stand for the average cone's height '*Hco*', the average diameter of the base of the cone '*Wco*', and the average diameter of the crater '*Wcr*' respectively. a) Comparison between parameters obtained from DLR DEM and LIDAR DEM. Open symbols represent non-inclined parameters, filled symbols represent inclined parameters. b) Boxplots of the differences between coefficients of variation (standard deviation/mean value) obtained from LIDAR DEM and DLR DEM for both inclined and non-inclined parameters. The dashed line represents no difference. The lower and upper limits of the box mark the 25th (Q1) and 75th (Q3) percentiles of the data distribution respectively. The horizontal line inside the box represents the median of the distribution. The vertical lines with caps (whiskers) extend up to the data points greater or equal than Q1 − 1.5*(Q3-Q1) and smaller or equal than Q3 + 1.5*(Q3-Q1) for the lower and upper whiskers respectively. Outliers are marked as points beyond the whiskers. c) Comparison between inclined and non-inclined parameters in both DEMs; filled symbols represent parameters obtained from DLR DEM and open symbols parameters obtained from LIDAR DEM d) Differences between coefficients of variation (standard deviation/mean value) obtained with non-inclined and inclined parameters for both DEMs. Dotted lines in b) and d) represent a null difference between the coefficients of variation.

and W_{cr} are only marginally sensitive to the DEM horizontal resolution in that range. The most affected parameter is the crater depth which appears to significantly decrease at the 30 m undersampled horizontal resolution. Also, this parameter is severely affected by the DEM vertical resolution as illustrated in the ASTER-DEM plot (diamonds in Fig. S1).

Similarly, morphometric parameters such as the slope-angle tangent *Z* and the crater depth to width ratio *CI* are strongly affected by low horizontal and vertical resolutions. The height of the cone H_{co} is mostly affected by reduced vertical accuracy, particularly for small cones, as illustrated in Fig. S1. The results of this analysis suggest that scoria cones exceeding a 0.05 km^3 volume may be characterized with

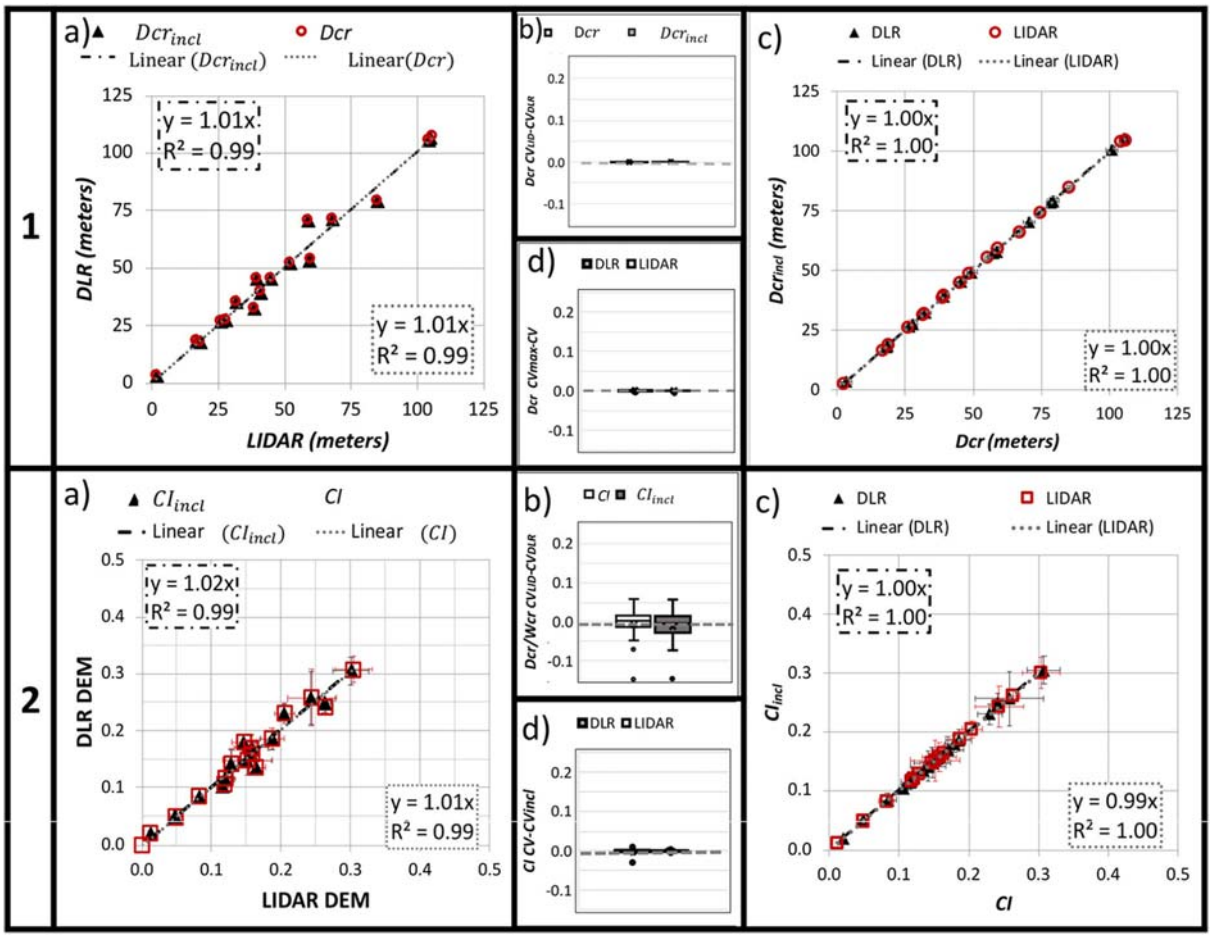

Fig. 7. Comparison between morphometric parameters calculated from DLR DEM and LIDAR DEM. 1) *Dcr*, depth of the crater. 2) CI, a ratio of the maximum depth to the average diameter of the crater. a) Comparison between parameters obtained from DLR DEM and LIDAR DEM. Open symbols represent non-inclined parameters, filled symbols represent inclined parameters. b) Boxplots of the differences between coefficients of variation (standard deviation/mean value) obtained from LIDAR DEM and DLR DEM for both inclined and non-inclined parameters. Outliers are marked as points beyond the whiskers. c) Comparison between inclined and non-inclined parameters in both DEMs; filled symbols represent parameters obtained from DLR DEM and open symbols parameters obtained from LIDAR DEM. d) Differences between coefficients of variation (standard deviation/mean value) obtained with non-inclined and inclined parameters for both DEMs. Other symbols as explained in Fig. 6.

reproducible morphometric parameters using DEMs with horizontal resolutions up to 30 m, provided that a vertical accuracy of at least 5 m can be attained. Otherwise, parameters such as the crater depth to width ratio may render inaccurate values, particularly for shallower craters, less than 100 m deep.

In Section 3.2, we discuss how the contour curves shape analysis provides a chronometrically relevant morphometric parameter, the *AEI*, calculated from an average measure of the amplitude and width of the contour undulations assumedly caused by the age-dependent erosion on a monogenetic scoria cone. The precision with which those widths and amplitudes can be measured using the Elliptical Fourier Descriptors method described in Zarazúa-Carbajal and De la Cruz-Reyna (2020) is limited by the number of contour points sampled from the DEM database through the Nyquist frequency constriction which prevents detecting contributions to the contour shape twice the separation of the sampled points along the contour. Therefore, a contour about 320 m in diameter, this is, about 1 km in perimeter, extracted from a 12 m resolution DEM would have nearly 80 points, while the same contour would have about 200 points in a 5 m resolution DEM database. This translates as a capability of resolving only contour undulations 25 m wide with the 12 m resolution DEM, and 10 m wide with the 5 m DEM, regardless of the amplitude of undulations narrower than those widths. Furthermore, the DEMs' vertical resolutions and the smoothing and interpolation algorithms used to construct a DEM database may affect the actual shape of a contour adding uncertainties to the EFD outcomes.

To illustrate this, we compared the *AEI* obtained from closed contours of Aholo, Xitle, and Pelado cones, which have different volumes and erosive degrees, but none of them have large rills or gullies. Therefore, we also include Atlacholoaya scoria cone (also located near the southern limits of Sierra Chichinautzin but not available in LIDAR DEM), a monogenetic volcano dated at ~1 Ma by the $^{40}Ar/^{39}Ar$ method by Arce et al. (2013), with an approximate volume of 0.14 km^3. Fig. S3 shows the contour shape differences from LIDAR, DLR, and ASTER DEMs, and the *AEI* dependence on the horizontal DEM resolution, obtained from the under sampled LIDAR DEM and how it compares to those obtained from DLR and ASTER DEMs. The plots in Fig. S3 suggest that DEMs with decreasing horizontal resolution lead to underestimations of the *AEI* parameter, even if the vertical accuracy is maintained. Such underestimation of the *AEI* is more evident in cones with well-formed and deep rills and gullies like Pelado or Atlacholoaya, while at cones lacking narrow, well-defined and deep rills, the *AEI* value remains almost constant. In conclusion, the *AEI* estimations obtained from DEM databases such as the 5 m resolution LIDAR DEM and the 12 m resolution DLR DEM render similar results, but that may not be the case for lower resolution DEMs, particularly when studying smaller cones.

4.4. Effects of the DEM resolution on age-related parameters

Next, we analyze the influence of the DEM resolution on the age-dependence of a frequently used morphometric parameter calculated

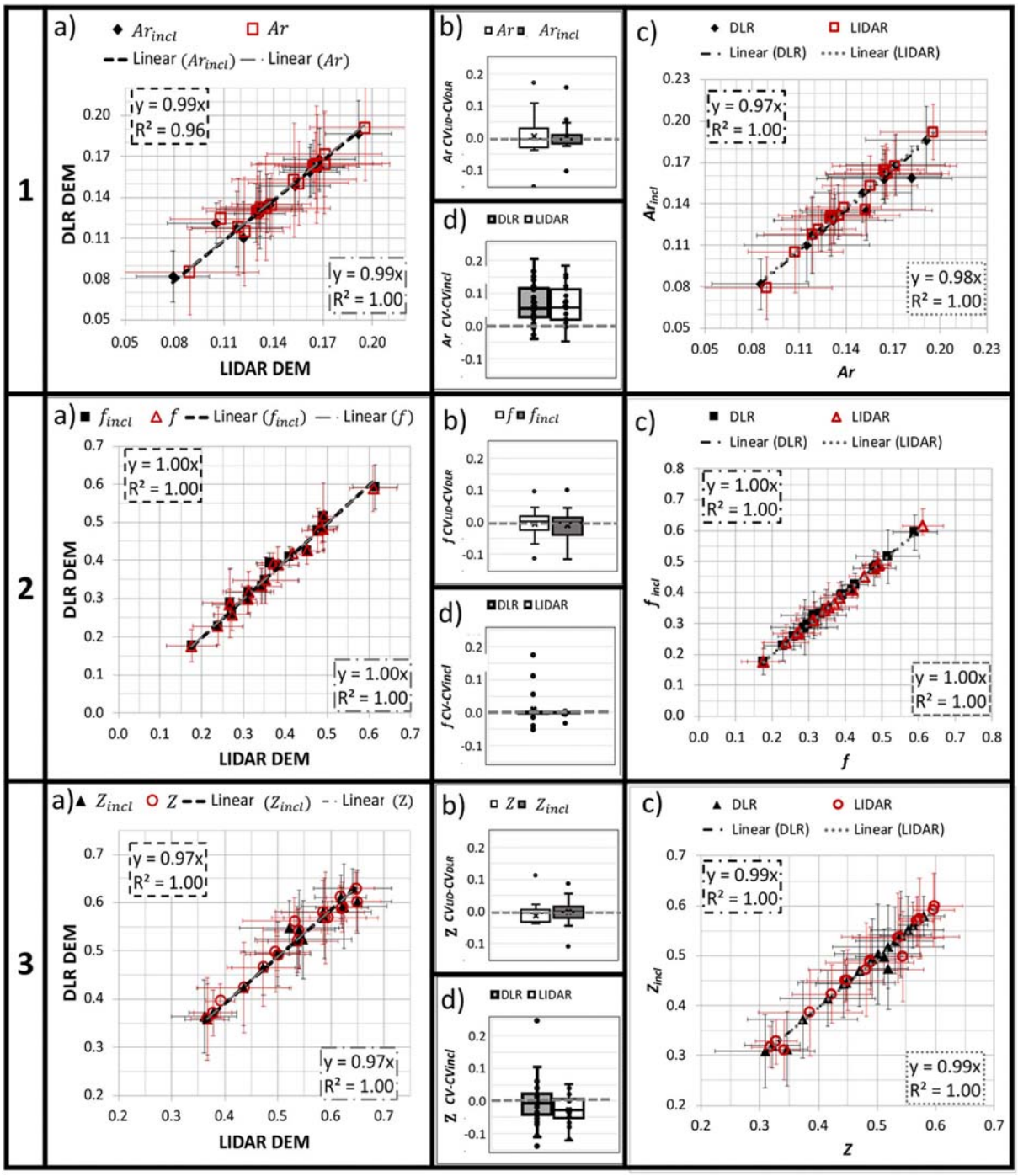

Fig. 8. Rows 1, 2, and 3 depict the Aspect ratio, flat-topped-ness, and the tangent of the hillslope angle respectively. a) Comparison between parameters obtained from DLR DEM and LIDAR DEM. Open symbols represent non-inclined parameters, filled symbols represent inclined parameters. b) Boxplots of the differences between coefficients of variation (standard deviation/mean value) obtained from LIDAR DEM and DLR DEM for both inclined and non-inclined parameters. Outliers are marked as points beyond the whiskers. c) Comparison between inclined and non-inclined parameters in both DEMs; filled symbols represent parameters obtained from DLR DEM and open symbols parameters obtained from LIDAR DEM. d) Differences between coefficients of variation (standard deviation/mean value) obtained with non-inclined and inclined parameters for both DEMs. Other symbols as explained in Fig. 6.

for selected volcanic cones in the SCMVF, the aspect ratio *Ar* (Wood, 1980a,b; Martin del Pozzo, 1982; Hooper, 1995; Hooper and Sheridan, 1998; Aguirre-Díaz et al., 2006; Inbar et al., 2011; Gilichinsky et al., 2010; Nieto-Torres and Martin Del Pozzo, 2019). The hillslope *Z* and the flat-topped-ness *f*, are additional parameters that Bemis and Ferencz (2017) suggested that should be used along with *Ar* for an unambiguous morphological characterization of a cone, since very different volcanic shapes may render the same value of *Ar*.

Other morpho-chronometric parameters that have been recently proposed and we also test below are the abovementioned *AEI* (Zarazúa-Carbajal and De la Cruz-Reyna, 2020), and the depth to width ratio of the volcano's craters *CI* (Eq. (12)), a parameter that Grosse et al. (2020) reported showing an inverse relationship with the age of volcanic cones in the Andean Puna region.

Since we are interested in assessing the influence of the DEM resolutions on the age-dependence of the morphometric parameters, we use the available datings listed in Table 1 to make a box plot

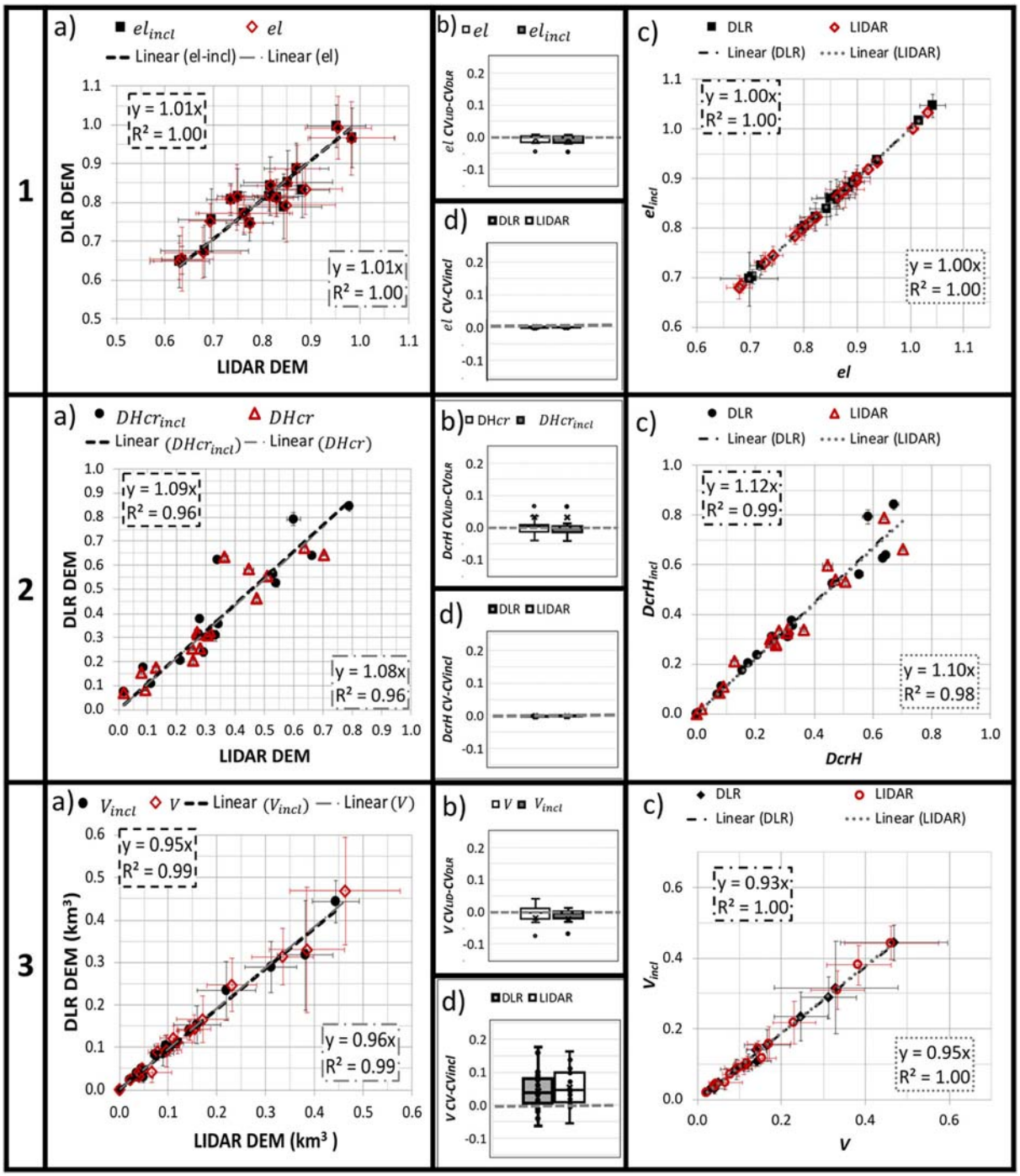

Fig. 9. Rows 1, 2, and 3 stand for elongation, crater depth to cone height ratio '*DcrH*', and Volume respectively. a) Comparison between parameters obtained from DLR DEM and LIDAR DEM. Open symbols represent non-inclined parameters, filled symbols represent inclined parameters. b) Boxplots of the differences between coefficients of variation (standard deviation/mean value) obtained from LIDAR DEM and DLR DEM for both inclined and non-inclined parameters. c) Comparison between inclined and non-inclined parameters in both DEMs; filled symbols represent parameters obtained from DLR DEM and open symbols parameters obtained from LIDAR DEM d) Differences between coefficients of variation (standard deviation/mean value) obtained with non-inclined and inclined parameters for both DEMs. Symbols as in Fig. 6.

representation of the parameters grouped in six age intervals measured in ka according to their radiometric ages, listed in Table 1, as follows: 0–10 ka; 5–20 ka; 15–30 ka; 25–40 ka, 85–100 ka, and 215 to 230 ka.

We obtain the age-dependency trends of the morphometric parameters by fitting the mean parameter value of each box to the mean value of the box age range. The resulting trends and coefficients are shown in Table 4 and Figs. 11, 12, and 13. Since the number of available radiometric datings of older cones (>35 ka) is rather small, we make these fittings considering first all cones in the age range 0 to 230 ka and then considering only cones younger than 35 ka.

Despite the radiometric data gap in the age range 35 to 85 ka and considering the limited number of dated cones older than 40 ka, the trends in Table 4 and Figs. 11 to 13 suggest that the different morphometric parameters have different functional dependencies on age. The parameters related to the vertical cone profiles such as Ar_{incl} and Z_{inc} show a weak decreasing linear trend with age, with a poor resolution in the range 0–40 ka, but with better resolution in the range of

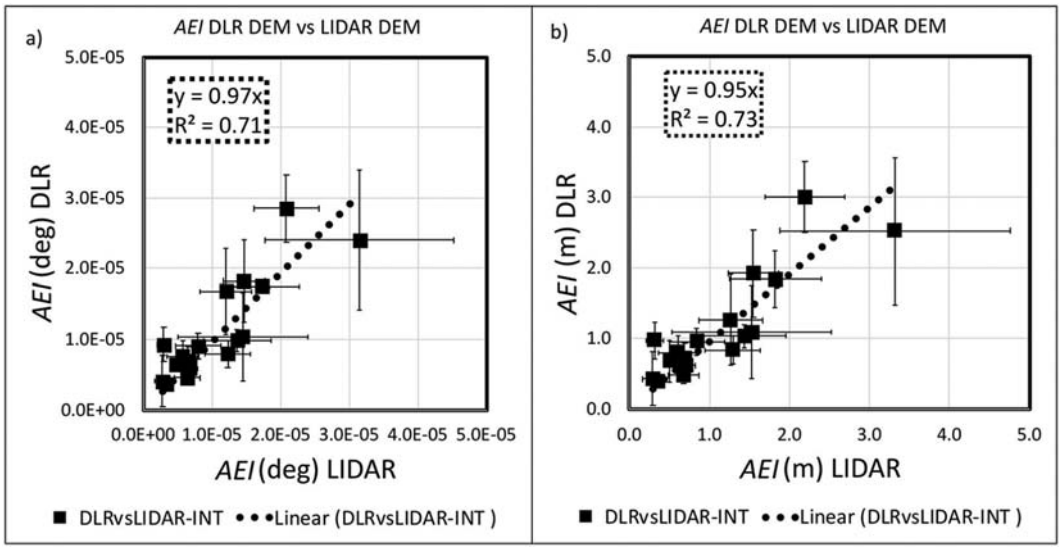

Fig. 10. Comparison between the average Erosion Index *AEI* (Zarazúa-Carbajal and De la Cruz-Reyna, 2020) obtained from DLR DEM and LIDAR DEM. a) Values on degrees. b) Values in meters. Error bars represent the standard deviation of the *AEI* obtained from the contours of each scoria cone.

hundreds of ka (in concordance with the age groups initially proposed by Wood to characterize cinder cone degradation) (Wood, 1980a,b). The parameter f_{incl} does not show any clear dependence on age over the range 0–250 ka.

The parameter CI_{incl}, related to the volcanic crater shape (Grosse et al., 2020) shows a clear inverse relationship of the age-interval mean parameter values with the age over its whole range. The analysis of 11 cones of the SCMVF selected for their well-defined craters suggests that the relationship may be approximated to a negative power function. If only cones with well-defined craters are considered to calculate the age dependence of the morphometric parameters Ar_{incl}, Z_{inc}, and f_{incl}, there is no significant change in the age model models with respect to those listed in Table 4.

The *AEI* parameter also shows a clear increasing dependence with age that may be approximated to a power function of the form $Age = \beta_1(AEI)^{\beta_2}$ (Zarazúa-Carbajal and De la Cruz-Reyna, 2020).

To compare among DEMs, we perform paired *t*-tests between the values of the parameters obtained using the regression coefficients for LIDAR DEM and DLR DEM (Table 4). For Ar_{incl}, f_{incl}, and CI_{incl}, the age dependency trends for cones younger than 250 ka are equivalent in both DEMs at a significance level 0.05, whereas for parameter Z-incl the equivalence is at a significance level 0.005. For the contour parameter *AEI*, the box-plot based trends are equivalent at a significance level 0.004, whereas the trends obtained considering all pair points individually and taking into account the uncertainties in both, age and *AEI* (Zarazúa-Carbajal and De la Cruz-Reyna, 2020), are equivalent at a significance level 0.05. Age trends obtained with regression coefficients from cones younger than 35 ka are all equivalent in both DEMs at a significance level of 0.05. Morphological characterization for age-related analysis is thus feasible and equivalent for both DEMs.

5. Discussion and conclusions

Monogenetic volcanic fields with complex origins and spatio-temporal evolutions (Yokoyama, 2019) are abundant on Earth. Time-sensitive hazard and risk assessment of this kind of volcanism may be enriched with a trustworthy knowledge of how the monogenetic

Table 3
Conversion factors C_f, average erosion index *AEI* and their respective standard deviations Δ*AEI* obtained for each scoria cone in each DEM, in degrees and meters Cones marked with * were not used in the comparison because their contours could not be properly set apart or resolved in the DLR DEM. Cone number (CN) according to Fig. 4.

CN	Volcano name	C_f (km)	DLR				LIDAR			
			AEI [de g]	Δ*AEI* [deg]	*AEI* [m]	Δ*AEI* [m]	*AEI* [de g]	Δ*AEI* [deg]	*AEI*[m]	Δ*AEI* [m]
1	Xitle	105.10	9.15E-06	2.70E-06	0.96	0.28	6.61E-06	1.78E-06	0.69	0.19
2	Jumento	105.12	6.08E-06	1.81E-06	0.64	0.19	5.96E-06	2.80E-06	0.63	0.30
3	Pelado	105.16	1.32E-05	2.84E-06	1.39	0.30	1.30E-05	2.87E-06	1.37	0.30
4	Cima	105.18	4.43E-05	8.94E-06	4.66	0.94	3.53E-05	1.44E-05	3.71	1.56
5	Ninfa	105.16	1.23E-05	8.20E-06	1.29	0.86	9.97E-06	4.01E-06	1.05	0.43
6	Raices	105.19	2.10E-05	5.92E-06	2.21	0.62	2.29E-05	4.02E-06	2.41	0.43
7	Malinal	105.11	1.84E-05	4.90E-06	1.93	0.51	2.18E-05	6.22E-06	2.29	0.67
8	Hoyo	105.20	1.31E-05	2.11E-06	1.38	0.22	1.06E-05	1.83E-06	1.12	0.20
9	Manteca	105.20	8.47E-06	1.60E-06	0.89	0.17	1.30E-05	3.55E-06	1.37	0.38
10	Pelagatos*	105.19	NA	NA	NA	0.52	5.63E-06	3.24E-06	0.59	0.36
11	Tlaloc	105.19	2.27E-05	6.24E-06	2.38	0.66	2.03E-05	8.07E-06	2.13	0.86
12	Oyameyo	105.14	4.08E-05	5.19E-06	4.29	0.55	4.08E-05	7.57E-06	4.29	0.80
13	Teuhtli	105.11	1.59E-05	6.11E-06	1.68	0.64	1.38E-05	4.91E-06	1.45	0.52
14	Hijo de Cuahutzin	105.16	2.14E-05	1.05E-05	2.25	1.11	2.08E-05	1.11E-05	2.18	1.20
15	Mezontepec	105.14	1.52E-05	3.42E-06	1.60	0.36	1.19E-05	3.19E-06	1.25	0.34
16	Aholo	105.19	8.84E-06	2.35E-06	0.93	0.25	6.22E-06	1.43E-06	0.65	0.15
17	Cuautepetl	105.19	1.94E-05	4.49E-06	2.04	0.47	2.24E-05	3.62E-06	2.36	0.39
18	Malacatepec*	105.15	NA	NA	NA	NA	2.74E-05	1.30E-05	2.88	1.39
19	Cuatzontle	105.10	4.60E-05	1.93E-05	4.84	2.03	4.05E-05	1.31E-05	4.26	1.46

Table 4
Fitting coefficients of morphometric parameters as a function of age. "*AEI* Paper 1" refers to the coefficients of the *AEI*-age power function obtained by Zarazúa-Carbajal and De la Cruz-Reyna (2020). In the last column, R^2 is the coefficient of determination and ($R^2_{ADJ} = 1(1 - R^2)(n - 1) / (n - p - 1)$) is the adjusted coefficient of determination, which is a p (number of model parameters) and n (number of data) sensitive, less biased estimator of the coefficient of determination in weakly dependent variables, admitting negative values for poorly correlated variables. Regressions of all parameters except *CI* were computed with those cones for which *AEI* methodology is applicable (i.e. cones in Table 1 except Oyameyo and Tlaloc in both DEMs and Pelagatos in DLR DEM), while for *CI* the breached cones and those without a well-delimited crater were also excluded in both DEMs (Ninfa, Jumento, Cuatzontle, Pelagatos, and Malacatepec). The model parameters in Paper 1 for *AEI* calculated from DLR DEM were computed for 25 cones up to 1 Ma. The model parameters for *AEI* for LIDAR DEM are computed for the same cones studied in the present paper.

Parameter (DEM)	Fitting function	Cones < 250 ka			Cones < 35 ka		
		$a \pm$ 95% confidence bound	$b \pm$ 95% confidence bound	R^2 (R^2_{ADJ})	$a \pm$ 95% confidence bound	$b \pm$ 95% confidence bound	R^2 (R^2_{ADJ})
Ar_{incl} (DLR)	$y = a * Age + b$	$(-3.0 \pm 0.4)E-04$	0.146 ± 0.004	0.93 (0.91)	$(-2.6 \pm 4.2)E-04$	0.147 ± 0.008	0.16 (−0.25)
Ar_{incl} (LIDAR)		$(-3.3 \pm 0.3)E-04$	0.152 ± 0.003	0.95 (0.94)	$(-3.8 \pm 4.4)E-04$	0.153 ± 0.009	0.26 (−0.09)
Z_{incl} (DLR)	$y = a * Age + b$	$(-0.9 \pm 0.3)E-03$	0.48 ± 0.03	0.69 (0.62)	$(-1.3 \pm 2.2)E-03$	0.50 ± 0.04	0.14 (−0.27)
Z_{incl} (LIDAR)		$(-1.0 \pm 0.3)E-03$	0.51 ± 0.03	0.68 (0.60)	$(-2.5 \pm 0.2)E-03$	0.55 ± 0.04	0.40 (0.10)
f_{incl} (DLR)	$y = a * Age + b$	$(0.4 \pm 0.4)E-03$	0.37 ± 0.04	0.21 (0.01)	$(-1.6 \pm 2.0)E-03$	0.42 ± 0.04	0.24 (−0.13)
f_{incl} (LIDAR)		$(0.2 \pm 0.4)E-03$	0.38 ± 0.05	0.04 (−0.19)	$(-2.8 \pm 0.2)E-03$	0.46 ± 0.04	0.42 (0.13)
CI_{incl} (DLR)	$y = a(Age)^b$	0.47 ± 0.24	-0.41 ± 0.21	0.94 (0.92)	0.41 ± 0.22	-0.35 ± 0.22	0.95 (0.93)
CI_{incl} (LIDAR)		0.42 ± 0.33	-0.37 ± 0.31	0.85 (0.80)	0.35 ± 0.36	-0.28 ± 0.41	0.80 (0.70)
AEI (DLR)	$y = a(Age)^b$	0.48 ± 0.17	0.37 ± 0.07	0.98 (0.98)	0.62 ± 0.60	0.34 ± 0.32	0.92 (0.88)
AEI (LIDAR)		0.47 ± 0.06	0.40 ± 0.02	0.99 (0.99)	0.44 ± 0.08	0.43 ± 0.06	0.99 (0.99)
AEI Paper 1 (DLR)	$y = a(Age)^b$	0.58 ± 0.05	0.38 ± 0.03	Pearson's $r = 0.93$			
AEI Paper 1 (LIDAR)	$b = 1/\beta_2$	0.53 ± 0.08	0.41 ± 0.07	Pearson's $r = 0.76$			
	$a = (1/\beta_1)^b$						

volcano births developed in time and space. DEMs of different types provide precise information about the spatial distribution of individual volcanoes in a volcanic field and may provide information about its time evolution through morpho-chronological date estimates when the DEMs have sufficient resolution to accurately characterize the age-dependent morphological features of the monogenetic cones

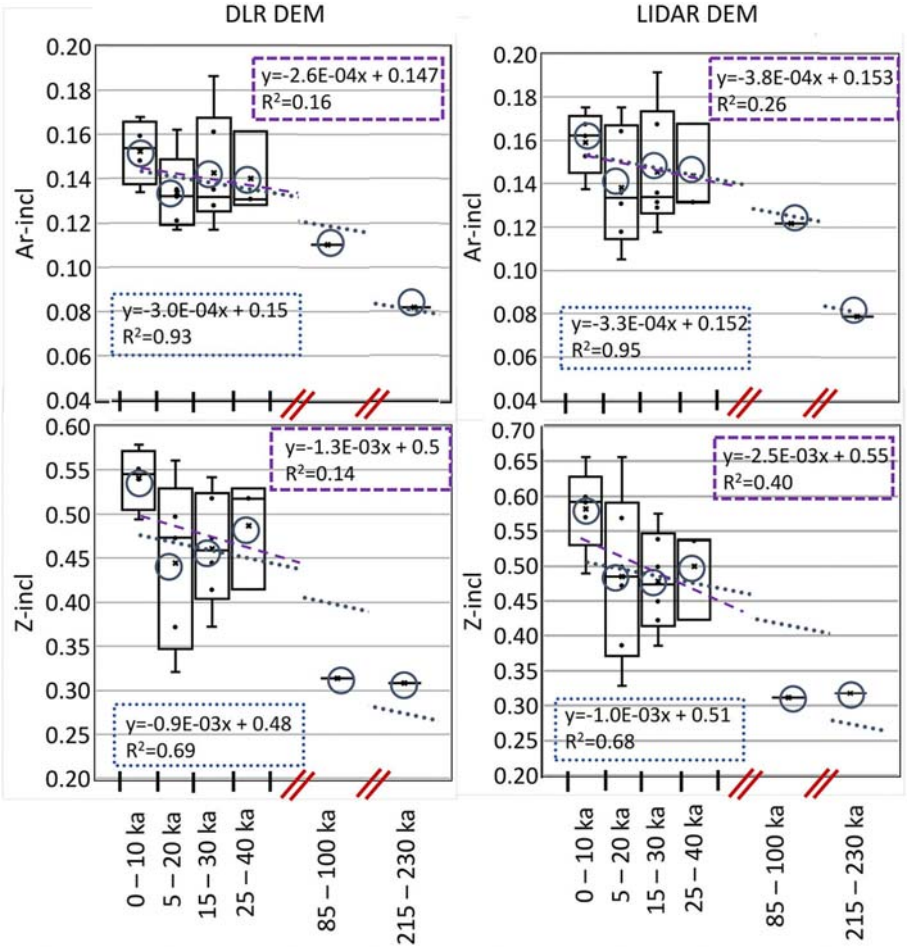

Fig. 11. Boxplots of Ar_{incl} and Z_{incl} age-dependence as a function of group-ages. Dotted lines show the linear regression for the mean box plot parameters vs the mean radiometric calibrated ages for the age-range 0–230 ka. Dashed lines show the linear regression for the mean box plot parameters vs the mean radiometric calibrated ages for the age-range 0–35 ka. Circles within the boxes enclose the average value of each box (x within the circle). Horizontal lines within the box represent the median value. Box ends denote the 25th and 75th percentiles. Whiskers extend up to the data points greater or equal than Q1 − 1.5*(Q3-Q1) and smaller or equal than Q3 + 1.5*(Q3-Q1) for the lower and upper whiskers respectively. Outliers are marked as points beyond the whiskers.

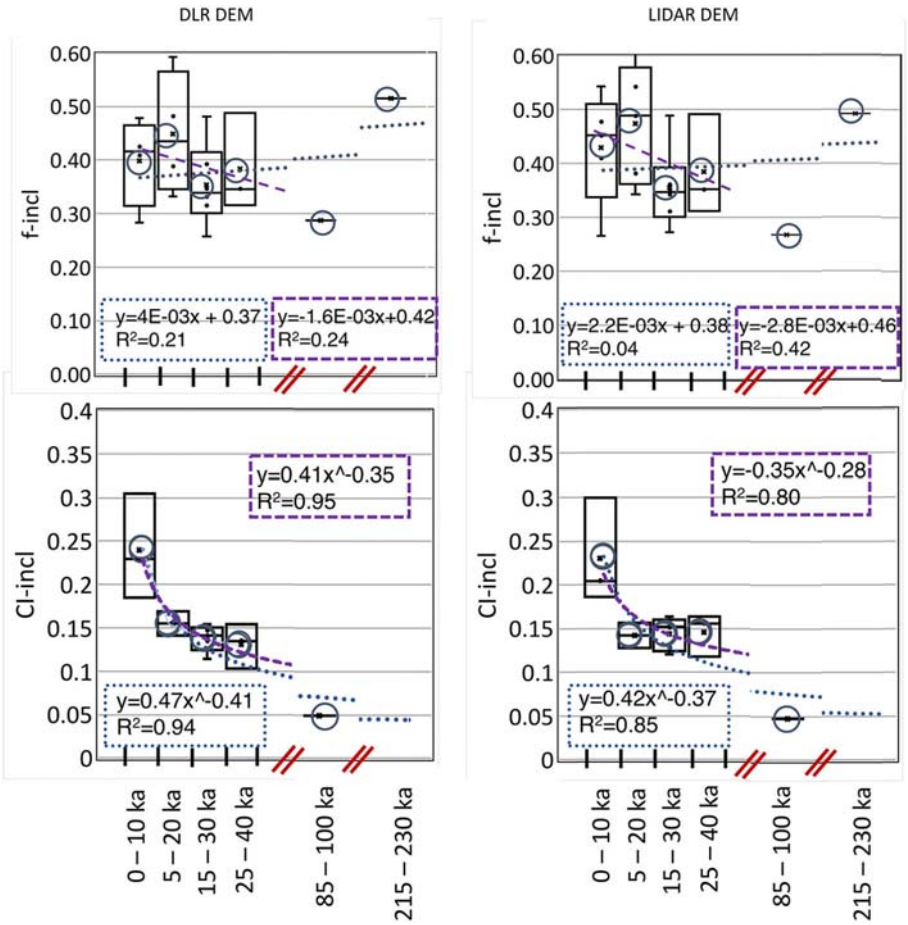

Fig. 12. Boxplots illustrating the age-dependence of f_{incl} and Cl_{incl}. The latter can only be calculated for cones with well-defined craters. Dotted lines show the obtained regression for the mean box plot parameters vs the mean radiometric calibrated ages for the age-range 0–230 ka. Dashed lines show the obtained regression for the mean box plot parameters vs the mean radiometric calibrated ages for the age-range 0–35 ka. Other symbols as explained in Fig. 11.

(Zarazúa-Carbajal and De la Cruz-Reyna, 2020). Performing equivalence tests on selected volcanoes of the Chichinautzin monogenetic volcanic field, we found comparably good results for most age-relevant morphometric parameters using a 12 m resolution satellite DEM with worldwide coverage and using a higher-resolution airborne 5 m Lidar DEM.

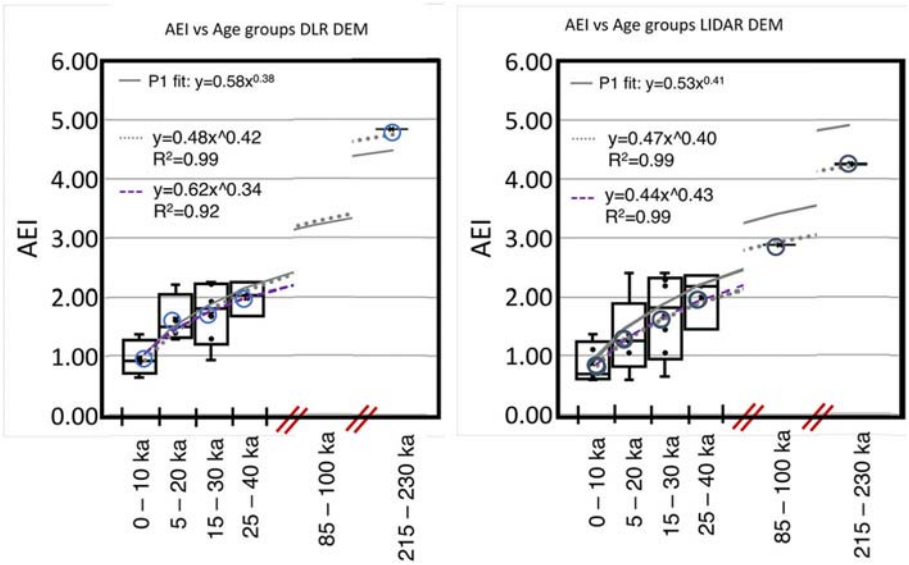

Fig. 13. For the *AEI* analysis, Cima, Tlaloc, and Oyameyo volcanoes were omitted, as the methodology cannot be applied to highly breached cones, multiple cones, or crater row cones lacking clear boundaries. A dotted line shows the power function obtained using the box plots averages of both *AEI* and calibrated radiometric ages for the age-range 0–230 ka. Dashed lines show the regression obtained considering the age-range 0–35 ka. The solid gray line shows the *AEI* vs the age power function $Age = \beta_1(AEI)^{\beta_2}$ of Zarazúa-Carbajal and De la Cruz-Reyna (2020). Other symbols as explained in Fig. 11.

The chronometrically relevant morphometric characterization of monogenetic volcanoes could be performed on most scoria cones included in both DEMs provided they were large enough to be accurately resolved with the criteria described in Section 3.2. Very small cones like the 50 m high Pelagatos, with a volume smaller than 0.01 km^3, and located close to a much higher landform could not be properly sampled by the DLR DEM, and no morphometric characterization allowing comparisons with a higher resolution DEM could be made with the methodologies described here.

The calculation of vertical parameters renders similar results with both DEMs, with marginally higher precision for LIDAR DEM. Regression and null-hypothesis testing support the equivalence of results obtained from those DEMs. However, it is important to emphasize that failing to make terrain inclination corrections may return incorrect values of some chronometry-oriented vertical parameters. The height of the cone is the morphological parameter most affected by regional inclination. As a consequence, vertical parameters depending on '*Hco*', such as the Aspect ratio '*Ar*' and the cone volume '*V*' may be consistently overestimated if the terrain inclination is neglected, whereas the crater's depth to cone's height ratio '*DcrH*', may be underestimated. On the other hand, the average slope values, the width of the crater, and the base of the cones are less sensitive to the terrain inclination. For the analyzed area of the Sierra Chichinautzin volcanic Field, with average terrain inclinations below 10°, the values of *Wco*, *Wcr*, and *Z* do not change significantly when correcting for terrain inclination. However, steeper terrains may require inclination corrections. Besides, the standard deviation of substratum inclination-corrected age estimates is generally smaller than the non-corrected for inclination, making this correction particularly important for improved morpho-chronological dating.

Regarding the *AEI*, derived from the EFD analysis of the contour level undulations, the results from both DEMs also render satisfactory results, except for cones with unresolvable contours because they are too small (Pelagatos) or lacking recognizable limits (Malacatepec). For the rest of the cones, the *AEI* analysis from the 12 m resolution DLR DEM and from the 5 m resolution LIDAR DEM are equivalent to a 0.05 significance level.

Our results confirm that the morphometric characterization of scoria cones using DEMs is affected by the horizontal resolution and the vertical accuracy. The *AEI* is especially sensitive, and although the 5 m horizontal resolution LIDAR DEM and the 12 m resolution DLR DEM render similar results for cones with volumes greater than 0.05 km^3, that may not be the case for lower resolution DEMs, particularly when studying smaller cones. Although average cone dimensions and shape parameters of scoria cones with volumes exceeding 0.05 km^3 may be reproducible with horizontal resolutions up to 30 m, and vertical accuracy of at least 5 m, parameters such as the crater depth to width ratio may render inaccurate values, particularly for shallower craters less than 100 m deep.

In conclusion, the morphometric age-related parameters *Arincl*, *fincl*, *Zincl*, *CIincl*, and *AEI*, render similar age-dependence in both DEMs except for a few cases, suggesting that the resolution of both LIDAR DEM and DLR DEM is adequate for morpho-chronological analysis.

Furthermore, a boxplot representation of the data shows that while the "vertical" morphometric parameters Ar_{incl}, Z_{incl}, and f_{incl} do not show a significant dependence on age for cones in the age group <40 ka, they seem to show a consistent age dependence for the age group of hundreds of ka. In contrast, CI_{incl} and *AEI* seem to resolve age differences in the order of 15 ka. However, it is important to emphasize that the trends and coefficients calculated in the previous sections may not be sufficiently precise for reproducible morphometric age dating, considering the small number of radiometrically dated cones older than 35 ka Moreover, adding robustness to the observed morphometric age trends would require an additional point-wise regression analysis considering the uncertainties in both the radiometric ages and morphometric parameters, an analysis that is beyond the scope of this paper aimed to analyze the equivalence between the two different resolution DEMs.

As a concluding remark, our results show that the relatively low resolution of the DLR TanDEM-X DEM is amply compensated by its lower cost (when compared with a LIDAR DEM) and by its worldwide coverage, as it renders equally reliable chronometrically-relevant morphometric characterizations of monogenetic scoria cones.

Declaration of competing interest

The authors declare that they have no known competing financial interests or personal relationships that could have appeared to influence the work reported in this paper.

Acknowledgments

The authors are grateful to the Mexican Science Council (CONACYT) and the National Researchers Systems (SNI) for the research assistant support grant (EXP. AYTE. 15617), to the DGAPA-PAPIIT-UNAM programme (grant IN-109616) for partially financing this research and very especially to the TanDEM-X satellite (DEM_GEOL1097) from the German Aerospace Center (DLR) and the Mexican National Institute of Geography and Statistics (INEGI) for providing the satellite and LIDAR DEMs. Special thanks to reviewers Pablo Grosse and Michael Gilichinsky and to the editor Y. S. Hayakawa whose comments and suggestions greatly helped to improve this paper.

Appendix A. Supplementary data

Supplementary data to this article can be found online at https://doi.org/10.1016/j.geomorph.2021.107842.

References

Aguirre-Díaz, G.J., Jaimes-Viera, M.C., Nieto-Obregón, J., 2006. In: Siebe, C., Macías, J.L., Aguirre-Díaz, G.J. (Eds.), The Valle de Bravo Volcanic Field. Geology and Geomorphometric Parameters of a Quaternary Monogenetic Field at the Front of the Mexican Volcanic Belt, in Neogene-Quaternary Continental Margin Volcanism: A Perspective From México. Geol. Soc. Am. Sp. P 402, pp. 125–140.

Agustín-Flores, J., Siebe, C., Guilbaud, M.-N., 2011. Geology and geochemistry of Pelagatos, Cerro del Agua, and Dos Cerros monogenetic volcanoes in the Sierra Chichinautzin volcanic field, south of México City. J. Volcanol. Geotherm. Res. 201, 143–162.

Arce, J.L., Layer, P.W., Lassiter, J.C., Benowitz, J.A., Macías, J.L., Ramírez-Espinosa, J., 2013. 40Ar/39Ar dating, geochemistry, and isotopic analyses of the quaternary Chichinautzin volcanic field, south of Mexico City: implications for timing, eruption rate, and distribution of volcanism. Bull. Volcanol. 75, 774. https://doi.org/10.1007/s00445-013-0774-6.

Arce, J.L., Muñoz-Salinas, E., Castilo, M., Salinas, I., 2015. The ~2000 yr BP Jumento volcano, one of the youngest edifices of the Chichinautzin Volcanic Field, Central Mexico. J. Volcanol. Geotherm. Res. 308, 30–38.

Avellán, D.R., Cisneros-Máximo, G., Macías, J.L., Gómez-Vasconcelos, M.G., Layer, P.W., Sosa-Ceballos, G., Robles-Camacho, J., 2020. Eruptive chronology of monogenetic volcanoes northwestern of Morelia–Insights into volcano-tectonic interactions in the central-eastern Michoacán-Guanajuato Volcanic Field, México. J. S. Am. Earth Sci. 100, 102554. https://doi.org/10.1016/j.jsames.2020.102554.

Baird, D.C., 1994. Experimentation: An Introduction to Measurement Theory and Experiment Design. 3rd ed. 978-0133032987 Benjamin Cummings.

Bebbington, M.S., Cronin, S.J., 2011. Spatio-temporal hazard estimation in the Auckland Volcanic Field, New Zealand, with a new event-order model. Bull. Volcanol. 73 (1), 55–72. https://doi.org/10.1007/s00445-010-0403-6.

Bemis, K., Ferencz, M., 2017. Morphometric analysis of scoria cones: the potential for inferring process from shape. Geol. Soc. Lond. Spec. Publ. 446, 17. https://doi.org/10.1144/SP446.9.

Bemis, K., Walker, J., Borgia, A., Turrin, B., Neri, M., Swisher III, M., 2011. The growth and erosion of cinder cones in Guatemala and El Salvador: models and statistics. J. Volcanol. Geotherm. Res. 201, 39–52. https://doi.org/10.1016/j.jvolgeores.2010.11.007.

Bloomfield, K., 1975. A late quaternary monogenetic volcano field in central Mexico. Geol. Rundsch. 6, 476–497.

Bronk Ramsey, C., 2008. Radiocarbon dating: revolutions in understanding. Archeometry 50 (2), 249–275.

De la Cruz-Reyna, S., Yokoyama, I., 2011. A geophysical characterization of monogenetic volcanism. Geofis. Int. 50 (4), 465–484.

Favalli, M., Karátson, D., Mazzarini, F., Pareschi, M.T., Boschi, E., 2009. Morphometry of scoria cones located on a volcano flank: a case study from Mt. Etna (Italy), based

on high-resolution LiDAR data. J. Volcanol. Geotherm. Res. 186, 320–330. https://doi.org/10.1016/j.jvolgeores.2009. 07.011.
Fornaciai, A., Favalli, M., Karátson, D., Tarquini, S., Boschi, E., 2012. Morphometry of scoria cones, and their relation to geodynamic setting: a DEM-based analysis. J. Volcanol. Geotherm. Res. 217, 56–72.
Fries, C., 1960. Geología del Estado de Morelos y partes adyacentes de México y Guerrero, región central meridional de México. Bol. Inst. Geol. UNAM 60 (236 pp.).
Gesch, D., Oimoen, M., Danielson, J., Meyer, D., 2016. Validation of the ASTER Global Digital Elevation Model version 3 over the conterminous United States. Int. Arch. Photogramm. Remote Sens. Spatial Inf. Sci. XLI-B4, 143–148. https://doi.org/10.5194/isprs-archives-XLI-B4-143-2016.
Gilichinsky, M., Melnikov, D., Melekestsev, I., Zaretskaya, N., Inbar, M., 2010. Morphometric measurements of cinder cones from digital elevation models of Tolbachik volcanic field, central Kamchatka. Can. J. Remote. Sens. 36 (4), 287–300. https://doi.org/10.5589/m10-049.
Grosse, P., van Wyk de Vries, B., Euillades, P.A., Kervyn, M., Petrinovic, I.A., 2012. Systematic morphometric characterization of volcanic edifices using digital elevation models. Geomorphology 136, 114–131. https://doi.org/10.1016/j.geomorph.2011.06.001.
Grosse, P., Ochi Ramacciotti, M.L., Escalante, F., Guzmán, S., Orihashi, Y., Sumino, H., 2020. Geomorphology, morphometry, spatial distribution and ages of mafic monogenetic volcanoes of the Peinado and Incahuasi fields, southernmost Central Volcanic Zone of the Andes. J. Volcanol. Geotherm. Res. 401, 106966. https://doi.org/10.1016/j.jvolgeores.2020.106966.
Guilbaud, M.N., Arana-Salinas, L., Siebe, C., Barba-Pingarrón, L.A., Ortiz, A., 2015. Volcanic stratigraphy of a high-altitude Mammuthus columbi (Tlacotenco, Sierra Chichinautzin), Central México. Bull. Volcanol. 77, 17.
Gunn, B.M., Mooser, F., 1971. Geochemistry of the volcanics of central Mexico. Bull. Volcanol. 34, 577–616.
Hasenaka, T., Carmichael, I.S., 1985. The cinder cones of Michoacán–Guanajuato, central Mexico: their age, volume and distribution, and magma discharge rate. J. Volcanol. Geotherm. Res. 25, 105–124.
Hooper, D., 1995. Computer-simulation Models of Scoria Cone Degradation in the Colima and Michoacán-Guanajuato Volcanic Fields, Mexico. Geofísica Internacional. 34. 321–340.
Hooper, D.M., Sheridan, M.F., 1998. Computer-simulation models of scoria cone degradation. J. Volcanol. Geotherm. Res. 83, 241–267.
Inbar, M., Gilichinsky, M., Melekestsev, I., Melnikov, D., Zaretskaya, N., 2011. Morphometric and morphological development of Holocene cinder cones: a field and remote sensing study in the Tolbachik volcanic field, Kamchatka. J. Volcanol. Geotherm. Res. 201, 301–311. https://doi.org/10.1016/j.jvolgeores.2010.07.013.
Jaimes-Viera, M.C., Martin Del Pozzo, A., Layer, P.W., Benowitz, J.A., Nieto-Torres, A., 2018. Timing the evolution of a monogenetic volcanic field: Sierra Chichinautzin, Central Mexico. J. Volcanol. Geotherm. Res. 356, 241–267. https://doi.org/10.1016/j.jvolgeores.2018.03.013.
Kereszturi, G., Németh, K., 2012. Monogenetic basaltic volcanoes: genetic classification, growth, geomorphology and degradation. In: Németh, K. (Ed.), Updates in Volcanology – New Advances in Understanding Volcanic Systems. InTech https://doi.org/10.5772/51387.
Kereszturi, G., Geyer, A., Martí, J., Németh, K., Dóniz-Páez, J.F., 2013. Evaluation of morphometry-based dating of monogenetic volcanoes – a case study from Bandas del Sur, Tenerife (Canary Islands). Bull. Volcanol. 75 (734), 1–19. https://doi.org/10.1007/s00445-013-0734-1.
Kervyn, M., Ernst, G.G.J., Goossens, R., Jacobs, P., 2008. Mapping volcano topography with remote sensing: ASTER v. SRTM. Int. J. Remote Sens. 29, 6515–6538. https://doi.org/10.1080/01431160802167949.
Kervyn, M., Ernst, G.G.J., Carracedo, J.C., Jacobs, P., 2012. Geomorphometric variability of 'monogenetic' volcanic cones: evidence from Mauna Kea, Lanzarote and experimental cones. Geomorphology 136, 59–75. https://doi.org/10.1016/j.geomorph.2011.04.009.
Kirianov, V.Y., Koloskov, A.B., la Cruz, De, 1990. The Major Stages of Manifestation of Recent Volcanism in the Chichinautzin Zone. Geological Series 311. USSR Academy of Sciences, pp. 432–434.
Kuhl, F., Giardina, C.R., 1982. Elliptic Fourier features of a closed contour. Comput. Graph. Image Process. 18, 236–258.
Lindsay J., Leonard G., 2009. Age of the Auckland Volcanic Field. Inst. Earth Sciences and Engineering Report 1-2009.02, U Auckland, NZ, ISBN: 978-0-473-15316-8 [PDF] 978-0-473-15416-5, (38 pp.)
Márquez, A., Surendra, P. Verma, Anguita, F., Oyarzun, R., Brandle, J.L., 1999. Tectonics and volcanism of Sierra Chichinautzin: extension at the front of the central trans mexican volcanic belt. J. Volcanol. Geotherm. Res. 93, 125–150.
Martin del Pozzo, A.L., 1982. Monogenetic vulcanism in Sierra Chichinautzin, México. Bull. Volcanol. 45, 9–24.
NASA/METI/AIST/Japan Spacesystems, U.S./Japan ASTER Science Team, 2019. ASTER Global Digital Elevation Model V003. Distributed by NASA EOSDIS Land Processes DAAC https://doi.org/10.5067/ASTER/ASTGTM.003.
NASA/METI/AIST/Japan Spacesystems, U.S./Japan ASTER Science Team, 2019. ASTER Global Digital Elevation Model V003. Distributed by NASA EOSDIS Land Processes DAAC https://doi.org/10.5067/ASTER/ASTGTM.003.
Nieto-Torres, A., Martin Del Pozzo, A.L., 2019. Spatio-temporal hazard assessment of a monogenetic volcanic field, near México City. J. Volcanol. Geotherm. Res. 371, 46–58. https://doi.org/10.1016/j.jvolgeores.2019.01.006.
Porter, S.C., 1972. Distribution, morphology, and size frequency of cinder cones on Mauna Kea Volcano, Hawaii. Geol. Soc. Am. Bull. 83, 3607–3612.
Riedel, C., Ernst, G.G.J., Riley, M., 2003. Controls on the growth and geometry of pyroclastic constructs. J. Volcanol. Geotherm. Res. 127, 121–152. https://doi.org/10.1016/S0377-0273(03)00196-3.
Rizzoli, P., Martone, M., Gonzalez, C., Wecklich, C., Borla Tridon, D., Bräutigam, B., Bachmann, M., Schulze, D., Fritz, T., Huber, M., Wessel, B., Krieger, G., Zink, M., Moreira, A., 2017. Generation and performance assessment of the global TanDEM-X digital elevation model. ISPRS J. Photogramm. Remote Sens. 132, 119–139. https://doi.org/10.1016/j.isprsjprs.2017.08.008.
Schmittbuhl, M., Allenbach, B., Le Minor, J.M., Schaaf, A., 2003. Elliptical descriptors: some simplified morphometric parameters for the quantification of complex outlines. Math. Geol. 35 (7), 853–871.
Scott, D.H., Trask, N.J., 1971. Geology of the Lunar Crater volcanic field, Nye County, Nevada. U.S.G.S. Professional Papers 599-I.
Settle, M., 1979. The structure and emplacement of cinder cone fields. Am. J. Sci. 279, 1089–1107.
Siebe, C., 2000. Age and archaeological implications of Xitle volcano, southwestern basin of Mexico-City. J. Volcanol. Geotherm. Res. 104, 45–64.
Siebe, C., Rodriguez-Lara, V., Schaaf, P., 2004. Radiocarbon ages of holocene Pelado, Guespalapa, and Chichinautzin scoria cones, south of Mexico city: implications for archaeology and future hazards. Bull. Volcanol. 66, 203–225.
Siebe, C., Arana-Salinas, L., Abrams, M., 2005. Geology and radiocarbon ages of Tlaloc, Tlacotenco, Cuauhtzin, Hijo del Cuauhtzin, Teuhtli, and Ocusacayo monogenetic volcanoes in the central part of the Sierra Chichinautzin, Mexico. J. Volcanol. Geotherm. Res. 141, 225–243.
Swinamer, R.T., 1989. The geomorphology, geochemistry and petrogenesis of the volcanic rocks in the Sierra del Chichinautzin, Mexico. MSc thesis, Queen's University, Kingston, Ontario,Canada, pp. 1–212.
Thompson, J.A., Bell, J.C., Buttler, C.A., 2001. Digital elevation model resolution: effects on terrain attribute calculation and quantitative soil-landscape modeling. Geoderma 100, 67–89.
Urrutia-Fucugauchi, J., Martin Del Pozzo, A.L., 1993. Implicaciones de los datos paleomagnéticos sobre la edad de la Sierra de Chichinautzin, cuenca de México. Geofis. Int. 32 (3), 523–533.
Wallace, P.J., Carmichael, I.S.E., 1999. Quaternary volcanism near the valley of Mexico: implications for subduction zone magmatism and the effects of crustal thickness variations on primitive magma compositions. Contrib. Mineral. Petrol. 135, 291–314. https://doi.org/10.1007/s004100050513.
Wood, C.A., 1980a. Morphometric evolution of cinder cones. J. Volcanol. Geotherm. Res. 7, 387–413.
Wood, C.A., 1980b. Morphometric analysis of cinder cone degradation. J. Volcanol. Geotherm. Res. 8, 137–160.
Yokoyama, I., 2019. Clusters of small monogenetic cones: a particular type of confined volcanism. Ann. Geophys. 62 (6), VO678. https://doi.org/10.4401/ag-8176.
Zarazúa-Carbajal, M.C., De la Cruz-Reyna, S., 2020. Morpho-chronology of monogenetic scoria cones from their level contour curves. Applications to the Chichinautzin monogenetic field, Central Mexico. J. Volcanol. Geotherm. Res. 407, 107093. https://doi.org/10.1016/j.jvolgeores.2020.107093.

CAPÍTULO 4

UNA APLICACIÓN DE MATLAB PARA CALCULAR EL GRADO DE EROSIÓN RELACIONADO CON LA EDAD DE CONOS DE ESCORIA MONOGENÉTICOS, A PARTIR DE MODELOS DIGITALES DE ELEVACIÓN.

En este artículo (https://doi.org/10.1016/j.mex.2021.101454) se presenta una aplicación de MATLAB, diseñada especificamente para facilitar la implementación del método propuesto para la caracterización morfométrica de conos de escoria a partir del análisis de las curvas de nivel.

Resumen:

Se presenta una aplicación de MATLAB construida para caracterizar el grado de erosión de los conos de escoria monogenéticos a partir de dos conjuntos independientes de parámetros morfométricos obtenidos del análisis de Modelos Digitales de Elevación (MDE). Uno cuantifica la forma y el tamaño de las ondulaciones en los contornos de nivel a través de un nuevo parámetro introducido por primera vez en Zarazúa-Carbajal y De la Cruz-Reyna (2020), el Índice Promedio de Erosión (*AEI*). El *AEI* es estimado utilizando Descriptores Elípticos de Fourier para calcular los espectros de longitud de onda de las ondulaciones en contornos seleccionados en un amplio rango de resoluciones de la base de datos, y después promediando los resultados de los contornos seleccionados. El otro es un conjunto de parámetros más convencionales que caracterizan los perfiles verticales de los conos. Este algoritmo permite corregir esos parámetros por la inclinación del terreno.

- Estos métodos tienen como objetivo una evaluación coherente de las edades relativas de los volcanes relacionadas con la erosión en campos monogenéticos extensos, a partir de un MDE

- El grado de erosión relacionado con la edad se revela mediante dos parámetros principales: el índice de erosión promedio (*AEI*), calculado a partir del espectro de los descriptores elípticos de Fourier de las curvas de contorno de un cono de escoria con la única suposición de que el cono adquirió una superficie lisa al terminar su proceso de formación; el otro parámetro es la relación de aspecto de un perfil vertical de los conos de escoria, considerando las inclinaciones del terreno, si se supone que todos los conos adquirieron la misma morfología de sus perfiles verticales en su fase de formación.
- El método proporciona métricas de erosión a partir de una gama considerable de resoluciones MDE. Para aplicaciones relacionadas con la edad, se recomienda utilizar resoluciones mejores que 12 m.

MethodsX 8 (2021) 101454

Contents lists available at ScienceDirect

MethodsX

journal homepage: www.elsevier.com/locate/mex

Method Article

A MATLAB App for calculating the age-dependent degree of erosion of monogenetic scoria cones from DEM data

María Cristina Zarazúa-Carbajal[a,*], Servando De la Cruz-Reyna[b]

[a] Posgrado en Ciencias de la Tierra, Instituto de Geofísica, Universidad Nacional Autońoma de Meẋico (UNAM), CDMX 04510, Mexico
[b] Instituto de Geofísica, Universidad Nacional Autońoma de Meẋico (UNAM), CDMX 04510, Mexico

A B S T R A C T

We present a MATLAB App aimed to characterize the degree of erosion of monogenetic scoria cones from two independent sets of morphometric parameters. One quantifies the shape and size of undulations in DEM level contours through a novel parameter, the Average Erosion Index (*AEI*), using Elliptical Fourier Descriptors to calculate the wavelength spectra of undulations in selected contours over an ample range of resolutions of the database. The other is a more conventional set of parameters characterizing the vertical profiles of cones. This algorithm permits correcting those parameters for terrain inclination.

- These methods aim for a consistent assessment of the erosion-related relative ages of volcanoes in extensive monogenetic fields, from DEM data.
- The age-related degree of erosion is revealed by two main parameters: The Average Erosion Index (*AEI*), calculated from the Elliptic Fourier Descriptor spectrum of a scoria cone contour lines; and the aspect ratio of a scoria cone vertical profile, considering terrain inclinations, if it is assumed that all cones acquired the same morphology at the time of their formation eruptions.
- The Method provides erosion metrics from a sizable range of DEM resolutions. For age-related applications, it is recommended to use resolutions better than 12 m.

A R T I C L E I N F O
Method name: Erosion metrics for monogenetic volcanic cones
Keywords: Elliptical Fourier Descriptors, Erosional features metrics, Morpho-chronometric tool, Monogenetic volcanic fields
Article history: Received 8 May 2021; Accepted 11 July 2021; Available online 13 July 2021

DOI of original article: 10.1016/j.jvolgeores.2020.107093
* Corresponding author.
E-mail address: mariac.zarazua@gmail.com (M.C. Zarazúa-Carbajal).

https://doi.org/10.1016/j.mex.2021.101454

Specifications table

Subject Area:	Earth and Planetary Sciences
More specific subject area:	Volcanology
Method name:	Erosion metrics for monogenetic volcanic cones
Name and reference of original method:	*AEI method:* Zarazúa-Carbajal,M.C. and De la Cruz-Reyna, S. (2020) . Morpho-chronology of monogenetic scoria cones from their level contour curves. Applications to the Chichinautzin monogenetic field, Central Mexico Journal of Volcanology and Geothermal Research, 407, 107093. https://doi.org/10.1016/j.jvolgeores.2020.107093 *Slope and Aspect ratio method:* Favalli, M., Karátson, D., Mazzarini, F., Pareschi, M.T. and Boschi, E. (2009). Morphometry of scoria cones located on a volcano flank: a case study from Mt. Etna (Italy), based on high-resolution LiDAR data. Journal of Volcanology and Geothermal Research, 186, 320–330, https://doi.org/10.1016/j.jvolgeores.2009.07.011 Bemis, K. and Ferencz, M. (2017). Morphometric analysis of scoria cones: the potential for inferring process from shape. Geol. Soc. Lond. Spec. Publ. 446, 17. https://doi.org/10.1144/SP446.9 Zarazúa-Carbajal, M.C. and De la Cruz-Reyna, S. (2021). Digital Elevation Model resolution: Effects on the chronometry-oriented morphological analysis of scoria cones in the Sierra Chichinautzin, central Mexico. Geomorphology, 389, 107842. https://doi.org/10.1016/j.geomorph.2021.107842
Resource availability:	*MATLAB app to run in MATLAB 2020a:* https://la.mathworks.com/matlabcentral/fileexchange/95398-erosionmetricsconicallandformsapp

Background

Measuring erosion in landforms over extensive areas is feasible if a digital elevation model (DEM) of the terrain with an appropriate resolution is available. This type of analysis is of particular interest in monogenetic volcanic fields comprising hundreds or even thousands of scoria cones for its potential capabilities to estimate their relative ages. Each of such volcanoes erupts once producing different landforms. Among the common is the cinder or scoria cone, which are relatively small structures compared with polygenetic volcanoes. The conical shape of such structures is mostly controlled by the repose angle of granular material (scoria) which determines the cone slope at the time of the formation eruption. Indeed, the conical shape may be disrupted by different factors: basal terrain inclination, phreatomagmatic eruptions, eruption style shifts, tephra mantling, welding or agglutination, breaching, lava flows, among others. However, in treating the problem of measuring the degree of erosion, it is frequently assumed that all scoria cones within a cluster of monogenetic volcanoes had similar slope angles and aspect ratios at the time of their formation and that all have a similar response when exposed to the same erosive conditions. Such assumptions overlook important internal and external processes directly affecting the initial morphology of a cone and others affecting its response to erosive factors [10–12]. Nevertheless, if those assumptions can be sustained, a measure of the relative degradation state among the cones in a cluster can be obtained from the angle of the flank slopes, or the aspect ratio (the height of the cone divided by the basal diameter) [16,22,23].

Recently, a new approach to measure the relative degradation state of scoria cones employs a method based on the analysis of the Elliptical Fourier Descriptor (EFD) spectra of the landform closed contour lines. If the assumption that the landform surface was smooth at the time of its formation can be sustained, it follows that, as time passes, the formation of erosional rills and gullies may be measured in terms of the extent (wavelength) and depth (amplitude) of the undulations of the level contour lines, and that this information can be condensed in a single parameter named as the Average Erosion Index *AEI* [24].

Furthermore, under the assumption that the group of scoria cones was exposed to similar erosive conditions, an appraisal of the relative age among cones can be made using the available radiometric ages of the studied cones to establish functional relationships between the measured ages and the erosive condition [2,8,9,15,23,24,26]. Consequently, these methods may represent a helpful tool for the study of the volcanic field spatio-temporal evolution and its consequences on the volcanic risk.

Both approaches, vertical profile analysis, and contour line undulations have advantages and disadvantages, both assume that cones within a region have been exposed to similar erosive conditions, and their applicability may depend on the actual state of the scoria cones, the available radiometric age data, and the characteristics of the used DEM database.

Average Erosion Index

The age-dependent erosive condition of the landform is appraised with a single parameter, the Average Erosion Index (*AEI*), calculated from a DEM database using the level contour shape description attributes of the Elliptical Fourier Descriptors (EFD) [13,17,24].

The (EFD) spectra of diverse shapes, including closed contour lines, have been used to characterize complex shapes in many geological, biological, paleontological, and anthropological studies (e.g., [7,18,20,21]), even if their outlines are non-holomorphic, this is, with radii emanating from a centroid intersecting the outline in more than one point. Monogenetic scoria cones are landforms with smooth truncated cone shapes at the time of their formation. The age-dependent erosion is evidenced as changes in the volcano flank slopes and as height-dependent undulations of the cone surface. The information on the width and depth of those undulations is condensed in a single parameter: The *AEI* [24].

The computation algorithm of the *AEI* develops in a series of steps [24], as follows: 1) Identification of the level contours of the volcanic edifice. 2) Decomposition of each contour in its EFD using a specific type of Fourier analysis [13,17]. 3) For each contour computes a Similarity function $\langle S1_k \rangle$ measuring the overall alikeness between the original and the *k*th-reconstructed EFD contour. Its value converges to zero as the contents of harmonics approach the Nyquist frequency ½ *n*, where *n* is the DEM-resolution dependent number of sampled points of the contour, thus measuring to what extent each partially reconstructed contour approximates to the original sampled one. 4) Calculates an Erosion Spectrum (D_k) for each contour which measures the contribution of each harmonic *k* to the reconstruction of the "original contour". 5) Computes for each contour the Erosion Index *D*, which is an average of the erosion spectra, considering only harmonics running from that of the reference "original" contour to the highest, corresponding to the Nyquist harmonic. 6) Computes the *AEI,* averaging the Erosion indexes of all of the selected contours of a scoria cone. All of these procedures and parameters are described in detail in [24]. The App allows the implementation of all the necessary pre-processing for non-closed level contours, or to analyze specific angular regions of a scoria cone.

The App introduced here performs all the calculations needed to compute the single *AEI* parameter from a TIFF or GeoTIFF DEM of the volcanic edifice, in a sequential and sectorized form, allowing control of the calculations and the possibility to make modifications according to the interests of the user. It returns a single file with the *AEI* value of the analyzed cone, but it is intended to be an "open box" creating files and figures that can be accessed to further understanding how the results were obtained (Fig. 1).

Volcanic cone slope and aspect ratio

There are several different methods to characterize the morphometry of a scoria cone, which have evolved as the quality of the maps improved, and even more drastically with the development of the Digital Elevation Models [6].

The aspect ratio is a frequently used morphometric parameter that can be strongly affected by factors highly sensitive to the DEM resolution, such as the criteria to define the limits of the base of a cone and the limits of the crater rim [6], as well as the definitions used to estimate the basal diameter of a cone, or the cone height [4].

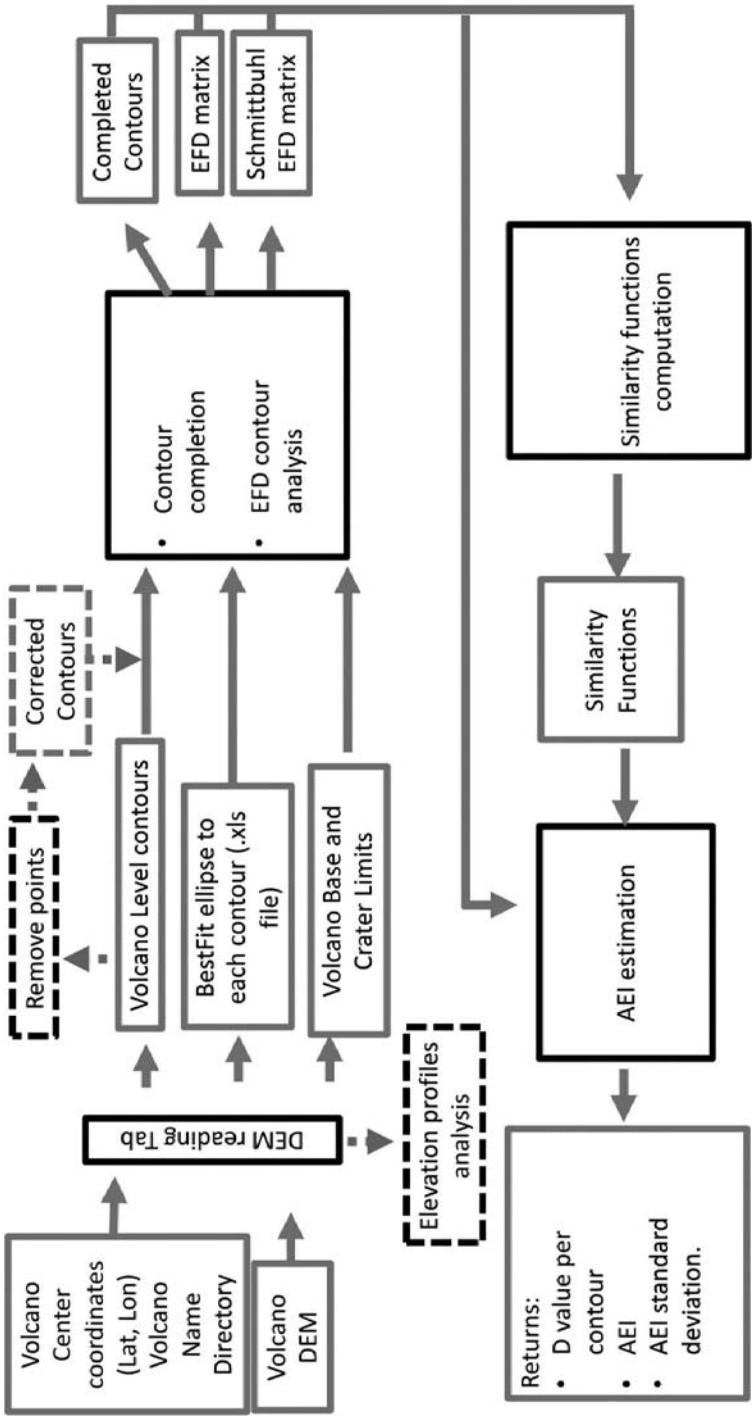

Fig. 1. Overview of the algorithm code. Black lines denote MATLAB codes. Gray lines denote Input and output information. Dotted lines show optional routines within the code.

In the methodology used in the App presented here, we implement an approach similar to that of Bemis and Ferencz [1], in which the cone dimensions are calculated from different elevation profiles, and then averaged. The sampling of different profiles provides more control on the characterization of cones with non-symmetric shapes affected by factors other than erosion, such as breached cones or crater rows. Additionally, we take into account the inclination of the underlying terrain to compute the height and basal diameter of the cone at each elevation profile obtained in the eight sampled cross-sections. This allows an equitable comparison of the aspect ratio (*Ar*) between cones emplaced in a horizontal terrain and those emplaced in an inclined one, as proposed and discussed by Favalli et al. [4].

This App is thus chiefly designed to compute the *AEI* index, and also can perform an analysis of the elevation profiles of a scoria cone, whose results generate a single Excel file containing the morphometric parameters obtained for 8 elevation profiles, 4 crossing the cones' center and 4 crossing the crater's center. Those profile parameters may be then used to estimate average parameters or managed according to the user interests.

Summarizing, the MATLAB scripts presented here can sample the DEM data, identify the volcanic structure, define the closed contours, select an option to calculate the EFD spectra at different heights of the cone, average them, and estimate the resulting *AEI*. The scripts can also estimate the parameters that characterize the morphometry of the scoria cones' elevation profiles and their dimensions.

The following table explains the different concepts, functions, and parameters used in the algorithms.

Method details

This App is composed of a succession of MATLAB functions. Each function automatically creates output files that are saved in a directory, which the user can check at any time to verify that all of the procedures are yielding results. The whole process is semi-automatic, but we recommend checking the outputs at each stage.

How to run?

Open a MATLAB Terminal and run the App "ErosionMetricsConicalLandforms". A Window with five tabs will be displayed. The App has a modular design, so every tab can be run independently if the files required for that step already exist.

The required INPUT parameters are: The name of the DEM file containing any number of scoria cones, coordinates of the particular cone to be analyzed, name of that cone, horizontal resolution of the DEM, and name of the directory in which all created files will be saved.

The App contains five Tabs: A. DEM reading, B. Remove contour points, C. AnalysisEFD, D. AEI and E. Multiple Cones Analysis. The classification of level contours and the option to analyze the elevation profiles of the scoria cone are included in Tab A. Tabs B to D include all steps to obtain the Average Erosion Index, from the analysis of level contours of a scoria cone. Tab E allows computing the AEI of multiple scoria cones, if the required pre-processing is previously implemented.

In some steps, the analysis requires input from the user. How and where such input is required is explained in the following description for each tab.

A. DEM reading Tab

In this first tab, the App loads a DEM comprising one or any number of scoria cones in the file format TIFF or GeoTIFF. It requires the following input parameters: DEM file name, a directory name (in which the results of the analysis will be saved), the cone's identification names, the DEM horizontal resolution in meters, and the Latitude and Longitude (in decimal degrees) of the center of the particular cone to be analyzed.

This App has been tested in DEMs with a Geographic Coordinate System.

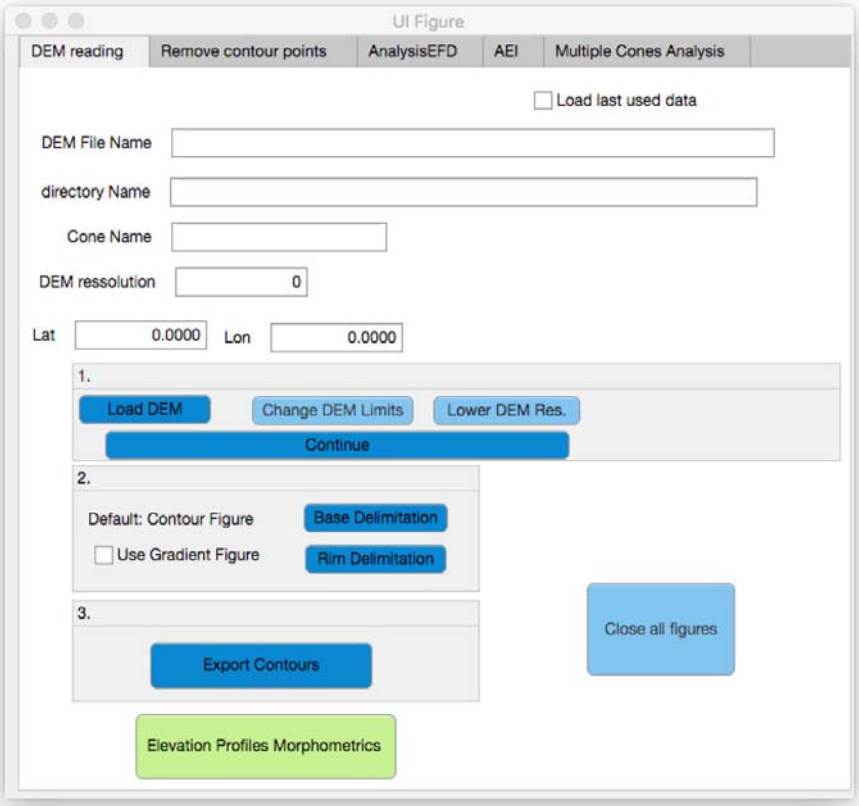

Fig. 2. Starting Tab to begin the analysis with the App. Mandatory buttons are shown in dark blue. Optional buttons are shown in light blue.

This tab includes several buttons, some of them mandatory and others optional (Fig. 2). Each of them is described next.

A.1 LOAD DEM (mandatory)

Clicking this button reads the DEM from file 'DEM File Name', which should be a DEM in TIFF or GeoTIFF format.

A figure window will pop out showing a selected region of the DEM. If the displayed area does not cover the cone edifice, click on the 'Change DEM Limits' button. Otherwise, click on the Continue Button.

All text fields in this tab are mandatory. If one of them is empty, an error signal will be displayed.

NOTE: This code has been tested with DEMs having the reference matrix types 'map.rasterref.GeographicCellsReference' or 'map.rasterref.MapCellsReference'. If while running the app an error concerning the type of reference matrix occurs, line 228 of the main App file (AppContoursMethodsX.mlapp) can be modified to fit the requirements of the Reference matrix in question.

A.2 Change DEM Limits (optional)

When this button is clicked, a figure displaying the DEM region will be activated. The user must first select with a mouse click a point in the lower left and then another in the upper right of the

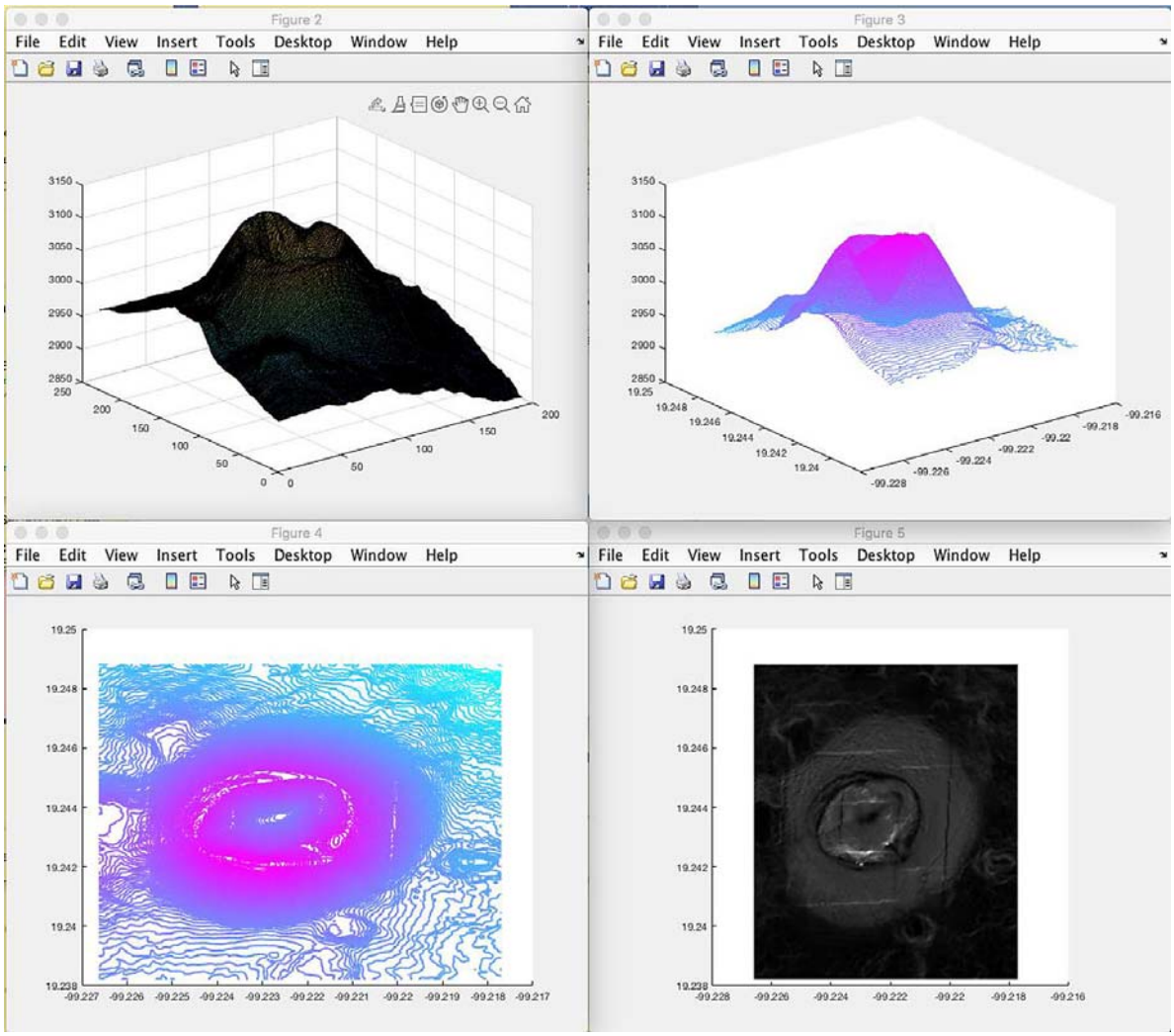

Fig. 3. a) 3-D visualization of the selected region b) 3D- visualization of level contours. c) 2-D visualization of level contours. d) Visualization of the norm of the gradient of the image.

image. The selected points will be shown as pink cross markers in the image. These points can be outside the plot axis limits but should be contained in the Figure window region.

After the two points are selected, press ENTER key on the keyboard.

A.3 Continue Button (Mandatory)

Once the limits of the region are defined, the program computes the contours of the DEM every 2 meters. Four figures containing the DEM gradient, the DEM 3-D contours, and a 3-D surface will be created, displayed, and saved (Fig. 3).

A.4 Lower resolution (optional)

When this button is pressed, the user has to specify the decrease factor (df=previous resolution/new resolution) in the correspondent field and then click the OK button (Fig. 4). This will create a subfolder “LResfdf” in which the under-sampled DEM will be saved. If the check box “Use existing raster” is active, then the LOAD DEM step can be omitted, and the under-sampling will be performed in the DEM saved in the ‘Datos.mat’ file stored in the ‘directory’/’cone name’ folder.

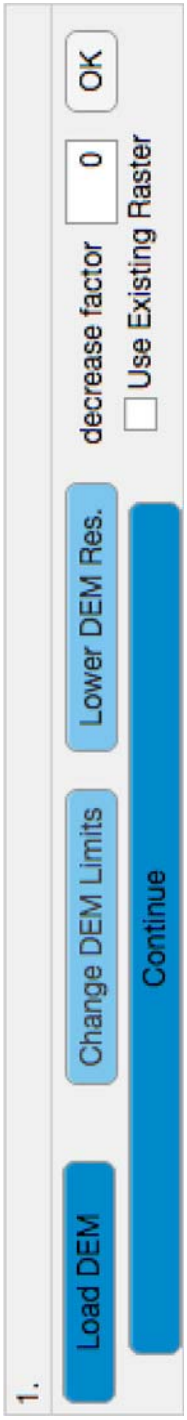

Fig. 4. Decrease resolution option.

To perform the analysis in the new reduced-resolution DEM press the button ‘Continue” and everything will be saved in the ““LResfdf” folder.

A.5 Base Delimitation Button (Mandatory)

Base delimitation is made by visual inspection. The user selects points along the border of the base of the cone and the program defines a best-fitted ellipse based on the selected points.

Delimiting the base of the cone should be performed by default on the contour image, but, if preferred, the gradient image may also be used selecting “Use Gradient image”.

When pressed, the Contour Image will be activated, the user should select at least 5 points delimiting the cone’s edifice. We suggest using 10-20 points. And then press the “ENTER” key on the keyboard. (Fig. 5a)

A.6 Rim Delimitation Button (Mandatory)

Rim delimitation is made by visual inspection. The user selects points along the border of the rim and the program defines a best-fitted ellipse based on the selected points.

Rim delimitation is performed by default on the 2-D contour image, if the gradient image is preferred, then select the “Use Gradient image” box.

When pressed, the Contour Image will be activated, the user should select at least 5 points delimiting the cone’s crater rim. If no crater rim is visible, then the selection should be a single point in the center of the cone or delimiting the highest contour. If the cone is breached, the selection should follow a circular or elliptical path from the part of the cone that is not breached. We suggest using 10-20 points. And then press the “ENTER” key on the keyboard Fig. 5b.

A.7 Export Contours Button (Mandatory)

This analysis identifies the contours belonging to the volcanic edifice on the image, based on the best-fitted ellipse [5] to the points delimiting the base of the cone (basal ellipse), and the best fit ellipse to points delimiting the crater rim (rim ellipse). Contours’ points located in the region delimited by the basal ellipse and the rim ellipse are classified as “Cone’s contours”. Contours’ points located within the rim ellipse are classified as “crater’s contours”. An identification number (ID) is assigned to each cone contour and crater contour. Lower ID valuers represent contours higher in elevation above mean sea level. These contours are saved in the folder “Salida2” to a ’.dat’ file, with names: ’contourID-Cone.dat’ or ’contourID-Crater.dat’.

After the classification is completed, the App displays two figures showing the rim ellipse and the crater ellipse on the left, and on the right figure the identified crater’s and cones’ contours (Fig. 6).

All variables related to the cones DEM section is saved to a .mat file: ‘Datos.mat’, which will be used for the next steps of the analysis.

The properties of the basal ellipse and rim ellipse are also saved in “Sheet 2” of the Excel file ’Morfometricos.xlsx’.

The delimitation of the base of the cone, the crater rim, and the process to export contours can be repeated until the user approves the selection.

A.8 Elevation Profile Analysis button (Optional)

NOTE: The file Datos.mat must be created first, with the Export Contours Button, otherwise an error will occur. The name of the cone to be analyzed should be written in the Field: Name.

This button performs the analysis of eight elevation profiles, four crossing the center of the crater and four crossing the center of the base of the cone. The profiles are generated with an azimuthal separation of 45 degrees with respect to the orientation of the major axis of the base ellipse and with respect to the major axis of the rim ellipse.

One by one, the elevation profiles will be displayed, and the user is requested to select 5 points along the profile: left base limit (P1), right base limit (P2), left crater rim limit (P3), right crater limit (P4) and the lower point within the crater (P5). The order in which the points are selected is important. From these points the following parameters will be estimated: θ_{sus}, θ_{cr}, Hco_1, Hco_2,

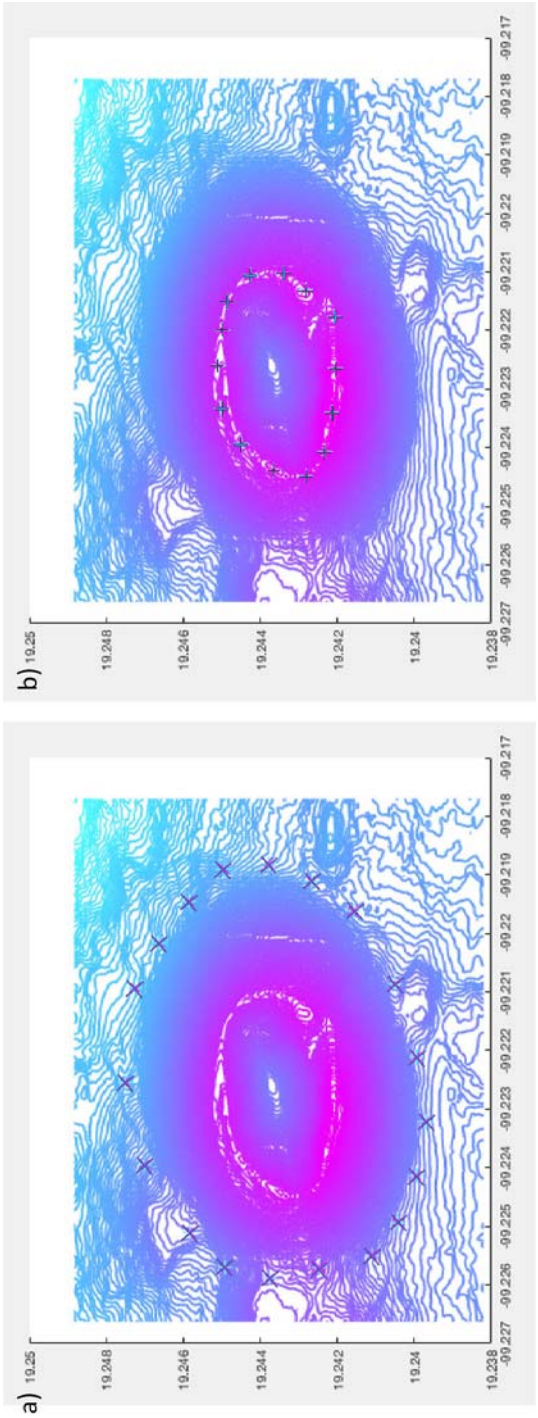

Fig. 5. a) Base delimitation, b) Cones' rim delimitation.

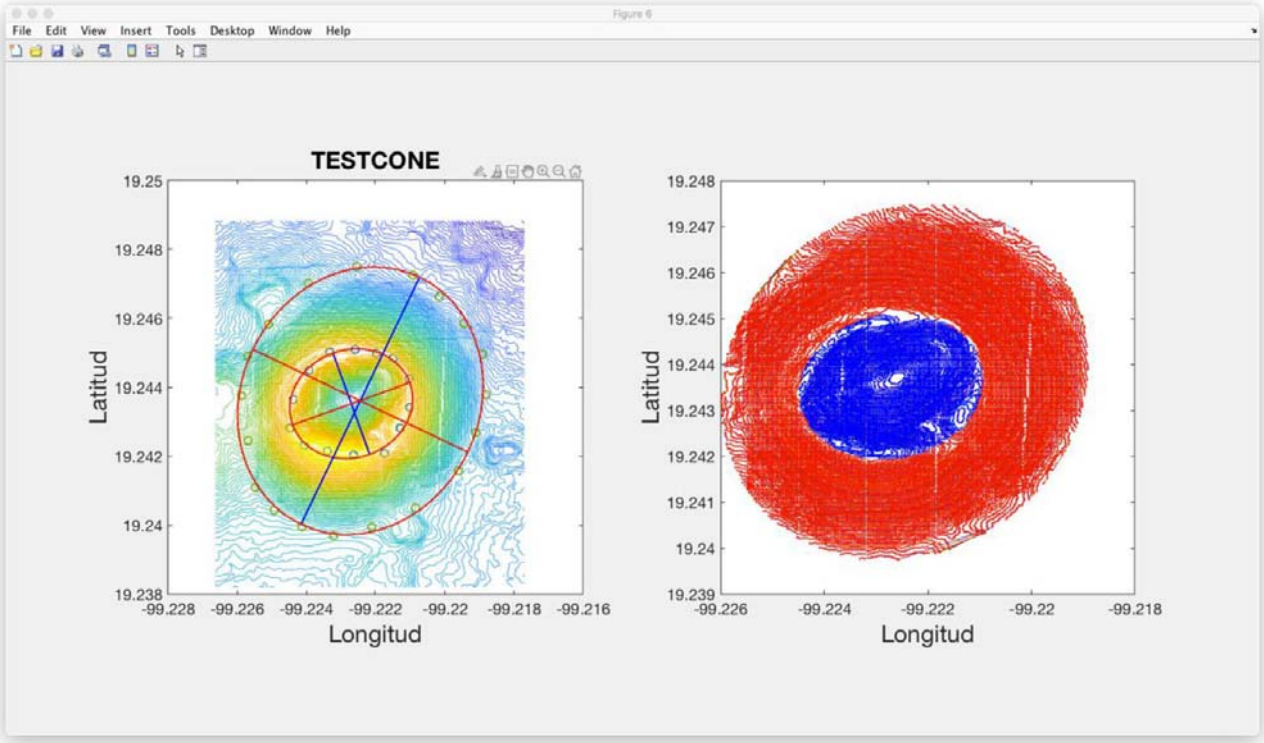

Fig. 6. LEFT: Best fitted ellipses to crater rim (rim ellipse), and base of the cone (base ellipse). RIGHT: Red contours are cone's contours; blue contours are crater contours.

Hco_{1incl}, Hco_{2incl}, θ_1, θ_2, θ_{1incl}, θ_{2incl}, Wco, Wco_{incl}, Wcr, Wcr_{incl}, Dcr, Dcr_{incl}, Z_1, Z_2, Z_{1incl}, Z_{2incl}, Ar_1, Ar_2, Ar_{1incl}, Ar_{2incl},f, f_{incl}. Fig. 7 shows a graphical representation of these parameters.

The obtained morphometric parameters for all profiles are saved in the "Sheet 3" of the Excel document: 'Morfometricos.xlsx'. The supplementary File 'MorphometricC.xlsx' exemplifies the estimation of additional parameters obtained from these values, such as: Volume, or average values of the dimensions of the cone.

We recommend the elevation profile approach to compute morphometric values of breached or horseshoe shaped cones as this allows excluding the profiles passing through such regions from the averaging calculations.

EFD Contour Analysis

B. REMOVE CONTOUR POINTS TAB

This part of the analysis is not mandatory. Ideally shaped cones on non-inclined terrains, will normally not require this step.

It is designed for the user to select and remove the information of a contour shape evidently unrelated to erosional processes such as lava flows, flank collapses, mined sectors or farming regions.

Input parameters: directory name and cone's Name. Fig. 8.

When is it necessary to remove points from contours?

This step of the analysis is required when the contours include regions that are evidently affected by phenomena other than erosion processes. For example: open-crater regions of horseshoe-shaped cones, mined regions, regions used for agriculture, or some points of the contours comprising lava flows Fig. 9.

B.1 See Contours (optional)

Displays Fig. 6, from which an assessment of which kind of point removal (if any) will be required.

B.2. Cone region Panel (mandatory)

Allows the selection of the contours from which points will be removed. "All cone" option considers all cone's contours. "Intermediate region" selects just the contours within the altitude interval: [*Hmin*+ 0.25**HT*, *Hmax*-0.25**HT*], where Hmin is the minimum altitude of the cone, Hmax is the highest point in the cone, *HT* is the net height of the cone in meters, i.e., *Hmax-Hmin*.

If a specific contour range is selected, the user is asked to fill in the contour ID of the contours to analyze (contour ID increases as Elevation of contour decreases). Contour ID according to elevation can be seen in file: 'XYSalida2.dat'

B.2. Remove Points panel

Contours can be edited in groups, or individually. We recommend simultaneous point removal for horseshoe shaped cones, or for cones with regions with human intervention (mining, agriculture, etc.) to be omitted from the analysis.

To select points, it is possible to use a 'brush' or a 'lasso' selection tool. This is done with the function selectdata.m [3].

B.3 Remove Points Button (mandatory)

When clicked, a Figure is displayed, showing the contours of the selected 'cone region', if the option 'all contours' is selected, or showing the first contour within the selected 'cone region'. Fig. 10 shows examples of all possibilities.

If the 'brush' option is selected, the user should move the mouse cursor over the points to be removed while pressing the right mouse button. Points selected for deletion will be marked in red.

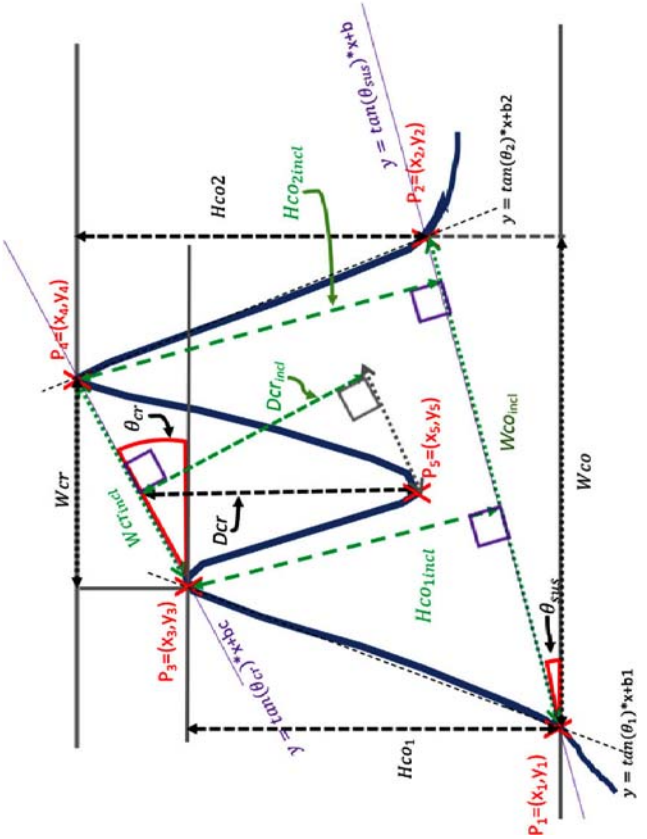

Fig. 7. Example of morphometric characterization of a scoria cone along an elevation profile.

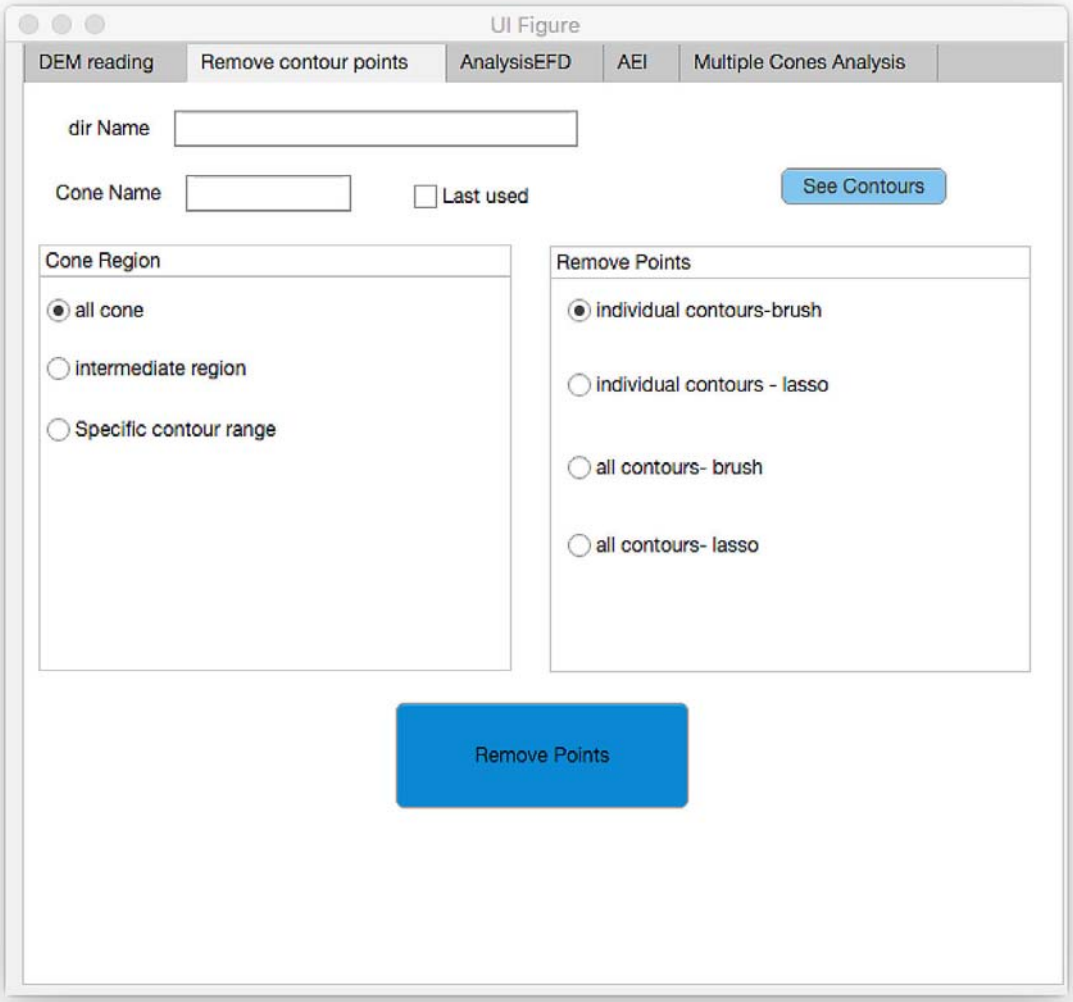

Fig. 8. The Remove contours tab

If the 'lasso' option is selected, the point at which the mouse is clicked defines the anchor point of the lasso, to select points the mouse should be moved while pressing the right mouse button.

Once the mouse is released, all selected points are marked in red, and a pop-out window appears to confirm the point selection. The 'Yes' option accepts the selected points and proceeds to save the modified contours in a .dat file; 'redo selection' unselects the previously selected points and allows the user to select new points, 'Cancel selection' continuous with the program as no points would be removed, in such a case the modified '.dat' file will contain exactly the same points as in the original.

For each modified contour a new file is created in the folder 'Salida2', with the name: 'contourID_Mod.dat'.

It is very important for the correct execution of the following functions, to remove points as illustrated in Fig. 11.

C. EFD Analysis Tab

This step computes the elliptical Fourier descriptors of each of the contours belonging to a volcanic cone.

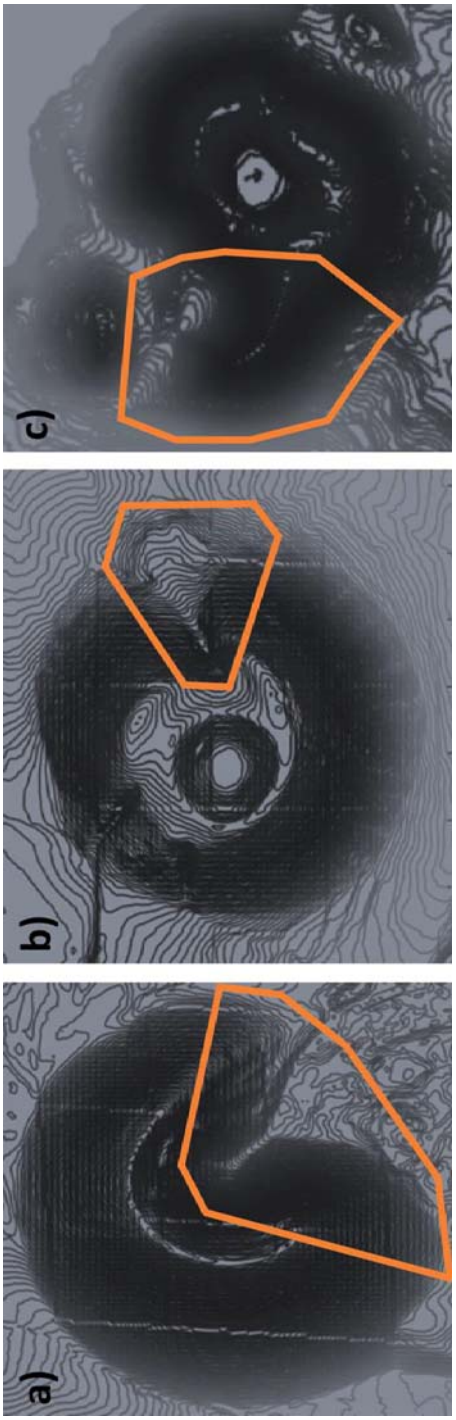

Fig. 9. Examples of regions requiring point removal. a) open-crater cone. b) landslide or lava flow, or other non-long-term erosive feature. c) part of an adjacent cone structure.

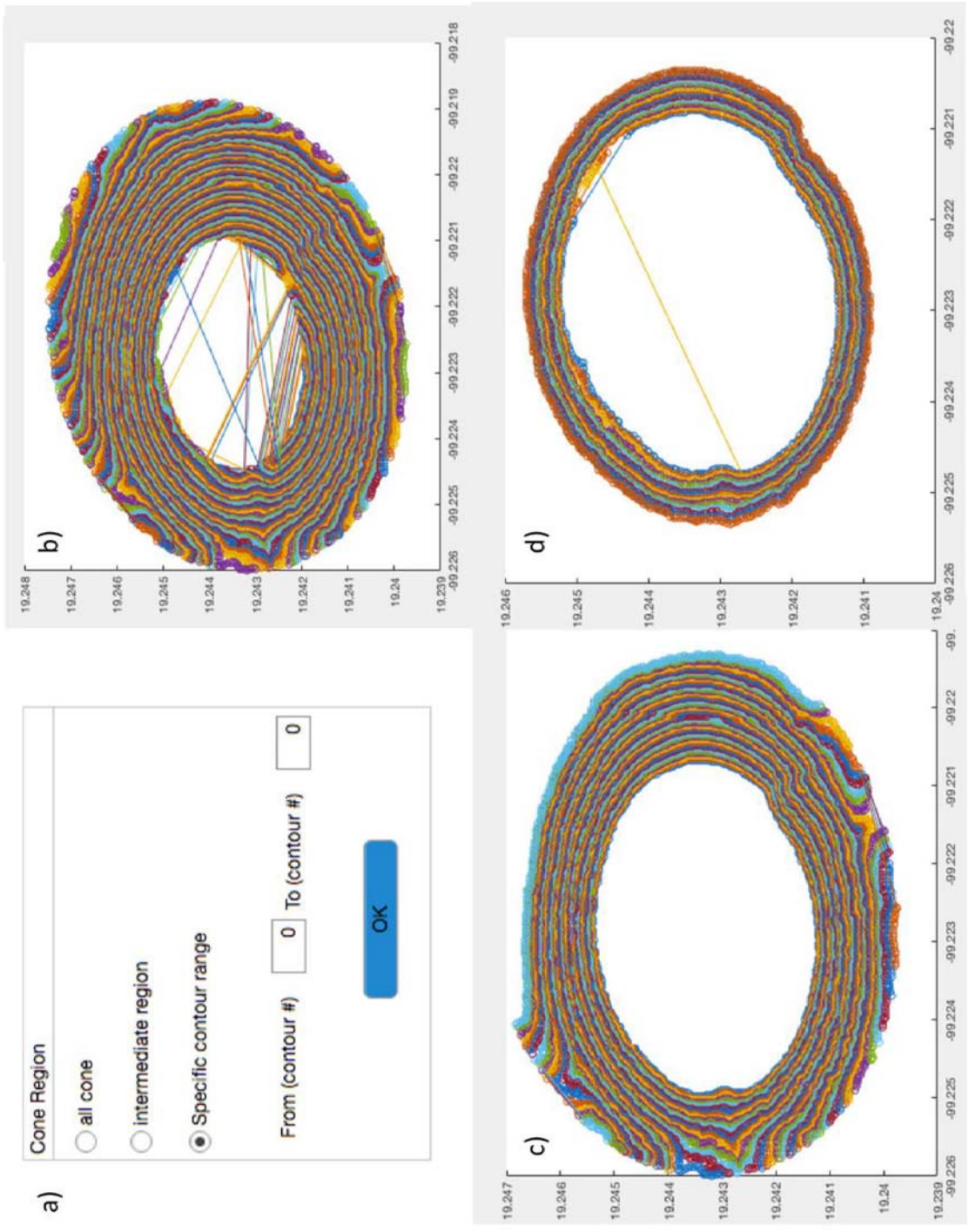

Fig. 10. a) options for selecting the vertical regions to be analyzed. b) All cone contours. c) intermediate region. d) specific contour range (contour 25 to 35 in this example)

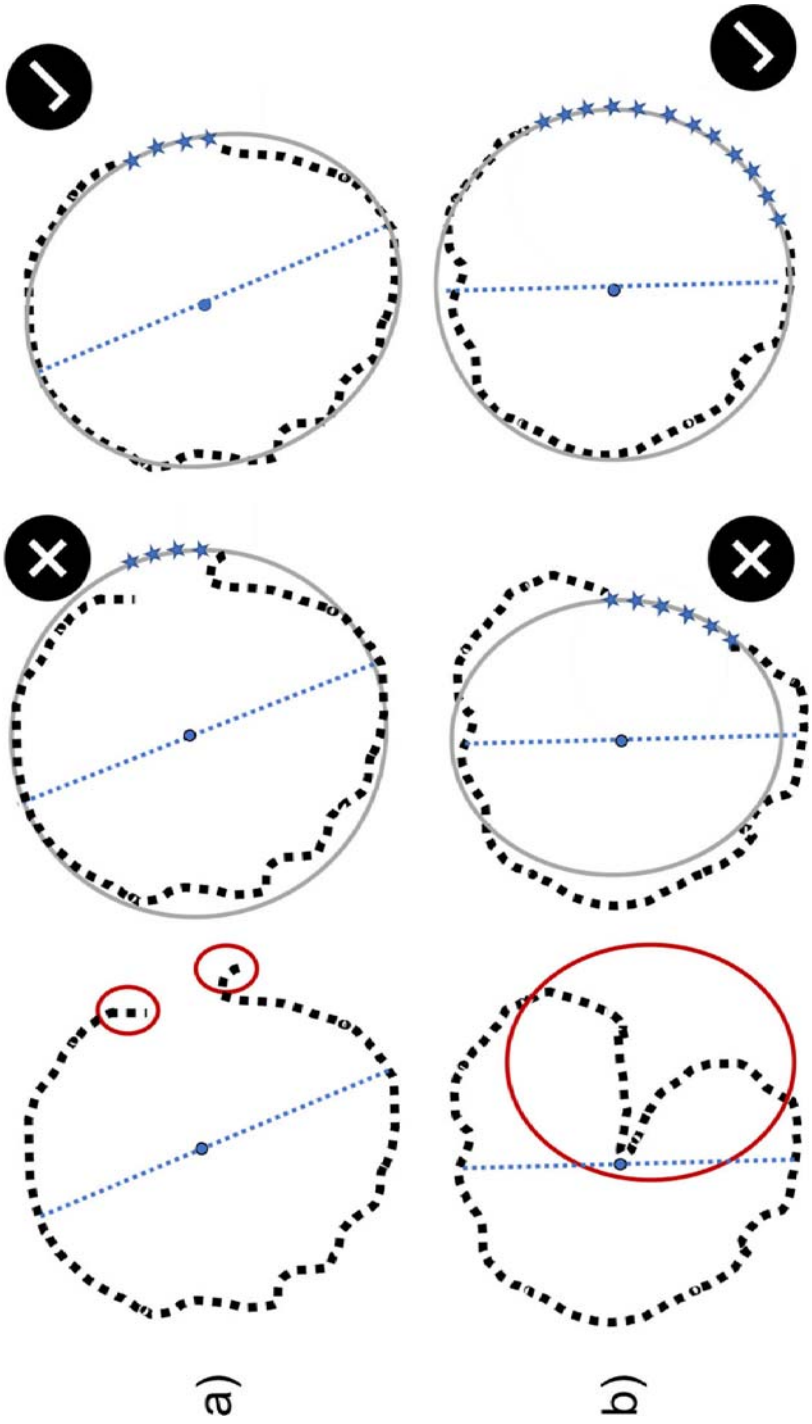

Fig. 11. Example showing correct and incorrect point removal for the correct execution of the EFD analysis.

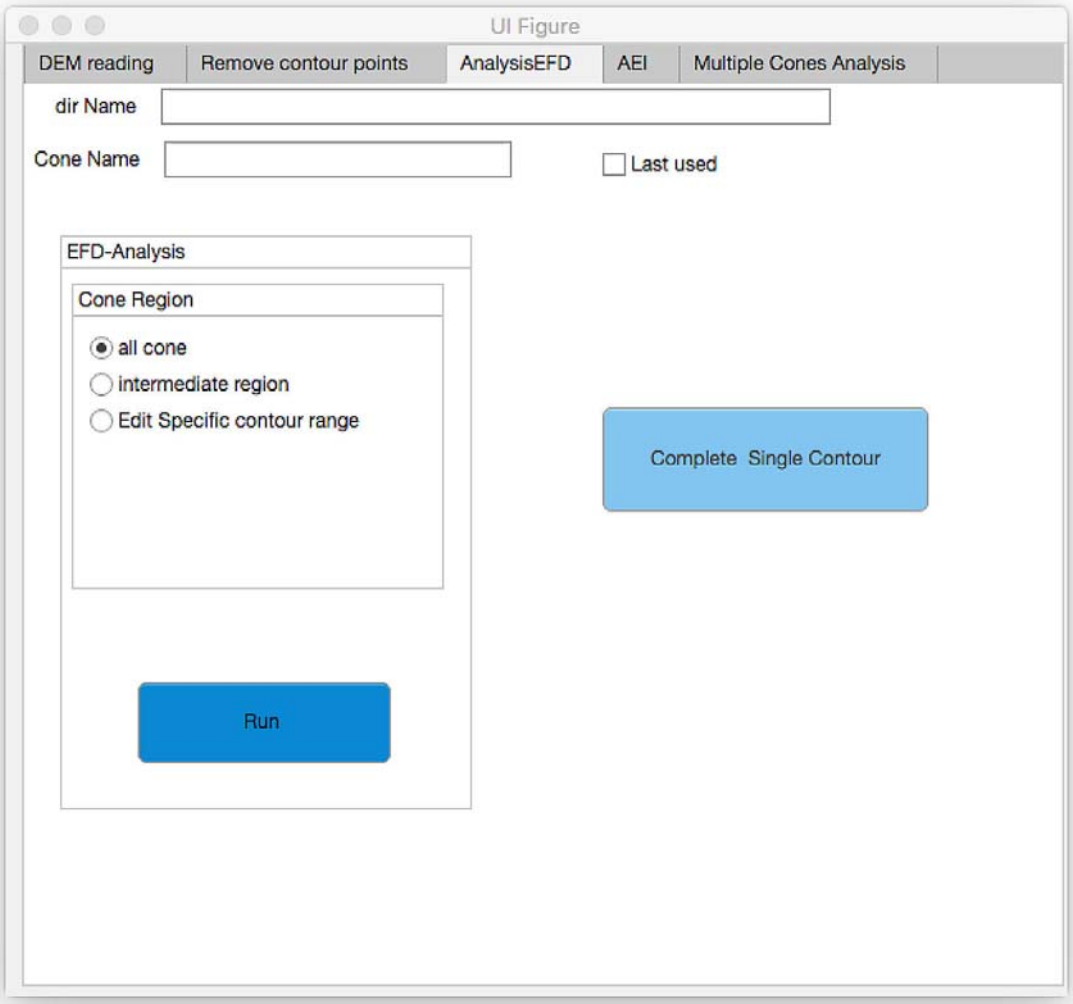

Fig. 12. The EFD Analysis Tab.

Input parameters are: Directory name and Cone Name (which should be the same as that used in the first Tab). If the analysis is performed for one cone sequentially, the check box “last used” can be selected Fig. 12.

C.1 Cone region selection

The user has to select the contours to be analyzed: all cone, intermediate region, or any specific region.

C.2 Run button (mandatory).

This button runs ’análisis_curvasN2B.m’ file for all contours in the selected region. The analysis is performed in three steps:

1) Identifies if a Contour is closed, if not, it marks the points delimiting the "uncompleted regions" (*iP1*, *iP2*).

2) Completes the "uncompleted" contours with an ellipse centered in the contour’s centroid, with its major axis in a given direction and passing through delimiting points (*iP1*, *iP2*). See

Table 1
Principal parameters and definitions.

K	Denotes the number of Elliptical Fourier Descriptors (EFD) used to reconstruct a contour. It is the equivalent of a Fourier harmonic.
Original contour	The contour extracted from the DEM being analysed.
Reference contour	A smooth contour, reconstructed with the lowest k harmonic having its best-fitted ellipse the same "flattening" value (1-ma/Ma) as the best-fitted ellipse to the original contour. Ma: major axis; ma: minor axis.
$< S1_k >$	Similarity function. The average distance between the original contour and the contour reconstructed using up to k EFD.
D_k	Erosion Spectrum. Is the net contribution of each EFD harmonic ***k*** to the full reconstruction of the original contour.
D	Erosion index. The average value of the Erosion Spectrum, from the harmonic k of the reference contour to the highest possible (Nyquist) k which is determined by the sampling rate of a contour line.
AEI	Average Erosion Index. The average of the Erosion index of the selected contours of a scoria cone.
Hco_1, Hco_2	Vertical distance between the base of the cone and the crater rim, for each cross-section of an elevation profile.
θ_1, θ_2	Angle of inclination of each of the flanks of the cone for an elevation profile.
Wco	Width (horizontal) of the base of the cone, from an elevation profile.
Wcr	Width (horizontal) of the rim of the crater, from an elevation profile.
Dcr	Vertical distance between the deepest point within the crater and the line crossing the outline of the crater rim, from an elevation profile.
θ_{sus}	Angle of inclination of the terrain underlying the base of the cone, for an elevation profile.
θ_{cr}	Angle of inclination of the line crossing the points delimiting the crater rim outline for an elevation profile.
Hco_{1incl}, Hco_{2incl}	Perpendicular distances between each of the two points delimiting the crater rim outline and the line joining the two points delimiting the base of the cone outline, for an elevation profile.
Wco_{incl}	Width of the base of the cone outline for an elevation profile, considering the terrain inclination θ_{sus}
θ_{1incl}, θ_{2incl}	Angles of inclination of each of the flanks of the cone for an elevation profile, with respect to the inclined base of the cone Wco_{incl}.
Wcr_{incl}	Width of the base of the cone outline for an elevation profile, considering the terrain inclination θ_{sus}
Dcr_{incl}	Perpendicular distances between the deepest point within the crater and the line crossing the two points delimiting the crater rim outline for an elevation profile.
Z_1, Z_2	The trigonometric tangents of the angles θ_1, θ_2 for an elevation profile.
Ar_1, Ar_2	The ratios Hco_1/Wco and Hco_2/Wco for an elevation profile.
f	The ratio Wcr/Wco for an elevation profile.
Z_{1incl}, Z_{2incl}	The trigonometric tangents of the angles θ_{1incl}, θ_{2incl} for an elevation profile.
Ar_{1incl}, Ar_{2incl}	The ratios Hco_{1incl}/Wco_{incl} and Hco_{2incl}/Wco_{incl} for an elevation profile.
f_{incl}	The ratio Wcr_{incl}/Wco_{incl} for an elevation profile.

Zarazúa-Carbajal and De la Cruz Reyna [24]. Each completed contour is saved in a file with name: 'SalidaComp_ID.dat'.

3) Once the contour is completed, estimates the Elliptical Fourier Descriptors of the contour (using the algorithm of Kuhl and Giardina [13] programmed by David Thomas [19]).

This step creates several files, listed in supplementary Table 1.

Sometimes the automatic process to complete the contours may fail or requires improvement, as shown in Fig. 13. In such cases, the 'Complete Single Contour' option can be used.

C.3 Complete Single Contour (optional)

When pressed, this button calls another App called CompContours.mlapp, which allows to manually modify the parameters: Major axis 's angle of inclination (*Phi*) measured with respect to the horizontal axis and contour centroid, aiming to find a better elliptical transect passing through points *iP1* and *iP2* to close the contour. It also allows to remove points of the contours or edit the location of points *iP1* and *iP2* (Fig. 14).

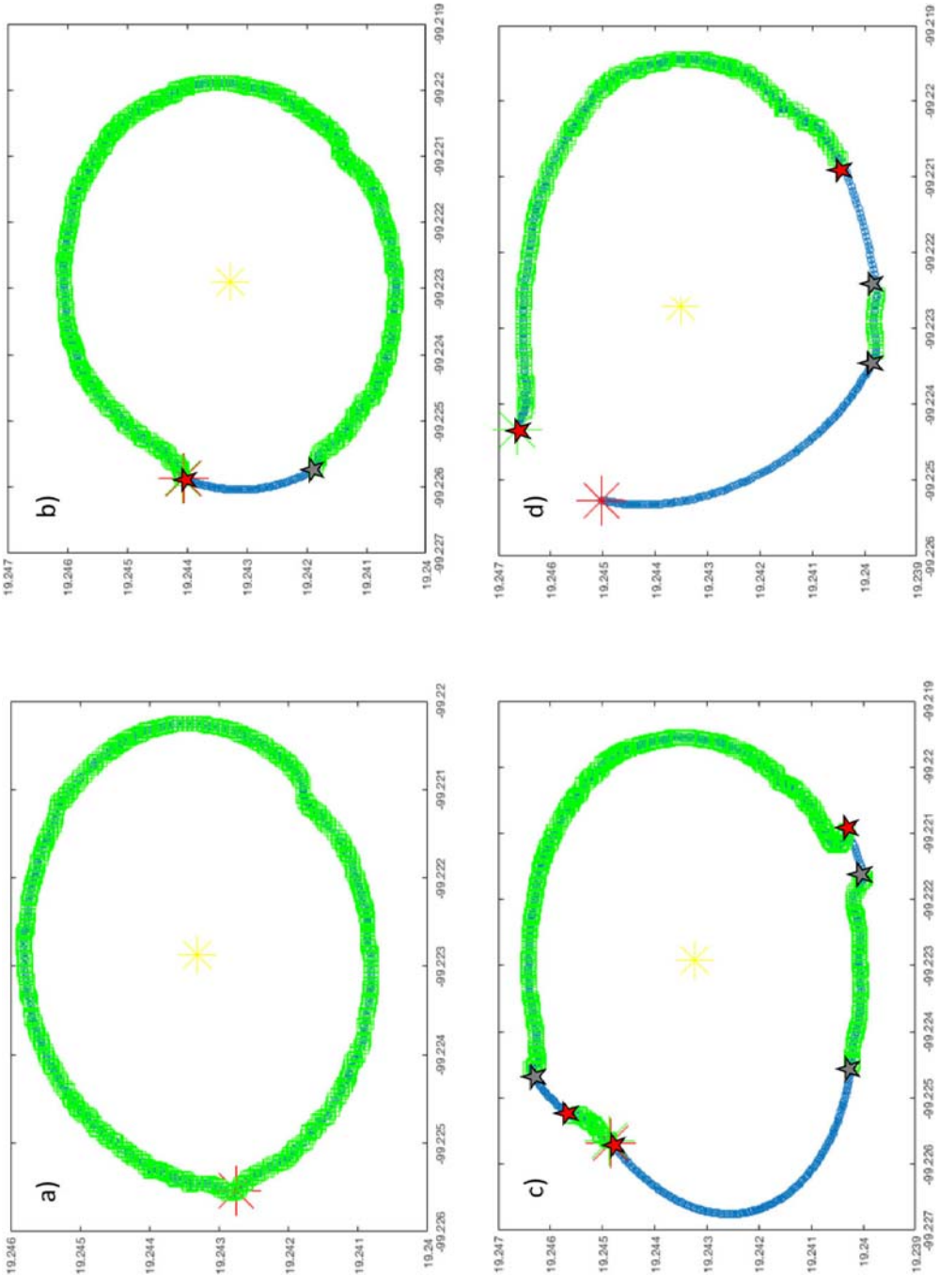

Fig. 13. a) contour not requiring competition. b) One-sector completed contour c) Three- sectors completed contour. Example of completion needing improvement. d) unsuccessful completion process in one of the sectors. Green squares represent points from the original contour. Blue sectors represent completed regions. Gray and red stars represent the first and second limits of the completed sectors respectively (*iP1* and *iP2*).

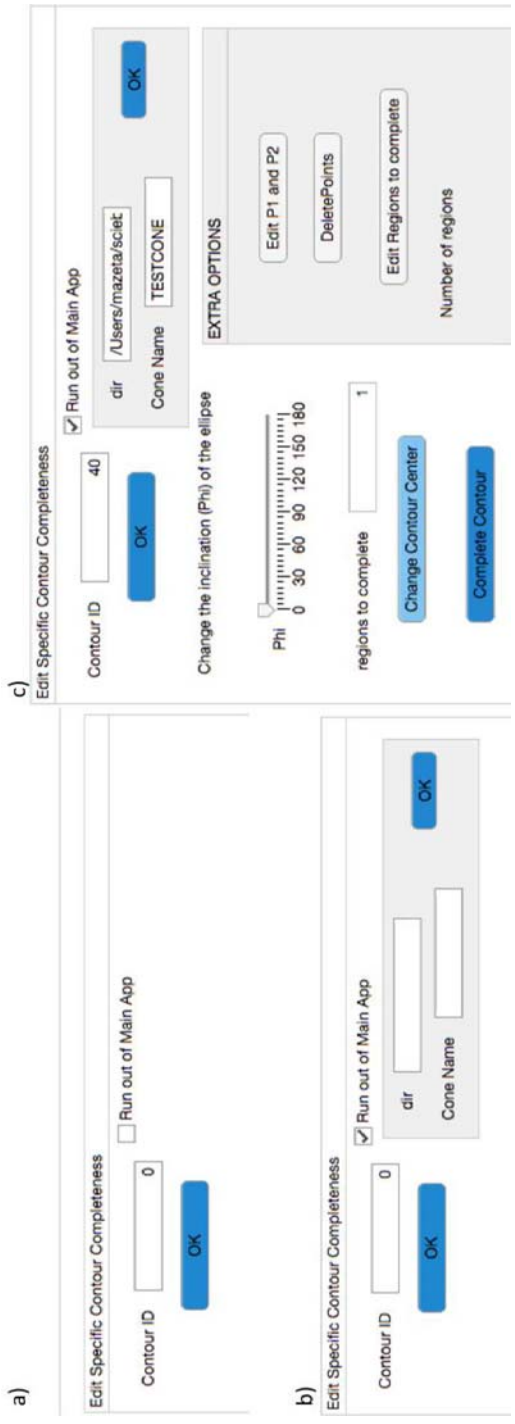

Fig. 14. The Single contour completion app. a) First b) After selection of "run out of Main App". C) After OK is clicked, all options are displayed.

Here the user needs to insert the contour ID number, and in case the app is running independently of the Main App, the directory and the cone name should be specified.

After the contour ID number is specified, press 'OK'. This displays a tab to control the inclination angle Phi of the major axis of the ellipse. The solution of the ellipse centered at the cone's center and passing through *iP1*, and *iP2* with the given *Phi* is displayed in a figure. The user selects the best solution and then clicks "Complete Contour". If no satisfactory solutions are found, then the user can change the centroid of the contour with the option "Change contour center".

C.3a Change Contour Center (optional)

This allows the user to manually change the center (centroid) of the contour. To do so, the desired centroid point should be clicked with the mouse, and then press the key 'ENTER' on the keyboard.

Then, after entering the *Phi* angle, a figure showing the completion ellipse option is displayed. Different completion ellipse options are displayed as the user rolls the "*Phi*" control.

C.3b Complete Contour (mandatory)

This button will proceed to complete the contour with the sector of the completion ellipses displayed in the figure. (see Fig. 15a and b). This step requires that the file 'analisisCurvasN2B.mat', generated in the EFDAnalysis Tab, exists.

If the contour contains more than one sector to complete, after clicking the "Complete contour" button, the user should repeat the selection of *Phi*, and a new figure displaying the solutions passing through the new sector limits *iP1* and *iP2* (Fig. 15c). Again, if no satisfactory solutions are found , the user can change the contour centroid, or the region limits *iP1* and *iP2* if needed. Then, when a satisfactory solution is met, click the button "Complete contour" again. This will display the completed contour as shown in the example from Fig. 15d.

The whole process should be repeated until the contour is fully completed. Therefore, the 'Complete Contour' button has to be clicked as many times as the number of regions to complete displayed in App. Only when this number is reached, the updated data related to that contour, including the EFD decomposition, is saved.

IMPORTANT: The main file '/analisisCurvasN2B.mat' is updated with edited data for selected contour. A backup file of the last run is automatically created. ('/analisisCurvasN2Bbakup.mat') . To recover the last version previous to edition, just change the name of the backup file to '/analisisCurvasN2B.mat'.

The following extra options are also included:

C.3c Edit region limits *iP1* and *iP2* (optional)

This option allows modifying the reference points *iP1* and *iP2*. After clicked, the user must select with a mouse click the points that will be used as *iP1* and *iP2* (in that order) and then press the key "ENTER". As a guide, small legends '1' and '2' are displayed in the figure to show which side should be clicked first.

C.3d. Edit number of regions (optional)

This option allows modifying the number of regions to complete. Click on the "Edit number of regions" button located inside the "OTHER OPTIONS" panel. This will display an editable field and an "OK" button. Insert the desired number of regions in the edit field and then press "OK".

The current figure will become editable. Proceed to click with the mouse in the points delimiting each of the regions. (2 points per region required) in the following order:

1 If the region limits are the first and last points of the contour, select first the last point and then the first point.
2 Otherwise, select the points in the opposite direction of the point-id increment. As shown in Fig. 16.

C.3e Delete Points

This option allows deleting points from the selected contour.

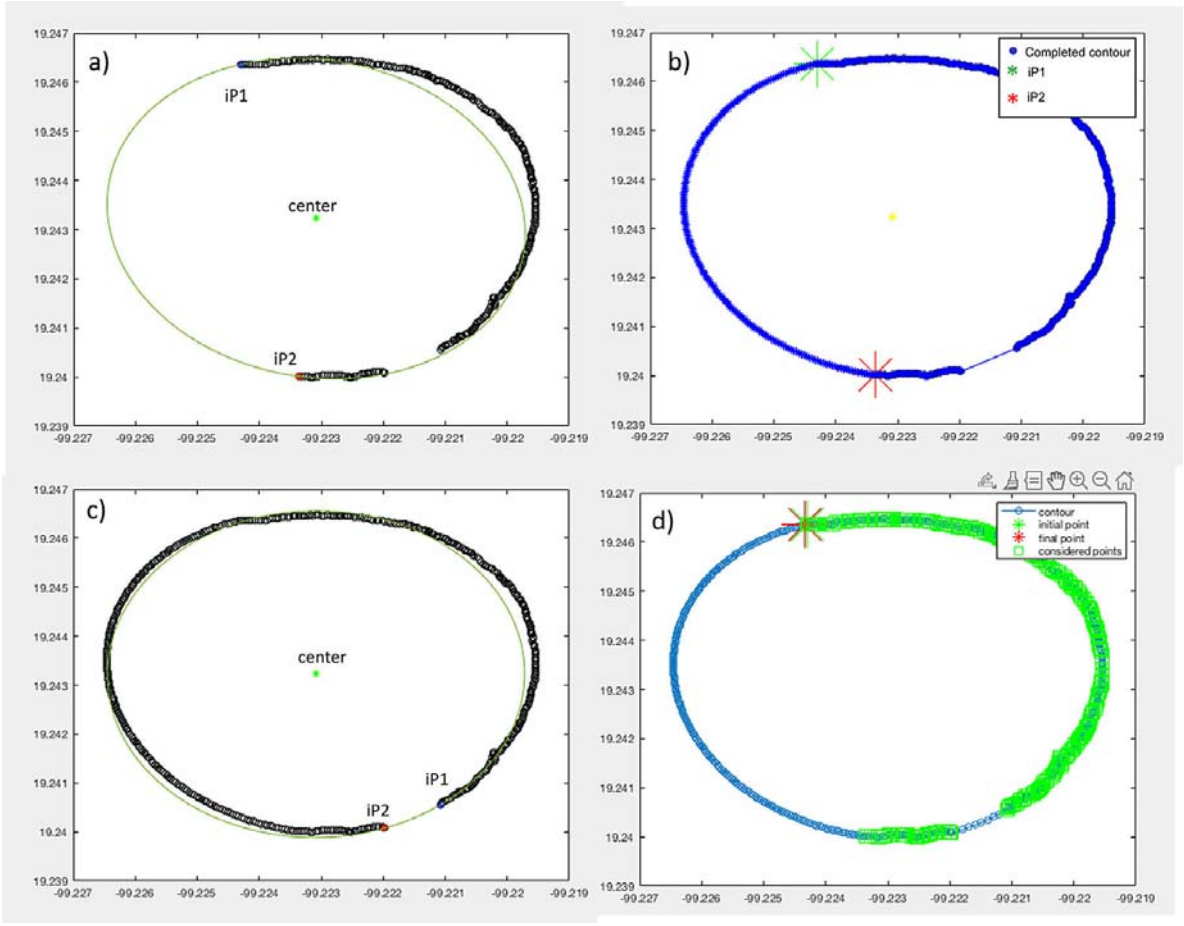

Fig. 15. Example of the single contour completion app applied on a contour with two open sectors to be completed. a) Completion of the first sector of a contour. Contour points are shown in black. The thin line represents the selected best-fitted ellipse with a specified center and major axis inclination *Phi* that crosses points *iP1* and *iP2*. b) The same contour as in a) after the first sector was completed with a sector of the selected ellipse. c) Completion of the second sector of the contour. The contour points are shown in black. The thin line represents the selected best-fitted ellipse with a specified center and major axis inclination *Phi* that crosses points *iP1* and *iP2*. d) Result after full completion of the contour. Original points are marked in green. Blue points show completed regions. The EFD analysis requires the completed ellipse. However, the *AEI* calculation only uses information from the green sectors.

When clicked, a plot of the editable contour will be displayed, the user is required to select with the “brush” the points to remove. After selection, the user must confirm the selection.

IMPORTANT: This does not overwrite 'ContourMod.dat', instead it creates 'ContourMod2.dat' which has priority over the other files.

As a second step, it is required that the user adds the number of regions to edit and their delimiting points, in the same way as required by the "Edit number of regions" option.

D. AEI TAB

This part of the analysis computes first the Similarity function and then the *AEI*. It requires the directory name and Cone name as input parameters (Fig. 17). Files created with previous steps (A-C) should exist, otherwise, an error will occur.

D.1 Similarity function Panel

To compute the Similarity function, the user has to select first the vertical region of the cone to analyze: all cone, intermediate region, or any specific contour range. The selected region must be the same or contained within the region selected in step C. Then click on “Run”.

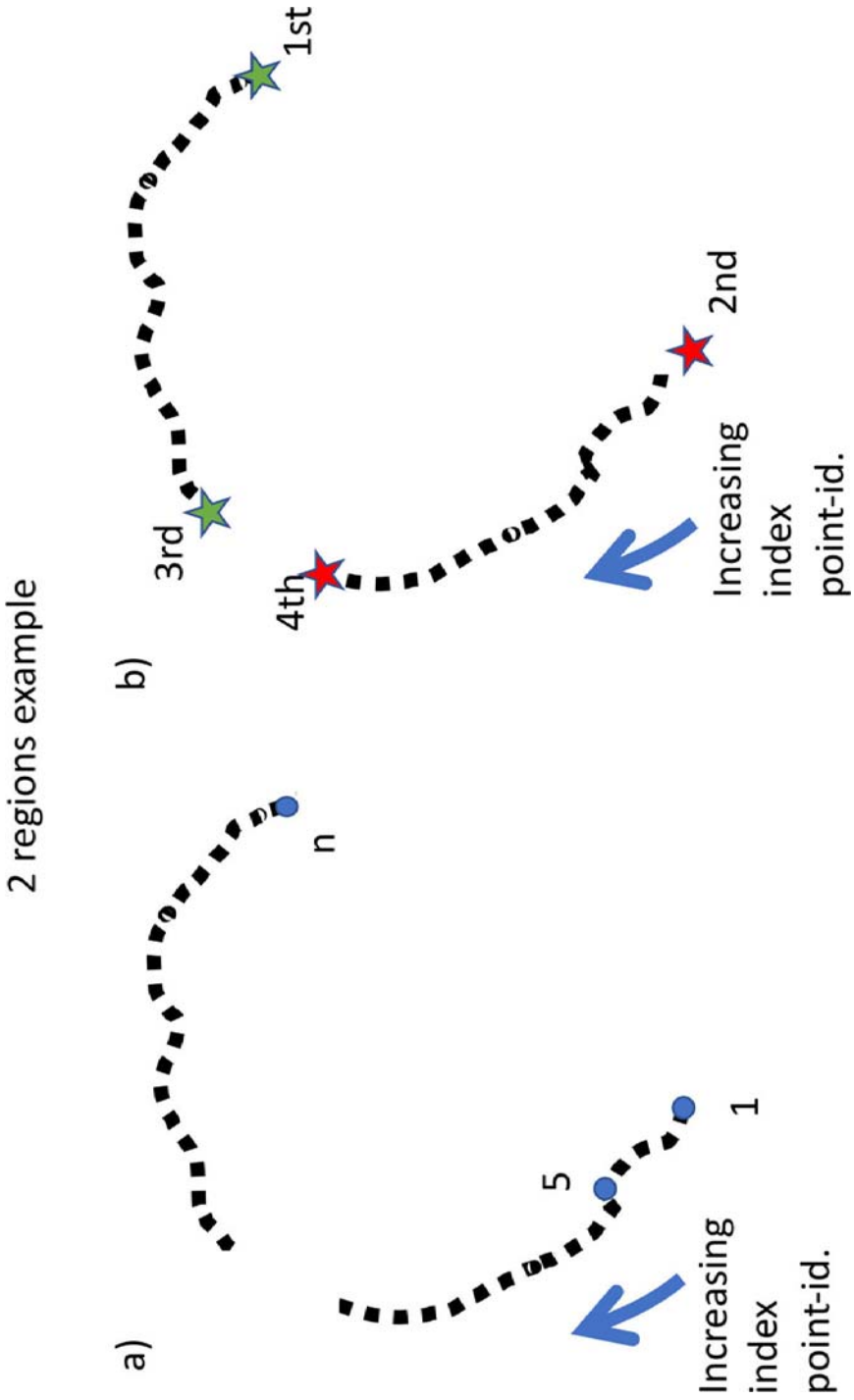

Fig. 16. Example of how limit points for edited regions should be selected.

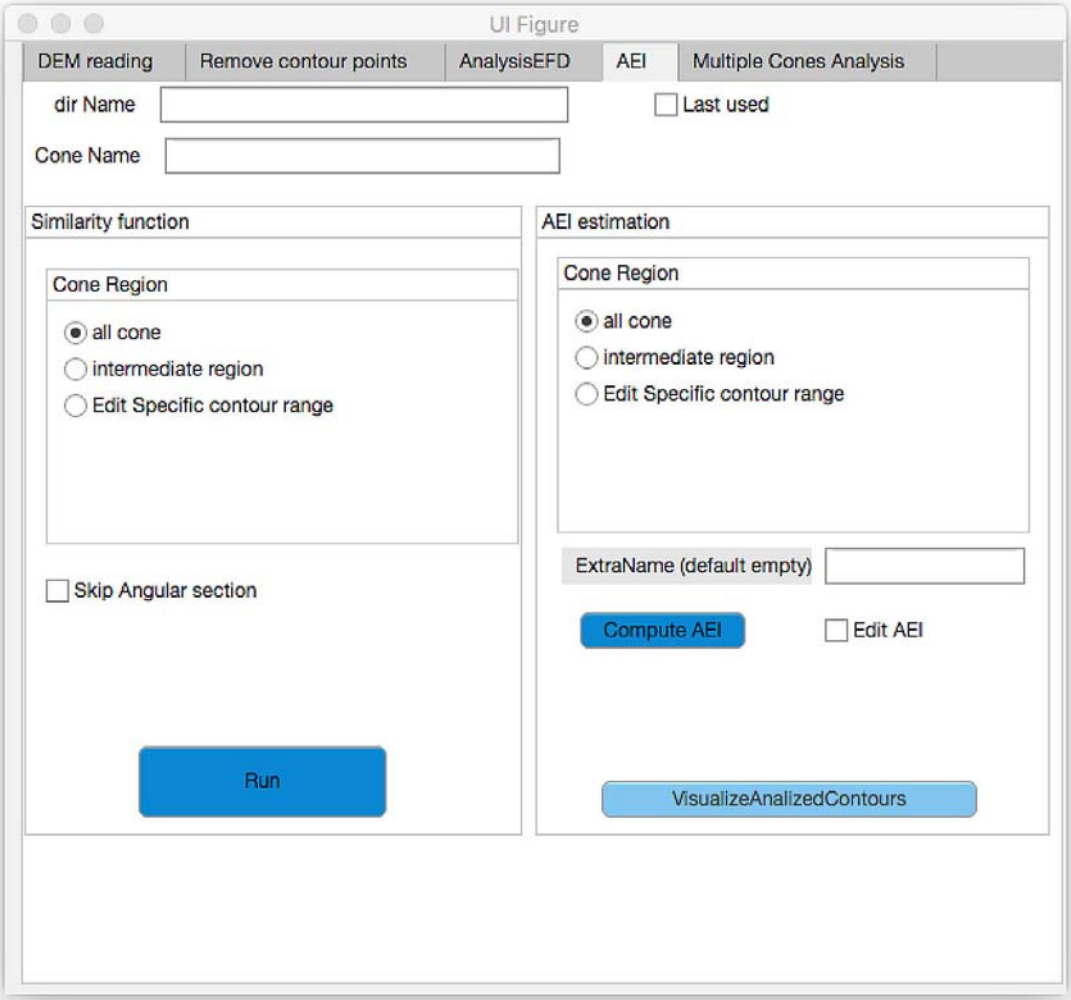

Fig. 17. The Average Erosion Index Tab.

For each contour, a control graph showing the points of the contour that are considered for the Similarity function calculation (considered points) is created and saved. Also, the mat files containing the Similarity functions for each contour are saved. Fig. 18 shows an example of the considered points in a contour.

The "skip angular section" is an optional feature allowing to omit points of an angular range of the contour, from the calculations of the Similarity function. The angle range must be in degrees. The user can optionally add another identification name to save the files created after the elimination of the selected angular region.

D.2 *AEI* computation

This step computes the Average Erosion Index of the contours comprising the selected region of the landform. This requires the existence of files created in previous steps (A to D.1).

After the selection of the analysis region in the *AEI* estimation-Cone Region Panel (Fig. 17), the user has the option to include an extra identifier name that will be included in the output file's

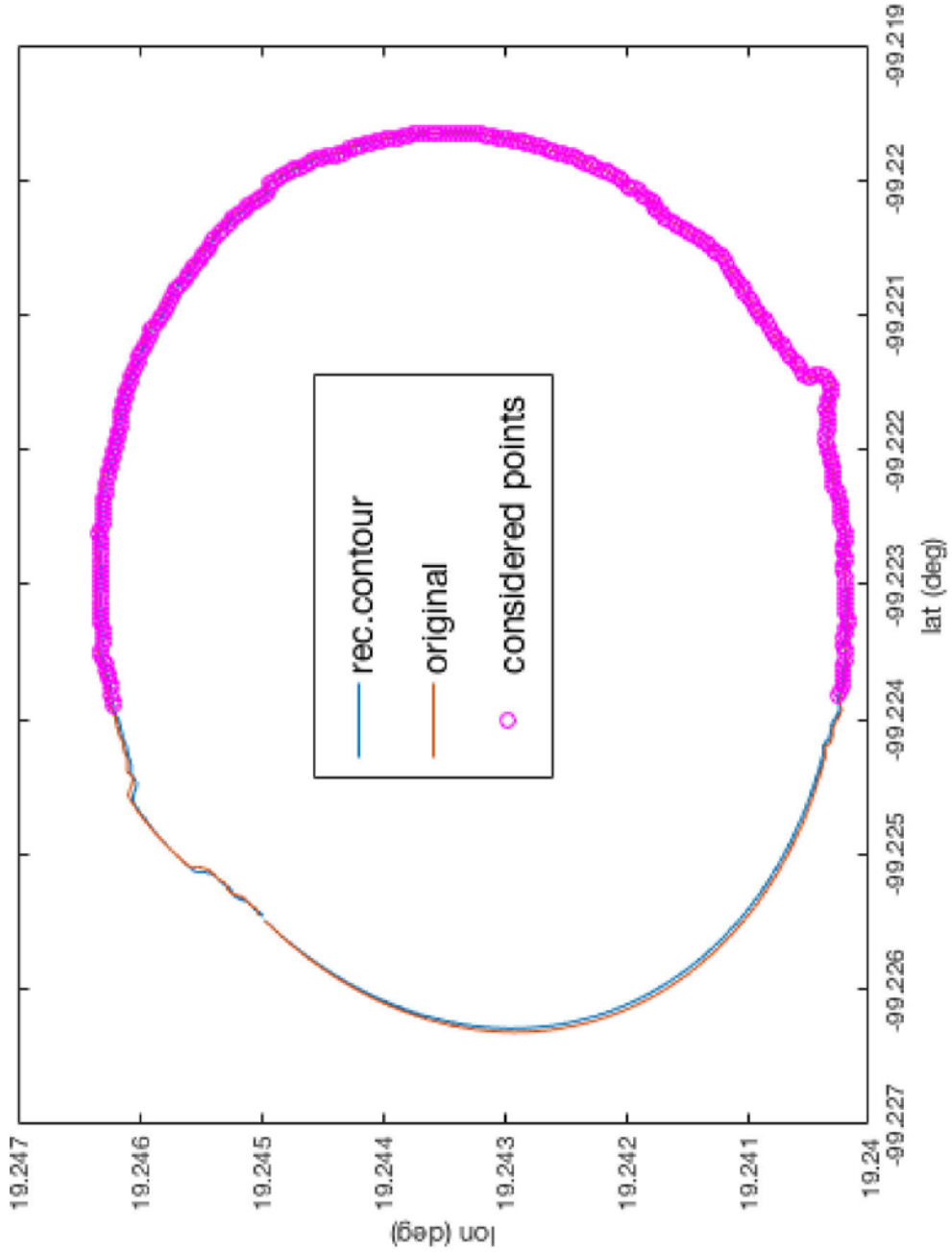

Fig. 18. Example of a control graph displaying a comparison between the closed contours rendered after a completion process (original completed) and the contour obtained using an inverse EFD transform, considering all harmonics up to the Nyquist harmonic (rec. contour), and in pink circles, the points belonging to the original contour selected for analysis. The expected output is that the EFD reconstructed contour and the original completed contour should coincide.

name. To proceed with the analysis, click on the “Compute AEI” button. This will perform a series of calculations: First, for each contour, within the selected region, the reference contour is identified, based on the characteristics of the best-fitted ellipses [5] to each of the reconstructed contours using up to *k* harmonics of the EFD [24]. For each contour, a ’.fig’ file showing the Flattening function of the best-fitted ellipses as a function of *k* is saved. Secondly, using the Similarity functions of each contour, the corresponding Erosion Spectrum *Dk* is computed. A ’.fig’ file containing the Erosion Spectrum graph is saved. Thirdly, for each contour, the Erosion Index *D* is computed. Finally, the *AEI* of the selected region is calculated, as the weighted average of the erosion index values of all contours within the selected region. A ’.mat’ and ’.fig’ files containing the *D* value for each ID contour and the obtained *AEI* are created and saved. Fig. 19 shows an example of the figures, created for the estimation of the erosion index of a single contour. Fig. 20 shows an example of the *AEI* estimation for a group of contours.

Results are summarized in sheet number 4 from the file ‘Morfometricos.xls’.

Outliers identification

When the number of contours analyzed is greater than 30, a histogram of the *D* value per contour is created. The data histogram is then fitted to a normal distribution. Outliers are those points with a *D* value greater or lower than the mean value of the normal distribution +/- 2 standard deviations. The *D* values, along with contours completeness information can help to identify possible reasons leading to an outlier *D* value. If needed, corrections can be performed using the functions in this App, such as the “complete single contours” or “remove points”. The histograms are saved to a ’.fig’ file.

D.2a Edit *AEI* (optional)

This option is useful when the *AEI* has already been computed for each contour and the user wishes to obtain an additional *AEI* average on another region of the cone, or after contours with outlier *D* values are identified.

Click the ’Edit AEI’ box. Then, if desired, insert an identification name in the “extra name” field. If no “extra name” is given, the output files will overwrite the existent files. Finally, click the ’Edit AEI’ button. This will launch a window containing a graph showing *D* for that contour ID. Right-click with the mouse over the points to be removed, and then press ENTER. A new figure will be displayed and saved, as well as a ’.mat’ file containing the updated *AEI* value (Fig. 21).

The edited results are saved in an extra sheet from the file ‘Morfometricos.xls’.

D.2b Visualize Analyzed Contours (optional)

When clicked, this button creates a plot highlighting the contours, and contour sectors that were analyzed. This figure is automatically saved in ’.fig’ format Fig. 22.

E. Multiple Cones Analysis Tab

This tab is intended to speed up the analysis if multiple cones should be analyzed. It is required that the files created with the DEM Tab exist, and that point removal has been already implemented for each cone when needed Fig. 23.

Input Parameters: Name of the directory in which the required files are located (same as used in the previous tabs), name of file ’.txt’ containing the list of names of the cones to be analyzed. These names should be the same used as “Cone name” in the DEM reading tab. The .txt file should be placed in directory”.

E.1 LOAD BUTTON

Loads a list of names from the given ’.txt’ file. All names should be written without spaces in a column.

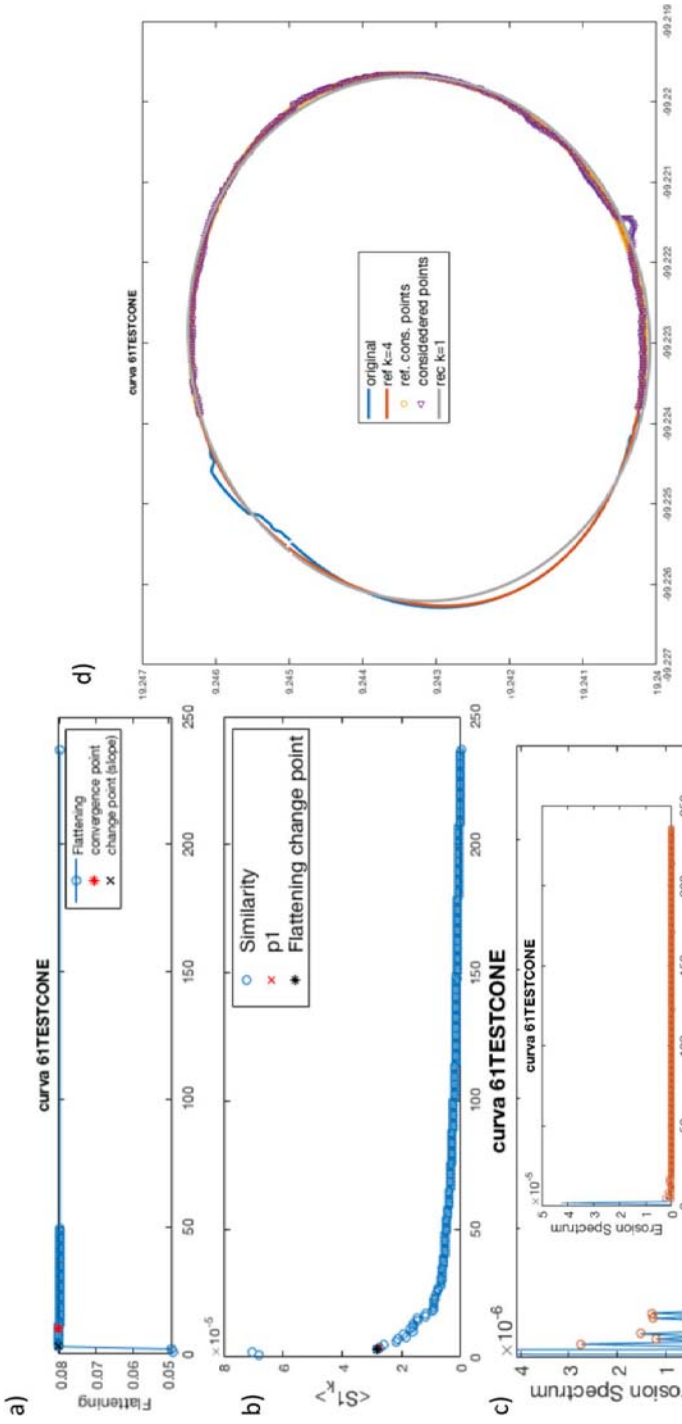

Fig. 19. Example of the calculations needed to compute the Erosion index D of the contour in Fig. 18. a) Flattening function with a well-defined change point. b) Similarity function showing reference harmonic (p1). c) Erosion spectrum of the region comprising harmonics greater than the reference harmonic. Inset shows the full Erosion Spectrum. d) Plot showing the identified reference contour, the reconstructed contour using just first harmonic (k=1) and the points of the contour considered to compute the Similarity function and Erosion Spectrum.

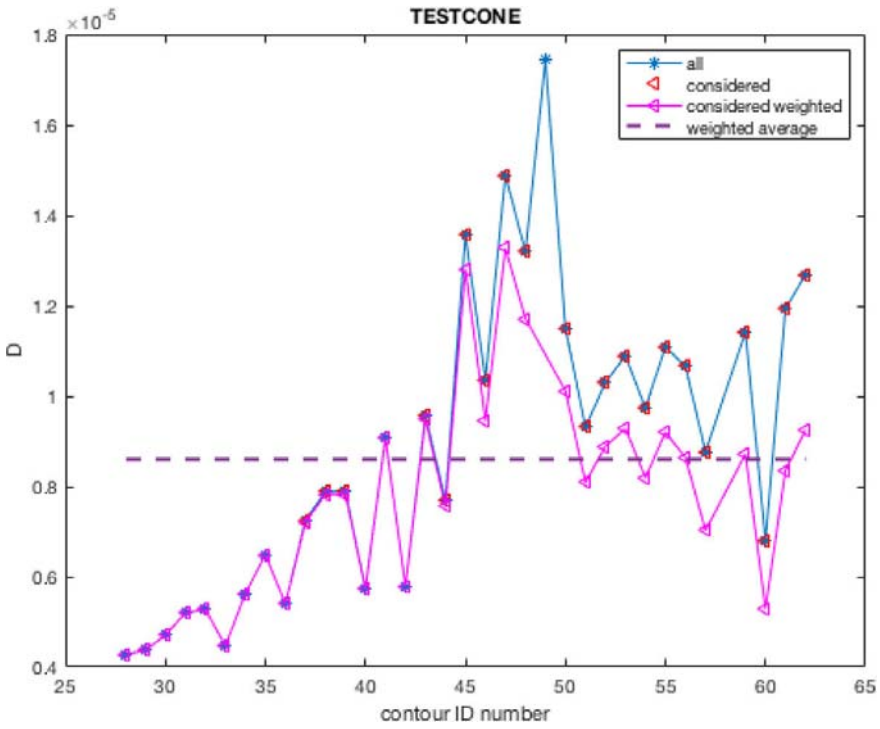

Fig. 20. Erosion index (D) for each contour in the analyzed region. Blue: D value for all analyzed contours, red: D value for contours selected for *AEI* estimation, (i.e. excluding contours with outlier D values). Pink: weighted D values of selected contours. Here, the D values are multiplied by a weighting factor between 0 and 1 depending on the number of "completed" points in a contour. So contours with no completed sectors have weight 1, and a maximum contribution to the AEI.

To run this option, the files created with the DEM reading tab should exist. And all contours should be ready for analysis, that is, unwanted regions should have been already removed.

E.2 Extra Identifiers Panel (optional)

If the files to be analyzed have or require "extra names", they can be included here. Notice that these extra names will be added to all cone names in the list.

- Extra Name: for files generated with AnalysisEFD.
- Extra Name B: for files generated in the Similarity function estimation.
- Extra Name C: for files generated in the *AEI* estimation.

E.3 Cone Region Panel

The user selects the vertical region of the cone for which the selected analysis will be performed.

E.4 RUN BUTTON

Executes each of the selected functions (Analysis EFD, Similarity function, AEI estimation, Visualize Analyzed Contour, or Final List) for the selected cone region.

Final List, reads results obtained with the *AEI* estimation step and creates a list with cone name, latitude, longitude, the resulting *AEI* and its standard deviation. This list is saved in the given directory, both in '.dat' and '.mat' files with name: "AnalisisAEIList".

Method validation

The methods described above have been applied to DEM data in two research articles: Zarazúa-Carbajal and De la Cruz-Reyna [24] and Zarazúa-Carbajal and De la Cruz-Reyna [25]. In the former, we introduced the Average Erosion Index *AEI*, which is a new measure of the age-dependent degree

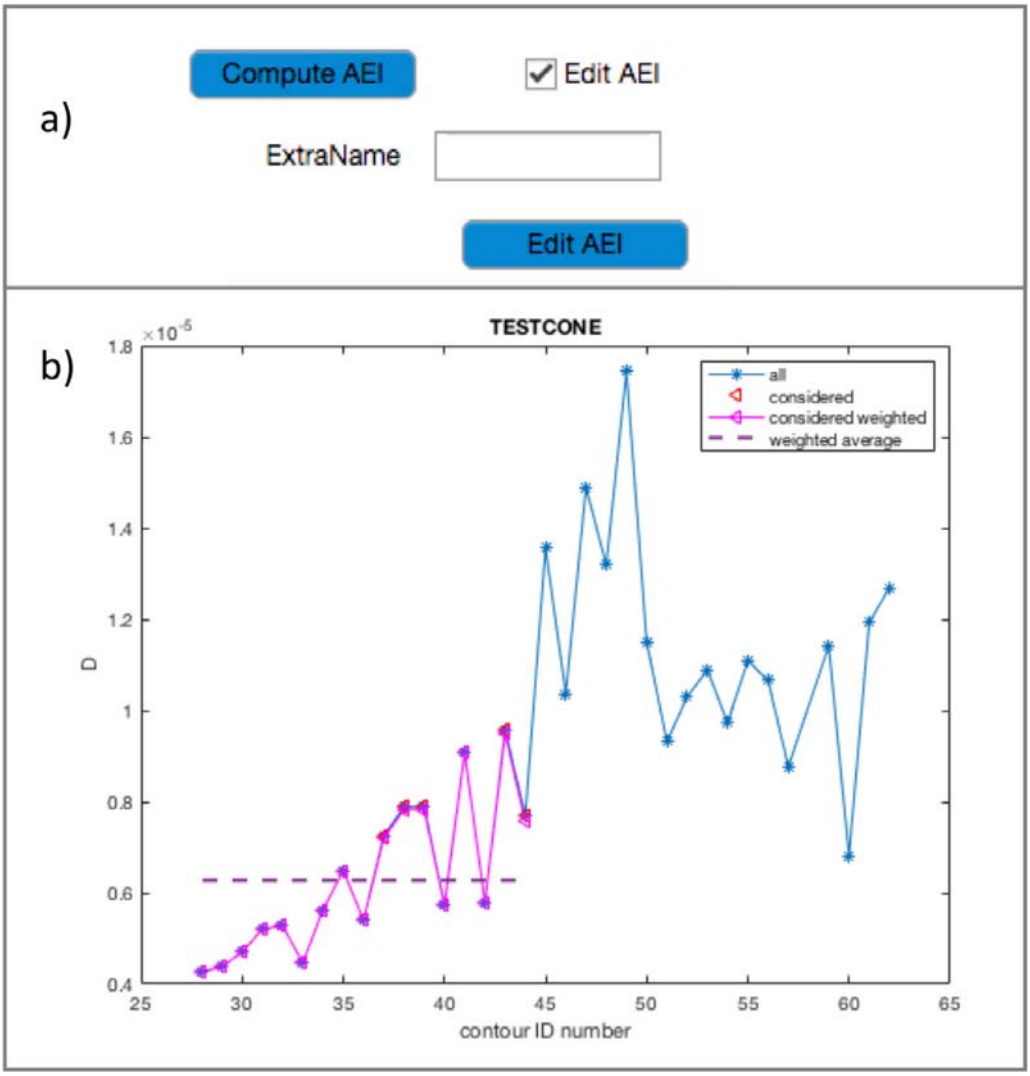

Fig. 21. a) When **Edit AEI** is selected, the user can introduce an Extra name for the file in which this will be saved (to avoid overwriting). b) Example of removing points from the example in Fig. 20.

of erosion in monogenetic volcanoes, requiring the assumptions that very young cones have smooth surfaces and that all cones within a region have been exposed to similar erosive conditions. Then, a novel morpho-chronometric relationship was established correlating published radiometric ages of scoria cones in the Sierra Chichinautzin volcanic field with *AEI* values calculated from two DEMs, a 5 m resolution airborne LIDAR DEM (INEGI, Mexico) and a 12 m resolution satellite radar mission (TanDEM DLR, Germany). This permitted to test the sensitivity of the methods to the DEM resolution, an analysis that rendered comparable results for both DEMs, opening the possibility to apply the methodology worldwide, in any volcanic field covered by satellite data with 12 m resolution or better.

In the second paper, we further discussed the effects of the DEM type and resolution on different morphometric parameters characterizing scoria cones of the Sierra Chichinautzin volcanic field, including the elevation profile analysis of their vertical cross-sections, and a more detailed analysis of the *AEI* level contour method. Both analyses were performed over a wider range of DEM resolutions, including the 5 m airborne LIDAR DEM (https://www.inegi.org.mx/), the 12 m TanDEM-X (TanDEM-X Science Serverdlr.de), and the 30-m ASTER GDEM-V3 [14]. We concluded that the morphometric characterizations of cones with volumes greater than 0.01km^3 render similar results with different DEM databases provided their resolutions are better than 12 m. Regarding the age dependence of

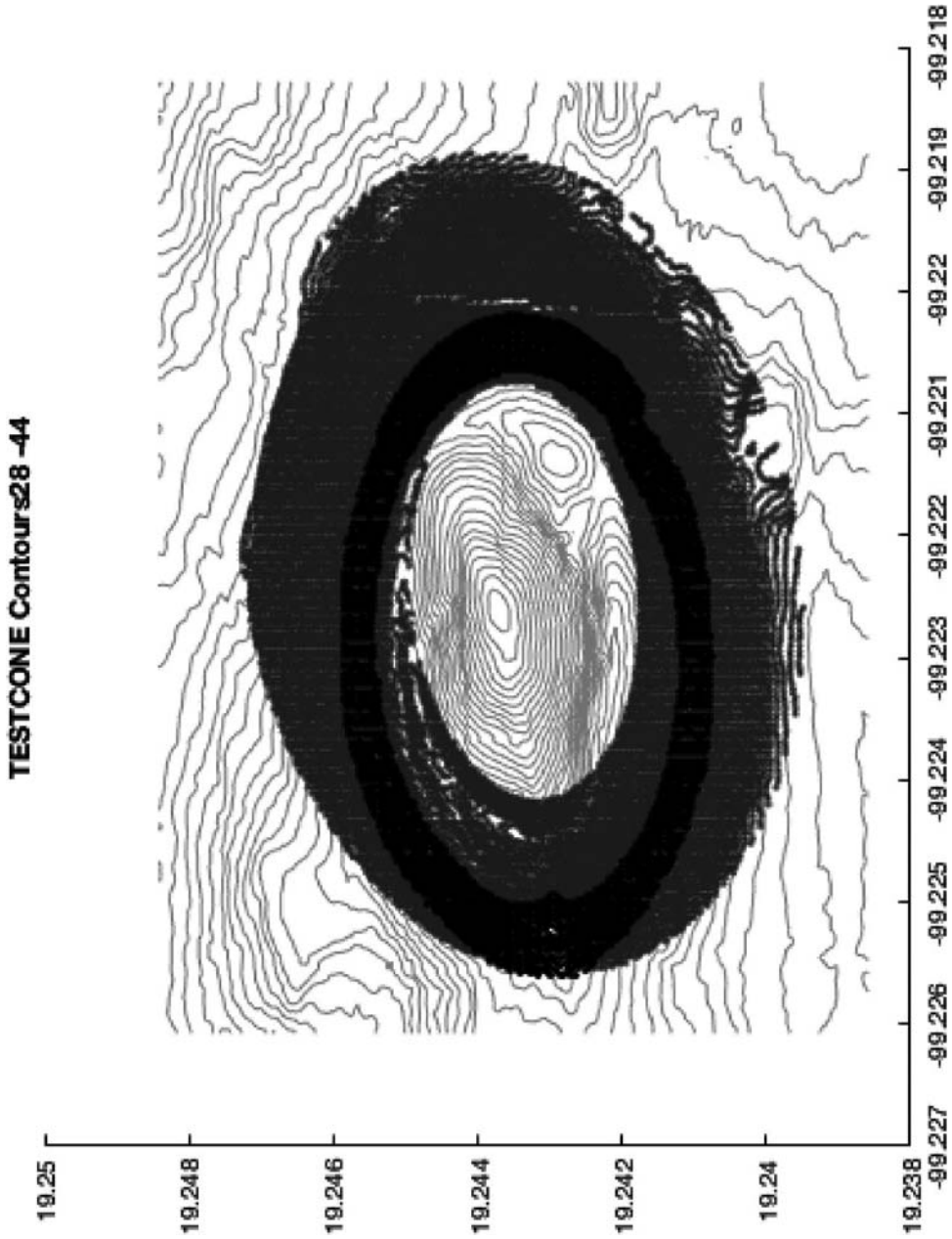

Fig. 22. Example of visualization of the contours from Fig. 22. Analyzed contours are shown in black. All contours of the volcanic cone are marked in dark gray.

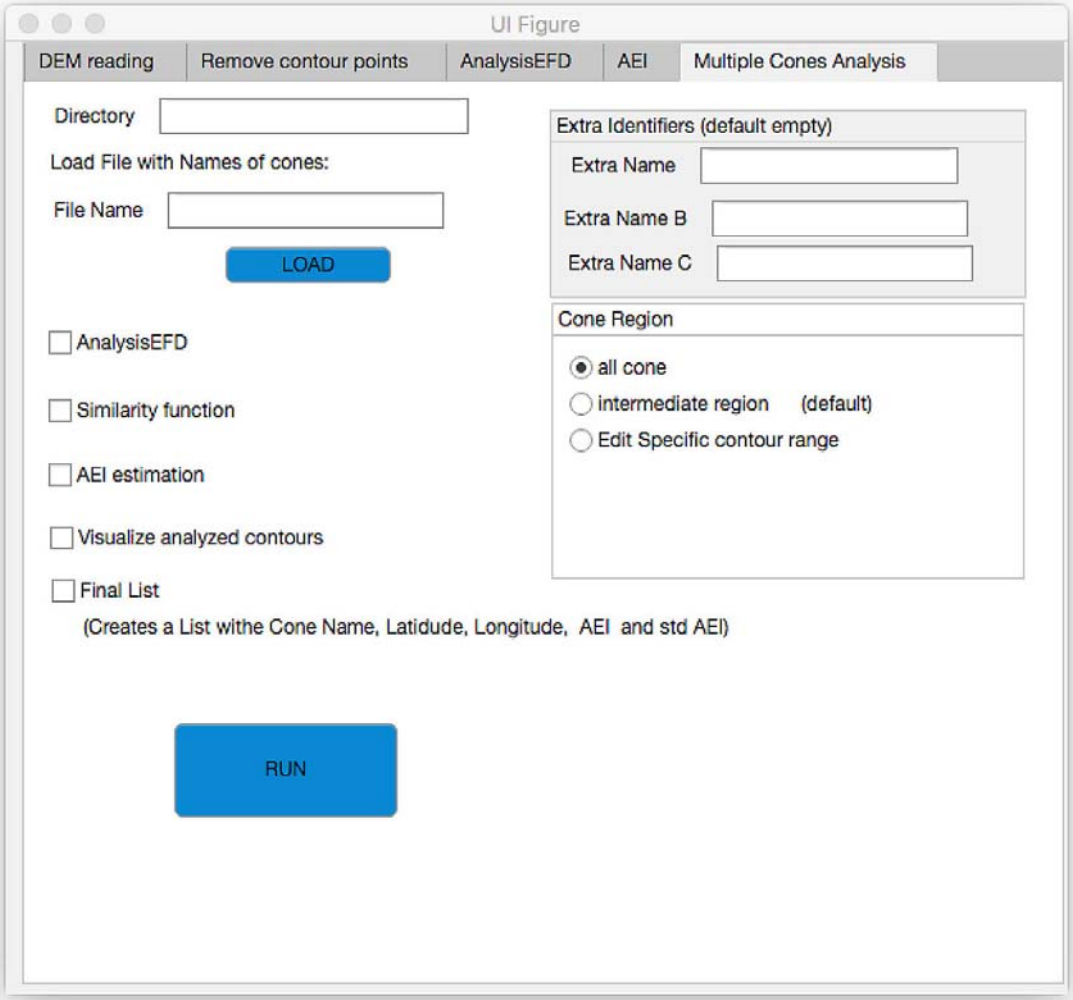

Fig. 23. The multiple cone analysis tab.

diverse scoria cone morphometric parameters, the *AEI* resulted to be a more sensitive age estimator than the aspect ratio of the vertical profiles. According to the results obtained from the SCMVF, while the *AEI* may be capable to resolve morpho-chronometric relative age differences of about 5 ka in cones in the age range 0-20 ka and about 15 ka in the range 20-230 ka, the Aspect ratio *Ar* may only resolve age differences of about 40 ka of cones up to 230 ka. It is important to emphasize that these results are statistical trends obtained from a limited number of scoria cones in a single monogenetic field [25]. We expect that as the number of cones in different volcanic fields analyzed with these methods increases, the age resolution and the ranges of applicability will become better defined.

Conclusions

In this work, we present a MATLAB App and the related scripts required to execute all the steps of a new method designed to appraise the age-dependent degree of erosion in landforms with closed level contours, particularly in monogenetic volcanic cones, using encompassing DEM databases over a wide range of resolutions and data types. In particular, this method may be used to estimate relative ages of scoria cones in extensive monogenetic volcanic fields, determining

functional relationships between the radiometric ages of some sampled volcanoes and the *Average Erosion Index*. This parameter provides a measure of the age-dependent degree of erosion calculated through the Elliptic Fourier Descriptors analysis of the undulations in the closed level contours of the volcanic cones. Additionally, the App can also calculate the cone dimensions and other commonly used morphometric parameters related to the vertical cross-sectional shape of a cone from the DEM database.

Acknowledgements

The authors are grateful to the Mexican Science Council (CONACYT) and the National Researchers Systems (SNI) for the research assistant support grant (EXP. AYTE. 15617) of MCZC, and to the DGAPA-PAPIIT- UNAM program (grant IN-109616) for partially financing this research, and very especially to the Tandem-X satellite (DEM_GEOL1097) from the German Aerospace Center (DLR) and to the Mexican National Institute of Geography and Statistics (INEGI) for providing the satellite and LIDAR DEMs

Declaration of Competing Interest

The authors declare that they have no known competing financial interests or personal relationships that could have appeared to influence the work reported in this paper.

Supplementary materials

Supplementary material associated with this article can be found, in the online version, at doi:10.1016/j.mex.2021.101454.

References

[1] K. Bemis, M. Ferencz, Morphometric analysis of scoria cones: the potential for inferring process from shape, Geol. Soc. Lond. Spec. Publ. 446 (2017) 17, doi:10.1144/SP446.9.
[2] K. Bloomfield, A late quaternary monogenetic volcano field in central Mexico, Geol. Rundschau 6 (1975) 476–497.
[3] J. D'Errico, Graphical Data Selection Tool, MATLAB Central File Exchange, 2020 https://www.mathworks.com/MATLABcentral/fileexchange/13857-graphical-data-selection-tool Retrieved December 15, 2020.
[4] M. Favalli, D. Karátson, F. Mazzarini, M.T. Pareschi, E. Boschi, Morphometry of scoria cones located on a volcano flank: a case study from Mt. Etna (Italy), based on high-resolution LiDAR data, J. Volcanol. Geotherm. Res. 186 (2009) 320–330, doi:10.1016/j.jvolgeores.2009.07.01.
[5] O. Gal, fit_ellipse, MATLAB Central File Exchange, 2020 https://www.mathworks.com/MATLABcentral/fileexchange/3215-fit_ellipse) Retrieved November 20, 2020.
[6] P. Grosse, B. van Wyk de Vries, P.A. Euillades, M. Kervyn, I.A. Petrinovic, Systematic morphometric characterization of volcanic edifices using digital elevation models, Geomorphology 136 (2012) 114–131, doi:10.1016/j.geomorph.2011.06.001.
[7] F. Guy, H.-T. Mackaye, A. Likius, P. Vignaud, M. Schmittbuhl, M. Brunet, Symphyseal shape variation in extant and fossil hominoids, and the symphysis of Australopithecus bahrelghazali, J. Hum. Evol. 55 (2008) 37–47.
[8] D.M. Hooper, M.F. Sheridan, Computer-simulation models of scoria cone degradation, J. Volcanol. Geotherm. Res. 83 (1998) 241–267.
[9] M. Inbar, M. Gilichinsky, I. Melekestsev, D. Melnikov, N. Zaretskaya, Morphometric and morphological development of Holocene cinder cones: a field and remote sensing study in the Tolbachik volcanic field, Kamchatka, J. Volcanol. Geotherm. Res. 201 (2011) 301–311, doi:10.1016/j.jvolgeores.2010.07.013.
[10] G. Kereszturi, G. Jordan, K. Németh, J. Dóniz-Páez, Syn-eruptive morphometric variability of monogenetic scoria cones, Bull. Volcanol. 74 (9) (2012) 2171–2185.
[11] M. Kervyn, G.G.J. Ernst, J.-C. Carracedo, P. Jacobs, Geomorphometric variability of "monogenetic" volcanic cones: evidence from Mauna Kea, Lanzarote and experimental cones, Geomorphology 136 (1) (2012) 59–75.
[12] G. Kereszturi, A. Geyer, J. Martí, K. Németh, F.J. Dóniz-Páez, Evaluation of morphometry-based dating of monogenetic volcanoes—a case study from Bandas del Sur, Tenerife (Canary Islands), Bull. Volcanol. 75 (7) (2013) 1–19.
[13] F. Kuhl, C.R. Giardina, Elliptic Fourier features of a closed contour, Comput. Graph. Image Process. 18 (1982) 236–258.
[14] NASA/METI/AIST/Japan Spacesystems, and U.S./Japan ASTER Science TeamASTER Global Digital Elevation Model V003, 2019 distributed by NASA EOSDIS Land Processes DAAC, doi:10.5067/ASTER/ASTGTM.003.
[15] A. Nieto-Torres, A.L. Martin Del Pozzo, Spatio-temporal hazard assessment of a monogenetic volcanic field, near México City, J. Volcanol. Geotherm. Res. 371 (2019) 46–58, doi:10.1016/j.jvolgeores.2019.01.006.
[16] S.C. Porter, Distribution, morphology, and size-frequency of cinder Cones on Mauna Kea Volcano, Hawaii, Geol. Soc. Am. Bull. 83 (1972) 3607–3612 https://doi.org/10.1130/0016-7606(1972)83[3607:DMASFO]2.0.CO;2.
[17] M. Schmittbuhl, B. Allenbach, J.M. Le Minor, A. Schaaf, Elliptical descriptors: some simplified morphometric parameters for the quantification of complex outlines, Math. Geol. 35 (7) (2003) 853–871.
[18] M.L.C. Soares, S.J. Mayo, R. Gribel, D. Kirkup, Elliptic Fourier Analysis of leaf out- lines in five species of Heteropsis (Araceae) from the Reserva Florestal Adolpho Ducke, Manaus, Amazonas, Brazil, Kew Bull 66 (2011) 1–8.

[19] D. Thomas, Elliptical Fourier Shape Descriptors, MATLAB Central File Exchange, 2020 (https://www.mathworks.com/MATLABcentral/fileexchange/12746-elliptical-fourier-shape-descriptors)Retrieved November 20, 2020.
[20] A. Tort, Elliptical Fourier functions as a morphological descriptor of the genus Stenosarina (Brachiopoda, Terebratulida, New Caledonia), Math. Geol. 35 (2003) 873–885, doi:10.1023/B:MATG.0000007784.18452.73.
[21] A. Tort, A. Finizola, The buried caldera of Misti volcano, Peru, revealed by combining a self-potential survey with elliptic Fourier function analysis of topography, J. Volcanol. Geotherm. Res. 141 (2005) 283–297, doi:10.1016/j. jvolgeores.2004.11.005.
[22] C.A. Wood, Morphometric evolution of cinder cones, J. Volcanol. Geotherm. Res. 7 (1980) 387–413.
[23] C.A. Wood, Morphometric analysis of cinder cone degradation, J. Volcanol. Geotherm. Res. 8 (1980) 137–160.
[24] M.C. Zarazúa-Carbajal, S. De la Cruz-Reyna, Morpho-chronology of monogenetic scoria cones from their level contour curves. Applications to the Chichinautzin monogenetic field, Central Mexico, J. Volcanol. Geotherm. Res. 407C (2020) 107093 https://doi.org/10.1016/j.jvolgeores.2020.107093.
[25] M.C. Zarazúa-Carbajal, S. De la Cruz-Reyna, Digital elevation model resolution: effects on the chronometry-oriented morphological analysis of scoria cones in the Sierra Chichinautzin, central Mexico, Geomorphology 389 (2021) 107842, doi:10.1016/j.geomorph.2021.107842.
[26] Michael Gilichinsky, Dmitry Melnikov, Ivan Melekestsev, Natasha Zaretskaya, Moshe Inbar, Morphometric measurements of cinder cones from digital elevation models of Tolbachik volcanic field, central Kamchatka, Canadian Journal of Remote Sensing 36 (4) (2010) 287–300.

CAPÍTULO 5

CONCLUSIONES

Los campos volcánicos monogenéticos representan una manifestación abundante del vulcanismo en el planeta Tierra. Su origen y evolución espacio-temporal aún plantean interrogantes cuyo entendimiento puede enriquecer la evaluación del peligro y riesgo asociados a este tipo de vulcanismo disperso, en el que no sólo la evolución temporal sino también la espacial son variables que deben considerarse

Los modelos digitales de elevación (MDE) de diferentes tipos proporcionan información precisa sobre la distribución espacial de los volcanes individuales en un campo volcánico, así como información sobre el estado actual de la morfología del volcán. Esto puede proporcionar información sobre su evolución temporal a través de estimaciones de fechas morfocronométricas cuando los MDE tienen la resolución suficiente para caracterizar con precisión las características morfológicas dependientes de la edad de conos monogenéticos.

Uno de los principales logros de este trabajo fue el desarrollo del parámetro AEI, con el cual ha sido posible cuantificar el estado relativo de erosión en conos de escoria, sin la necesidad de asumir que todos los conos tienen la misma morfología al momento de formarse. Como todo método, la estimación del AEI y la validez de su interpretación como medida relacionada con la edad relativa de un cono de escoria tiene limitantes. La aplicación del método depende tanto de las dimensiones del cono como de la resolución horizontal y la precisión vertical del MDE, así como de la información complementaria que se tenga del uso del suelo del cono de escoria en cuestión. Conos cuyas dimensiones sean menores a 0.01 km3, al ser analizados con un MDE con una resolución horizontal de más de 12 m, muy posiblemente carezcan de un muestreo suficiente para poder obtener curvas de elevación bien definidas y en consecuencia el AEI obtenido no pueda interpretarse para obtener una edad relativa dentro de un grupo de conos de

mayor dimensión. Algo similar sucede con conos en los que su superficie se utiliza para agricultura o minería, por lo que un *AEI* obtenido no puede ser interpretado para asignar una edad relativa en ese caso, ya que no sería posible argumentar que su morfología actual sea efecto únicamente de factores erosivos, a menos de que la región minada o dedicada a la agricultura sea solo una fracción (<70%) de la superficie total del cono y pueda ser excluida durante la obtención del *AEI*. Los resultados obtenidos al aplicar esta metodología a conos de escoria de la Sierra del Chichinautzin sugieren que el análisis de las curvas de contorno propuesto representa un método que ofrece importantes perspectivas para el fechamiento relativo y eventualmente absoluto de conos monogenéticos.

Adicionalmente, los resultados obtenidos de una comparación morfométrica completa de 19 conos de escoria pertenecientes al campo volcánico monogenético de la Sierra del Chichinautzin, utilizando dos MDEs de distintas resoluciones (5 m y 12 m de resolución horizontal) muestran que en ambos MDEs la caracterización morfométrica es equivalente e intercambiable, tanto en las dimensiones del cono y del cráter como en los parámetros adimensionales que describen su forma (pendiente, razón de aspecto, *AEI*, entre otros). El análisis realizado permitió incluso identificar que la resolución horizontal de 12 m define un límite para describir con precisión las dimensiones de conos de escoria de volúmenes mayores a 0.01 km^3 y resolver la morfología de sus cráteres, siendo la altura del cono, la profundidad del cráter y los parámetros derivados de ellas, los más sensibles a los cambios en la resolución del MDE.

Asimismo, fue posible identificar que para el caso del SCVF hay 3 parámetros morfométricos que dependen significativamente de la edad del cono en el rango de resoluciones mencionado anteriormente: la razón de aspecto *Ar*, la razón entre la profundidad del cráter y su diámetro *CI* (Grosse et al., 2020) y el nuevo *AEI* desarrollado en esta investigación (Tabla 1). Siendo las dos primeras medidas derivadas de la caracterización vertical y la última, resultado de la caracterización horizontal del cono.

Parámetro	Resolución horizontal de DEM	Relación obtenida con la Edad (ky) en rango 0-222 ka	R^2
AEI	12m	$0.48(AEI)^{0.42}$	0.99
		$0.58(AEI)^{0.38}$ **	0.94
	5m	$0.47(AEI)^{0.40}$	0.99
CI_{incl}	12m	$0.47CI_{incl}^{-0.41}$	0.94
	5m	$0.42CI_{incl}^{-0.37}$	0.85
Ar_{incl}	12m	-3.0E-04* Ari_{ncl}+0.15	0.93
	5m	-3.3E-04* Ari_{ncl}+0.15	0.95
F	12m	4.0E-03* fi_{ncl}+0.37	0.21
	5m	2.2.E-03* fi_{ncl}+0.38	0.04
Z_{incl}	12	-9.0E-04* Zi_{ncl}+0.48	0.69
	5m	-10E-04* Zi_{ncl}+0.55	0.68

Tabla 1. Parámetros morfométricos que varían significativamente en función de la Edad del cono, en el caso de conos de la Sierra del Chichinautzin fechados radiométricamente en el rango 0-220 ka (Zarazúa-Carbajal y De la Cruz Reyna, 2021). R2 representa el coeficiente de determinación. ** Relación válida solo para conos con edades menores a 1200 ka (Zarazúa-Carbajal y De la Cruz Reyna, 2020).

Los resultados encontrados sugieren que los parámetros obtenidos, tanto de la caracterización morfológica vertical, como de la horizontal de los conos contienen información sobre el estado erosivo del cono. Sin embargo, parámetros de caracterización vertical como la razón de aspecto y la pendiente de la superficie de los conos, ambos dependientes de la forma del cono en el momento de su formación son ambiguos si esa información se desconoce y los resultados obtenidos con ellos serán funciones de la forma original supuesta. Aun así, en el caso de la SCVF esos parámetros pueden diferenciar edades relativas en el orden de 40 mil años. En contraste, el AEI, que solamente supone ausencia de cárcavas en el estado inicial, así como el CI, que supone que en un cono muy erosionado se desvanece el cráter, pueden diferenciar edades relativas con una mayor precisión, del orden de 10-15 mil años. Llama la atención que el CI de tan buenos resultados, aún cuando la forma del cráter puede resultar muy alterada

durante distintas fases de la erupción, como reporta Wood en su artículo de 1980a. En ese contexto, el AEI es un parámetro menos sensible a la forma original del volcán.

Es importante enfatizar que las relaciones funcionales entre los parámetros morfométricos y edad radiométrica obtenidas en este trabajo de investigación (i.e. los valores de coeficientes y exponentes), no necesariamente son válidas para otros campos volcánicos con condiciones erosivas distintas, ya que se ha observado que la evolución post-eruptiva de la morfología de los conos de escoria depende de las condiciones climáticas de la región en la que se encuentren (Hooper y Sheridan,1998; Németh and Cronin, 2007; Kereszturi and Németh , 2012). Sin embargo, la metodología propuesta en este trabajo si puede ser utilizada para buscar las posibles relaciones funcionales morfocronométricas en otros campos volcánicos.

Una comparación directa entre los resultados de la variación de los parámetros morfométricos en función de la edad obtenidos para la SCVF y los publicados para otros campos volcánicos puede conducir a conclusiones sesgadas, ya que las distintas condiciones climáticas afectan las tasas de erosión y en consecuencia la tasa de variación del parámetro razón de aspecto en función de la edad radiométrica (Hooper y Sheridan,1998), sin embargo, en el caso de los campos volcánicos de San Francisco , Springville y Cima, con climas semi-áridos y árido, se observa que la razón de aspecto se mantiene con variaciones mínimas en periodos de millones de años (Hooper & Sheridan 1998, Dohrenwend et al., 1986) mientras que en el caso del campo volcánico Cima, en ese mismo rango de tiempo, la formacion de carcavas es más significativa (Dohrenwend et al., 1986) y más claramente perceptible en MDEs. Esto es una consecuencia de que la cantidad de masa que debe ser removilizada por factores erosivos es mucho mayor para modificar la razón de aspecto que para producir cárcavas.

En cambio, al realizar una comparación entre nuestros resultados y los obtenidos usando valores para la razón de aspecto y edades radiométricas publicados en estudios previos de la SCVF (Jaimes-Viera et al. 2018, Nieto-Torres y Martin del Pozzo, 2019) es posible observar una discrepancia en los valores estimados de la razón de aspecto y en su variación con respecto a la Edad (Figura 1). Esto podría ser debido a diferencias en la metodología utilizada para la estimación del diámetro de la base y la altura del cono,

que pueden alterar significativamente el valor de la razón de aspecto (Tabla 2). Sin embargo, en todos los casos la tasa de variación de la razón de aspecto en función de la edad radiométrica es menor o del orden de la incertidumbre promedio asociada a la estimación de dicho parámetro (~0.03). Adicionalmente los efectos de esta diferencia requerirían una comparación detallada entre los escenarios probables de la evolución espacio-temporal obtenida con las distintas aproximaciones, un trabajo que aún no hemos concluido y que esta fuera de los objetivos de esta investigación. Lo anterior ejemplifica la importancia de desarrollar parámetros alternativos para cuantificar la erosión, y el parámetro *AEI* propuesto en este trabajo, parece ser una alternativa prometedora.

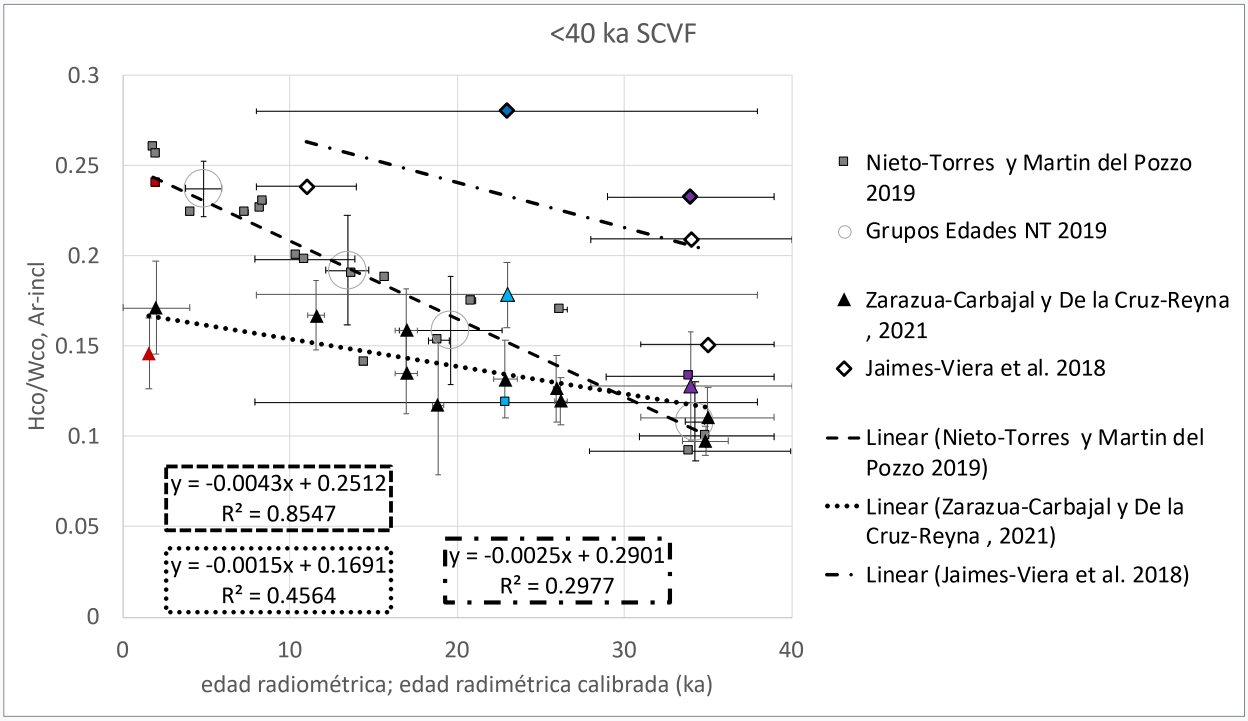

Figura 1: Razón de aspecto contra la edad radiométrica para conos menores a 40 ka del campo volcánico SCVF. Los símbolos rojos son los valores de la razón de aspecto obtenidos para el Xitle, los símbolos azul claro para el Aholo y los morados para el Cuautepel. Los valores de razón de aspecto de Zarazúa-Carbajal y De la Cruz-Reyna son los obtenidos mediante la aproximación del promedio de 8 perfiles de elevación corregidos por inclinación de terreno (Ari_{incl}), mientras que los de los otros trabajos son obtenidos mediante la aproximación 1 de la tabla 2.

	Aholo (~22 ky +/-11)			Xitle (~1.6 ky)			Cuautepel (~34 ky)		
Método aproximación H y Wco	H [m]	Wco [m]	H/Wco	H[m]	Wco [m]	H/Wco	H [m]	Wco [m]	H/Wco
A1	159	546 (56)	0.29 (0.03)	197	806 (110)	0.24 (0.03)	235	1058 (165)	0.22 (0.03)
A2.	106 (25)	546 (56)	0.19 (0.05)	116 (33)	806 (110)	0.14 (0.02)	121 (47)	1058 (165)	0.11 (0.05)
A3	132 (22)	616	0.21 (0.03)	137 (3)	871	0.16 (<0.01)	162 (31)	1170	0.14 (0.03)
*A3**	129 (4)	618	0.21 (<0.01)	137 (19)	873	0.16 (0.02)	164 (43)	1171	0.14 (0.03)
A4	108 (23)	551 (45)	0.19 (0.03)	121 (27)	801 (49)	0.15 (0.03)	138 (28)	1051 (114)	0.13 (0.02)
*A4**	106 (18)	552 (45)	0.19 (0.03)	119 (22)	803 (49)	0.15 (0.02)	139 (32)	1052 (113)	0.13 (0.02)

Tabla 2. Variación de razón de aspecto en función de estimación de altura de cono (H) y el diámetro de la base del cono (Wco). Métodos de aproximación: A1- *H: altura máxima cráter- altura mínima base del cono, Wco: Promedio eje mayor y eje menor base del cono; A2- H: Elevación promedio cráter- elevación promedio base, Wco: Promedio eje mayor y eje menor base; A3- A partir de 1 perfil de elevación a lo largo de eje mayor de base. H: altura promedio borde cráter. Wco: Diámetro base a lo largo de perfil; A4- considera el promedio de parámetros obtenidos en 8 perfiles de elevación.* Los valores entre paréntesis representan la desviación estándar del valor estimado. * indica que se corrigieron H y Wco por la inclinación del terreno. Las áreas sombreadas representan a las aproximaciones de la razón de aspecto empleadas en este trabajo *Ar y* $Ar_{incl.}$.

Finalmente, como producto de aplicación inmediata de este trabajo de investigación, se condensó la metodología propuesta en una App de Matlab de libre descarga, lo que abre la posibilidad de que pueda ser utilizada y probada en otros campos monogenéticos, con lo que se espera sea factible entender mejor sus alcances y limitaciones, así como contribuir al estudio del vulcanismo disperso.

CAPÍTULO 6

TRABAJO A FUTURO

La realización de esta investigación dio pie a que surgieran muchas preguntas. En un intento de encontrar respuestas hemos iniciado otros trabajos, algunos de ellos ya en proceso, otros apenas en planes.

- ¿Es el *AEI* un buen indicador de la edad en otros campos volcánicos?
- ¿Cómo cambia la relación funcional Edad vs *AEI* para distintas condiciones erosivas, ¿Sigue siendo una función potencial?,
- ¿Está el exponente de la función potencial directamente relacionado con la tasa erosiva?

Partiendo de que el proceso erosivo de conos de escoria se puede modelar físicamente como la combinación de un proceso advectivo y un proceso difusivo (Perron et al. [2008, 2009]; Mc Guire et al., 2010; Perron et al., 2011), la evolución de la morfología del cono va a depender del tipo de proceso erosivo dominante, es decir, si domina el proceso difusivo, los bordes del cráter se van redondeando, el cráter va reduciendo sus dimensiones, el cono va reduciendo su altura conforme aumenta el diámetro de su base, la aparición de cárcavas y canales es lenta. En cambio, si domina un proceso advectivo, la aparición de cárcavas y canales es más rápida, mientras que los bordes del cráter no se redondean. Entonces,

- ¿Puede obtenerse información sobre qué procesos han dominado en un campo volcánico a partir de las relaciones funcionales entre la edad y parámetros morfométricos de los conos?

Los modelos morfocronométricos aquí descritos suponen que todos lo conos están expuestos a las mismas condiciones erosivas, y por tanto que los materiales con los que esta formados los conos tienen las mismas características y estructura interna.

Sobre estas suposiciones recaen los principales cuestionamientos a los métodos morfocronométricos. En este contexto surgen otras preguntas:

- ¿Es posible cuantificar qué tanto y en qué escalas de tiempo afectan las diferencias en la composición y estructura interna de conos de escoria, mediante simulaciones numéricas de procesos erosivos basadas en modelos físicos de advección-difusión?
- ¿Será posible encontrar factores de corrección que ayuden a hacer fechamientos relativos más confiables?
- ¿Podrán hacerse correcciones para tomar en cuenta el impacto en las condiciones erosivas debido a piroclastos depositados en la superficie de conos ya formados por erupciones aledañas posteriores?

Para abordar todas estas preguntas, estamos utilizando un programa de simulación de erosión en laderas llamado “Channel-Hillslope Integrated Landscape Development“ (CHILD) (Tucker et al. 2001a) , desarrollado por el grupo de investigación de Rafael Bras del Departamento de Ingeniería Civil y Ambiental del Instituto de tecnología de Massachusetts (MIT). Usando el MDE de un cono prístino, utilizamos CHILD para modelar la evolución de la morfología de un cono bajo distintas condiciones erosivas. Luego caracterizamos con la metodología desarrollada los distintos MDE generados con CHILD a distintos tiempos de erosión, con lo que es posible analizar la evolución de los parámetros morfométricos en función de procesos erosivos controlados. Esperamos que este proyecto, en complemento con el análisis de conos de escoria pertenecientes a otros campos monogenéticos como el de Michoacán-Guanajuato y el de Los Tuxtlas, ambos localizados en México y con condiciones climáticas distintas, puedan en el transcurso de pocos años darnos más información para encontrar respuestas a estas preguntas.

APÉNDICE

PARÁMETROS MORFOMÉTRICOS DE LOS CONOS ANALIZADOS.

Volcano name	Lat(N)	Lon (E)	Elevation of cone base (m.a.s.l)	Radiometric age ka ($\pm\delta Age$)	Calibrated age ka ($\pm\delta Age$)	Reference
Malinal	19.2228	-99.2179	3000	18.9±0.6 (^{14}C)	22.896±0.714	1
Xitle	19.2467	-99.2223	2900	1.67±0.035 (^{14}C)	1.580±0.049	3
Pelado	19.1511	-99.2175	3350	10±0.5 (^{14}C)	11.599±0.683	4
Ninfa (S dos Cerros)	19.1530	-98.9322	2850	14±0.5 (^{14}C)	16.978±0.667	2
Raices	19.1041	99.2566	3000	15.57±0.30 (^{14}C)	18.87±0.345	1
El Hoyo	19.0893	-99.1688	3060	>2.835±0.070 (^{14}C)	>2.961±0.094	4
				<4.690±0.090 (^{14}C)	<5.415±0.120	
Manteca	19.0894	-99.1780	3100	>2.835±0.070 (^{14}C)	>2.961±0.094	4
				<4.690±0.090 (^{14}C)	<5.415±0.120	
Teuhtli	19.2242	-99.0294	2540	>14±0.5 (^{14}C)	>16.978±0.667	5
				<31.790+0.755/-0.690 (^{14}C)	<35.908+0.908	6
Hijo de Cuauhtzin	19.1558	-99.0927	3200	>20.895±0.245 (^{14}C)	>25.150±0.322	5
Jumento	19.21	-99.31	3620		ca. 2	7,11
Pelagatos	19.09	-98.96	2960	>2.520±0.105 (^{14}C)	>2.566±0.122	2
				<14 (^{14}C)	<16.978±0.667	
Cuatzontle	19.2392	-99.2117	2930	222±52 (^{40}Ar/^{39}Ar)		8
Cuautepel	19.0911	-98.8603	2550	34±5 (^{40}Ar/^{39}Ar)		8
Malacatepec	19.1625	-99.2592	3200	95±12 (^{40}Ar/^{39}Ar)		8
Aholo	19.0911	-98.8544	2550	23±15 (^{40}Ar/^{39}Ar)		8
Mezontepec	19.1883	-99.2292	3450	11±3 (^{40}Ar/^{39}Ar)		8
*Tlayacapan	18.9729	-98.9358	1850	133±32 (^{40}Ar/^{39}Ar)		8
*Yuhualixqui	19.3178	-99.0317	2250	62±98 (^{40}Ar/^{39}Ar)		8
*Zitlaltepetl	18.9820	-98.8936	1930	35±4 (^{40}Ar/^{39}Ar)		8
*Chimalhuacan	19.2392	-99.2117	2250	1124±23 (^{40}Ar/^{39}Ar)		8
*La Estrella	19.3989	-98.9562	2250	765±30 (^{40}Ar/^{39}Ar)		8

*Jumiltepec	18.9086	-98.7822	1100	846±8 ($^{40}Ar/^{39}Ar$)		8
*Tezontle	19.0311	-99.4616	2600	21.860±0.380 (^{14}C)	26.21±0.405	9
*15 Santa Fe	19.1647	-99.4461	2660	30.500±1.160 (^{14}C)	34.87±1.365	9
*Cuauatl	19.1647	-99.4208	2800	<19.630±0.160 (^{14}C)	<23.52±0.222	9
*Tres Cruces	19.0925	-99.4841	2900	<8.490±0.070 (^{14}C)	<9.44±0.700	9
*Atlacholoaya	18.7252	-99.21150	1050	1020±160 ($^{40}Ar/^{39}Ar$)		10
**Tespomayo (N dos Cerros)	19.1530	-98.9400	2920	14±0.5 (^{14}C)	16.978±0.667	2
Paricutin	**19.4925**	**-102.2511**	**2550**	**0.075**		**Historic**

*Tabla A1. Ubicación y fechas radiométricas calibradas de conos de escoria seleccionados. Se obtuvieron edades calibradas para conos fechados con 14-C usando OxCal 4.2 2 (https://c14.arch.ox.ac.uk/embed.php?File=oxcal.html). Referencias: (1) Kirianov, 1990; (2) Agustín-Flores et al., 2011; (3) Siebe, 2000; (4) Siebe et al., 2004; 5) Siebe et al., 2005; (6) Guilbaud et al., 2015; (7) Arce et al., 2015; (8) Jaimes-Viera et al., 2018; (9) Bloomfield, 1975; (10) Arce et al. 2013, (11) Alcalá-Reygosa et al. 2018. * Solo disponible en DLR DEM. El cono marcado en negrita pertenece al Campo Volcánico Michoacán-Guanajuato.*

Volcano name		DLR		LIDAR	
	C_f (km)	$\langle D \rangle$ [m]	ΔD [m]	$\langle D \rangle$ [m]	ΔD [m]
Xitle	105.10	0.96	0.28	0.69	0.19
Jumento	105.12	0.64	0.19	0.63	0.30
Pelado	105.16	1.39	0.30	1.37	0.30
Raices	105.19	2.21	0.62	2.41	0.43
Ninfa	105.16	1.29	0.86	1.05	0.43
Malinal	105.11	1.93	0.51	2.29	0.67
Cuautepetl	105.19	2.04	0.47	2.36	0.39
Hoyo	105.20	1.38	0.22	1.12	0.20
Manteca	105.20	0.89	0.17	1.37	0.38
Pelagatos	105.19	NA	NA	0.59	0.36
Hijo de Cuahutzin	105.16	2.25	1.11	2.18	1.20
Teuhtli	105.11	1.68	0.64	1.45	0.52
Malacatepec	105.15	NA	NA	2.88	1.39
Mezontepec	105.14	1.60	0.36	1.25	0.34
Aholo	105.19	0.93	0.25	0.65	0.15
Cuatzontle	105.10	4.84	2.03	4.26	1.46
Jumiltepec	105.42	7.26	4.17	NA	NA

Tlayacapan	105.27	5.22	1.95	NA	NA
Yuhualixqui	105.05	2.24	0.61	NA	NA
Zitlaltpel	105.26	1.63	0.16	NA	NA
Chimalhuacan	105.03	8.92	3.34	NA	NA
La Estrella	105.00	10.09	1.86	NA	NA
Tezontle	105.23	4.34	1.13	NA	NA
15 Santa Fe	105.15	1.74	0.28	NA	NA
Cuauatl	105.15	2.30	1.17	NA	NA
Trescruces	105.19	1.83	0.45	NA	NA
Atlacholoaya	105.42	10.15	1.63	NA	NA
Tespomayo	105.16	1.56	0.66	NA	NA
Paricutin	104.94	0.35	0.09	NA	NA

Tabla A2: Factores de conversión Cf, AEI 〈D〉 y su respectiva desviación estándar obtenida para cada cono de escoria individual en cada DEM, en metros. La correlación con las edades radiométricas se estableció utilizando los conos de escoria en negrita.

		Hco				**Hco(inclinado)**		
	DLR		LIDAR		DLR		LIDAR	
Cono	Valor Promedio	std	Valor Promedio	std	Valor Promedio	std	Valor Promedio	std
PELAGATOS			51.56	7.24			52.74	5.15
NINFA	128.63	26.06	130.27	25.75	115.19	10.61	117.32	10.81
JUMENTO	129.65	28.00	131.98	31.42	126.79	17.84	129.24	19.62
TLALOC	141.62	13.33	140.61	12.73	141.34	12.70	141.07	9.47
OYAMEYO	210.43	56.66	203.23	49.45	203.22	21.61	198.72	20.85
HCUAUTZIN	68.13	23.21	67.15	23.40	66.46	16.62	65.54	15.42
TEUHTLI	116.88	26.25	116.67	27.56	115.05	13.15	114.81	13.63
XITLE	121.19	27.44	120.41	26.54	119.56	22.20	118.90	22.04
HOYO	80.20	17.36	81.28	18.45	79.84	16.18	80.77	16.96
MANTECA	89.99	22.93	95.31	23.24	87.72	17.58	93.42	18.04
PELADO	176.87	35.92	183.62	33.69	175.99	32.10	182.51	28.34
CIMA	102.64	5.63	91.36	26.86	99.99	7.64	89.46	26.51
RAICES	112.51	35.45	110.93	33.05	111.48	29.49	110.24	30.19
MALINAL	102.22	39.57	102.21	32.10	101.25	29.34	101.90	23.10
CUATZONTLE	58.40	25.60	67.88	35.85	56.00	15.71	59.85	18.82
CUAUTEPETL	136.78	32.75	137.86	27.91	137.54	35.66	138.89	32.81
MALACATEPEC	143.03	63.20	175.66	34.51	138.59	55.35	174.83	25.47
MEZONTEPEC	119.41	20.01	112.54	20.54	119.02	17.95	111.59	16.56
AHOLO	109.92	26.35	108.36	23.37	107.66	20.27	106.50	18.57
JUMILTEPEC	213.45	27.75			212.55	19.90		
CHILMAHUACAN	224.74	47.74			222.77	28.87		

TLAYACAPAN	106.74	22.81			106.85	22.30		
YUHUALIXQUI	159.73	15.11			160.24	22.81		
ZITLALTEPETL	93.71	17.71			92.69	13.33		
LAESTRELLA	145.19	25.97			145.47	23.99		
TEZONTLE	177.09	27.99			176.57	18.33		
15STAFE	48.29	28.75			43.85	17.52		
CUAUATL	156.41	42.77			153.64	26.49		
TRESCRUCES	102.67	35.24			99.98	30.01		
PARICUTIN	173.46	66.58			173.19	65.71		

Tabla A3: Altura de cono, considerando y no considerando la inclinación del terreno. DLR se refiere al DEM con resolución horizontal de 12m. LIDAR se refiere al DEM con resolución horizontal de 5m.

		Wco				**Wco(inclinado)**		
	DLR		LIDAR		DLR		LIDAR	
Cono	Valor Promedio	std	Valor Promedio	std	Valor Promedio	std	Valor Promedio	std
PELAGATOS			298.78	15.04			299.25	14.95
NINFA	840	80.04	849.59	64.75	842	78.92	851.87	63.69
JUMENTO	751	70.39	765.95	61.13	752	70.90	767.14	61.68
TLALOC	870	67.24	861.83	77.95	870	66.99	862.31	77.88
OYAMEYO	1284	80.57	1226.58	71.84	1288	83.06	1229.64	73.81
HCUAUTZIN	512	90.88	490.87	75.29	514	90.38	492.39	75.23
TEUHTLI	711	19.01	682.03	28.28	712	18.35	683.79	27.90
XITLE	801	49.73	772.39	54.69	803	49.48	774.21	54.59
HOYO	592	59.24	582.90	66.31	592	59.29	583.11	66.41
MANTECA	543	63.28	570.32	75.09	545	62.36	571.53	74.25
PELADO	1079	127.95	1106.99	95.50	1080	128.19	1107.60	95.97
CIMA	779	118.44	791.57	116.18	779	118.44	791.61	116.17
RAICES	945	65.73	923.89	75.76	946	65.46	924.18	75.82
MALINAL	781	155.26	795.55	166.61	782	156.67	782.61	150.62
CUATZONTLE	678.86	64.99	754.39	99.29	680.13	66.54	757.84	102.44
CUAUTEPETL	1043.56	108.56	1051.46	114.05	1044.61	108.09	1052.39	113.72
MALACATEPEC	1214.87	282.10	1437.06	111.16	1217.55	280.43	1438.11	110.39
MEZONTEPEC	902.85	125.20	857.72	96.67	903.19	125.05	858.28	96.31
AHOLO	571.90	45.93	550.88	45.53	573.67	45.76	552.28	45.24
JUMILTEPEC	1892.73	174.75			1892.94	174.77		
CHILMAHUACAN	2039.51	325.01			2041.06	324.60		
TLAYACAPAN	883.33	107.18			883.43	107.10		
YUHUALIXQUI	1076.11	158.88			1076.91	158.81		
ZITLALTEPETL	578.30	47.50			579.06	47.37		
LAESTRELLA	2803.91	538.04			2803.94	538.01		
TEZONTLE	1481.50	126.79			1481.96	126.65		
15STAFE	573.23	39.04			575.55	37.98		
CUAUATL	871.78	51.65			873.42	51.22		

TRESCRUCES	689.78	125.32			690.79	125.13		
PARICUTIN	841.53	179.99			841.70	180.10		

Tabla A4: Diámetro de base de cono, considerando y no considerando la inclinación del terreno. DLR se refiere al DEM con resolución horizontal de 12m. LIDAR se refiere al DEM con resolución horizontal de 5m.

		Wcr				**Wcr(inclinado)**		
	DLR		LIDAR		DLR		LIDAR	
Cono	Valor Promedio	std	Valor Promedio	std	Valor Promedio	std	Valor Promedio	std
PELAGATOS			157.14	44.69			161.70	50.57
NINFA	409.25	78.47	427.69	61.48	411.53	74.62	428.37	60.66
JUMENTO	328.81	11.92	323.19	11.92	318.23	21.08	324.26	11.23
TLALOC	249.41	9.94	259.95	14.90	250.10	10.58	260.89	16.21
OYAMEYO	317.33	45.95	316.16	43.01	317.35	45.94	316.21	43.01
HCUAUTZIN	178.45	5.59	180.33	4.43	178.52	5.58	180.39	4.39
TEUHTLI	238.88	24.64	235.75	18.93	238.97	24.69	235.87	19.04
XITLE	348.48	26.88	347.78	30.56	349.33	27.09	348.82	30.77
HOYO	280.44	27.67	277.52	25.40	281.15	28.12	278.11	25.59
MANTECA	153.63	11.95	155.50	10.82	153.71	11.92	155.57	10.81
PELADO	421.43	58.16	432.40	66.98	421.73	57.73	432.70	66.53
CIMA	462.41	103.70	486.53	102.82	465.75	102.57	489.69	101.71
RAICES	321.43	57.40	306.50	9.67	321.98	57.50	307.12	9.88
MALINAL	307.03	54.26	296.14	69.10	307.64	53.43	296.87	68.04
CUATZONTLE	392.56	30.67	403.10	46.02	393.27	30.95	403.96	45.97
CUAUTEPETL	509.05	34.20	507.95	37.65	513.20	34.34	512.55	35.50
MALACATEPEC	375.88	61.59	346.60	56.08	376.59	61.84	347.44	56.10
MEZONTEPEC	164.03	24.97	149.65	12.22	164.58	25.11	150.19	12.13
AHOLO	155.15	16.64	151.76	16.55	155.64	16.61	152.21	16.43
JUMILTEPEC	189.81	171.35			190.31	171.64		
CHILMAHUACAN	196.00	97.26			196.08	97.28		
TLAYACAPAN	289.70	54.19			290.65	55.43		
YUHUALIXQUI	338.60	67.26			343.09	67.01		
ZITLALTEPETL	133.49	25.65			133.63	25.68		
LAESTRELLA	283.19	201.86			284.68	203.14		
TEZONTLE	496.40	30.81			496.52	30.82		
15STAFE	262.01	14.70			262.02	14.70		
CUAUATL	255.85	17.75			257.26	17.50		
TRESCRUCES	207.75	26.05			208.12	25.95		
PARICUTIN	260.15	8.99			260.19	8.96		

Tabla A 5: Diámetro de borde de cráter , considerando y no considerando la inclinación del terreno. DLR se refiere al DEM con resolución horizontal de 12m. LIDAR se refiere al DEM con resolución horizontal de 5m.

	Dcr		**Dcr -incl**	
	DLR	LIDAR	DLR	LIDAR
Cono	Valor máximo	Valor Promedio	Valor Promedio	Valor Promedio
NINFA	105.56	104.23	105.56	104.23
JUMENTO	79.37	85.15	79.26	85.00
TLALOC	39.50	41.20	39.47	40.92
OYAMEYO	26.58	25.96	26.58	25.96
HCUAUTZIN	27.58	28.19	27.57	28.19
TEUHTLI	32.34	38.67	32.30	38.63
XITLE	107.22	105.69	106.50	104.69
HOYO	52.13	51.96	51.99	51.95
MANTECA	35.33	31.86	35.33	31.84
PELADO	71.47	68.07	71.46	68.06
RAICES	45.63	39.39	45.55	39.38
MALINAL	45.39	45.03	45.39	45.03
CUATZONTLE	70.49	59.13	70.49	59.13
CUAUTEPETL	53.84	60.13	53.23	59.54
MALACATEPEC	18.64	16.80	18.60	16.70
MEZONTEPEC	3.41	1.80	3.39	1.79
AHOLO	17.97	18.33	17.85	18.26

Tabla A6: Profundidad máxima de cráter , considerando y no considerando la inclinación del terreno. DLR se refiere al DEM con resolución horizontal de 12m. LIDAR se refiere al DEM con resolución horizontal de 5m.

		Dcr		
	DLR		LIDAR	
Cono	Valor Promedio	std	Valor Promedio	std
PELAGATOS			32.63	9.11
NINFA	89.60	14.53	92.43	11.54
JUMENTO	81.27	12.91	95.83	11.69
TLALOC	45.32	5.65	46.36	7.10
OYAMEYO	14.25	8.19	16.28	8.02
HCUAUTZIN	26.17	3.62	24.78	8.37
TEUHTLI	27.45	9.81	30.34	10.53
XITLE	112.57	12.45	108.65	13.64
HOYO	55.33	7.07	52.39	6.02
MANTECA	36.59	2.64	30.83	1.97
PELADO	70.91	13.69	70.03	13.41
CIMA	78.51	18.77	75.59	31.26
RAICES	49.60	4.60	44.73	4.66
MALINAL	42.82	3.93	41.13	3.36
CUATZONTLE	66.83	3.88	63.20	5.74

CUAUTEPETL	91.47	31.38	94.58	30.08
MALACATEPEC	23.34	10.15	24.30	9.06
MEZONTEPEC	4.53	4.02	5.25	2.90
AHOLO	20.53	4.86	21.06	5.15
JUMILTEPEC	17.21	18.34		
CHILMAHUACAN	3.10	3.10		
TLAYACAPAN	15.24	9.05		
YUHUALIXQUI	59.21	22.37		
ZITLALTEPETL	5.92	3.90		
LAESTRELLA	30.25	32.19		
TEZONTLE	111.68	9.85		
15STAFE	13.49	2.39		
CUAUATL	57.40	18.86		
TRESCRUCES	46.66	19.40		
PARICUTIN	63.85	14.17		

Tabla A7: Profundidad promedio de cráter , considerando y no considerando la inclinación del terreno. DLR se refiere al DEM con resolución horizontal de 12m. LIDAR se refiere al DEM con resolución horizontal de 5m.

		Ar				**Ar-incl**		
	DLR		LIDAR		DLR		LIDAR	
Cono	Valor Promedio	std	Valor Promedio	std	Valor Promedio	std	Valor Promedio	std
XITLE	0.15	0.03	0.16	0.03	0.15	0.02	0.15	0.02
HOYO	0.13	0.02	0.14	0.02	0.13	0.02	0.14	0.02
MANTECA	0.16	0.04	0.17	0.03	0.16	0.02	0.16	0.02
PELADO	0.16	0.02	0.17	0.02	0.16	0.02	0.16	0.02
CIMA	0.12	0.01	0.11	0.03	0.12	0.01	0.11	0.03
RAICES	0.12	0.04	0.12	0.03	0.12	0.03	0.12	0.03
MALINAL	0.13	0.04	0.13	0.03	0.13	0.02	0.13	0.02
NINFA	0.15	0.04	0.15	0.04	0.14	0.02	0.14	0.02
TEPOSMAYO	0.18	0.05			0.16	0.02		
JUMENTO	0.17	0.03	0.17	0.03	0.17	0.02	0.17	0.02
TLALOC	0.16	0.01	0.16	0.02	0.16	0.01	0.16	0.02
OYAMEYO	0.16	0.04	0.17	0.04	0.16	0.02	0.16	0.02
HCUAUTZIN	0.13	0.04	0.14	0.04	0.12803986	0.01611209	0.13183287	0.01535236
TEUHTLI	0.16	0.04	0.17	0.04	0.16	0.02	0.17	0.02
CUATZONTLE	0.09	0.03	0.09	0.04	0.08	0.02	0.08	0.02
CUAUTEPETL	0.13	0.02	0.13	0.02	0.13	0.03	0.13	0.03
MALACATEPEC	0.11	0.04	0.12	0.02	0.11	0.03	0.12	0.02
MEZONTEPEC	0.13	0.02	0.13	0.02	0.13	0.01	0.13	0.02
AHOLO	0.19	0.04	0.20	0.03	0.19	0.02	0.19	0.02

JUMILTEPEC	0.11	0.02			0.11	0.01		
CHILMAHUACAN	0.11	0.03			0.11	0.02		
TLAYACAPAN	0.13	0.03			0.13	0.03		
YUHUALIXQUI	0.14	0.02			0.14	0.02		
ZITLALTEPETL	0.16	0.03			0.16	0.02		
LAESTRELLA	0.05	0.01			0.05	0.01		
TEZONTLE	0.12	0.02			0.12	0.01		
15STAFE	0.12	0.01			0.10	0.01		
CUAUATL	0.18	0.05			0.18	0.03		
TRESCRUCES	0.15	0.04			0.14	0.02		
PARICUTIN	0.20	0.04			0.20	0.04		

Tabla A8: Razón de aspecto, considerando y no considerando la inclinación del terreno. DLR se refiere al DEM con resolución horizontal de 12m. LIDAR se refiere al DEM con resolución horizontal de 5m.

		f				**f-incl**		
	DLR		LIDAR		DLR		LIDAR	
Cono	Valor Promedio	std	Valor Promedio	std	Valor Promedio	std	Valor Promedio	std
XITLE	0.43	0.04	0.45	0.04	0.43	0.04	0.45	0.04
HOYO	0.48	0.06	0.48	0.04	0.48	0.06	0.48	0.04
MANTECA	0.29	0.04	0.27	0.04	0.28	0.04	0.27	0.04
PELADO	0.39	0.05	0.38	0.05	0.39	0.05	0.38	0.05
CIMA	0.59	0.06	0.61	0.06	0.59	0.06	0.62	0.05
RAICES	0.33	0.05	0.34	0.05	0.33	0.05	0.34	0.05
MALINAL	0.39	0.03	0.37	0.03	0.39	0.03	0.36	0.03
NINFA	0.48	0.03	0.49	0.04	0.48	0.03	0.49	0.04
TEPOSMAYO	0.31	0.09			0.33	0.07		
JUMENTO	0.42	0.01	0.42	0.02	0.41	0.03	0.41	0.01
TLALOC	0.30	0.04	0.31	0.02	0.30	0.04	0.31	0.02
OYAMEYO	0.23	0.05	0.24	0.06	0.23	0.05	0.24	0.06
HCUAUTZIN	0.35	0.06	0.35	0.08	0.34	0.06	0.35	0.08
TEUHTLI	0.32	0.05	0.31	0.06	0.32	0.05	0.31	0.05
CUATZONTLE	0.52	0.09	0.49	0.03	0.52	0.09	0.49	0.03
CUAUTEPETL	0.48	0.04	0.49	0.03	0.49	0.04	0.49	0.04
MALACATEPEC	0.29	0.09	0.27	0.07	0.29	0.09	0.27	0.06
MEZONTEPEC	0.18	0.04	0.18	0.06	0.18	0.04	0.18	0.06
AHOLO	0.26	0.04	0.27	0.04	0.26	0.04	0.27	0.04
JUMILTEPEC	0.10	0.11			0.10	0.09		
CHILMAHUACAN	0.10	0.05			0.10	0.05		
TLAYACAPAN	0.33	0.06			0.33	0.06		
YUHUALIXQUI	0.32	0.07			0.32	0.07		
ZITLALTEPETL	0.23	0.06			0.23	0.06		
LAESTRELLA	0.11	0.07			0.11	0.07		

TEZONTLE	0.34	0.04			0.34	0.04		
15STAFE	0.46	0.05			0.46	0.05		
CUAUATL	0.29	0.02			0.30	0.02		
TRESCRUCES	0.31	0.09			0.31	0.09		
PARICUTIN	0.32	0.08			0.32	0.08		

Tabla A9: Achatamiento (Wcr/Wco) considerando y no considerando la inclinación del terreno. DLR se refiere al DEM con resolución horizontal de 12m. LIDAR se refiere al DEM con resolución horizontal de 5m.

		Z				**Z-incl**		
	DLR		LIDAR		DLR		LIDAR	
Cono	Valor Promedio	std	Valor Promedio	std	Valor Promedio	std	Valor Promedio	std
XITLE	0.55	0.06	0.60	0.05	0.55	0.07	0.60	0.07
HOYO	0.54	0.03	0.57	0.03	0.54	0.04	0.57	0.05
MANTECA	0.49	0.04	0.49	0.04	0.49	0.08	0.49	0.07
PELADO	0.56	0.03	0.57	0.03	0.56	0.05	0.57	0.05
CIMA	0.51	0.05	0.48	0.10	0.50	0.06	0.47	0.09
RAICES	0.37	0.09	0.39	0.09	0.37	0.08	0.39	0.09
MALINAL	0.45	0.08	0.45	0.06	0.45	0.04	0.45	0.04
NINFA	0.52	0.03	0.54	0.03	0.47	0.08	0.50	0.09
TEPOSMAYO	0.50	0.07			0.50	0.10		
JUMENTO	0.58	0.03	0.60	0.03	0.58	0.04	0.59	0.07
TLALOC	0.47	0.07	0.49	0.08	0.47	0.07	0.49	0.05
OYAMEYO	0.44	0.05	0.45	0.05	0.44	0.07	0.45	0.06
HCUAUTZIN	0.42	0.08	0.42	0.07	0.41	0.06	0.42	0.06
TEUHTLI	0.52	0.09	0.54	0.10	0.52	0.08	0.54	0.08
CUATZONTLE	0.31	0.08	0.32	0.03	0.31	0.07	0.32	0.04
CUAUTEPETL	0.53	0.07	0.54	0.08	0.53	0.07	0.54	0.09
MALACATEPEC	0.35	0.04	0.34	0.03	0.31	0.08	0.31	0.06
MEZONTEPEC	0.32	0.05	0.33	0.04	0.32	0.05	0.33	0.04
AHOLO	0.54	0.05	0.57	0.04	0.54	0.09	0.57	0.08
JUMILTEPEC	0.24	0.06			0.24	0.05		
CHILMAHUACAN	0.27	0.10			0.27	0.09		
TLAYACAPAN	0.37	0.14			0.37	0.14		
YUHUALIXQUI	0.45	0.16			0.45	0.17		
ZITLALTEPETL	0.44	0.06			0.42	0.08		
LAESTRELLA	0.11	0.04			0.11	0.04		
TEZONTLE	0.40	0.11			0.40	0.11		
15STAFE	0.30	0.13			0.30	0.05		
CUAUATL	0.54	0.09			0.54	0.08		
TRESCRUCES	0.45	0.08			0.45	0.12		
PARICUTIN	0.61	0.06			0.61	0.06		

Tabla A10: Pendiente considerando y no considerando la inclinación del terreno. DLR se refiere al DEM con resolución horizontal de 12m. LIDAR se refiere al DEM con resolución horizontal de 5m.

		elongacion				**elongacion-incl**		
	DLR		LIDAR		DLR		LIDAR	
Cono	Valor Promedio	std	Valor Promedio	std	Valor Promedio	std	Valor Promedio	std
XITLE	0.89	0.01	0.87	0.01	0.89	0.01	0.87	0.01
HOYO	0.81	0.01	0.73	0.02	0.81	0.01	0.73	0.02
MANTECA	0.75	0.02	0.69	0.02	0.75	0.02	0.69	0.02
PELADO	0.75	0.01	0.77	0.01	0.75	0.01	0.77	0.01
CIMA	0.77	0.03	0.76	0.01	0.77	0.03	0.76	0.01
RAICES	0.97	0.01	0.98	0.01	0.97	0.01	0.98	0.01
MALINAL	0.65	0.01	0.63	0.01	0.65	0.01	0.63	0.01
NINFA	0.85	0.02	0.85	0.01	0.85	0.02	0.85	0.01
TEPOSMAYO	0.80	0.04			0.81	0.03		
JUMENTO	0.82	0.03	0.81	0.01	0.82	0.03	0.81	0.01
TLALOC								
OYAMEYO	0.83	0.02	0.89	0.01	0.83	0.02	0.88	0.01
HCUAUTZIN	0.65	0.05	0.63	0.02	0.65	0.05	0.63	0.02
TEUHTLI	0.99	0.02	0.95	0.01	1.00	0.02	0.95	0.01
CUATZONTLE	0.79	0.03	0.85	0.03	0.79	0.03	0.84	0.03
CUAUTEPETL	0.81	0.02	0.75	0.02	0.81	0.02	0.75	0.02
MALACATEPEC	0.67	0.02	0.68	0.02	0.68	0.02	0.68	0.02
MEZONTEPEC	0.84	0.02	0.82	0.02	0.84	0.02	0.82	0.02
AHOLO	0.81	0.04	0.83	0.04	0.81	0.04	0.83	0.04
JUMILTEPEC	0.91	0.01			0.91	0.01		
CHILMAHUACAN	0.75	0.01			0.75	0.01		
TLAYACAPAN	0.74	0.03			0.74	0.03		
YUHUALIXQUI	0.93	0.02			0.93	0.02		
ZITLALTEPETL	0.97	0.03			0.97	0.03		
LAESTRELLA	0.75	0.01			0.75	0.01		
TEZONTLE	0.95	0.01			0.95	0.01		
15STAFE	0.83	0.04			0.83	0.04		
CUAUATL	0.86	0.02			0.86	0.02		
TRESCRUCES	0.68	0.04			0.68	0.04		
PARICUTIN	0.58	0.04			0.58	0.04		

Tabla A11: Elongación de la base del cono considerando y no considerando la inclinación del terreno. DLR se refiere al DEM con resolución horizontal de 12m. LIDAR se refiere al DEM con resolución horizontal de 5m.

		Dcr(max)/Hco(max)				**Dcr(max)/Hco(max) (inclinado)**		
	DLR		LIDAR		DLR		LIDAR	
Cono	Valor Promedio	std	Valor Promedio	std	Valor Promedio	std	Valor Promedio	std

XITLE	0.64	0.01	0.70	0.01	0.64	0.01	0.66	0.01
HOYO	0.55	0.01	0.51	0.01	0.56	0.01	0.53	0.01
MANTECA	0.32	0.01	0.27	0.01	0.38	0.01	0.28	0.01
PELADO	0.33	0.00	0.31	0.00	0.35	0.00	0.34	0.00
CIMA	0.00	0.00	0.00	0.00	0.00	0.00	0.00	0.00
RAICES	0.31	0.01	0.27	0.01	0.31	0.01	0.28	0.01
MALINAL	0.25	0.01	0.25	0.01	0.30	0.01	0.30	0.01
NINFA	0.67	0.02	0.64	0.01	0.84	0.02	0.79	0.01
TEPOSMAYO	0.00	0.01			0.00	0.02		
JUMENTO	0.46	0.01	0.47	0.01	0.52	0.01	0.54	0.01
TLALOC	0.31	0.01	0.31	0.01	0.31	0.01	0.32	0.01
OYAMEYO	0.08	0.01	0.09	0.00	0.11	0.01	0.11	0.00
HCUAUTZIN	0.26	0.02	0.28	0.01	0.31	0.02	0.33	0.01
TEUHTLI	0.20	0.01	0.25	0.01	0.24	0.02	0.29	0.01
CUATZONTLE	0.58	0.02	0.45	0.02	0.79	0.03	0.60	0.02
CUAUTEPETL	0.63	0.01	0.36	0.01	0.62	0.01	0.34	0.01
MALACATEPEC	0.16	0.01	0.08	0.01	0.18	0.01	0.08	0.01
MEZONTEPEC	0.07	0.01	0.02	0.01	0.07	0.01	0.02	0.02
AHOLO	0.17	0.01	0.13	0.01	0.21	0.01	0.21	0.02
JUMILTEPEC	0.18	0.00			0.18	0.00		
CHILMAHUACAN	0.04	0.00			0.04	0.00		
TLAYACAPAN	0.22	0.01			0.22	0.01		
YUHUALIXQUI	0.46	0.01			0.44	0.01		
ZITLALTEPETL	0.10	0.01			0.11	0.01		
LAESTRELLA	0.42	0.01			0.44	0.01		
TEZONTLE	0.51	0.00			0.57	0.01		
15STAFE	0.23	0.01			0.26	0.02		
CUAUATL	0.35	0.00			0.39	0.01		
TRESCRUCES	0.48	0.01			0.54	0.01		
PARICUTIN	0.32	0.00			0.33	0.00		

Tabla A12: Razón entre la profundidad máxima del cráter y la altura máxima del cono considerando y no considerando la inclinación del terreno. DLR se refiere al DEM con resolución horizontal de 12m. LIDAR se refiere al DEM con resolución horizontal de 5m.

		Orientacion EM				**Crat off-set (metros)**		
	DLR		LIDAR		DLR		LIDAR	
Cono	GRADOS	GEOG	GRADOS	GEOG	METROS		METROS	
XITLE	127.62	NW-SE	125.18	NW-SE	28.39		26.72	
HOYO	74.01	N-S	77.59	N-S	38.33		34.51	
MANTECA	100.07	N-S	106.44	N-S	29.64		34.28	
PELADO	130.16	NW-SE	129.77	NW-SE	24.59		44.70	
CIMA	170.59	E-W	3.18	E-W	59.71		35.49	

RAICES	31.98	NE-SW	20.74	NE-SW	32.84		35.03	
MALINAL	130.82	NW-SE	132.92	NW-SE	11.36		40.53	
NINFA	47.50	NE-SW	54.02	NE-SW	103.34		98.66	
TEPOSMAYO	73.31	N-S			99.03			
JUMENTO	164.96	E-W	167.72	E-W	53.71		47.47	
TLALOC	21.73	E-W	21.51	E-W	175.74		182.48	
OYAMEYO	172.96	E-W	147.75	E-W	160.38		141.85	
HCUAUTZIN	110.65	N-S	107.58	N-S	43.90		63.51	
TEUHTLI	163.22	E-W	141.01	NW-SE	50.93		72.62	
CUATZONTLE	167.20	E-W	165.15	E-W	161.76		148.67	
CUAUTEPETL	94.66	N-S	98.01	N-S	57.14		69.11	
MALACATEPEC	101.00	N-S	97.45	N-S			56.23	
MEZONTEPEC	149.61	NW-SE	125.40	NW-SE	57.73		44.32	
AHOLO	75.10	N-S	73.55	N-S	22.29		28.31	
JUMILTEPEC	37.89	NE-SW			0.09			
CHILMAHUACAN	8.10	E-W			142.41			
TLAYACAPAN	179.85	E-W			84.90			
YUHUALIXQUI	90.39	N-S			38.19			
ZITLALTEPETL	152.48	NW-SE			37.96			
LAESTRELLA	100.12	N-S			333.92			
TEZONTLE	98.34	N-S			60.06			
15STAFE	81.48	N-S			40.12			
CUAUATL	133.93	NW-SE			55.10			
TRESCRUCES	166.51	E-W			81.87			
PARICUTIN	46.02	NE-SW			31.67			

Tabla A13: Orientación del eje mayor de la base del cono y distancia entre centro de la base del cono y centro del cráter. DLR se refiere al DEM con resolución horizontal de 12m. LIDAR se refiere al DEM con resolución horizontal de 5m.

		VOLUMEN (Km^3)				VOLUMEN INCLINADO (Km^3)		
	DLR		LIDAR		DLR		LIDAR	
Cono	(KM^3)		(KM^3)		(KM^3)		(KM^3)	
XITLE	0.12	0.03	0.11	0.03	0.10	0.02	0.09	0.02
HOYO	0.04	0.01	0.04	0.01	0.04	0.01	0.04	0.01
MANTECA	0.03	0.01	0.04	0.01	0.03	0.01	0.04	0.01
PELADO	0.31	0.07	0.33	0.06	0.29	0.06	0.31	0.05

RAICES	0.17	0.05	0.17	0.05	0.15	0.04	0.16	0.05
MALINAL	0.09	0.04	0.10	0.03	0.09	0.03	0.09	0.02
NINFA	0.14	0.03	0.15	0.03	0.11	0.01	0.12	0.01
TEPOSMAYO					0.05	0.01		
JUMENTO	0.11	0.03	0.12	0.03	0.10	0.02	0.10	0.02
TLALOC								
OYAMEYO	0.47	0.13	0.46	0.11	0.44	0.05	0.44	0.05
HCUAUTZIN	0.02	0.01	0.02	0.01	0.02	0.01	0.02	0.01
TEUHTLI	0.09	0.02	0.08	0.02	0.08	0.01	0.07	0.01
CUATZONTLE	0.04	0.02	0.07	0.04	0.03	0.01	0.05	0.02
CUAUTEPETL	0.25	0.06	0.23	0.05	0.23	0.07	0.22	0.06
MALACATEPEC	0.33	0.15	0.38	0.08	0.32	0.13	0.38	0.06
MEZONTEPEC	0.14	0.02	0.14	0.03	0.14	0.02	0.14	0.02
AHOLO	0.05	0.01	0.05	0.01	0.05	0.01	0.04	0.01
JUMILTEPEC	0.94	0.12			0.90	0.09		
CHILMAHUACAN	1.36	0.29			1.34	0.18		
TLAYACAPAN	0.12	0.03			0.11	0.03		
YUHUALIXQUI	0.30	0.03			0.27	0.04		
ZITLALTEPETL	0.05	0.01			0.04	0.01		
LAESTRELLA	1.66	0.30			1.58	0.27		
TEZONTLE	0.52	0.09			0.46	0.06		
15STAFE	0.03	0.02			0.02	0.01		
CUAUATL	0.15	0.04			0.14	0.03		
TRESCRUCES	0.07	0.02			0.06	0.02		
PARICUTIN	0.14	0.06			0.13	0.05		

Tabla A14: Aproximación del volumen del cono considerando y no considerando la inclinación del terreno. DLR se refiere al DEM con resolución horizontal de 12m. LIDAR se refiere al DEM con resolución horizontal de 5m.

		CI				CI-incl		
	DLR		LIDAR		DLR		LIDAR	
NINFA	0.258	0.049	0.244	0.035	0.256	0.047	0.243	0.034
JUMENTO	0.241	0.009	0.263	0.010	0.249	0.016	0.262	0.009
TLALOC	0.158	0.006	0.158	0.009	0.158	0.007	0.157	0.010
OYAMEYO	0.084	0.012	0.082	0.011	0.084	0.012	0.082	0.011
HCUAUTZIN	0.155	0.005	0.156	0.004	0.154	0.005	0.156	0.004
TEUHTLI	0.135	0.014	0.164	0.013	0.135	0.014	0.164	0.013
XITLE	0.308	0.024	0.304	0.027	0.305	0.024	0.300	0.026
HOYO	0.186	0.018	0.187	0.017	0.185	0.018	0.187	0.017
MANTECA	0.230	0.018	0.205	0.014	0.230	0.018	0.205	0.014
PELADO	0.170	0.023	0.157	0.024	0.169	0.023	0.157	0.024
RAICES	0.142	0.025	0.129	0.004	0.141	0.025	0.128	0.004

MALINAL	0.148	0.026	0.152	0.035	0.148	0.026	0.152	0.035
CUATZONTLE	0.180	0.014	0.147	0.017	0.179	0.014	0.146	0.017
CUAUTEPETL	0.106	0.007	0.118	0.009	0.104	0.007	0.116	0.008
MALACATEPEC	0.050	0.008	0.048	0.008	0.049	0.008	0.048	0.008
MEZONTEPEC	0.021	0.003	0.012	0.001	0.021	0.003	0.012	0.001
AHOLO	0.116	0.012	0.121	0.013	0.115	0.012	0.120	0.013

Tabla A15: Profundidad promedio de cráter , considerando y no considerando la inclinación del terreno. DLR se refiere al DEM con resolución horizontal de 12m. LIDAR se refiere al DEM con resolución horizontal de 5m.

REFERENCIAS

Agustín-Flores, J., Siebe, C., Guilbaud, M-N. (2011). Geology and geochemistry of Pelagatos, Cerro del Agua, and Dos Cerros monogenetic volcanoes in the Sierra Chichinautzin volcanic field, south of México City. Journal of Volcanology and Geothermal Research, 201:143–162.

Alcalá-Reygosa, J., Arce, J.L., Schimmelpfennig, I., Muñoz Salinas, E., Castillo Rodriguez, M., Léanni, L., ASTER Team, Aumaître, G., Bourlès, D., Keddadouche, K., 2018. Revisiting the age of the Jumento volcano, Chichinautzin Volcanic Field (Central Mexico), using in situ-produced cosmogenic 10Be. J. Volcanol. Geotherm. Res. 366, 112–119.

Arce, J.L., Layer, P.W., Lassiter, J.C., Benowitz, J.A., Macías, J.L., Ramírez-Espinosa, J. (2013). 40Ar/39Ar dating, geochemistry, and isotopic analyses of the quaternary Chichinautzin volcanic field, south of Mexico City: implications for timing, eruption rate, and distribution of volcanism. Bull. Volcanol. 75, 774. https://doi.org/10.1007/ s00445-013- 0774-6.

Arce, J.L., Muñoz-Salinas, E., Castillo, M., Salinas, I.(2015). The ~2000 yr BP Jumento volcano, one of the youngest edifices of the Chichinautzin Volcanic Field, Central Mexico, Journal of Volcanology and Geothermal Research, 308: 30-38.

Avellán, D.R., Cisneros-Máximo, G., Macías, J.L., Gómez-Vasconcelos, M.G., Layer, P.W., Sosa-Ceballos, G., Robles-Camacho, J. (2020). Eruptive chronology of monogenetic volcanoes northwestern of Morelia–Insights into volcano-tectonic interactions in the central-eastern Michoacán-Guanajuato Volcanic Field, México. Journal of South American Earth Sciences, 100, p.102554. https://doi.org/10.1016/j.jsames.2020.102554

Bemis, K., Ferencz, M., (2017). Morphometric analysis of scoria cones: the potential for inferring process from shape. Geol. Soc. Lond., Spec. Publ. 446, 61–100. https://doi.org/ 10.1144/SP446.9.

Ban, M., Hasenaka, T., Delgado Granados, H., Takaoka, N. (1992). K-Ar ages of lavas from shield volcanoes in the Michoacán-Guanajuato volcanic field, Mexico: Geofísica Internacional, 31, 467-473.

Bloomfield, K. (1975). A late quaternary monogenetic volcano field in central Mexico. Geologische Rundschau, 6: 476–497.

Chevrel, M.O., Siebe, C., Guilbaud, M.N., Salinas, S. (2016). The AD 1250 El Metate shield (Michoacán): Mexico's most voluminous Holocene eruption and its significance for archaeology and hazards: The Holocene, 26(3), 471-488, https://doi.org/10.1177/0959683615609757

Connor, C.B., (1987). Structure of the Michoacán-Guanajuato volcanic field, Mexico,Journal of Volcanology and Geothermal Research,Vol. 33, Issues 1–3, 91-200. https://doi.org/10.1016/0377-0273(87)90061-8.

Dohrenwed, J.C., Wells, S.G., Turrin, B.D. (1986), Degradation of Quaternary cinder cones in the Cima volcanic field, Mojave Desert, California. . *Geological Society of American Bulletin* , 97, 421-427.

Espindola, J.M., Lopez-Loera, H., Mena,M., Zamora-Camacho, A. (2016). Internal architecture of the Tuxtla volcanic field, Veracruz, Mexico, inferred from gravity and magnetic data, Journal of Volcanology and Geothermal Research, Vol. 324, 15-27. https://doi.org/10.1016/j.jvolgeores.2016.05.006.

Hasenaka, T. and Carmichael, Ian S.E.(1985) A compilation of location, size and geomorphological parameters of volcanoes of the Michoacán-Guanajuato volcanic field, central Mexico. Geofisica Internacional, 24(4):577–607.

Hasenaka, T., (1994). Size, distribution, and magma output rate for shield volcanoes of the Michoacán-Guanajuato volcanic field, Central Mexico, Journal of Volcanology and Geothermal Research, Vol. 63, Issues 1–2, 13-31. https://doi.org/10.1016/0377-0273(94)90016-7.

Hooper, D.M., Sheridan, M.F., (1994) Computer-simulation models of scoria cone degradation and the geomorphologic dating of scoria cones in the Colima volcanic complex, Mexico Abstract. Volcán de Colima: 4th. International Meeting and Decade Volcano Workshop, Universidad de Colima, Colima, Mexico, pp. 103–105.

Hooper, D.M., Sheridan, M.F., (1998) Computer-simulation models of scoria cone degradation. Journal of Volcanology and Geothermal Research, Vol. 83:241–267,

Kereszturi, G. and Németh, K. (2012) Structural and morphometric irregularities of eroded Pliocene scoria cones at the Bakony–Balaton Highland Volcanic Field, Hungary. Geomorphology, Vol. 136, 45–58.

Kereszturi, G. and Németh, K. (2012). Monogenetic Basaltic Volcanoes: Genetic Classification, Growth, Geomorphology and Degradation, Updates in Volcanology - New Advances in Understanding Volcanic Systems, Dr. Karoly Nemeth (Ed.), InTech, DOI: 10.5772/51387. Available from: http://www.intechopen.com/books/updates-in-volcanology-new-advances-in-understanding-volcanic- systems/monogenetic-basaltic-volcanoes-genetic-classification-growth-geomorphology-and-degradation

Kirianov, V.Y., Koloskov, A.B., la Cruz, De, 1990. The Major Stages of Manifestation of Recent Volcanism in the Chichinautzin Zone. Geological Series 311. USSR Academy of Sciences, pp. 432–434.

Kuhl, F., and Giardina, C. R., (1982), Elliptic Fourier features of a closed contour: Comput. Graph. Image Process., v. 18, p. 236–258.

Gómez-Vasconcelos, M.G., Garduño-Monroy, V.H., Macías, J.L., Layer, P.W., and Benowitz, J.A. (2015). The Sierra de Mil Cumbres, Michoacán, México: Transitional volcanism between the Sierra Madre Occidental and the Trans-Mexican Volcanic Belt: Journal of Volcanology and Geothermal Research, Vol. 301, p. 128–147, https://doi.org/10.1016/j.jvolgeores.2015.05.005.

Gómez-Vasconcelos, M.G., Macías, J.L., Avellán, D.R. , Sosa-Ceballos, G., Garduño-Monroy, V.H., Cisneros-Máximo, G., Layer, P.W., Benowitz, J., López-Loera, H., Mendiola López, F. , Perton, M. (2020). The control of preexisting faults on the distribution, morphology, and volume of monogenetic volcanism in the Michoacán-Guanajuato Volcanic Field. GSA Bulletin ; 132 (11-12): 2455–2474.
doi: https://doi.org/10.1130/B35397.1

Gómez-Vasconcelos, M.G., Avellán, D.R., Soria-Caballero, D., Macías, J.L., Velázquez-Bucio, M.M., Jiménez-Haro, A., Israde-Alcántara, I., Garduño- Monroy, V.H., Ávila-Olivera, J.A., Figueroa-Soto, A., Cisneros-Máximo, G., Cardona-Melchor, S. (2021). Geomorphic characterization of faults as earthquake sources in the Cuitzeo Lake basin, central México: Journal of South American Earth Sciences, 103196, https//doi.org/10-1016/j. jsames.2021.103196

Grosse, P., Ochi Ramacciotti, M. L., Escalante, F., Guzmán, S., Orihashi, Y., Sumino, H., (2020). Geomorphology, morphometry, spatial distribution and ages of mafic monogenetic volcanoes of the Peinado and Incahuasi fields, southernmost Central Volcanic Zone of the Andes. Journal of Volcanology and Geothermal Research, 401. Article 106966. https://doi.org/10.1016/j.jvolgeores.2020.106966

Guilbaud, M.-N., Siebe, C., Layer, P., Salinas, S., Castro-Govea, R., Garduño- Monroy, V.H., Le Corvec, N. (2011). Geology, geochronology, and tectonic setting of the Jorullo volcano region, Michoacán, México: Journal of Volcanology and Geothermal Research, 201, 97-112, https://doi. org/10.1016/j.jvolgeores.2010.09.005

Guilbaud, M.-N., Siebe, C., Layer, P., Salinas, S. (2012). Reconstruction of the volcanic history of the Tacámbaro-Puruarán area (Michoacán, México) reveals high frequency of Holocene monogenetic eruptions: Bulletin of Volcanology, 74, 1187-1211, https://doi.org/10.1007/s00445-012-0594-0

Guilbaud, M.N., Arana-Salinas, L., Siebe, C., Barba-Pingarrón, L.A., Ortiz, A. (2015). Volcanic stratigraphy of a high-altitude Mammuthus columbi (Tlacotenco, Sierra Chichinautzin), Central México. Bulletin of Volcanology: 77:17.

Guilbaud, M.N., Hernández-Jiménez, A., Siebe, C., Salinas, S. (2021). Las Cabras volcano, Michoacán-Guanajuato Volcanic Field, México: Topographic, climatic, and shallow magmatic controls on scoria cone eruptions. Revista Mexicana de Ciencias Geológicas. Vol. 38- 2. 101-121.
htt|p:/v/.d3x8.do|i.onrúgm/1.02.22|20w1w/cwge.rom.2c0g0.u7n2a9m02.me.2x0|21D.2O.1I:6h4t5tp:

Jaimes-Viera, M.C., Martin Del Pozzo, A., Layer, P.W., Benowitz, J.A., Nieto-Torres, A., (2018). Timing the evolution of a monogenetic volcanic field: Sierra Chichinautzin, Central Mexico. Journal of Volcanology and Geothermal Research, 356: 241–267 https://doi.org/10.1016/j.jvolgeores.2018.03.013

Kervyn M., Ernst G.G.J., Carracedo, J.C, and Jacobs, P. (2012). Geomorphometric variability of "monogenetic" volcanic cones: Evidence from mauna kea, lanzarote and experimental cones. Geo- morphology, 136:59–75.

Kshirsagar, P., Siebe, C., Guilbaud, M.N., Salinas, S., (2016). Geological and environmental controls on the change of eruptive style (phreatomagmatic to Strombolian-effusive) of Late Pleistocene El Caracol tuff cone and its comparison with adjacent volcanoes around the Zacapu basin (Michoacán, México): Journal of Volcanology and Geothermal Research, 318, 114-133, https://doi.org/10.1016/j.jvolgeores.2016.03.015

Kirianov, V.Y., Koloskov, A.B., De la Cruz, S., Martin del Pozzo, A.L. (1990). The Major Stages of Manifestation of Recent Volcanism in the Chichinautzin Zone. Geological Series 311. USSR Academy of Sciences, pp. 432–434

Larrea, P., Siebe, C., Juárez-Arriaga, E., Salinas, S., Ibarra, H., Böhnel, H. (2019b). The ~AD 500-700 (Late Classic) El Astillero and El Pedregal volcanoes (Michoacán, Mexico): a new monogenetic cluster in the making?: Bulletin of Volcanology, 81(10), 59, https://doi.org/10.1007/s00445-019-1318-5

Mahgoub, A.N., Böhnel, H., Siebe, C., Salinas, S., Guilbaud, M.N. (2017) Paleomagnetically inferred ages of a cluster of Holocene monogenetic eruptions in the Tacámbaro-Puruarán area (Michoacán, Mexico): Implications for future hazards: Journal of Volcanology and Geothermal Research, 347, 360-370, https://doi.org/10.1016/j.jvolgeores.2017.10.004

Martin del Pozzo, A.L.(1982). Monogenetic vulcanism in sierra Chichinautzin, México. Bulletin Volcanology, 45(1):9–24.

McGuire, L. A., J. D. Pelletier, and J. J. Roering (2014), Development of topographic asymmetry: Insights from dated cinder cones in the western United States, J. Geophys. Res. Earth Surf., 119, 1725–1750, doi:10.1002/2014JF00308

Németh, K., and S. J. Cronin. 2007. Syn- and post-eruptive erosion, gully formation, and morphological evolution of a tephra ring in tropical climate erupted in 1913 in West Ambrym, Vanuatu. Geomorphology 86:115-130.

Nieto-Torres, A., Martin Del Pozzo, A.L. (2019). Spatio-temporal hazard assessment of a monogenetic volcanic field, near México City. Journal of Volcanology and Geothermal Research, Vol. 371, 46–58. https://doi.org/10.1016/j.jvolgeores.2019.01.006..

Osorio-Ocampo, S., Macías, J.L., Pola, A., Cardona-Melchor, S., Sosa-Ceballos, G., Garduño-Monroy, V.H., Layer, P.W., García-Sánchez, L., Perton, M., Benowitz, J.,(2018) The eruptive history of the Pátzcuaro Lake area in the Michoacán Guanajuato Volcanic Field, central México: Field mapping, C-14 and 40Ar/39Ar geochronology: Journal of Volcanology and Geothermal Research, 358, 307-328.

Ownby, S.E., Lange, R.A., Hall, C.M., Delgado-Granados, H. (2011) Origin of andesite in the deep crust and eruption rates in the Tancítaro–Nueva Italia region of the central Mexican arc. Geol Soc Am Bull 123(1– 2):274–294

Parrot, J.F. (2009) Tri-dimensional parameterisation: an automated treatment to study the evolution of volcanic cones , *Géomorphologie : relief, processus, environnement*. URL : http://geomorphologie.revues.org/2723 ; DOI : 10.4000/ geomorphologie.2723

Perron, J. T., W. E. Dietrich, and J. W. Kirchner (2008), Controls on the spacing of first-order valleys, *J. Geophys. Res.*, *113*, F04016, doi:10.1029/2007JF000977.

Perron, J. T., J. W. Kirchner, and W. E. Dietrich (2009), Formation of evenly spaced ridges and valleys, Nature, 460, 502–505, doi:10.1038/nature08174.

Perron, J. T. (2011), Numerical methods for nonlinear hillslope transport laws, *J. Geophys. Res.*, *116*, F02021, doi:10.1029/2010JF001801.

Porter, S.C. (1972). Distribution,morphology, and sizefrequency of cinder Cones on Mauna Kea Volcano, Hawaii. Geol. Soc, Am. Bull. 83, 3607–3612. http://dx.doi.org/10.1130/0016- 7606(1972)83[3607:DMASFO]2.0.CO;2

Reyes-Guzmán, N., Siebe, C., Chevrel, M.O., Guilbaud, M.N., Salinas, S., Layer, P., (2018). Geology and radiometric dating of Quaternary monogenetic volcanism in the western Zacapu lacustrine basin (Michoacán, México): implications for archeology and future hazard evaluations: Bulletin of Volcanology, 80(2), 18, 1-20, https://doi.org/10.1007/s00445-018-1193-5

Siebe, C., (2000). Age and archaeological implications of Xitle volcano, southwestern basin of Mexico-City. Journal of Volcanology and Geothermal Research, 104:45–64.

Siebe, C., Rodriguez-Lara, V., Schaaf, P. (2004). Radiocarbon ages of holocene Pelado, Guespalapa, and Chichinautzin scoria cones, south of Mexico city: implications for archaeology and future hazards. Bulletin of Volcanology, 66:203–225.

Siebe, C., Arana-Salinas, L., Abrams, M., (2005). Geology and radiocarbon ages of Tlaloc, Tlacotenco, Cuauhtzin, Hijo del Cuauhtzin, Teuhtli, and Ocusacayo monogenetic volcanoes in the central part of the Sierra Chichinautzin, Mexico. Journal of Volcanology and Geothermal Research, 141:225–243.

Siebe, C., Guilbaud M-N, Salinas S, Kshirsagar P, Oryaëlle Chevrel M, Fuente JR, Hernández-Jiménez A,, Godínez L. (2014). Monogenetic volcanism of the Michoacán-Guanajuato Volcanic Field:Maar craters of the Zacapu basin and domes, shields, and scoria cones of the Tarascan highlands (Paracho-Paricutin region). Pre-meeting field guide for the 5th International Maar Conference, Querétaro, México. http://maar2014.geociencias.unam.mx/

Sieron, K., Juárez Cerrillo, S.F., González-Zuccolotto, K. (2021). Morphology and distribution of monogenetic volcanoes in Los Tuxtlas Volcanic Field, Veracruz, Mexico: implications for hazard assessment. *Bull Volcanol* **83,** 47. https://doi.org/10.1007/s00445-021-01467-y

Schmittbuhl M.,, Allenbach B., Le Minor J.M., Schaaf A. (2003), Elliptical Descriptors: Some Simplified Morphometric Parameters for the Quantification of Complex Outlines, Mathematical Geology, Vol. 35, No. 7.p.853-871.

Tucker, G.E., Lancaster, S.T., Gasparini, N.M., and Bras, R.L. (2001a) The Channel-Hillslope Integrated Landscape Development (CHILD) Model, in Land- scape Erosion and Evolution Modeling, edited by R.S. Harmon and W.W. Doe III, Kluwer Academic/Plenum Publishers, pp. 349-388.

Wood, C.A.(1980a) Morphometric evolution of cinder cones. Journal of Volcanology and Geothermal Research, 7:387–413.

Wood, C.A.(1980b) Morphometric analysis of cinder cone degradation. Journal of Volcanology and Geothermal Research, 8:137–160.

Zarazúa-Carbajal, M.C. and De la Cruz-Reyna, S. (2020) . Morpho-chronology of monogenetic cones from their level contour curves and vertical cross sections. Applications to the Chichinautzin monogenetic field, Central Mexico, Journal of Volcanology and Geothermal Research, Vol 407C, 107093. https://doi.org/10.1016/j.jvolgeores.2020.107093

Zarazúa-Carbajal, M.C. and De la Cruz-Reyna, S. (2021a) Digital Elevation Model resolution: Effects on the chronometry-oriented morphological analysis of scoria cones in the Sierra Chichinautzin, central Mexico. Geomorphology, Vol 389, 107842. https://doi.org/10.1016/j.geomorph.2021.107842

Zarazúa-Carbajal, M.C. and De la Cruz-Reyna, S. (2021b). A Matlab App for calculating the age-related degree of erosion of monogenetic scoria cones from DEM data. MethodsX, Vol. 8C, 101454, 10.1016/j.mex.2021.101454.